Advanced models and algorithms to provide multiple grid services with battery storage systems

THÈSE N^O 8734 (2018)

PRÉSENTÉE LE 21 SEPTEMBRE 2018
À LA FACULTÉ DES SCIENCES ET TECHNIQUES DE L'INGÉNIEUR
GROUPE SCI STI RC
PROGRAMME DOCTORAL EN ENERGIE

ÉCOLE POLYTECHNIQUE FÉDÉRALE DE LAUSANNE

POUR L'OBTENTION DU GRADE DE DOCTEUR ÈS SCIENCES

PAR

Emil NAMOR

acceptée sur proposition du jury:

Prof. D. Dujic, président du jury
Dr S.-R. Cherkaoui, Dr D. Torregrossa, directeurs de thèse
Prof. J. A. Pecas Lopes, rapporteur
Dr S. Colombi, rapporteur
Prof. M. Paolone, rapporteur

A nonno Dante,

Acknowledgements

Abstract

Battery energy storage systems (BESSs) are expected to play a major role in the power grid of the near future. These devices, capable of storing and returning electrical energy, are valuable assets to a grid that integrates more and more distributed, intermittent and renewable generation. Compared to renewable energy sources, however, battery storage systems are still in an early stage of deployment and the way to exploit them in an optimal way is still subject of research. In this respect, this thesis develops two lines of investigation to reach an optimal utilisation of these devices. In its first part, the thesis proposes a control framework to operate a utility-scale BESS connected to a distribution feeder. This control framework allows to provide a set of services: dispatch of the operation of such feeder, load levelling, frequency response. It is structured in a period-ahead and a real-time phase. The former plans the BESS operation for a given time horizon through the solution of optimization problems. These take into account the BESS state of energy as well as forecast scenarios of quantities such as the feeder prosumption and of the BESS energy needs due to the frequency response service. The real-time phase determines the BESS power injections a resolution as fast as 1 second and, in the case of the dispatch, relies on model predictive control. Moreover, the thesis proposes the formulation of a framework for the simultaneous deployment of multiple services. The objective of this is to maximise the BESS exploitation in the presence of uncertainty. All the proposed methods are validated experimentally, on the 560 kWh/720 kVA BESS installed on EPFL campus. This extensive validation demonstrates their effectiveness and deployability. In its second part, the thesis discusses the integration of electrochemical models in the control of BESSs. Such models, compared to more conventional equivalent circuits or empirical ones, can provide deeper insight in the processes occurring within Li-ion cells - the founding elements of BESSs - and by consequence a more effective operation of BESSs. The thesis proposes a method to identify the parameters of one of such models - the single particle model - and, again, validates it experimentally. Moreover, in its final chapter, the thesis provides a proof-of-concept by simulations of the advantages of the integration of electrochemical models in the control framework proposed in its first part and, in general, in BESS control.

Résumé

Les dispositifs de stockage électrochimique d'énergie (*battery energy storage systems* ou BESSs) sont supposés jouer un role fondamental dans les réseaux électriques du futur. Ces dispositifs, capables de stocker et fournir de l'energie électrique, sont des atouts de valeur pour les réseaux qui intègrent de plus en plus de generation distribuée, intermittente et renouvelable. Toutefois, par rapport aux sources d'énergie renouvelable, les dispositifs de stockage électrochimique sont encore dans une phase initial de déploiement et la façon optimale de les exploiter est encore sujette à de la recherche. A cet égard, cette thèse développe deux directions de recherche pour atteindre une utilisation optimale de ces dispositifs. Dans sa premiere partie, la thèse propose une structure de contrôle pour exploiter un dispositif BESS à l'échelle industrielle, connecté à un réseau de distribution. Cette structure de contrôle permet de fournir un ensemble de services, à savoir le dispatch du feeder, le nivellement de sa charge, la réponse en fréquence. C'est organisée en une phase *jour d'avant*, exécutée à l'avance, et une phase en temps reel. La premiere planifie l'operation du BESS pour un horizon temporel donné à travers la solution dun problème d'optimisation. Cela prend en considération l'état de charge du BESS ainsi que des scenarios de prevision de quantités comme la prosumption du feeder et les besoins en énergie du BESS dus au déploiement de la réponse à la variation de fréquence. La phase en temps réel determine les injections de puissance du BESS avec une resolution d'un second et, pour le cas particulier du dispatch, elle est basée sur du contrôle predictive. De plus, cette thèse propose la formulation d'une structure de contrôle pour le déploiement simultané de plusieurs services. L'objectif est de maximiser l'exploitation du BESS vis à vis des sources d'incertitude. Toutes les méthodes proposés sont validé expérimentalement, grace au BESS de 560 kWh/720 kVA BESS installé sur le campus du EPFL. Cette validation extensive démontre leur efficacité et leur applicabilité. Dans sa deuxième partie, la thèse discute l'integration de modèles électrochimiques dans le contrôle du BESS. Ces modèles, comparés à des modèles plus conventionnels, circuitales ou empiriques, peuvent fournir une compréhension en profondeur des processus qui ont lieu dans les cellules aux ions de Lithium - les elements fondamentaux des BESSs - et en consequence un contrôle des BESSs plus efficace. La thèse propose une méthode pour identifier les paramètres d'un de ces modèles - le single particle model - et, encore, sa validtion expérimentale. De plus, dans le chapitre finale, la thèse fournit une preuve de concept à travers des simulations des advantages de l'integration des modèles électrochimiques dans la structure de contrôle proposée dans la premiere partie de la thèse et, en general, dans le contrôle des BESSs.

Contents

Contents

List of Figures

List of Tables

List of Tables

List of acronyms

AR	Autoregressive (model)
BESS	Battery energy storage system
DOD	Depth of discharge
EFR	Enhanced frequency response
EOL	End of life
EPFL	École Polytechnique Fédérale de Lausanne
GCP	Grid connection point
GITT	Galvanostatic intermittent tritation technique
LTO	Lithium titanate oxide
MPC	Model predictive control
NCA	Lithium Nichel Cobalt Aluminium Oxide
P2D	Pseudo-2-dimensional (model)
SEI	Solid-electrolyte interphase
SOC	State of charge
SOE	State of energy
SPM	Single particle model

Introduction

Motivations of the Thesis

In the early two-thousands, power systems went through a revolution, caused by the integration of distributed renewable energy sources. These are today ubiquitous and cheap. However, their integration poses considerable challenges, related to the variability of their power output and the strain that this causes to the grid infrastructure. Storage technologies are seen as the answer to many of these challenges and a constitutional element of future decarbonized power systems. Therefore, a similar trend of massive deployment is expected for energy storage devices in the upcoming years. Among various contenders, battery energy storage systems (BESSs) - and in particular Li-ion based BESSs - have emerged as a strong candidate as main energy storage technology. They are reliable, have high efficiency, high power and power rates capabilities and long lifetime. However, their cost is still high and to enable the widespread deployment of these devices, several technical improvements are needed. Some are matter for chemists: build better and cheaper cells. Others are research subjects for power systems and control engineers. This thesis focuses on the latter ones. It aims at developing and demonstrating techniques to operate BESSs so that their power and energy capabilities are maximally exploited, despite the uncertainties related to BESS operation and despite the ageing that this operation causes to these devices.

The methods proposed and demonstrated throughout this thesis follow two interconnected lines of research, developed in the two parts of the manuscript. BESSs have limited energy capacity and the deployment of the services for which their are installed depends heavily on uncertain variables. These are for example the stochastic *prosumption* of the resources to which they are coupled or the regulating signal they follow when providing ancillary services. Optimal control needs therefore to be planned so to take into account these uncertainties and, at the same time *i)* ensure that the services are provided reliably and *ii)* possibly ensure that the BESS is exploited as much as possible, so that assets that are so valuable do not remain unused or partially used. The first part of the thesis deals with this challenge and proposed and validates several control algorithms to provide grid services in such an optimal way. Moreover, this thesis aims at integrating in the control of BESS the consideration of their ageing. Being valuable assets, BESSs should be exploited for as many years as possible, i.e. their lifetime should be maximised. This thesis considers this issue, by presenting a method

for the empirical assessment of ageing and integration in control.

The second part of the thesis focuses on another specific (but equally important) aspect of BESS control. In fact, the algorithms presented in the first part exploit, in various ways, battery models. These are used, for instance, to predictively determine BESS power trajectories that satisfy the constraints or for the aforementioned ageing assessment. These models can be trivial as well as extremely complex and, most often, the models used in control are rather simple. This allows for their easy integration into the control, at the expense of some accuracy and some insight in the processes actually governing the storage of energy in BESSs. This thesis shows how using more complex, advanced electrochemical models can, on the contrary, bring substantial benefit to BESS operation. Such models allow to increase the operating domain of BESS and to take into account more accurately the battery dynamics and their degradation phenomena. The tradeoff is, of course, a higher complexity in the models, their identification and usage. This thesis, in its second part, discusses this tradeoff and provides a set of methods to facilitate the integration of such advanced models in BESS control.

Those briefly described above, are some among many aspects in BESS operation that need thorough and extensive research, in order to achieve truly optimal BESS control and the widespread deployment of these devices in power systems. While other aspects are briefly mentioned in the conclusion, we believe that the core chapters of this thesis, with the methods proposed and their validation, constitute few important steps toward this goal.

Original Contributions of the Thesis

The original contributions of this thesis are:

1. the formulation and experimental validation of a set of algorithms to provide several services to the grid via BESSs. These services, namely, are *i)* the dispatch of the operation of an active distribution feeder, *ii)* the levelling of the load of the same feeder and *iii)* the provision and deployment of enhanced frequency response (EFR). These algorithms rely on a two-phase structure composed by a period-ahead phase, whose goal is to optimally plan the BESS operation and a real-time control, determining at a fast time resultion, the BESS power setpoints. The proposed algorithms are able to manage the BESS state of energy (SOE) so to ensure continuous operation despite the uncertainty related to the deployment of such services (i.e. the uncertainty in the feeder load consumption, PV production and grid frequency). This is done by exploiting forecasts of such quantities, integrated in the control via robust optimization techniques.

2. The formulation and experimental validation of a framework to provide, simultaneously all the above mentioned services. This is with the objective of maximizing the exploitation of a precious resource such as a BESS, despite the aforementioned uncertainties. Services that are different in nature are coupled with one another by defining for each of them an energy budget and a power budget that can be integrated homogeneously.

The method is first formulated in generic terms and then applied to the problem of simultaneously dispatching a distribution feeder and providing EFR to the upper grid layer. Finally, it is validated both through simulations and experiments carried out with the BESS installed at EPFL.

3. The formulation of an empirical method to assess the ageing of BESS. This method, the weighted energy thoughput, takes the BESS power as input variable and takes into account the effect that different power rates have on ageing. A further contribution is the assessment, via such method, of the cycling ageing induced in a BESS used to level the load of a distribution feeder. Finally, we formulate an extension of the framework to provide such service that, based on the weighted energy throughput method, is able to constrain the ageing of the BESS to a chosen threshold.

4. A discussion on the integration of advanced electrochemical models of Li-ion cells in the control of BESSs (and specifically, in the framework outlined in the previous points). Electrochemical models are potentially very powerful tools to enhance the efficacy of BESS control and operation. However, besides bringing numerous advantages, their integration poses several challenges. A chapter of this thesis is dedicated to a throughout review of these advantages and challenges.

5. The formulation and experimental validation of a method to identify the parameters of an electrochemical model - the so-called single particle model (SPM) - of Li-ion cells. First, a reformulation of a SPM from the literature is carried out, with the objective of reducing the number of parameters necessary to represent the internal dynamics of a Li-ion cells. These parameters are then clustered in relevant subsets and testing procedures specifically conceived to identify each subset are formulated. The proposed method is innovative in the fact that it requires only conventional laboratory equipment, while it does not require cell teardown nor computationally-heavy optimization processes. Moreover, for the first time in the Author's knowledge, such a method is validated both against a reference model and against experimental data.

6. The illustration, via simulations, of the potential advantages of integrating a SPM in the control of a BESS dispatching the operation of a distribution feeder via the control framework mentioned above. Such type of physics-based control has been proposed for a grid application of BESS for the first time, in the Author's knowledge. The final chapter of this thesis demonstrates how this approach could lead to an increased insight in BESS dynamics, an enhanced BESS operating domain and an accurate ageing assessment and limitation through explicit modelling of Li-ion cell degradation processes.

Structure of the Thesis

The core of the thesis is divided in six chapters, each elaborating one of the points in the contributions list. The six chapters are clustered in two parts. The first three focus on the BESS

control framework developed to provide multiple services, while the second discusses the improvements that advanced Li-ion battery models could bring to such framework, as well as to BESS control in general.

The first chapter describes a framework to provide services to power systems using a BESS. First, it defines the context of this framework by providing a set of definitions on BESSs and a state of the art on the applications of these devices in power grids. Then it proposes a set of algorithms to provide the services listed in point 1) of the contribution of this thesis, it describes in detail their formulation and it provides extensive experimental data demonstrating the efficacy and deployability of such algorithms.

The second chapter describes and validates experimentally an extension of this framework to provide and deploy several services simultaneously. As the first chapter did, it provides first a state of the art defining the context and motivations to provide simultaneously multiple services. Then, it describes the methods developed to achieve their provision and control the BESS accounting for different sources of uncertainty. This is done first in a generalized manner and then casted in the case of dispatching the operation of a MV feeder and providing EFR. As in the previous chapter, an experimental validation, carried out on the EPFL BESS, is presented.

The third chapter discusses how strategies to assess and limit the ageing of these devices can be integrated in such framework. First, it provides a few definitions and a state of the art on the empirical methods to account for BESS ageing. Based on this, it then formulates the novel *weighted energy throughput* method, which improves a set of methods from the literature. The proposed method is then used to assess the ageing of a BESS carrying out a load-levelling application. Finally the chapter proposes the integration of a constraint based on such method in the BESS control framework and demonstrates the effectiveness of this approach through a set of simulation results.

The fourth chapter analyses the recent efforts made by researchers worldwide to exploit advanced physics-based models of Li-ion cells for control purposes. First it provides the most important definitions concerning Li-ion cells and their models. Than it discusses the potential advantages and the challenges of integrating advanced physics-based models in BESS control.

The fifth chapter describes in detail one of such advanced models - the SPM. It then proposes a reformulation of such model, with the intent of reducing the number of parameters necessary to fully describe its dynamics. Finally, it proposes and validates, both in a simulation environment and against experimental data, a procedure to identify the parameters of the reformulated single particle model.

The sixth chapter proposes the integration of a single particle model in the real-time stage of the framework described in the first chapter. Via simulation results, it shows the advantages that such approach may have, both with respect to enhanced operating domain and to ageing assessment and limitation. In the conclusion, it provides a discussion on the work still needed

to achieve such goals.

Finally, the conclusion of the thesis sums up the proposed methods, highlights the most relevant outcomes and discusses the perspectives opened by these contributions.

PART I

A FRAMEWORK TO PROVIDE GRID SERVICES VIA BATTERY STORAGE SYSTEMS

1 Experimental validation of algorithms for a grid-connected BESS

This chapter describes a framework to provide multiple services to power systems via BESSs. First it presents the state of the art concerning the services that BESSs are able to provide to power systems and the most relevant aspects that need to be addressed in their control. Second, it proposes a framework to provide such services and reports a wide set of experimental data demonstrating its operation. The considered services are i) *the dispatch of the operation of an active distribution feeder,* ii) *the load levelling of such feeder and* iii) *primary frequency regulation. For each of these three services a control algorithm is proposed, detailed theoretically and validated experimentally on a grid-connected 560 kWh BESS. These algorithms rely on a two-phase control structure exploiting local measurements, data-driven forecasting and scenario-based optimization.*

1.1 Definition of a battery storage system

A battery storage system is a device that can accumulate electrical energy under the form of chemical energy and release it in a following phase. We provide here few definitions.

The fundamental components of a BESS are the electrochemical cells. These are the unitary elements that store and releases energy and will be described more in detail in Chapter 4. In a BESS, many cells are connected in a modular fashion in series and parallel, so to constitute modules or packs. All cells and modules are monitored via electronic systems called battery management systems (BMSs) and, altogether, form a unique energy storage device, that is the battery. The battery is connected, through a DC bus to a power converter. This transforms the DC current and voltages of the battery into AC current and voltages. In the case of BESS connected to distribution grids (as is the case in this thesis) the converter is connected, in turn, to a step up transformer, connecting the overall system to the grid. Further auxiliary components, such as air conditioning, lighting and fire extinguishing systems compose the system. A central electronic system, called energy management system (EMS) controls the elements of the BESS (battery, converter and auxiliaries) and determines its operation. Figure 1.1 summarizes the structure described here above.
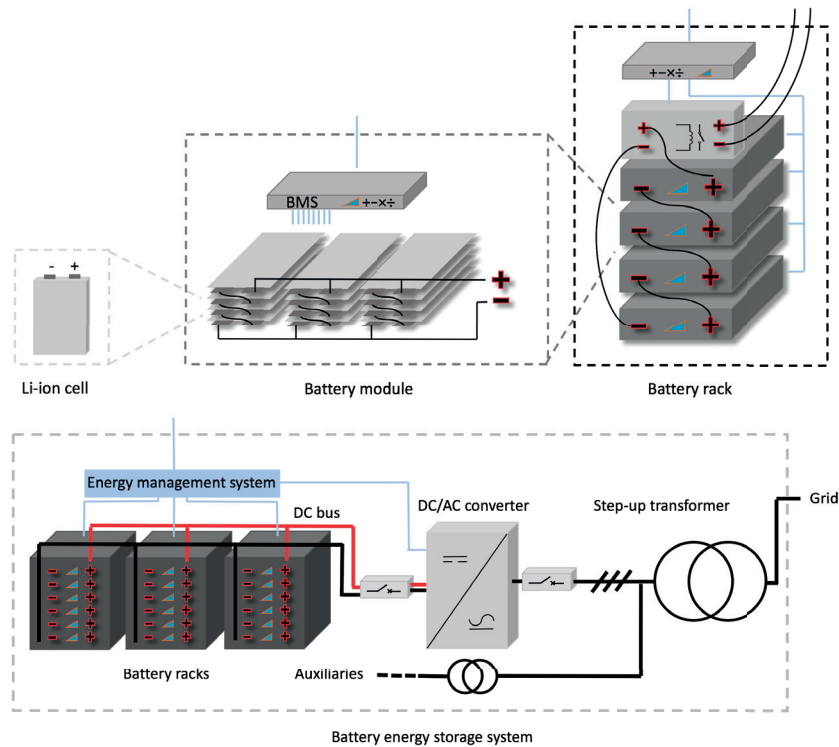
Figure 1.1 – Schematic representation of a BESS

1.2 State of the Art on BESS Grid Applications

The utilization of battery energy storage systems (BESSs) in power systems has been studied thoroughly in the recent years. These devices are characterized by a long lifetime, high round-trip efficiency and high ramping capabilities. For this reason, their utilization has been envisioned for a wide set of services. The algorithms for their control, the strategies for their siting and sizing and those for operation planning have been the object of recent research. In recent years, demonstrator sites, located in several campuses and locations around the world, have provided experimental validation to the methods presented in scientific literature, which is - to date - mainly simulation-oriented. This section recalls the main applications for which BESS usage is envisaged, the main common challenges in BESS deployment and control and the main solutions proposed by recent research. Finally, the last paragraph of this state of the art is dedicated to recall the experiences of similar demonstrators installed in universities across the world. This is with the intent of positioning the work presented in the rest of this chapter.

Utility-scale BESSs are installed at medium- or high-voltage level of power systems and may be managed by grid operators [76], operators of power plants (e.g. wind farms [1, 105] or photovoltaic power plants [153]) or - in the case of energy arbitrage - by energy-merchant entities [115]. They have power ratings going from hundreds of kW [167] to tens of MW [52].

Exploitation of BESSs has been considered, studied and tested - to date - in several different contexts and with different goals. First, its deployment and control has been considered in coupling with a non-dispatchable renewable energy sources, such as wind or solar [2, 109, 178]. This is to manage and compensate for the intrinsic variability and intermittency of these generation resources. The power injection from the BESS is modulated to achieve a more stable and predictable power output of the aggregated system. The operation of the BESS, in this case, is to compensate fast variation [130] as well as daily variations [120]. Second, its usage for energy arbitrage (i.e. the control of a BESS so to absorb power when electricity prices are low and sell it when electricity prices are high, in order to generate revenue) has been considered in [90, 104, 115]. Third, BESSs can provide grid ancillary services - such as frequency regulation and others [85, 110, 195] and energy management of local resources (e.g. load levelling) [84, 129, 132]. In this respect, BESSs can be deployed and operated by system operators, in order to improve the quality of power system operations, at local and system level. The usage of BESSs has been investigated for primary frequency regulation [113] or management of contingencies [121]. BESSs can be deployed as well to manage local grid issues. [44] proposes for instance the usage of BESSs to address local power quality issues related to power flickering. [64] proposes the usage of a BESS to control the voltage of a radial grid characterized by high penetration of distributed generation. [87] proposes the use of a BESS to alleviate the congestions on distribution lines in a similar case. Finally, it is worth to mention the deployment and control of BESSs within islanded or grid-coupled microgrids [53, 99, 123, 200]. In fact, BESSs are fundamental components of microgrids, since they constitute a buffer that ensure the power supply of small independent grids detached from the main grid. Works covering the control of BESSs in the context of microgrids are, for instance, [123, 165, 171].

The control methods developed in the articles mentioned above deal with the peculiar features of BESSs. These are devices with limited energy capacity. This is the main difference with - for instance - thermal power plants providing a similar set of services and poses the fundamental issue of providing a determined service without interruption. This is challenging due to the limited energy capacity of the BESSs and requires strategies to avoid reaching the depletion of the stored energy (or, similarly reaching the fully-charged condition, which would prevent the BESS to absorb additional energy). BESS operation therefore always requires the presence of a thorough state of charge management strategy, to allow the continuous operation of the system without degrading the quality of the provided service.

This can be done by integrating SOC constraints in the scheduling problems determining BESS power injections [126] or superimposing a constant power set-point, computed periodically to keep an adequate SOC, to the power set-points computed to satisfy a given service. This is done for example for primary frequency regulation in [195]. Other solutions may be to exploit activation deadbands [113] or to allow a tolerance around the power set-points determined by the service provision and to regulate the power within that tolerance band [65].

Several other aspects affect BESS operations and need to be taken into account in the develop-

ment of their control. A first one is that the control objectives of BESSs are formulated with respect to quantities that are not known deterministically a priori, but rather uncertain and stochastic in nature. This is the case for BESSs used to compensate for fluctuations in the production of intermittent generation [103] as well as BESSs used to perform frequency regulation [85] or react to market prices [86]. The control strategies need to take into account the inherent variability of these quantities, so that reliable operation (i.e. non attainment of BESS capacity limits) is granted regardless of the behaviour of the associated uncertain quantities. This is achieved by methods ranging from stochastic [112] and robust [199] optimization to rolling horizon scheduling schemes [10].

Considering longer time scales, a further aspect to consider in the development of control strategies of the batteries is their degradation. Li-ion based BESS are characterised by a longer lifetime than other storage technologies (typically 3-5000 cycles [50]). Nevertheless, maximising the lifetime of these devices is a fundamental challenge. The approach typically used in the literature is to use data-driven empirical models to assess the degradation due to a given BESS operation [175, 186] and eventually to integrate these models in the control schemes (see, for instance [15, 69, 97, 196]).

Recent literature has put also the focus on the development of strategies to schedule BESS operation so to minimize grid losses and to respect the constraints imposed by the surrounding grid [61, 75, 188] as well as the development of control strategies that coordinate a set of resources in a distributed fashion [18, 117, 198].

Finally, the scheduling and control problems developed in the literature, exploit different mathematical methods to tackle the complexity of considering one or more of the aforementioned issues in the control. Among these we recall convex optimization [26, 167], mixed integer linear programming [86, 189, 198], fuzzy logic [201], stochastic [112] and robust [199] optimization, Markov chains [13, 66], rule-based algorithms [83], particle-swarm optimization [8, 40].

With respect to the body of literature presented above, the control methods developed within this thesis focus on SOC management in presence of uncertainty and - as detailed in section 1.4 as well as in Chapter 4 - on BESS degradation. It will be highlighted that the optimization problems solved for the scheduling of the BESS power injections are convex, hence ensuring the determination of optimal schedules for the BESS operation. Grid constraints and losses and distributed control mechanisms are not covered by this thesis, although these topics have been developed in the publications [168] and [55], respectively.

Finally, we highlight here that an overwhelming majority of the research papers addressing the operation and control of BESS relies on computer simulations for the validation of the proposed algorithms and methods. While this certainly allows a fast development of such algorithms, the experience provided by physical demonstrators constitutes a valuable element for the research in this topic, since it provides considerable amount of experimental data, as well as the opportunity to validate the proposed methods in a realistic environment, i.e. in a context that is not subject to those assumptions that can be done in simulations. Such

experimental experience and field validation is a relevant contribution of this thesis and we report here references pointing to similar filed experiences. [88] summarises the experience with a 1 MW/580 kWh grid-connect BESS installed in Zurich and used to provide primary frequency control, peak shaving and islanded operation. [174] presents the filed experience gained from a 1.6 MW/400 kWh Lithium-based BESS installed in Western Denmark, with specific focus on primary frequency control and assessment of the degradation generated by such usage. [170] provides an assessment of the environmental impacts of deploying a 3.2 MWh/6 MW BESS in the grid of Graciosa, a Portugese island whose electricity supply is secured by wind power and diesel generators. [185] and [29] report field experience from operating a 1 MW/2 MWh BESS within a 10 MW wind park, in Canada, to provide generation shifting and to respond to automatic generation control (AGC) signals. The work described in the first Part of this thesis adds to this growing literature in providing field experience concerning the operation of BESS and the effectiveness of control methods developed to provide several services. It differentiates however from the above mentioned works in terms of: *i)* relying on a BESS with different chemistry - Lithium-titanate and *ii)* validating a set of original control algorithms. These are, in particular, algorithms to dispatch the operation of an active medium voltage feeder, to achieve load levelling of such feeder and to provide, simultaneously dispatchability and frequency response.

1.3   The EPFL experimental setup

The experimental setup upon which the work presented in this chapter is based consists in a 720 kW/560 kWh BESS connected to a 20 kV distribution feeder. It is based on the Lithium titanate technology, which can perform up to 20.000 complete charge-discharge cycles at their maximum C-rate[1] of 4C. The feeder serves five office buildings of the EPFL campus, which have a peak power consumption of about 300 kW and are equipped with 95 kWp of PV rooftop installations, as sketched in Fig. 1.2. It is completely instrumented with a pervasive real-time PMU-based monitoring infrastructure [138]. The presented algorithms rely on this infrastructure for the measurement of the aggregated power consumption at the grid-connection point and of the grid frequency. They are developed in Matlab and run on common PCs with Debian operative system. The local measurements upon which the algorithms rely, as well as the most relevant measurements from the BESS (e.g. SOC, DC voltage and current, etc.) are stored in the time-series database InfluxDB with time resolution of 1 second. Finally, the PCs implementing the algorithms communicate via Modbus/TCP serial communications protocol with the internal controller of the BESS, which implements the determined power setpoints.
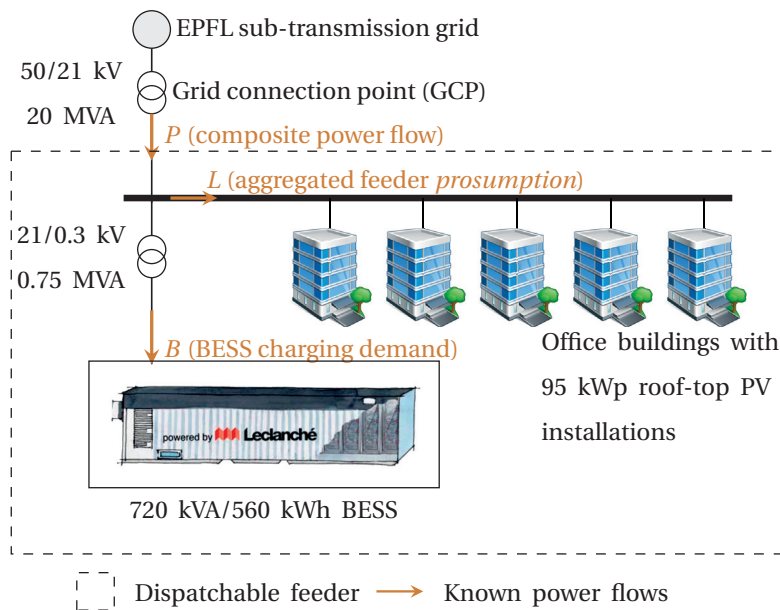
Figure 1.2 – Structure of the EPFL experimental setup

Table 1.1 collects the main parameters of the EPFL BESS and a view of the experimental BESS is shown in Fig. 1.3.

---

[1]The C-rate is rate at which a battery is charged or discharged, normalized over its nominal capacity.

Table 1.1 – EPFL BESS parameters

Parameter	Value
System parameters	
Nominal Energy Capacity	560 kWh
Maximum Power	720 kVA
Battery configuration	9p{15s{3p{20s}}}
Communication protocols (cycle time)	Modbus (>100 ms), Ethercat (10 ms)
Cell parameters	
Nominal capacity	30 Ah
Nominal voltage	2.3 V
Voltage range	1.7-2.7 V
Maximum current	120 A (4C)
Impedance	2 mOhm
Expected cycle life	20000 full cycles
Expected calendar life	20 years
Weight	1100 g
Dimensions (LxWxT)	287x179x12 mm
Inverter parameters	
Maximum AC-power	720 kVA
Rated AC-power	615 kVA
Rated grid voltage	300 V, three-phase
Maximum AC-current	1385 A
AC-current distortion (THD)	3%
Nominal DC Voltage	750 V
DC Voltage range	500-890 V
Efficiency	>97%
Transformer parameters	
Rated power	630 kVA
High voltage	3x21 kV
Low voltage	3x300 V
Group	Dd5

Figure 1.3 – An outside (top picture) and inside view (bottom picture) of the 720 kVA/500 kWh Lithium Titanate-based BESS installed at EPFL (picture of Alain Herzog, EPFL).

1.4 Dispatch of the operation of a MV feeder via a BESS

The control framework described in this Chapter has been first developed with the objective of achieving the dispatchability of the active distribution feeder described in section 1.3. This framework constituted the basis (both conceptually and chronologically) for the work in Sections 1.5 and 1.6 on the provision of further services as well as the context in which to integrate advanced battery models (as detailed in Chapter 4 of this thesis). Given the relevance of this work for the remainder of this thesis, this Chapter describes such control framework, the concept of *dispatchable feeder* and its experimental validation extensively.

To dispatch an active distribution feeder means, in simple terms, to determine in advance (24 hours in advance, in this case) the power profile that the feeder is expected to follow and then, in real-time, controlling the flexible resources connected to this feeder (in this case, the EPFL BESS) so that the predetermined profile is respected. The portion of the grid under consideration, being controlled in such way, won't need reserve power to be provided by the upper grid layer to satisfy its demand when this varies from its expected value. Decreasing the need of reserve power necessary to operate distribution feeder would finally allow for a greater penetration of intermittent renewable energy sources in power systems. The proposed approach can be seen as a bottom-up method to achieve this goal, since the feeder dispatch is reached without the need of a coordinated action at system level, nor of information other than that locally available.

Formally, the problem consists in dispatching the feeder described in Section 1.3, such that the composite power transit at the grid-connection point (GCP) follows a power consumption sequence with 5 minutes resolution, called *dispatch plan*, which is established the day before the beginning of the operation. Similarly to the conventional way of planning power system operation, the control strategies consists in a two-stage process:

- **Day-ahead operation**. The dispatchable feeder operator determines the *dispatch plan* accounting for the forecast of the prosumption and the energy need to restore an adequate BESS state-of-energy (SOE) to ensure continuous operation. The *dispatch plan* is a sequence of average power consumption values with 5 minutes resolution that the feeder should follow during the next day of operation. The day-ahead procedure is repeated every day. At the beginning of the next day, the *dispatch plan* comes into effect and real-time operation begins.

- **Real-time operation**. This phase starts at the beginning of each day of operation, and lasts for the next 24 hours period. The BESS power injection B is adjusted to compensate for the mismatch between the *dispatch plan* and the power prosumption realization, which are likely to occur due to forecasting errors. This is accomplished by applying model predictive control (MPC), accounting for the dynamic behavior of the BESS voltage and SOC thanks to dynamic grey-box models identified from BESS measurements, and including short-term forecasts of the prosumption.

The operation timeline is also sketched in Fig. 1.4, which shows the interactions between the operator of the upper grid layer (as for example described in [11]), the dispatchable feeder operator (which implement the proposed control strategy) and the BESS.

The choice of the 5 minute dispatch interval is according to the envisaged trend for real-time electricity markets. Although not specifically discussed in this work, this formulation potentially allows for day-ahead scheduling considering also dynamic electricity prices, in a similar way as done in [24, 190, 197].
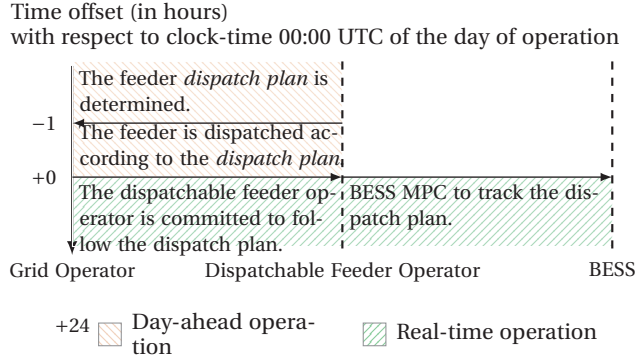
Figure 1.4 – Dispatchable feeder operation: the day before operation, the dispatchable feeder operator determines the *dispatch plan* for the next day.

1.4.1   Day-ahead phase

The objective of the day-ahead phase of the proposed framework is to determine the *dispatch plan*, which is the power consumption profile at 5 minutes resolution that the feeder should follow during the next day operation. The *dispatch plan* is denoted by the sequence $\widehat{P}_i$, $i = 0, 1, \ldots, N-1$ where the index i represents the 5-minute interval of the day of operation, and $N = 288$ is the number of 5-minute intervals in 24 hours. It is defined as:

$$\widehat{P}_i = \widehat{L}_i + F_i^o, \qquad\qquad i = 0, \ldots, N-1, \qquad\qquad (1.1)$$

where $\widehat{L}_0, \ldots, \widehat{L}_{N-1}$ are prosumption point predictions and the sequence $F_0^o, \ldots, F_{N-1}^o$ is called offset profile (the notation ^{o} means "optimal" and denotes the output of an optimization problem, as detailed hereafter). The latter accounts for the amount of BESS energy necessary to restore an adequate level of flexibility. For example, at the end of each day of operation, the BESS residual charge might be close to the upper or lower bounds; the offset plan biases the *dispatch plan* such that the BESS will discharge or charge, therefore re-establishing a suitable energy level to compensate for the mismatch between the *dispatch plan* and the prosumption realization. As similarly envisaged in [2], scheduling the BESS energy demand in the *dispatch plan* to manage its residual charge intrinsically enables continuous-time operation. Especially, it avoids the need of assuming an initial state of energy (SOE) level or imposing a dedicated constraint on the final SOE at the end of the day of operation (see for example [108, 176, 179]).

Although several methods may be alternatively used to calculate the offset plan and implement this intuitive concept, we here decide to adopt a framework based on robust convex optimization. The main reason for this choice is that convex optimization is a well-established discipline for which there exist several mature off-the-shelf software libraries, which guarantees a robust and bug-free implementation while allowing to focus only on the problem formulation.

Day-ahead Prosumption Forecasting

Consumption and generation forecasting at local level is a relatively new topic, as opposed to forecasting at higher levels of aggregation. For the proposed application, we apply a fairly simple non-parametric forecasting strategy that is able to capture the prosumption daily and seasonal components. It consists in selecting and averaging a number of historical power consumption sequences that are relevant for the period to predict according to the value of certain prosumption data features.

Formally, we consider a series of historical power prosumption measurements collected at the GCP at 5 minutes resolution organized in daily sequences of length N (the bold typeface denotes a sequence of scalars obtained by stacking the time evolving value of the referenced variable):

$$\boldsymbol{l}_{y,d} = \left[l_{y,d,0}, l_{y,d,1}, \ldots, l_{y,d,N-1} \right] \tag{1.2}$$

where y and d respectively denote the calendar year $(2015, 2016, \ldots)$ and calendar day-of-year $(1, 2, \ldots, 365)$ of the observation. Also, historical measurements of the daily global horizontal radiation (kWh per day per m^2) are available and are denoted by $R_{y,d}$. Assuming being on a given day, the objective is to determine the prosumption forecast at 5 minutes resolution for the time interval from hour 0 to hour 24 of the incoming day, called *target day*. The information associated with the target day are the calendar day-of-year d^*, calendar year y^* and the forecasted global horizontal radiation R^*. The last information is obtained by applying the model in [80] starting from forecast of the cloud coverage.The first step to compute the prosumption forecast is to select from the historical data a number of sequences $\boldsymbol{l}_{y,d}$ with similar features as those of the target day. This is done by applying the following heuristic:

- a set Ω_A is composed by selecting among historical observations the couples (y, d) which refer to calendar non-working days (weekends and bank holidays) if (y^*, d^*) correspond to a non-working day, and vice-versa.

- A set Ω_B is obtained by selecting the first 10 couples (y, d) in Ω_A chosen in increasing order of time-distance with respect to the target day. The time-distance is evaluated as $365 \cdot (y - y^*) + |d - d^*|$.

- A set Ω_C is obtained by selecting the first 5 couples (y, d) in Ω_B chosen in increasing order of distance between the respective observed cumulated irradiance $R_{y,d}$ and the

target radiance R^*, evaluated as $\left|R^* - R_{y,d}\right|$.

Summarizing, the set Ω_C is composed of 5 couples of indexes (y, d) which are i) closest in time to the target-day, ii) same kind as the target day, and iii) closest in amount of radiation to the GHI forecast for the target-day.

Finally, the couples in Ω_C are used to select as many sequences of historical prosumption measurements (1.2), which are regarded to as potential realizations of the next day prosumption. In particular, the set with the estimates of the prosumption realization is given as:

$$L_i = \left\{ l_{d,y,i} \; \forall (d, y) \in \Omega_C \right\}, \tag{1.3}$$

for each time interval $i = 0, 1, 2, \ldots, N-1$. At the current stage, realizations from the uncertainty sets are assumed independent in time, in other words, time correlation is not modeled. The prosumption point predictions $\widehat{L}_0, \ldots, \widehat{L}_{N-1}$ are obtained by averaging the elements in the respective estimates set:

$$\widehat{L}_i = \frac{1}{|L_i|} \sum_{l \in L_i} l, \qquad\qquad i = 0, 1, \ldots, N-1, \tag{1.4}$$

where $|L_i|$ denotes the number of elements in L_i (set cardinality).

Determination of the Offset Profile

The BESS injection required during real-time operation to compensate the mismatch between the dispatch plan and the prosumption realization L_i is given as:

$$B_i = \widehat{P}_i - L_i = \widehat{L}_i + F_i^o - L_i, \qquad\qquad i = 0, \ldots, N-1 \tag{1.5}$$

where (1.1) has been used in the last equality to explicitly express the BESS power B_i as a function of the consumption forecast uncertainty and offset plan. Since L_i is unknown at the current time, we model it as a random realization l_i from the uncertainty set L_i. Therefore from (1.5), an estimate $\widehat{B}_i$ of the BESS compensation action at time interval i is:

$$\widehat{B}_i = F_i^o + \widehat{L}_i - l_i, \qquad\qquad l_i \in L_i. \tag{1.6}$$

The smallest and largest BESS power realization are respectively:

$$\inf\left\{\widehat{B}_i\right\} = F_i^o + \widehat{L}_i - \sup_{l_i \in L_i}\{l_i\} = F_i^o + L_i^{\downarrow} \tag{1.7}$$

$$\sup\left\{\widehat{B}_i\right\} = F_i^o + \widehat{L}_i - \inf_{l_i \in L_i}\{l_i\} = F_i^o + L_i^{\uparrow} \tag{1.8}$$

where the quantities $L_i^{\downarrow} = \widehat{L}_i - l_i^{\uparrow}$ (negative by construction) and $L_i^{\uparrow} = \widehat{L}_i - l_i^{\downarrow}$ (positive by construction) are introduced.

20

In this part of the problem, we use the notion of BESS SOE. Its evolution is expressed as the following linear function of the BESS power:

$$\text{SOE}_{i+1} = \text{SOE}_i + \beta(\widehat{B}_i) \cdot \widehat{B}_i \tag{1.9}$$

where $\beta(\widehat{B}_i)$ is the charge/discharge efficiency (we neglect at this stage its dependency on temperature and power magnitude)

$$\beta(\widehat{B}_i) = \begin{cases} \beta^+ = T_s/3600/E_n \cdot \eta, & \widehat{B}_i \geq 0 \\ \beta^- = T_s/3600/E_n \cdot 1/\eta, & \widehat{B}_i < 0, \end{cases} \tag{1.10}$$

$E_n = 560\ kWh$ is the BESS energy capacity, $T_s = 300$ s (5 minutes) is the length of the discretization step, and η is the conversion efficiency[2], assumed constant and estimated from measurements considering values of the BESS charge/discharge rate close to the operating ones (i.e. C/5 in our case). We re-write (1.9) as:

$$\text{SOE}_{i+1} = \text{SOE}_i + \beta^+ \left[\widehat{B}_i\right]^+ - \beta^+ \left[\widehat{B}_i\right]^- \tag{1.11}$$

where the operator $[\cdot]^+$ is

$$[x]^+ = \begin{cases} x, & x > 0 \\ 0, & \text{otherwise} \end{cases} \tag{1.12}$$

and viceversa for $[\cdot]^-$.

The lowest and highest possible BESS SOE are given by propagating for $i = 0, \ldots, N-1$ the dynamic equation (1.9) from a known initial state-of-charge $\text{SOE}_0^{\downarrow} = \text{SOE}_0^{\uparrow} = \text{SOE}_0$ ([3]) accounting for the smallest and largest $\widehat{B}_i$ in (1.7) and (1.8), respectively:

$$\text{SOE}_{i+1}^{\downarrow} = \text{SOE}_i^{\downarrow} + \beta^+ \left[F_i^o + L_i^{\downarrow}\right]^+ + \beta^- \left[F_i^o + L_i^{\downarrow}\right]^- \tag{1.13}$$

$$\text{SOE}_{i+1}^{\uparrow} = \text{SOE}_i^{\uparrow} + \beta^+ \left[F_i^o + L_i^{\uparrow}\right]^+ + \beta^- \left[F_i^o + L_i^{\uparrow}\right]^- \tag{1.14}$$

The two expressions above are embedded into the following optimization problem, which has the objective of determining the offset plan $\boldsymbol{F}^o = [F_0^o, \ldots, F_{N-1}^o]$ such that BESS SOE and power

---

[2]Throughout the thesis, various techniques to include the efficiency in the proposed algorithms are exploited. Here, it is modeled via the value η while, for example, in Chapter 2 the BESS is modeled as ideal and its efficiency is taken into account by adding appropriate back-off terms in the problem constraints. These differences are due to the peculiarities of the algorithms. Due to these, each time one specific technique becomes preferable over others. We observe, moreover, that since the BESS roundtrip efficiency is extremely high ($\eta = 0.97$), the proposed algorithms would perform satisfactorily even considering a unitary efficiency, i.e. an ideal BESS. Including a proper treatment of the efficiency, however, is valuable since it allows the extension of the proposed algorithms to less efficient energy storage devices.

[3]Since the dispatch plan is computed one hour before the beginning of the day of operation, the initial BESS state-of-charge SOE_0 is unknown and should be therefore predicted. At the current stage we use a persistent predictor, namely $\text{SOE}_0 = \text{SOC}_{-5 \times 12}$.

are always in the respective allowed bounds $(\text{SOE}_{\min}, \text{SOE}_{\max})$ and $(B_{\min}, B_{\max})$ in the worse case scenarios:

$$\boldsymbol{F}^o = \underset{\boldsymbol{F} \in \mathbb{R}^N}{\arg\min} \left\{ \sum_{i=1}^{N} F_i^2 \right\} \tag{1.15}$$

subject to

$$\text{SOE}^{\downarrow}_{i+1} = \text{SOE}^{\downarrow}_i + \beta^+ \left[F_i^o + L_i^{\downarrow} \right]^+ + \beta^- \left[F_i^o + L_i^{\downarrow} \right]^- \tag{1.16}$$

$$\text{SOE}^{\uparrow}_{i+1} = \text{SOE}^{\uparrow}_i + \beta^+ \left[F_i^o + L_i^{\uparrow} \right]^+ + \beta^- \left[F_i^o + L_i^{\uparrow} \right]^- \tag{1.17}$$

$$\text{SOE}^{\downarrow}_{i+1} \geq \text{SOE}_{\min}, \tag{1.18}$$

$$\text{SOE}^{\uparrow}_{i+1} \leq \text{SOE}_{\max} \tag{1.19}$$

$$F_i + L_i^{\downarrow} \geq B_{\min} \tag{1.20}$$

$$F_i + L_i^{\uparrow} \leq B_{\max} \tag{1.21}$$

$$\widehat{P}_i \leq P_{\max}, \tag{1.22}$$

for $i = 0, \ldots, N-1$, $\text{SOE}^{\downarrow}_0 = \text{SOE}^{\uparrow}_0 = \text{SOE}_0$ and SOE_0 is given. The inequality constraint (1.22) is to ensure that the dispatch plan is smaller than a tunable threshold. The value of the latter can be designed by the modeller to peak shave the real power power transit at the GCP (as it will be shown in the Section 1.4.3). The formulation in (1.15)-(1.22) is nonconvex due to the relationship (1.16)-(1.17). In the real implementation and experiments, an equivalent convex formulation, described in Appendix A.1 is solved.

1.4.2 Real-time operation

The objective of the real-time operation is to adjust the BESS real power injection such that the average power consumption at the end of each 5-minute period matches the respective set-point from the dispatch plan. The control is actuated with a sample time of 10 s. This period has been chosen in order to capture early time BESS dynamics and assure good control performance. In the remainder of this section, the index $k = 0, 1, 2, \ldots, K-1$ denotes the rolling 10 seconds time interval of the current day of operation, where $K = 8640$ is the number of 10 seconds period in 24 hours. At the beginning of each interval k, the real power flow at the GCP, the BESS flow, and the real power of the prosumption realization for the previous interval $k-1$ become known thanks to measurements. They are respectively denoted by P_{k-1}, B_{k-1} and L_{k-1}. The value of the prosumption set-point to match, denoted by P_k^*, is retrieved from the *dispatch plan* $\widehat{P}_0, \widehat{P}_1, \ldots, \widehat{P}_{N-1}$ as:

$$P_k^* = \widehat{P}_{floor * \frac{k}{30}}, \tag{1.23}$$

where $floor * \cdot$ denotes the nearest lower integer of the argument, and 30 is the number of 10-second intervals in a 5-minute slot. The k-index of the first 10-second interval for the current 5-minute slot is denoted as $\underline{k}$ and is:

$$\underline{k} = floor * \frac{k}{30} \cdot 30. \tag{1.24}$$

For example, at time 00:16, $k = 96$, $P_k^* = \widehat{P}_3$, and $\underline{k} = 90$. Similarly, the k-index of the last 10-second interval for the current 5-minute slot is:

$$\overline{k} = \underline{k} + 30 - 1. \tag{1.25}$$

The control action consists in actuating the set-point for the BESS converter real power demand (in kilowatt, kW). It is denoted by B_k^o and is piecewise constant in the interval k. It is determined by the model predictive control algorithm detailed herefater.

The nomenclature is also exemplified in Fig. 1.5, which sketches, for example, the situation at the beginning of the time interval $k = 2$ (clock-time 00:00:20 UTC): the BESS real power set-points B_0^o and B_1^o were actuated already in the previous two intervals, B_2^o has been just determined using the most recent information (namely, the prosumption realizations L_0 and L_1), and the average prosumption set-point to achieve in the 5 minute interval is given by the first value of the dispatch plan, $\widehat{P}_0$.
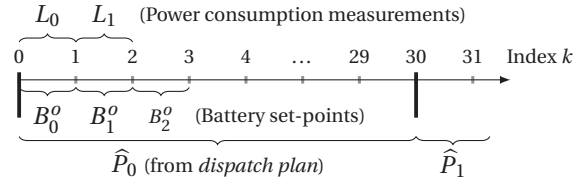
Figure 1.5 – The first 31 10-second intervals of the day of operation. It is sketched the situation at the beginning of the time interval 2.

Formulation of the Control Objective

say being at the beginning of the time interval k, the average composite power flow at the GCP (prosumption + BESS injection) for the current 5 minute slot is given by averaging the available information until k. If k corresponds to the beginning of a 5 minute period, no information is available yet, and we say that the average composite consumption is zero. Formally, it is:

$$P_k = \begin{cases} 0 & k = \underline{k} \\ \frac{1}{k - \underline{k}} \cdot \sum_{j=\underline{k}}^{k-1} \left(L_j + B_j\right) & k > \underline{k}. \end{cases} \tag{1.26}$$

We augment the definition in (1.26) by including short-term point predictions of the prosump-

tion $\widehat{L}_{k|k}, \widehat{L}_{k+1|k}, \ldots, \widehat{L}_{\overline{k}|k}$. This allows to calculate the *expected* average composite consumption for the whole duration of the current 5 minute slot. By exploiting the definition given in (1.26), the expected average consumption accounting for the short-term point predictions is:

$$P_k^+ = \frac{1}{30} \left((k - \underline{k}) \cdot P_k + \sum_{j=k}^{\overline{k}} \widehat{L}_{j|k} \right). \tag{1.27}$$

At the current stage, we use a persistant predictor to model future realizations, namely $\widehat{L}_{j|k} = L_{k-1}$, $j = k, \ldots, \overline{k}$.

The energy error, expressed in kWh, between the realizations and the dispatch plan in the current 5-minute slot (*dispatch plan error*):

$$e_k = \frac{300}{3600} \cdot \left(P_k^* - P_k^+ \right), \tag{1.28}$$

where 300 and 3600 are respectively the number of seconds in a 5 minutes interval and 1 hour interval, P_k^* and P_k^+ are as defined in (1.23) and (1.27), respectively.

Formulation of Model Predictive Control (MPC)

In general, MPC consists in determining the control action for a given system by solving at each time step an optimization problem with updated information, where the system constraints are enforced by implementing prediction models in the optimization problem. MPC has been widely adopted in several engineering fields, and proposed also in application to power system operation, for example for control of demand response and storage [71, 131]. In this work, the MPC goal is to determine the BESS real power injection B_k^o in order to achieve zero *dispatch plan error* (1.28) by the end of each 5-minute slot while obeying to BESS SOC, DC voltage and current operational limits.

The main reason for implementing the control problem with a MPC framework rather than a PID-based regulator is the following: for the latter, the control action depends only on current and past values; MPC allows to schedule the whole power trajectory withing the targeted time horizon, therefore, it is more suitable to solve an energy management problem. For example, let us assume that reliable short-term predictions indicate that there will be a significant mismatch between realization and dispatch plan in the second half of a certain 5-minute time slot. The predictive control framework could preemptively react while respecting BESS operational constraints thanks to enforcing them explicitly in the formulation. On the contrary, a feedback control loop will react only when measurements are available, i.e. in the second half of the time slot. This myopic approach may have larger chances not to achieve the control objective, since the compensation for the mismatch will be concentrated in a shorter time interval and the resulting higher power demand may clash with the BESS operational constraints. In the MPC optimization problem, there are two potential candidates for decision variables: *i)*, the real power injection on the AC side, and *ii)*, the current on the

DC side. We adopt the second solution because it admits a convex equivalent formulation of the optimization problem, as shown in the following. We explicitly seek for convexity because convex optimization problems, besides having a single minimum point which is the global one (provided that the solution exists), can be solved efficiently and in a reliable way.

We model the BESS energy throughput (in kWh) on the AC bus in the discretized time period from k to $\overline{k}$:

$$E_{\overline{k}|k}(v_k, \ldots, v_{\overline{k}}, i_k, \ldots, i_{\overline{k}}) = \alpha \sum_{j=k}^{\overline{k}} v_j i_j, \tag{1.29}$$

where v_k and i_k are the battery DC voltage and current (positive when charging and vice-versa), respectively, and the scale factor $\alpha = 10/3600 \cdot 0.97$ is to convert from power (in kW) in the discretized 10 seconds time interval to energy (in kWh), and the coefficient 0.97 models the converter losses (estimated from measurements). The formula above can be expressed as the following matrix product:

$$E_{\overline{k}|k}(\cdot) = \alpha \boldsymbol{v}_{\overline{k}|k}^T \boldsymbol{i}_{\overline{k}|k}, \tag{1.30}$$

where the bold notation denotes sequences obtained by stacking in column vectors the realizations in time of the referenced variables, e.g. $\boldsymbol{v}_{\overline{k}|k} = \left[v_k, \ldots, v_{\overline{k}} \right]^T$. Since the voltage on the DC bus is modeled by using a linear electrical circuit (as detailed in 1.4.2), its dynamic evolution can be expressed as a linear function of the battery current. By applying the transition matrices $\phi^v, \psi_i^v, \psi_1^v$ (which are developed starting from the voltage discrete state-space model representation, as described in Appendix A.2), the battery voltage can be expressed by:

$$\boldsymbol{v}_{\overline{k}|k} = \phi^v x_k + \psi_i^v \boldsymbol{i}_{\overline{k}|k} + \psi_1^v \mathbf{1}, \tag{1.31}$$

where x_k is the state vector of the voltage model and is known from measurements.

It is to note that the voltage evolution also depends on the BESS SOC. This dependency is captured by identifying five linear models for as many different SOC ranges. The linear transition matrices in (1.31) are obtained by selecting the appropriate voltage model according to the current measured BESS SOC (*model scheduling*). Moreover, we assume that the BESS SOC does not vary significantly in the actuation period, so we can write the voltage as a time invariant linear function of the BESS current, therefore retaining linearity.

Replacing (1.31) into (1.30) yields to:

$$\begin{aligned} E_{\overline{k}|k}(\boldsymbol{i}_{\overline{k}|k}) &= \alpha \left(\phi^v x_k + \psi_i^v \boldsymbol{i}_{\overline{k}|k} + \psi_1^v \mathbf{1} \right)^T \boldsymbol{i}_{\overline{k}|k} = \\ &= \alpha \left(x_k^T \phi^{v\,T} \boldsymbol{i}_{\overline{k}|k} + \boldsymbol{i}_{\overline{k}|k}^T \psi_i^{v\,T} \boldsymbol{i}_{\overline{k}|k} + \mathbf{1}^T \psi_1^{v\,T} \boldsymbol{i}_{\overline{k}|k} \right), \end{aligned} \tag{1.32}$$

where $\mathbf{1}$ denotes the all-ones vector.

We now explore the requirements for $E_{\overline{k}|k}(\cdot)$ in (1.32) being a convex function of $\boldsymbol{i}_{\overline{k}|k}$. Since the nonnegative sum between functions preserves convexity, the convexity of (1.32) requires that all its three addends are convex. The first and third addend are linear in $\boldsymbol{i}_{\overline{k}|k}$, therefore convex. The second term is a quadratic form of $\boldsymbol{i}_{\overline{k}|k}$: the necessary and sufficient condition for its convexity is given by ψ_i^v being semidefinite positive. This hypothesis has been verified numerically for all the BESS identified voltage models, which are presented in Section 1.4.2. We conclude that $E_{\overline{k}|k}$ in (1.32) is convex in $\boldsymbol{i}_{\overline{k}|k}$.

The energy tracking problem (given by achieving zero *dispatch plan error* at the end of the 5-minute slot) could be formulated by minimizing the squared deviation of (1.32) from (1.28), such as:

$$\left(E_{\overline{k}|k}(\boldsymbol{i}_{\overline{k}|k}) - e_k \right)^2 . \tag{1.33}$$

However, as known from the functions composition rules [23], the convexity of $p(x) = q(r(x))$ when $r(x)$ is convex requires q convex non decreasing, which is not the case because the squared function of the difference is convex but not nondecreasing on all its domain. Therefore, we reformulate the objective and achieve a convex equivalent formulation of the original problem: it consists in maximizing the BESS DC current while imposing that the convex BESS energy throughput (1.32) is smaller than or equal to the energy target (1.28); this achieves the energy throughput to hit the upper bound of the inequality , thus achieving the same value as the target energy. The combination of a linear cost function with an inequality constraint in the form "$f(x) \leq 0$, with f convex in x" is a convex optimization problem.

Overall, the formulation of the MPC optimization problem is given by augmenting the just described formulation with *i)* constraints on the BESS current and its rate of change and *ii)* open open-loop predictive constraints on BESS voltage and BESS state-of-charge (SOC). It is worth noting that, whereas in the day-ahead problem the constraints on the BESS flexibility were enforced by considering the BESS power and SOE, in this case we consider BESS current, SOC and voltage. This allows for a higher degree of modeling detail and is indeed more suitable for the control problem, where the primary objective is to determine a control decision compliant with BESS operation constraints.

Formally, the decision problem is:

$$\boldsymbol{i}_{\overline{k}|k}^o = \arg\max_{\boldsymbol{i} \in \mathbb{R}^{(k-\overline{k}+1)}} \left\{ \mathbf{1}^T \boldsymbol{i}_{\overline{k}|k} \right\} \tag{1.34}$$

subject to

$$\alpha \left(x_k^T \phi^{\nu T} \boldsymbol{i}_{\overline{k}|k} + \boldsymbol{i}_{N|t}^T \psi_i^{\nu T} \boldsymbol{i}_{\overline{k}|k} + \boldsymbol{1}^T \psi_r^{\nu T} \boldsymbol{i}_{\overline{k}|k} \right) \le e_k \tag{1.35}$$

$$\boldsymbol{1} \cdot i_{\min} \preccurlyeq \boldsymbol{i}_{\overline{k}|k} \preccurlyeq \boldsymbol{1} \cdot i_{\max} \tag{1.36}$$

$$\boldsymbol{1} \cdot \Delta_{i,\min} \preccurlyeq H \boldsymbol{i}_{\overline{k}|k} \preccurlyeq \boldsymbol{1} \cdot \Delta_{i,\max} \tag{1.37}$$

$$\boldsymbol{v}_{\overline{k}|k} = \phi^{\nu} v_k + \psi_i^{\nu} \boldsymbol{i}_{\overline{k}|k} + \psi_1^{\nu} \boldsymbol{1} \tag{1.38}$$

$$\boldsymbol{1} \cdot v_{\min} \preccurlyeq \boldsymbol{v}_{\overline{k}|k} \preccurlyeq \boldsymbol{1} \cdot v_{\max} \tag{1.39}$$

$$\mathbf{SOC}_{\overline{k}|k} = \phi^{\mathrm{SOC}} \mathrm{SOC}_k + \psi_i^{\mathrm{SOC}} \boldsymbol{i}_{\overline{k}|k} \tag{1.40}$$

$$\boldsymbol{1} \cdot \mathrm{SOC}_{\min} \preccurlyeq \mathbf{SOC}_{\overline{k}|k} \preccurlyeq \boldsymbol{1} \cdot \mathrm{SOC}_{\max}, \tag{1.41}$$

where $\boldsymbol{i}_{\overline{k}|k}^o \in \mathbb{R}^{(k-\overline{k}+1)}$ is the computed control action trajectory, $\boldsymbol{1}$ denotes the all-ones column vector, the multiplication $\boldsymbol{1} \cdot \gamma$ denotes the all-γ column vector, and the symbol $\preccurlyeq$ is the component-wise inequality. The cost function (1.34) consists in maximizing the sum of the equally weighted current values over the shrinking horizon from k to $\overline{k}$. This, in combination with the inequality (1.35), achieves the BESS energy throughput to be as close as possible to e_k, as introduced earlier. The inequalities (1.36) and (1.37) respectively enforce minimum and maximum magnitude and rate of change for the BESS current, where $(i_{\min}, i_{\max})$ and $(\Delta_{i,\min}, \Delta_{i,\max})$ are the respective limits and the matrix $H \in \mathbb{R}^{(k-\overline{k}+1)\times(k-\overline{k}+1)}$ is:

$$H = \begin{bmatrix} 1 & 1 & 0 & 0 & \dots & 0 \\ 0 & 1 & 1 & 0 & \dots & 0 \\ \vdots & \vdots & \vdots & \vdots & \ddots & \vdots \\ 0 & 0 & 0 & \dots & 1 & 1 \end{bmatrix}. \tag{1.42}$$

The equality (1.38) is the electrical equivalent circuit model of the the BESS according to the notation previously discussed for (1.31), while (1.39) imposes BESS voltage limits, which are denoted by the couple $(v_{\min}, v_{\max})$.

Analogously, the equality constraint in (1.39) is the evolution of the BESS SOC as a linear function of the variable $\boldsymbol{i}_{\overline{k}|k}$, where $\phi^{\mathrm{SOC}}, \psi_i^{\mathrm{SOC}}$ are transition matrices calculated using the SOC model in 1.60. Finally, (1.41) imposes the limits on the BESS SOC, which are given by the couple $(\mathrm{SOC}_{\min}, \mathrm{SOC}_{\max})$.

The optimization problem (1.34)-(1.41) is convex since the cost function is linear and all the inequality constraints are convex in $\boldsymbol{i}_{\overline{k}|k}$. It is noteworthy that if the real power injection had instead being adopted as the optimization variable, the problem would not have been convex because the BESS voltage evolution is a nonlinear function of the power and thus the constraints in (1.31) would have been nonconvex. The optimization problem is solved at each time step k (with updated information) on a shrinking horizon from the index k to $\overline{k}$, namely from current time until the end of the current 5-minute slot. At each k, the control trajectory for the whole residual horizon is available, however only the first component of the current

control law is considered for actuation, which we denote by i_k^o. Since the BESS power flow is controlled by using a real power reference signal, it is required to transform from i_k^o to the power set-point B_k^o. By using the same model applied in (1.29), it is:

$$B_k^o = v_k \cdot i_k^o. \tag{1.43}$$

Since the control decision is re-evaluated every 10 seconds, errors on the voltage predictions and short-term consumption forecast which arise in the current actuation period are absorbed in the next cycle, where updated measurements are used. It is noteworthy that the current implementation does not prevent the tracking problem to fail, for example if the accumulated mismatch between realizations and *dispatch plan* is larger than the BESS capacity.

Prediction Models

Battery voltage models for control application are normally based on electric equivalent circuits, which trade detailed modelling of the electrochemical reactions for increased tractability, see for example [9, 31, 98]. A voltage model commonly adopted in the literature is the so-called two time constants model (TTC): it consists in a linear second order dynamic model, where the value of the model parameters depend on the battery SOC, temperature and C-rate. In this work, we augment the classical TTC formulation by implementing grey-box modelling, a set of rigorous and systematic methods for data-driven dynamic model identification (see for example [91, 166]). It consists in increasing the complexity of the model (by adding a order, for example) until reaching a satisfactory behavior of the model prediction errors, which at the final stage should be i.i.d. (independent and identically distributed) random noise with zero mean. This is with the main objective of obtaining a prediction model that is tuned to capture accurately the dynamics of the BESS that is used in the experimental validation of the control framework. The adopted modelling procedure initially consists in recording a series of experimental measurements of the BESS DC voltage and current while requiring to the BESS a random power flow according to a PRBS (pseudo random binary signal). The PRBS is a two levels square wave (in this case ±200 kW) with on-off periods of random durations. It is normally adopted in model identification because it is able to excite a wide range of system dynamics. As mentioned earlier, model parameters normally depend on the BESS SOC: in order to capture this dependence, a number of PRBS experimental sessions are performed when the BESS is in different SOC ranges (0-20%, 20-40%, 40-60%, 60-80%, 80-100%). The dependencies between model parameters and both C-rate and temperature are not modeled at this stage, and it will the objective of future investigations. Nevertheless, it is worth noting that the latter dependency is expected to play a minor role because the batteries are installed in a temperature controlled environment at $20°C$.

The BESS voltage model is formulated by using the continuous time stochastic state-space

28

model representation:

$$dx = \mathscr{A}_c(\theta)x\,dt + \mathscr{B}_c(\theta)u(t)\,dt + \mathscr{K}_c(\theta)\,d\omega \tag{1.44}$$

$$v_k = \mathscr{C}x_k + \mathscr{D}(\theta)u_k + \mathscr{G}(\theta)g_k, \tag{1.45}$$

where $x \in \mathbb{R}^n$ is the system state vector, n the model order, $\mathscr{A}_c$ is the system matrix, $\mathscr{B}_c$ input matrix, $\mathscr{K}_c$ the input disturbance matrix (used later to implement Kalman filtering for state reconstruction), C output matrix, D feedforward matrix, $\mathscr{G}$ is the measurement noise matrix, g_k is i.i.d. standard normal noise, u input vector, ω a n-dimension standard Wiener process, and θ is the set of model parameters to estimate. Model parameters are estimated by using the *greyest* function in MATLAB and minimizing the sum of the model one-step-ahead prediction errors. It was found that the model with best performance (namely, with uncorrelated model residuals) for the considered experimental BESS is a three time constant model ($n = 3$) with structure as shown in Fig. 1.6.
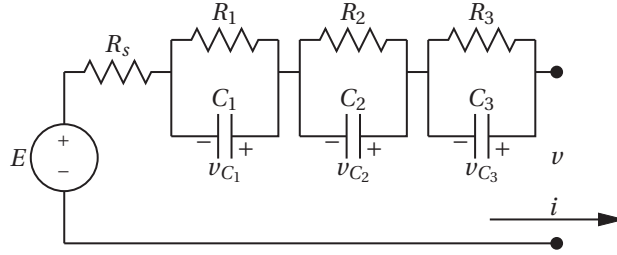
Figure 1.6 – Equivalent circuit model of the BESS. The quantities v and i are respectively the BESS terminal voltage and DC current, while $v_{C_1}, v_{C_2}, v_{C_3}$ are the components of the state vector x in (1.44)-(1.45).

The model is given by applying Kirchhoff laws to the circuit in Fig. 1.6 and is:

$$x = \begin{bmatrix} v_{C_1} & v_{C_2} & v_{C_3} \end{bmatrix}, u_{tk} = \begin{bmatrix} i_{tk} & 1 \end{bmatrix}^T \tag{1.46}$$

$$\mathscr{A}_c = \begin{bmatrix} \frac{-1}{R_1 C_1} & 0 & 0 \\ 0 & \frac{-1}{R_2 C_2} & 0 \\ 0 & 0 & \frac{-1}{R_3 C_3} \end{bmatrix}, \mathscr{B}_c = \begin{bmatrix} \frac{1}{C_1} & 0 \\ \frac{1}{C_2} & 0 \\ \frac{1}{C_3} & 0 \end{bmatrix} \tag{1.47}$$

$$\mathscr{K}_c = \mathrm{diag}(k_1, k_2, k_3), \tag{1.48}$$

$$\mathscr{C} = \begin{bmatrix} 1 & 1 & 1 \end{bmatrix}, \mathscr{D} = \begin{bmatrix} R_s & E \end{bmatrix}, \mathscr{G} = \sigma_g. \tag{1.49}$$

where $R_1, C_1, R_2, C_2, R_3, C_3, k_1, k_2, k_3, R_s, E, \sigma_g$ is the set of parameters to estimate. The estimated values of the system parameters according to the BESS SOC ranges are summarized in Table 1.2.

Figure 1.7 shows the autocorrelation function (ACF) of the time series of model prediction errors (or model residuals), that is the difference between the training set of current/voltage measurements and the respective model predictions. Checking for model residuals correlation

Table 1.2 – Estimated BESS voltage model parameters for different SOC ranges

SOC	0-20%	20-40%	40-50%	60-80%	80-100%
E	592.2	625.0	652.9	680.2	733.2
R_s	0.029	0.021	0.015	0.014	0.013
R_1	0.095	0.075	0.090	0.079	0.199
C_1	8930	9809	13996	9499	11234
R_2	0.04	0.009	0.009	0.009	0.010
C_2	909	2139	2482	2190	2505
R_3	2.5e-3	4.9e-5	2.4e-4	6.8e-4	6.0e-4
C_3	544.2	789.0	2959.7	100.2	6177.3
k_1	0.639	0.677	0.617	0.547	0.795
k_2	-5.31	-0.22	-0.36	-0.28	0.077
k_3	5.41	40	0.40	2.83	-0.24
σ_g^2	-1.31	-0.42	0.3426	3.5784	2.7694

is a test widely adopted in system identification (see for example [92]) to validate the ability of identified models of capturing the dynamics contained in the training data set. The test consists in comparing the ACFs of model residuals and white noise (which is i.i.d., therefore uncorrelated by definition): if all the components of the former ACF falls in the 95% confidence interval of the latter, the test is successful and the dynamic performance of the model are considered satisfactory. The situation in Figure 1.7 refers to 50% SOC and shows uncorrelated model residuals, thus denoting that the identified model is able to capture all dynamics contained in the training data set. Although not shown here for a reason of space, the same behavior was observed also for the other SOC ranges of Table 1.2.
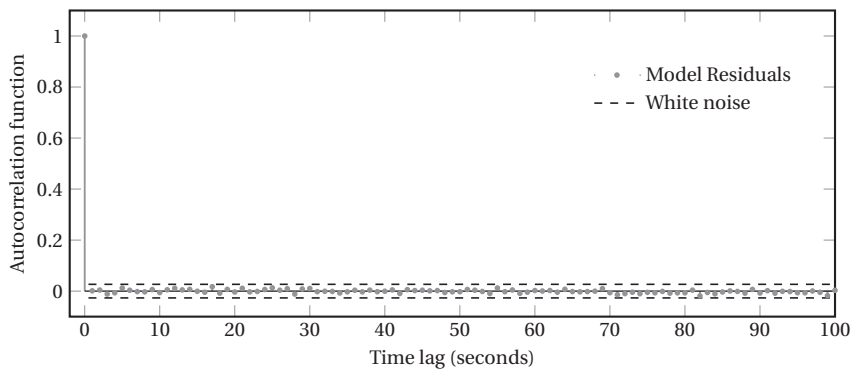
Figure 1.7 – Autocorrelation function (ACF) of model residuals (full line) and white noise (horizontal lines) at 95% confidence level.

The continuous time model in (1.44) is discretized at $T_s = 10$ seconds resolution in order to be implemented in the MPC constraints in (1.38). Discretization is performed with the forward difference (or forward Euler). However, in order not to incur in numerical instability, the smallest time constant given by the (R_3, C_3) branch is dropped in favor of an algebraic state by using the matched DC gain method. Let $\mathscr{A}_r, \mathscr{B}_r, \mathscr{K}_r$ be the continuous time system, input and system noise matrices of the reduced order model, the discretized system and input matrices are given by:

$$\mathscr{A} = 1 + \mathscr{A}_r T_s \tag{1.50}$$

$$\mathscr{B} = \mathscr{B}_r T_s \tag{1.51}$$

$$\mathscr{K} = \mathscr{M}_1 \mathscr{M}_2^T, \tag{1.52}$$

where $\mathscr{M}_1$ and $\mathscr{M}_2$ are given according to the Van Loan's method [102] and are matrix exponentials, which are approximated by the first order truncation of their respective Taylor expansions:

$$\mathscr{M}_1 = e^{\mathscr{K}_r T_s} = 1 + \mathscr{K}_r T_s \tag{1.53}$$

$$\mathscr{M}_2 = e^{A_r^T T_s} = 1 + \mathscr{A}_r^T T_s. \tag{1.54}$$

The matrices $\mathscr{A}, \mathscr{B}, \mathscr{K}$ in (1.50)-(1.52) and $\mathscr{C}, \mathscr{D}, \mathscr{G}$ in (1.49) constitute the skeleton of the discrete time state-space of the BESS equivalent circuit model. These are used to generate the transition matrices $\phi^v, \psi_i^v, \psi_1^v$, which are finally used to implement the MPC voltage constraints in (1.38).

The components of the system state in (1.44) are a modelling abstraction and cannot be measured. However, their value must be known in order to compute the BESS voltage predictions. In turns, the state is estimated from measurements of the battery DC voltage by applying Kalman filtering (KF, [169]). As known, it consists in a two-stage procedure, repeated at each discrete time interval: a prediction step to determine the system evolution (state expected value and covariance matrix P) solely on the basis of the knowledge on the system

$$x_{k|k-1} = \mathscr{A} x_{k-1|k-1} + \mathscr{B} u_{k-1} \tag{1.55}$$

$$P_{k|k-1} = \mathscr{A} P_{k-1|k-1} \mathscr{A}^T + \mathscr{K} \mathscr{K}^T, \tag{1.56}$$

and an update stage, where the predicted state is corrected accounting for the last measurement v_k

$$x_{k|k} = x_{k|k-1} + G(y_k - \mathscr{C} x_{k|k-1}) \tag{1.57}$$

$$P_{k|k} = \left(P_{k|k-1}^{-1} + \mathscr{C}^T \sigma_g^{-1} \mathscr{C} \right)^{-1}. \tag{1.58}$$

where G is the Kalman gain:

$$G = P_{k|k-1}\mathscr{C}^T \left(\mathscr{C} P_{k|k-1} \mathscr{C}^T + \sigma_g^2 \right)^{-1}, \tag{1.59}$$

and σ_g is the measurement noise (known from the parameters estimation). KF requires full system observability, that in our case is enforced by construction since the model is estimated from measurements.

The BESS SOC model is:

$$SOC_{k+1} = SOC_k + \frac{10}{3600} \frac{i_k}{C_{\text{nom}}}, \tag{1.60}$$

where $C_{\text{nom}} = 810\ Ah$ (ampere-hour) is BESS capacity from datasheet information. It is worth noting that we neglect here the dependency of the BESS capacity with respect to the C-rate and cells temperature, see for example [17]. The discretized state-space matrix are easily found from (1.60) and are $A = 1$, $B = 10/3600/C_{\text{nom}}$, $C = 1$, $D = 0$. These are used to generate the transition matrices $\phi^{\text{SOC}}, \psi_i^{\text{SOC}}$ for the SOC predictive constraints in (1.39).

On the use of BESS models in the day-ahead and real-time stages

Open-loop constraints on BESS operation are enforced in both day-ahead and real-time stages. The main differences between the two implementations are the decision variables, the time resolution and time horizon at which they are computed (5 minutes and 24 hours and 10 s and 5 minutes, respectively), and the fact that the latter problem is re-evaluated at each time interval by incorporating new information from real-time measurements. From the point of view of their practical purpose, BESS models are integrated with the objective of modeling the storage capacity and constraints. However, while in the day-ahead formulation they are to represent the long-term flexibility, in real-time operation they model short-term operational constraints, therefore enabling the computation of reliable control actions which are respectful of the BESS operational limits. This explains the reason why more accurate BESS models are implemented in the latter stage than in the former, where a high level of details is not needed, especially considering that a more conservative plan for the BESS usage can be achieved by adding back-off terms to SOC and power flow constraints in (1.18)-(1.21).

Temporary We observe here as well that, throughout the thesis both the concepts of state of charge (SOC) and state of energy (SOE) are used. This distinction is related to the reasons discussed above. The period-ahead phases of the various proposed control algorithms are characterised by longer time horizons and lower time resolutions than the real-time controls. Moreover, while the latter use detailed models, having the BESS DC current as decision variable, the decision variable of the former is the BESS active power. It follows that the concept of SOE (the SOE being determined by the integration of a power profile) is exploited in the various period-ahead problems, while the concept of SOC (determined through the integral of the BESS DC current) is used in the real-time control.

Implementation of the real-time strategy

The flow of operation during the real-time strategy is sketched in Figure 1.8. Real-time operation is implemented as a Matlab script and executed daily on the same computer as the day-ahead strategy. Also, information which become available from real-time measurements (power flow at the GCP, DC voltage, DC current, SOC, AC power flow of the BESS) are acquired and stored in a time series database with 1 second resolution.
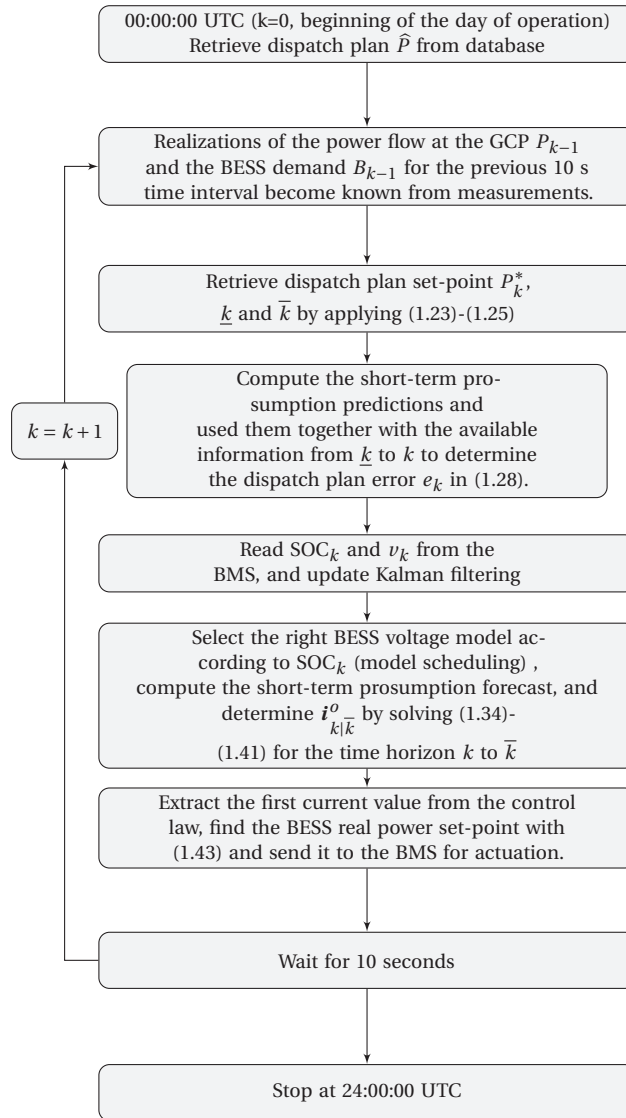
Figure 1.8 – Flow chart showing real-time operation during 24 hours.

1.4.3 Experimental Validation

In this section, we show the experimental results obtained by dispatching the operation of the MV feeder described in Section 1.3. We start by describing three contiguous days of operation

(denoted by day 0, day 1 and day 2) in order to illustrate the ability of the proposed method to manage the SOC and achieve continuous time operation. Results are shown in figures 1.9a-1.11c. Each figure consists in three main plots *a, b, c, d*, which respectively shows:

(a) the extreme values of the prosumption uncertainty sets $\left(l_i^{\downarrow}, l_i^{\uparrow}\right)$, the expected prosumption $\widehat{L}_i, i = 0, \ldots, N-1$, and the offset profile F^o. The first two quantities are the outcome of the forecasting tool discussed in 1.4.1, while the last is computed as detailed 1.4.1. The second and third quantities are used to generate the *dispatch plan* according to (1.1) $\widehat{P}_i$;

(c) the *dispatch plan* $\widehat{P}_i$, the power transit at the GCP realizations P_i and the prosumption realizations L_i;

(d) the measurements of the BESS SOC, DC current i and voltage v and their respective limits.

As visible from Fig. 1.9c, the BESS starts the operation in the day 0 experiment with a very low SOC. In general (and assuming for one moment unbiased prosumption forecast), this is not a desirable situation because the BESS capacity of absorbing forecasting errors is not symmetric. The specific objective of the offset profile is to restore a sufficient BESS SOC in order that enough BESS energy capacity is available along the day to compensate for forecasting errors, which are modeled in the optimization problem in (1.15)-(1.22) by the prosumption uncertainty sets (shown in Fig. 1.9a with the shaded band). In this case, the offset profile is such that the *dispatch plan* overestimates the prosumption, therefore implicitly achieving the BESS to absorb the increased level of demand and slowly charge. As visible from Fig. 1.9b, during operation the power flow at the GCP P follows precisely the *dispatch plan* $\widehat{P}$, thus denoting the good tracking performance of the MPC. A more accurate numerical comparison is shown later in this section. Fig. 1.9c shows the details of BESS operation. The BESS is controlled in order to compensate for the mismatch between prosumption realization and dispatch plan, and, in this case, it slowly charges along the day, as imposed by the offset plan. The BESS constraints, which are enforced in the MPC are generally respected during operation.

The BESS terminates the day 0 experiment with a SOC above the 50% level. This is reflected on the operation of the next day (experiment day 1, in Fig. 1.10), which is characterized by a slightly negative offset plan (F^o in Fig. 1.10a) to restore a lower BESS SOC, as visible in Fig. 1.10c. As shown in Fig. 1.10b, the algorithm achieves to track the *dispatch plan* successfully. As visible by comparing figures 1.9c and 1.10c, the BESS SOC variation in the latter case is smaller than in the former, thus denoting a smaller accumulated forecasting error.

Fig. 1.11 shows the operation of the experiment on day 3. In this case, the BESS SOC is below the 50% level since the previous day of operation, and a positive offset profile F^o (Fig. 1.11a) is necessary to raise the SOC. During operation, the algorithm is able to control the BESS in
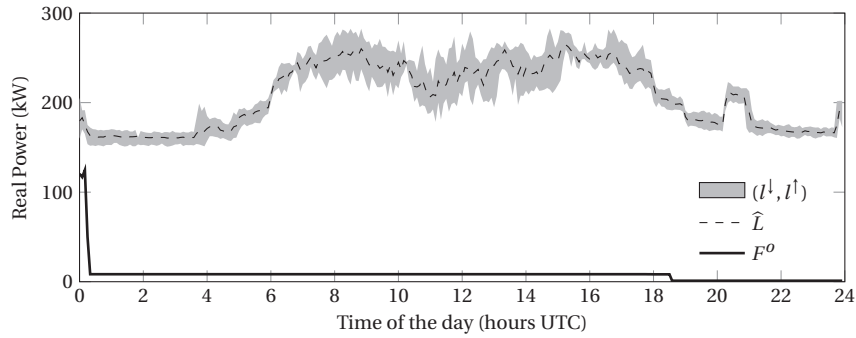
(a) **Day-ahead: prosumption uncertainty sets and expected value, and offset plan.**
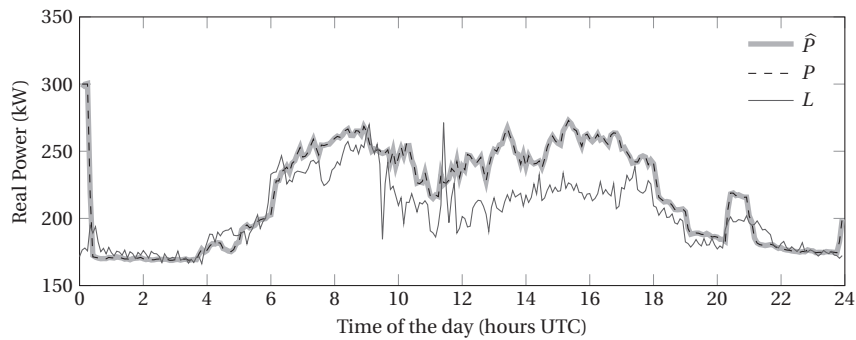
(b) **Real-time:** *dispatch plan vs* **realization of GCP power transit and prosumption.**
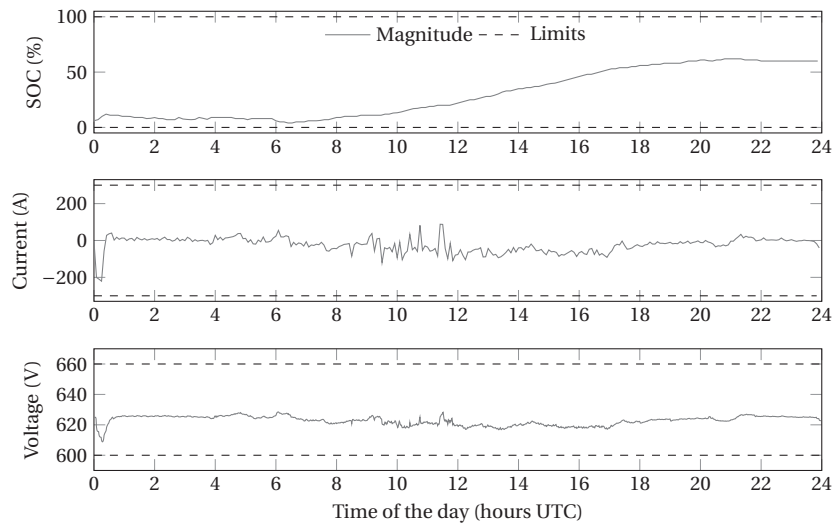
(c) **Realizations of BESS SOC, DC current and voltage and respective limits.**

Figure 1.9 – Day 0: experimental results.

order to track the dispatch plan successfully (Fig. 1.11b). However, the BESS SOC slowly drifts away from the 50% level during the day, as visible in Fig. 1.11c, to compensate for a moderate overestimation of the average PV production.

Table 1.3 summarizes the tracking performance of the proposed control strategy in the experi-

mental results. For each day experiment, two cases are considered:

- **no dispatch**: this corresponds to nowadays conventional operation, namely when prosumption is not dispatched but simply forecasted (although on a higher aggregation level than as done here). In this context, the tracking error is defined as the difference between the prosumption forecast and the prosumption realization;

- **dispatch**: the operation of the feeder is dispatched as described previously. The error here is given by the difference between the dispatch plan and the power flow realizations at the GCP.

Three metrics are considered: the root mean square error (RMSE) along with its mean and maximum absolute value. As visible from Table 1.3, dispatched operation achieves better figures than the base case. The tracking performance of the MPC are fairly accurate, with an RMS value less than 0.5 kW, which is approximately the 0.2% of the feeder average power consumption (200 kW).

Table 1.3 – Tracking Error Statistics (in kW) for Experiments Day 0 to 2

Experiment		RMSE	Mean	Max
Day 0	no dispatch	19.20	4.68	50.82
	dispatch	0.43	< 0.01	1.54
Day 1	no dispatch	18.71	-0.39	72.150
	dispatch	0.25	< 0.01	0.740
Day 2	no dispatch	18.06	-4.92	54.45
	dispatch	0.42	< 0.01	1.41
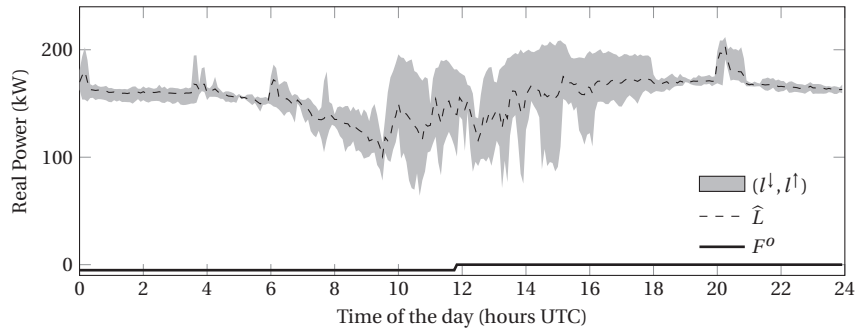
(a) **Day-ahead: prosumption uncertainty sets and expected value, and offset plan.**
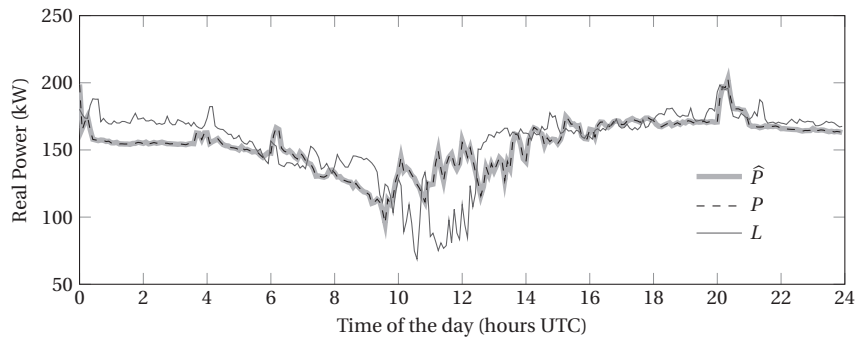
(b) **Real-time:** *dispatch plan vs* **realization of GCP power transit and prosumption.**
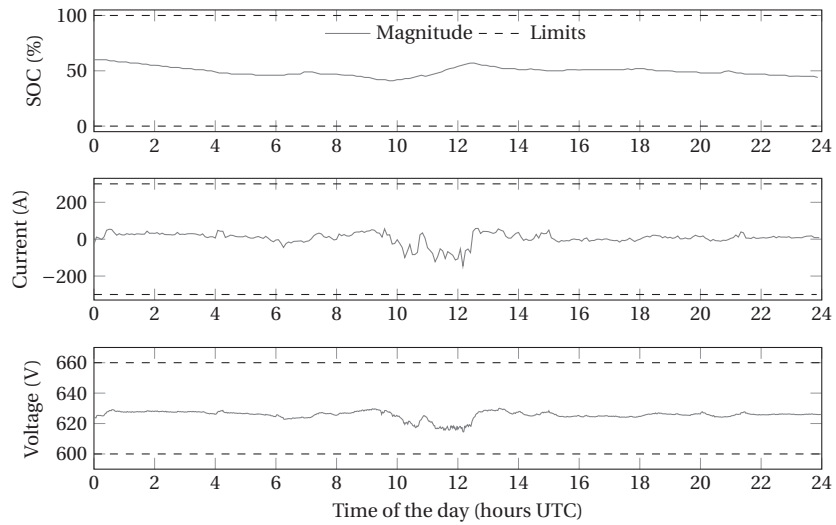
(c) **Realizations of BESS SOC, DC current and voltage and respective limits.**

Figure 1.10 – Day 1: experimental results.
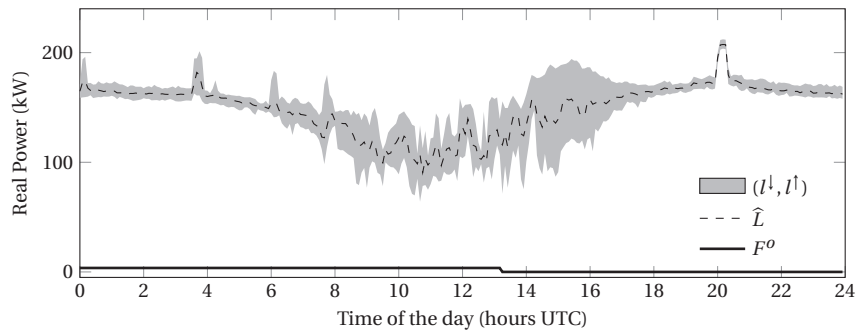
(a) **Day-ahead: prosumption uncertainty sets and expected value, and offset plan.**
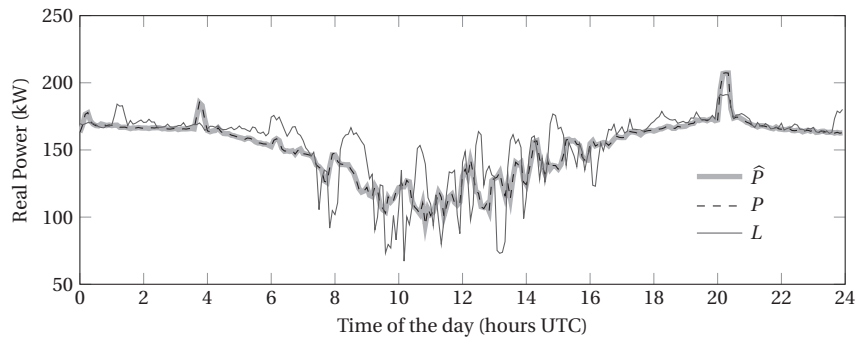
(b) **Real-time:** *dispatch plan vs* **realization of GCP power transit and prosumption.**
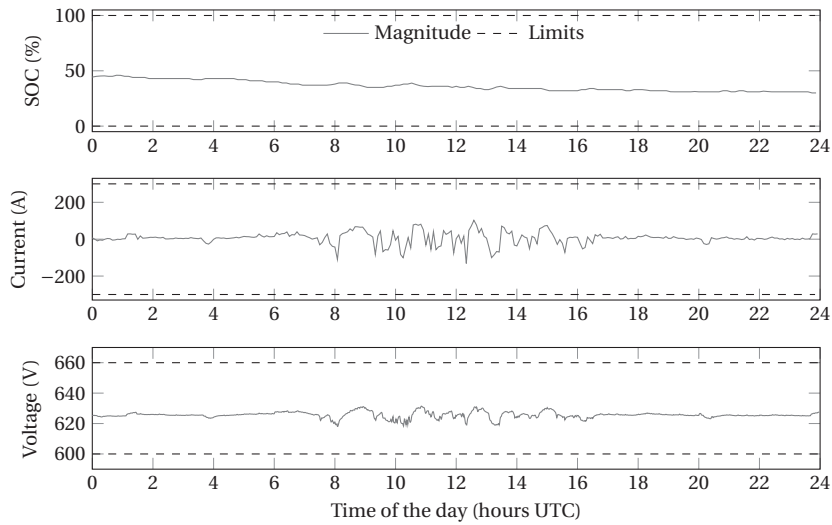
(c) **Realizations of BESS SOC, DC current and voltage and respective limits.**

Figure 1.11 – Day 2: experimental results.

1.5 Load-leveling

The framework developed to dispatch the operation of a set of prosumers has been extended to include further objectives beyond the sole dispatchability. The dispatch plan, can indeed satisfy more stringent conditions and the system will therefore achieve further local objectives just by tracking a carefully built dispatch plan. In this section, a control scheme that achieves load levelling of the feeder is formulated. This is done by modifying the optimisation problem of the day-ahead phase presented in Section 1.4, so to achieve that energy is shifted from hours of peak load to hours of low demand. This can have an economical value where time-of-use energy prices are present but in general has a beneficial effect on the grid, since it relieves it of part of the consumption in the hours of peak demand. Load leveling is similar to peak shaving unless for the fact that, while the latter aims at reducing the peak consumption, the former has the primary objective of flattening the consumption profile [84]. Load leveling is relevant to power systems operation for several reasons, both from a consumer and system perspective: *i)* reduced electricity cost, since customers are normally penalized for the peak consumption; *ii)* at system level, it reduces peak demand, which is in many cases served by expensive peaking power plants; *iii)* reduced distribution and possibly transmission losses [127]; *iv)* postponement the grid infrustructure upgrades.

1.5.1 Methods

Problem statement

We consider a group of prosumers, for which we would like to smooth the consumption profile and dispatch their operation. As in the case of the dispatch operation, the problem is formulated according to a two-stage procedure: day-ahead and intra-day phase. In the day-ahead stage, the objective is to determine the *dispatch plan*, namely the power consumption profile that the group prosumers is willing to follow during real-time operation. The *dispatch plan* is built as the sum of the forecasted power consumption profile, obtained through data-driven forecasting, and an *offset profile*. With respect to the dispatching operation, this latter quantity, which is obtained by solving a convex optimization problem, has the objective of generating a *dispatch plan* with minimum variance, namely with minimum variation with respect to its average value such that, during operation, the BESS will charge (discharge) when the power profile exceeds (is below) the levelled profile and viceversa.

The intra-day operation consist in controlling the BESS active power injection in order to track the *dispatch plan*, namely compensating for deviations between the dispatch plan and actual consumption, which are likely to differ due to the offset profile and to forecasting errors. This is accomplished using MPC, as detailed in Section 1.4.2[4].

---

[4]In the problem formulation we do not consider the operational constraints associated to the grid. In other words, we assume that the battery power rating results in grid voltages and currents within operational bounds. This is the case for stiff medium voltage grids.

Day-ahead problem

The objective is to build the *dispatch plan*, namely the power consumption profile that the feeder should follow during operation, the day after. The *dispatch plan* $\widehat{P}$ is defined as the sequence of $N = 288$ (i.e., the number of 5-minute intervals in 24 hours) average power consumption values for the incoming day. The feeder *dispatch plan* is composed by the sum of the prosumption forecast profile $\widehat{L}_t$ and the *offset profile* F_t:

$$\widehat{P}_t = \widehat{L}_t + F_t \qquad\qquad t = 1,\ldots,N \qquad\qquad (1.61)$$

The prosumers forecasted consumption profile, denoted by $\widehat{L}$, is produced through a nonparametric black-box method based on vector auto-regression as described in Section 1.4.1.

The objectives of the *offset profile* are *i)* altering the dispatch plan so that it is with mininum variance and *ii)* making sure that an adequate level of charge is available in the BESS to achieve dispatchability during intra-day operation. We define the average daily power consumption value as:

$$\widehat{L}_{avg} = \frac{1}{N}\sum_{t=1}^{N}\widehat{L}_t. \qquad\qquad (1.62)$$

The offset profile $\boldsymbol{F}^o = \left(F_1^o,\ldots,F_N^o\right)$ is determined by a constrained optimization problem that minimizes the movement of the forecasted consumption sequence $\widehat{L}_1,\ldots,\widehat{L}_N$ around its average daily value $\widehat{L}_{avg}$. The optimization problem constraints are *i)* the BESS apparent power injections should respect the BESS converter nominal power and *ii)* the BESS state of energy (SOE) should be within its nominal limits.

The BESS constraints are built by adopting a robust optimization approach: each forecast consumption scenario (as defined in Section 1.4.1) is implemented in the constraints to model the fact that it may be actually realized during real-time operation. This is with the objective of ensuring that enough energy and power capacity are available in the BESS to accomplish the dispatchability, therefore enforcing the feasibility of the intra-day control objective. The optimization problem is formulated as:

$$\boldsymbol{F}^o = \arg\min_{\boldsymbol{F}\in\mathbb{R}^N}\sum_{t=1}^{N}\left(\left(\widehat{L}_t - \widehat{L}_{avg}\right) - F_t\right)^2 \qquad\qquad (1.63)$$

subject to:

$$\widehat{P}_t = \widehat{L}_t + F_t \tag{1.64}$$

$$\widehat{B}_t^d = \widehat{P}_t - \mathscr{L}_t^d \tag{1.65}$$

$$\left| \widehat{B}_t^d \right| < B_{\max} \tag{1.66}$$

$$\mathrm{SOE}_t^d = \mathrm{SOE}_0 + \eta \frac{\Delta T}{C_{nom}} \sum_{j=1}^{t} \widehat{B}_j^d \tag{1.67}$$

$$\mathrm{SOE}_{min} < \mathrm{SOE}_t^d < \mathrm{SOE}_{max} \tag{1.68}$$

for $t = 1, \ldots, N$ and $d = 1, \ldots, p$, where t is the time step and d is an index denoting the scenario. The equality constraint (1.64) sets the relationship between *dispatch plan*, prosumers consumption forecast and *offset profile*, (1.65) is the predicted BESS active power injection for each consumption forecast scenario $\mathscr{L}^d$ with $d = 1, \ldots, p$, and (1.66) imposes that the BESS injection is within the nominal power capacity of the BESS converter (BESS operates at unitary power factor). Finally, (1.67) and (1.68) respectively models the SOE evolution as a function of the BESS injection for each consumption forecast scenario and imposes that the SOE is within the limits. The SOE model is from [107].

The parameter C_{nom} is the rated energy capacity of the BESS. The charging-discharging efficiency η normally depends on the sign of the battery demand and is normally modeled as:

$$\eta = \begin{cases} \beta & B \geq 0 \\ 1/\beta & B < 0. \end{cases} \tag{1.69}$$

which is non-linear for $\beta \neq 1$ and originates a non-convexity in the optimization problem. In this respect, we performed a series of cycling experiments on the BESS in the SOE range from 10% to 90%, with power rates from -100 to 100 kW and depth of discharge (DOD) of $\pm 5\%$ and assessed values of effiecncy higher than 0.95 for all the operating conditions. It results that we can assume $\beta = 1$ without introducing any relevant error in a 24 hours horizon preserving therefore the convexity of the problem.

Real-time operation

The real-time operation is performed via the methods described in Section 1.4.2.

1.5.2 Experimental results

In this section, the performance of the proposed load leveling/dispatching strategy is shown and analyzed. First, results are presented graphically in order to exemplify the operation of load levelled dispatchable feeder. Second, a quantitative analysis is provided.

Experimental operation of the proposed strategy

Fig. 1.12 and 1.13 show the BESS experimental results during a typical day of operation. The experiment refers to March, 14th 2016. Fig. 1.12, shows the forecasted power consumption profile, the leveled dispatch plan, the *offset profile* and the predicted BESS SOE, which are determined in the day-ahead operation.
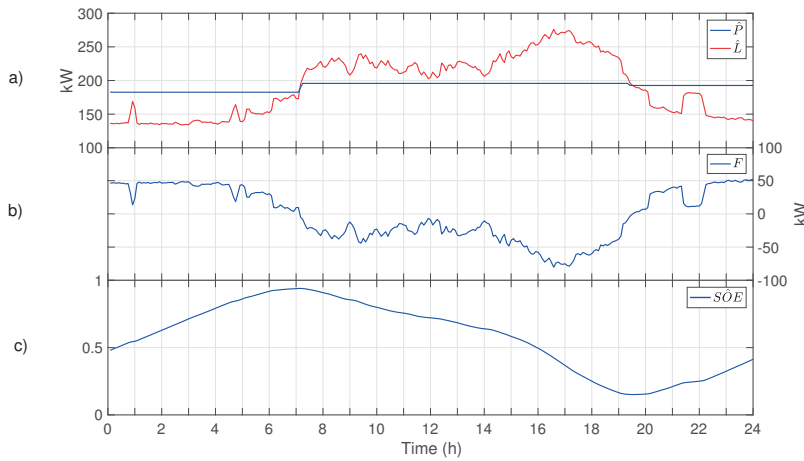
Figure 1.12 – Day-ahead scheduling: a) consumption forecast $\widehat{L}$ and leveled dispatch plan $\widehat{P}$; b) offset profile F; c) forecasted BESS stored energy evolution ($\widehat{SOE}$).

Fig. 1.13 shows the loads power consumption, feeder power demand, BESS power injection and BESS SOE realization in the day of operation. For the sake of comparison, the plots are obtained through 5-minutes averaging of the measurement data. It is therefore averaged the effect of the 15 seconds correction, so that the actual 5 minutes profile can be compared with the one defined the day-ahead operation. It can be observed that while deviating from the *dispatch plan*, the SOE remains within feasible boundaries and thus the dispatchability is maintained along the whole day.

Performance assessment of the proposed strategy for a day of operation

The overall performance of the control strategy is evaluated with respect to three objectives. The first is the ability of performing load leveling. This is measured by the load peak reduction $max(L_1, \ldots, L_N) - max(P_1, \ldots, P_N)$, the amount of energy shifted from the peak-demand to low-demand period $E_{shifted}$, and the ratio r_{var} between the consumption profile and load-
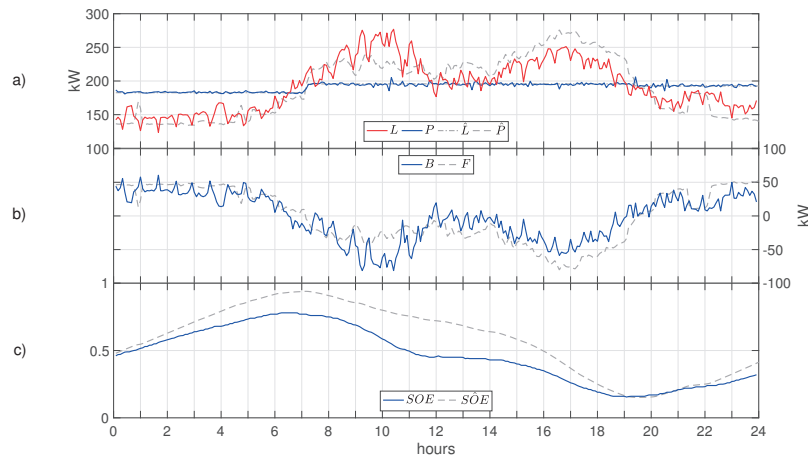
Figure 1.13 – Intra-day operation: a) actual feeder consumption L and leveled feeder power profile P; b) actual BESS power injection B; c) actual BESS SOE evolution. The profiles forecasted in the day-ahead scheduling are reported in grey color.

leveled profile variance. The second is the ability to dispatch the operation of the feeder, through evaluating the maximum, mean and root mean square of the tracking error (e_{max}, e_{mean} and e_{rms} respectively) in the realization of the dispatch plan are numerically presented, both in absolute and relative terms. The third is the robustness of the dispatch plan. This is quantified namely by the distance between the BESS SOE and its respective upper and lower bounds evaluated by measuring the maximum and minimum SOE reached during the day of operation, SOE_{max} and SOE_{min}, and the portion of the BESS capacity used to perform the load leveling and the dispatch respectively, i.e. ΔSOE_{LL} and ΔSOE_D. ΔSOE_{LL} is computed as the difference between SOE_{max} and SOE_{min}, whereas ΔSOE_D corresponds to the maximum deviation of the SOE along the day from its forecasted evolution. All the metrics calculated for the performed experiment are summarized in tables 1.4-1.6.

Table 1.4 – Load Leveling Performance Evaluation

Metric	Value
P_{max}	206 kW
L_{max}	277 kW
$|L-P|_{max}$	81 kW
$E_{shifted}$	365 kWh
r_{var}	42.14

It can be observed in table 1.4 that the peak power consumption is reduced from 277 kW to 206 kW and that 365 kWh are shifted from the peak-demand to the low-demand period. The realized power profile is greatly smoothed, with regard to the actual consumption profile, the ratio between the variances of these two profiles being $r_{var} = 42.14$. Table 1.5 describes the performance of the feeder dispatch operation. It can be seen that the mean tracking error

Table 1.5 – Feeder Dispatch Performance Evaluation

Metric	Value
e_{max}	13.35 kW
	7.16 %
e_{mean}	1.43 kW
	0.75 %
e_{rms}	2.19 kW
	1.13 %

Table 1.6 – Control Strategy Robustness Evaluation

Metric	Value
SOE_{max}	78 %
SOE_{min}	15.5%
ΔSOE_{LL}	62.5%
ΔSOE_D	26.7%

along the day is lower than 1%. Finally, it can be seen in table 1.6 how the BESS SOE remains within its limits along the day of operation.

1.6 Frequency regulation

This Section proposes an algorithm to control a BESS to provide a frequency response service. Conventionally, grid frequency is regulated through primary and secondary frequency control (PFC and SFC, respectively). PFC, performed by conventional generators, implies an adaptation of the generators' active power output within few tens of seconds after the occurrence of frequency perturbations. Recently, however, the increasing penetration of renewable energy sources lowered the grid inertia and increased the need for faster frequency regulation. This need can be satisfied effectively by BESSs, since these devices are characterized, typically, by response times faster than those of conventional generators. Several grid operators worldwide have implemented a new class of ancillary services, to accommodate the fast-response capabilities of these devices. This is the case, for instance, of the the "Regulation D" signal used by the american grid operator PJM [139] and the "enhanced frequency response" implemented by National Grid [51], in the United Kingdom. The latter requires the deployment, within 1 seconds, of a power that is proportional to the grid frequency deviations. The control developed in this Section falls within this class of new "advanced" frequency regulation services. In particular, it is similar to the one proposed by National Grid[5]. Therefore, in the remainder of this section, we will refer to the service provided by the EPFL BESS as enhanced frequency response (EFR).

The provision and deployment of such service is carried out exploiting a framework similar to the one already discussed in the previous sections. In fact, similarly to the cases of dispatching the operation of a feeder and achieving the levelling of its load, providing frequency regulation requires the managing of the BESS SOC. This can be done by exploiting deadbands [113], tolerances around the regulation setpoints [65] or other heuristic concepts. These methods, however, require the BESS not to follow accurately its regulation set-points and are therefore hardly scalable: what would happen, at system level, if all BESSs participating to the regulation would use such heuristics? A more viable approach is to exploit a control structure already presented in the previous sections. This is a two stage structure, in which the SOE management is carried out in a period-ahead stage that takes into account the current SOE and the energy needs predicted for the upcoming period. At this stage, a fixed offset power value is determined, with the objective of maintaining an adequate SOC level. The real time control consists in the sum of this offset and of the regulating power, which now tracks precisely the frequency deviation signal. The remainder of this sections presents the details of the proposed frequency response algorithm as well as the results obtained in its validation. First, it proposes a method to forecast the energy required to operate the service for a given time horizon. Then it describes the control algorithm itself, showing how the aforementioned forecast can be integrated to achieve better performances. Finally, it presents the results of an extensive validation, performed by means of simulations and experiments.

---

[5]In the specific case of National Grid, the minimum power to participate to the provision of EFR is 1 MW. However, there is a growing trend to allow the participation to the ancillary services markets of distributed yet smaller devices. The EPFL BESS, while not satisfying the current requirement of 1 MW of power, may be well suited to provide EFR in such a context.

1.6.1 Forecast of energy required for the EFR deployment

Since BESSs can store a limited amount of energy, in order to provide a given amount of regulating power for a predetermined duration, they need to continuously adapt their reservoir level. Therefore, in order to maximise the capacity of providing regulating power, it is important to quantify the energy that the BESS needs to make available to accomplish the EFR service deployment over a period T. Since regulating power P^{efr} is proportional to frequency deviations Δf from the nominal frequency, we have that regulating energy E^{efr} is proportional to the integral of such deviations over the considered time window:

$$E^{efr} = \int_T P^{efr} dt = \int_T \alpha \Delta f dt = \alpha \int_T \Delta f dt = \alpha W_f, \tag{1.70}$$

where W_f is the integral over a time window T of the deviations of frequency from its nominal value, and α is the droop coefficient, measured in $kW \cdot Hz^{-1}$. The quantity W_f, over long time horizons is equal to zero (considering a power grid with a sufficient amount of secondary frequency control reserve). However, this is not generally true for shorter time windows, and we show that it is possible to forecast the value of W_f and use it to achieve efficient EFR strategies. The analysis detailed in these paragraphs has been carried out on two separate datasets, composed respectively by two years (2014-2015) of frequency measurements provided by National Grid Electricity Transmission (NGET)[6] and by one year (2016) of on-site frequency measurements at EPFL [138]. From the frequency timeseries, we have computed several W_f timeseries, with integration intervals T of increasing length from 1 to 24 hours. We show that autoregressive (AR) models are capable to forecast W_f (and hence the energy E^{efr} required for the service deployment).

The usage of AR models requires the analysis of the probability density function of the variable W_f and its autocorrelation [106]. Figure 1.14 shows the normal probability plots for two W_f timeseries respectively from the a) NGET and b) EPFL databases and with different T. Such plots demonstrate that the data of such timeseries are close to normally distributed and justify the usage of AR models.

Figure 1.15-a shows the autocorrelation of the timeseries composed by subsequent W_f values computed for the NGET database and with T=1h as an example. Modelling such timeseries as a persistent process (i.e. assuming that there are not relevant dynamics that can be captured), at every timestep we predict the value $\hat{W}_f(k) = \mu_f = 0$. For such model (hereafter AR(0)), the model residual corresponds the value of W_f itself, being $r_k = W_f(k) - \hat{W}_f(k) = W_f$. We see that the residuals for such model present an autocorrelation that is, for the lower lags, higher than the one of white noise (indicated by the blue lines in the plot). This suggests that W_f contains in fact dynamics that can be modelled with an higher order model. Figure 1.15-b shows the autocorrelation of the model residuals obtained, for the same dataset, with an autoregressive model of order 8 (this being the lowest order that successfully captures all the relevant dynamics for all the period lengths T), hereafter referred as AR(8). It can be

---

[6]http://www2.nationalgrid.com/Enhanced-Frequency-Response.aspx
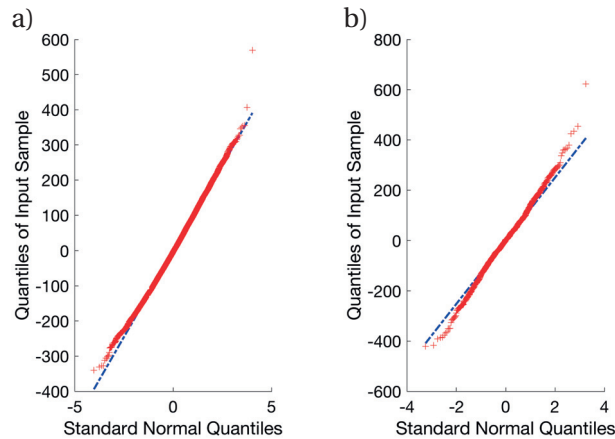
Figure 1.14 – Q-Q plot of the residuals of W_f (red) versus the normal standard (blue) built using a) $T = 1h$, data from the NGET database and b) $T = 6h$, data from EPFL database.
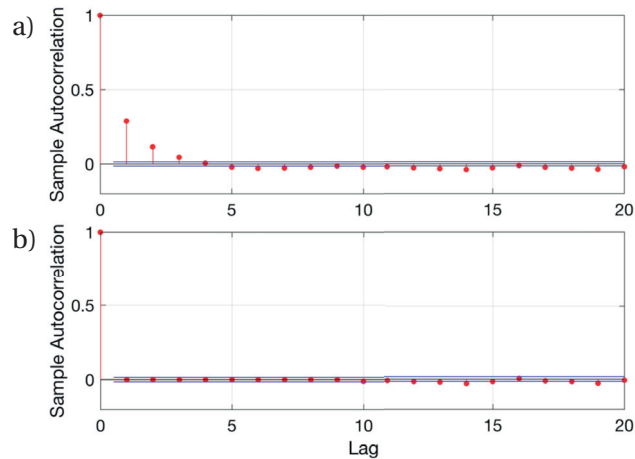
Figure 1.15 – Autocorrelation function of the residuals of a) $AR(0)$ and b) $AR(8)$, both computed with T=1h and data from the NGET database.

seen that the residual autocorrelation does not show, in this case, any value outside the band identifying white noise. Similar results are obtained for all values of T and for both datasets considered (not reported here for sake of spare). Table 1.7 compares the standard deviation of the residuals obtained with the two models (AR(0) and AR(8) respectively) for integration periods T of increasing duration. It can be observed that this value is lower for the AR(8) model for all T.

Using such a model provides two results relevant for the EFR control strategy. First, a model having lower variance allow to use a higher droop coefficient and therefore provide higher regulating power (as will be detailed in the first subsection of Section 1.6.2, "Droop coefficient computation"). Second, the predicted value $\hat{W}_f$, recomputed periodically, can be used to improve the state of energy management algorithm associated to such droop coefficient (as detailed in the second subsection of Section 1.6.2, "State-of-Energy Management").

Table 1.7 – Residual standard deviation σ for AR(0) and AR(8), data from NGET database.

T $[h]$	1	2	3	4	6	12	24
$AR(0)$	96	154	201	243	312	428	575
$AR(8)$	92	150	197	239	307	408	516

1.6.2 Control strategy

The BESS control consists in a droop-based strategy where the BESS active power output is given by the sum of the regulating power P^{efr} and an offset term P^{offset}, computed periodically to keep the SOE within its technical bounds. The optimal value of the droop coefficient α (i.e. the proportionality coefficient between the frequency deviations and the BESS power setpoints) is computed *a-priori* and hereafter called α_{max}. The determination of α_{max} for periods of given duration T, takes into account the statistical properties of W_f. The control is designed to restore for every subsequent period of duration T the optimal condition of SOE, so that the service can be deployed without interruptions with a known level of reliability. As for the other algorithms presented in this Chapter, the present control acts in two stages:

1. the period-ahead operation in which, on the basis of the forecast of the energy required for one period of operation i of duration T and of the knowledge of the current value of the BESS SOE, the offset term P_i^{offset} is computed. Such task is defined hereafter as *SOE management* and is executed periodically (i.e. every T, for each period i);

2. the real-time control, where the regulating action is actuated with 1 second resolution.

The following three paragraphs describe: *i)* how α_{max} is computed, *ii)* the SOE management mechanism and *iii)* the real-time control.

Droop coefficient computation

The optimal value of the droop coefficient α_{max} is computed based on two assumptions. First, a SOE management mechanism, described in the following section, is in place. This is to shift, within each period, the SOE to the value that allows for the maximum upward and downward regulation. Second, the SOE deviations due to EFR depend on the values of W_f, which follow the equations defined in Section 1.6.1. The optimal value α_{max} is defined as the higher possible value of α, that can be achieved compatibly with the operational constraints of the battery. This is of course because higher values of α correspond to more regulating power provided by the BESS to the grid.

α_{max} is computed so to respect, over each time interval the SOE energy constraints[7]. In other

---

[7]We observe that for the EPFL BESS and for small values of T (e.g. one or two hours), the power limits
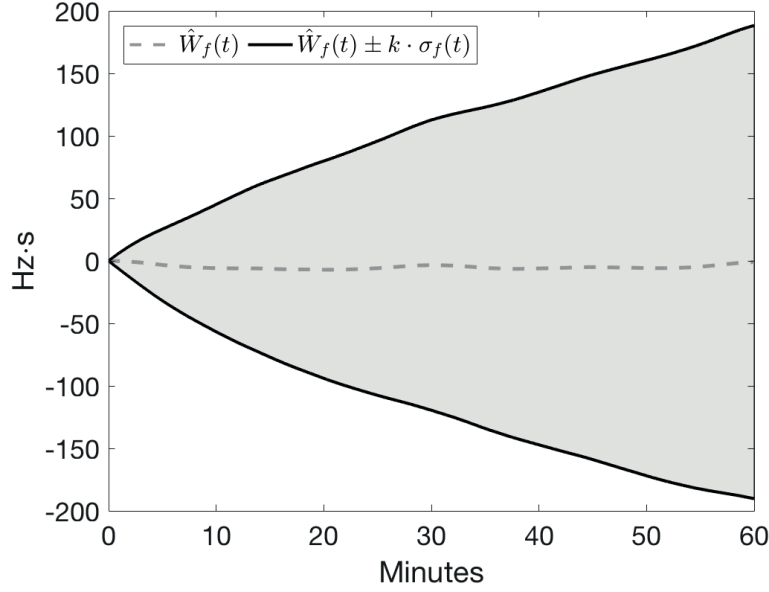
Figure 1.16 – In light grey, the confidence interval of the expected evolution of $W_f(t)$ in 1-hour time intervals, NGET dataset.

words, the SOE must always be within its limits $SOE_{max} = 1$ and $SOE_{min} = 0$.

We assume that the time evolution of $W_f(t)$ within each period is in a domain having upper and lower bounds that are monotonously increasing and decreasing, respectively. This is proven to be true experimentally. Fig. 1.16 shows, for instance the expected domain for $W_f(t)$ computed on the NGET dataset and with $T = 1$ h. This is computed using a model AR(0), applied at every time step t within the hour. $\hat{W}_f(t)$ is the expected profile of W_f within the interval, $\sigma_f(t)$ is standard deviation at each time step and k is equal to 1.96. It is clearly visible that the upper and lower bounds of this domain are monotonous. With this assumption, we can impose punctual SOE limits at the end of each period i, rather than explicitly constraining the SOE evolution along the whole interval. The SOE value at the end of each period i, hereafter SOE_i, should be:

$$SOE_i \leq SOE_{max} \tag{1.71}$$
$$SOE_i \geq SOE_{min} \tag{1.72}$$

The value of SOE_i is determined by several components:

$$SOE_i = SOE_{i-1} + \Delta SOE_i^{offset} + \Delta SOE_i^{efr}. \tag{1.73}$$

$[-P_{max}, +P_{max}]$ are more stringent than the SOE limits used here. However, we can consider that for a generic BESS providing EFR, power and SOE limits can be chosen coherently in the design phase. In Section 1.6.3 further details about the specific case of the EPFL BESS are provided.

Here, SOE_{i-1} is the SOE at the end of the previous period, ΔSOE_i^{offset} is the SOE variation due to the SOE management mechanism and ΔSOE_i^{efr} is the SOE variation due to the deployment of the EFR. The value of ΔSOE_i^{efr} for each period can be forecasted remembering (1.70) and remembering that the values of W_f can be predicted via autoregressive models. It is:

$$\Delta S\hat{O}E_i^{efr} \in \left[\frac{\alpha}{E_n} \left(\hat{W}_{f,i} - k\sigma_f \right), \frac{\alpha}{E_n} \left(\hat{W}_{f,i} + k\sigma_f \right) \right] \tag{1.74}$$

where $\hat{W}_{f,i}$ is the value predicted through the models AR(0) or AR(8) described in the previous section, σ_f is the associated residual variance and k is a coefficient related to the confidence level chosen for these bounds. Since W_f follows a normal distribution, it is that $k = 1.96$ for a 95% probability of the bounds to be respected, $k = 2.58$ for a 99% probability, etc.

Equation 1.73 becomes:

$$SOE_i \in SOE_{i-1} + \Delta SOE_i^{offset} + \frac{\alpha}{E_n} \hat{W}_{f,i} \pm \frac{\alpha}{E_n} k\sigma_f \tag{1.75}$$

We observe that, in this expression:

1. the confidence interval $\pm \frac{\alpha}{E_n} k\sigma_f$ is symmetric;

2. the terms SOE_{i-1} and $\frac{\alpha}{E_n} \hat{W}_{f,i}$ are known through measurement[8] and prediction, respectively;

3. the term ΔSOE_i^{offset} is controllable by definition.

By consequence, ΔSOE_i^{offset} can be determined to compensate for the terms SOE_{i-1} and $\frac{\alpha}{E_n} \hat{W}_{f,i}$ and to bring the BESS SOE to the value that ensures the maximum upward and downward regulation. Since the confidence interval $\pm \frac{\alpha}{E_n} k\sigma_f$ is symmetric, $SOE = 0.5$. It is therefore:

$$SOE_{i-1} + \Delta SOE_i^{offset} + \frac{\alpha}{E_n} \hat{W}_{f,i} = 0.5. \tag{1.76}$$

The value of α_{max} is found by transforming constraints 1.71 and 1.72 in equalities (describing the condition in which the operating limits are reached but not exceeded) and using (1.76):

$$0.5 + \frac{\alpha_{max}}{E_n} k\sigma_f = SOE_{max} \tag{1.77}$$

$$0.5 - \frac{\alpha_{max}}{E_n} k\sigma_f = SOE_{min} \tag{1.78}$$

From both (1.77) and (1.78) results that:

$$\alpha_{max} = \frac{(SOE_{max} - SOE_{min}) E_n}{2k\sigma_f} = \frac{E_n}{2k\sigma_f}, \tag{1.79}$$

---

[8]Strictly speaking, the SOE is estimated rather than measured. However, we used here the term "measured", to emphasize the difference with the prediction used for $\frac{\alpha}{E_n} \hat{W}_{f,i}$.

assuming $SOE_{max} = 1$ and $SOE_{min} = 0$. Theoretically, this is the maximum value of α allowing to deploy the EFR service without exceeding the selected bounds, with a confidence level k. We recall, finally, that the value of the standard deviation of the residuals σ_f depends on the autoregressive model used and on the length of the period T. An autoregressive model of higher order, such as AR(8), has a lower variance of the residuals in comparison with an AR(0) model. Therefore, the use of the higher-order autoregressive model results in a higher value for α_{max} and a higher provision of regulating power.

State-of-Energy Management

As already stated, the objective of the SOE management is to shift the BESS SOE to the value that ensures the maximum flexibility, i.e. 0.5. To achieve this, it compensates for two terms: *i)* the SOE at the beginning of the period i, SOE_{i-1}, which is measured and *ii)* the prediction of the SOE variation due to the EFR service, $\frac{\alpha_{max}}{E_n} \hat{W}_{f,i}$. Rearranging (1.76), it is:

$$\Delta SOE_i^{offset} = 0.5 - \left(SOE_{i-1} + \frac{\alpha}{E_n} \hat{W}_{f,i} \right) \tag{1.80}$$

We chose to provide this SOE variation by a power that is constant over the duration T of the intervals:

$$P_i^{offset} = \frac{\Delta SOE_i^{offset}}{T} \tag{1.81}$$

This constant power is superimposed in the realtime control to the regulating power P^{efr}. Since P_i^{offset} is known, predetermined before every period i and constant over i, the contibutions of these two terms can be easily decoupled. This is helpful when assessing the efficacy of the EFR service and the effect on the grid of the two terms. We observe, moreover, that this superposition is similar to the one of power plants providing PFC. These, in fact, provide a baseline power (determined by the unit commitment) and, on the top of it, a power variation to participate in the regulation. Similarly to this case, the value of P_i^{offset} constitutes a "BESS power baseline", which could eventually be traded on the day-ahead or intra-day energy markets (depending on the length T of the intervals for the SOE management mechanism).

The functioning of the SOE management mechanism is shown graphically in Figure 1.17. At the beginning of each period i, the SOE could assume any value within $[0, 1]$, due to the EFR deployed in the previous period. During period i, without SOE management, the SOE would vary of a quantity in the interval $\left[\frac{\alpha_{max}}{E_n} \left(\hat{W}_{f,i} + k\sigma_f \right), \frac{\alpha_{max}}{E_n} \left(\hat{W}_{f,i} - k\sigma_f \right) \right]$. In figure 1.17-a, the grey areas represent the domain of all the expected SOE trajectories. The black line represent the average profile of this domain, as well as the SOE profile that is, statistically, more probable. In the absence of a SOE management mechanism, and assuming EFR is provided with α_{max}, the SOE at the end of the period may result beyond the BESS SOE limits (dark grey area). In other words, the deployment of EFR cannot be ensured with the desired reliability level and may fail due to hitting the BESS SOE limits. Figure 1.17-b shows the expected SOE behavior
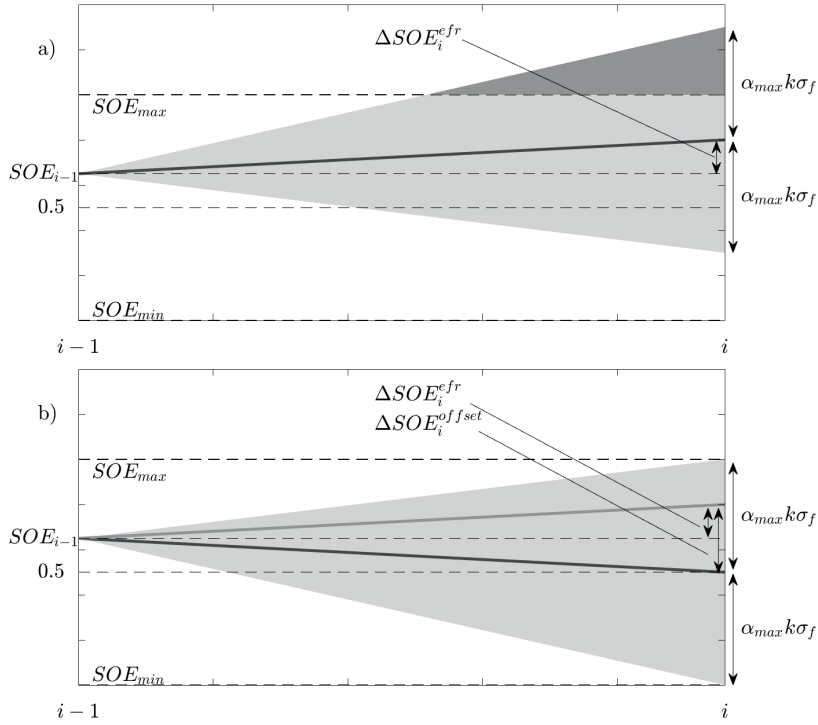
Figure 1.17 – Expected trajectories of the energy stored in the BESS over a period T a) without and b) with the action of the SOE-M.

when adding a SOE management mechanism. Again the grey areas represent the domain of all the expected SOE trajectories. The black line represent the average of this domain, while the dark grey line is such curve in absence of this mechanism (it corresponds to the black line in figure 1.17-a). We observe that, due to the presence of ΔSOE_{offset}, the grey domain is shifted, so to be completely within the BESS SOE limits. In other words, we expect now to be able to deploy the EFR service with the desired level of reliability.

Real-time control

In real-time, the frequency deviation Δf is measured with 1 second resolution and every second the BESS power set-point is refreshed as:

$$P_j^{BESS} = \Delta f_j \cdot \alpha_{max} + P_i^{offset}. \tag{1.82}$$

where the subscript i refer to the period of duration T as in the previous sections, the subscript j refer to the 1 second time step, the value of α_{max} is determined a priori as defined in subsection 1.6.2 and the value of P_i^{offset} is computed as described in Section 1.6.2 and updated periodically every T. Figure 1.18 summarizes the functioning of the proposed control
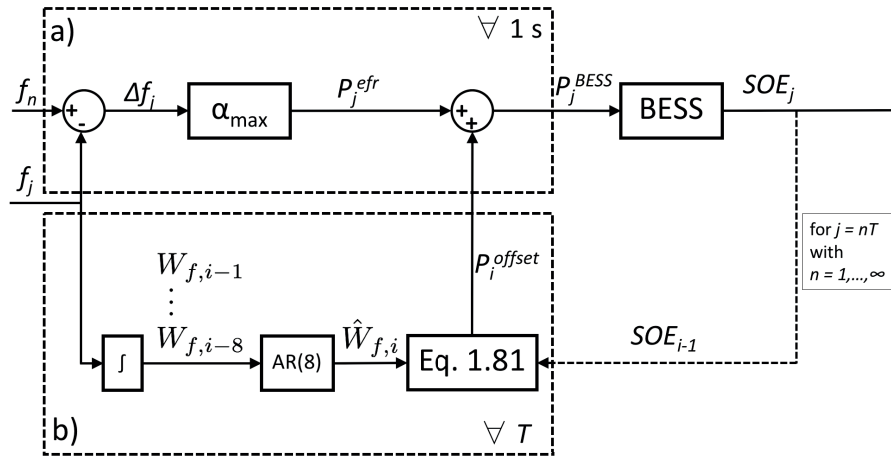
Figure 1.18 – Block diagram of the proposed control scheme: a) real-time control, operating at 1 second resolution, b) SOE management, operating at time resolution T.

scheme.

1.6.3 Results

In this Section the main results obtained by applying the proposed methods are shown. The first subsection, "Droop coefficient computation", shows the values of droop coefficients determined for the two datasets (EPFL and NGET), the two forecasting models and for various values of T. The second subsection, "Simulations", shows the simulation results obtained for such values and compares the performances of the control based on AR(0) and on AR(8). Finally, the subsection "Experiments" shows the results obtained by applying the proposed methods to the control of a 720 kVA/560 kWh grid-connected BESS. These are with the objective of validating experimentally the proposed methods, evaluating the BESS performances in performing EFR and validating the simulation environment used to obtain the first sets of results.

Droop coefficient computation

The algorithm for the computation of the droop coefficient α_{max} has been used for each of the considered periods. Tables 1.8 and 1.9 show such results. Notably, Table 1.8 refers to the droop coefficient values computed from the frequency dataset provided by NGET. Table 1.9, refers to the data collected in one year at the EPFL campus. These have been used in the experiments described in last paragraph of this Section.

The method presented in Section 1.6.2 determines the value of α_{max} on the basis of the energy capability of the BESS. In the case of the EPFL 720 kVA/560 kWh BESS, the nominal power

should be considered when determining α_{max}. The theoretical value of α_{max} corresponds to the minimum value between α_{max}^e (i.e. the maximum droop coefficient based on the BESS energy capability, found as in Section 1.6.2) and α_{max}^p (i.e. the maximum droop coefficient compatible with the BESS power ratings). The latter term can be computed as follows:

$$P_{max}^{offset} = \frac{SOE_0 \cdot E_n}{T_{i+1} - T_i}, \tag{1.83}$$

$$P_{max}^{efr} = P_n - P_{max}^{offset}, \tag{1.84}$$

$$\alpha_{max}^p = \frac{P_{max}^{efr}}{\Delta f_{max}}, \tag{1.85}$$

where P_{max}^{offset} is the maximum possible value of the power offset, P_n is the rated power of the BESS, and P_{max}^{efr} is the maximum regulating power. All the values in Table 1.9 have been computed considering a grid-connected 720 kVA/560 kWh BESS and the activation of full reserve power for frequency deviation beyond ±200 mHz, as dictated by ENTSO-E grid codes [195].

Table 1.8 – Values of α_{max}^e, in $[kW/Hz]$, NGET database.

T [h]	1	2	3	4	6	12	24
AR(0), $\rho = 95\%$	5325	3321	2555	2115	1646	1201	893
AR(0), $\rho = 99\%$	4046	2523	1941	1607	1251	913	679
AR(8), $\rho = 95\%$	5567	3415	2607	2144	1674	1259	995
AR(8), 99%	4230	2595	1981	1629	1272	957	756

Table 1.9 – Droop coefficient values $[kW/Hz]$, EPFL database ($\rho = 95\%$).

T[h]	1	2	3	4	6	12	24
AR(0), α_{max}^e	14807	8524	6278	4959	3623	2270	1270
AR(0), α_{max}^p	2200	2900	3133	3250	3366	3483	3541
AR(8), α_{max}^e	17216	9751	7337	5895	4302	2633	1386
AR(8), α_{max}^p	2200	2900	3133	3250	3366	3483	3541

Table 1.9 shows that for the EPFL 720 kVA/560 kWh BESS and for the $T \leq 6$h, the theoretical value of α_{max} is determined by the BESS power ratings rather than its energy capability. In Section "Experiments", details are given about the values of T and α_{max} used to experimentally validate the proposed methods with the specific ratings of the EPFL BESS.

Simulations

The performance of the proposed control framework is validated by simulations in Matlab/Simulink. The simulator uses one year of frequency measurements for the NGET database as input and the BESS state of energy as output. It presents two different models of BESS. In the *ideal* model the losses are not taken into account, whereas in the *real* one the losses are modeled as in [167]. Specifically the battery is considered as the series of a voltage source and a resistance and the values of both depend on the battery state of charge (SOC). The SOE-M performance in the simulation environment has been evaluated for three periods T, two different confidences levels (95% and 99%), and for the two different autoregressive models ($AR(0)$ and $AR(8)$). The results of these simulations are evaluated by quantifying the failure rate λ_T. The SOE-M fails in its control when the BESS reaches its capability limits and cannot provide power for the EFR. The control failure rate λ_T corresponds to the duration of the period in which the BESS is not able to perform its tasks, expressed in percentage of the simulation duration. From the definition of the droop coefficient given in Section 1.6.2, over one period of operation the expected failure rate is related to the confidence ρ on the control action as follows:

$$\tilde{\lambda}_T = 1 - \rho. \tag{1.86}$$

Table 1.10 presents the results of the simulations. The failure rate λ_T is on average equal to

Table 1.10 – Simulation results, NGET Database

			$AR(0)$		$AR(8)$	
BESS model	ρ	T	α_{max}	$\tilde{\lambda}_T$	α_{max}	$\tilde{\lambda}_T$
	[%]	[h]	[kW/Hz]	[%]	[kW/Hz]	[%]
Ideal	95%	24	893	3.631	995	4.723
Real	95%	24	893	4.423	995	6.410
Real	99%	24	679	0.358	755	0.358
Ideal	95%	12	1201	4.087	1259	4.609
Real	95%	12	1201	4.779	1259	5.223
Real	99%	12	912	0.616	957	0.799
Ideal	95%	1	5325	2.992	5567	2.472
Real	95%	1	5325	5.086	5567	2.452
Real	99%	1	4045	0.408	4229	0.350

3.8% for the simulation based on a ρ=95% and a BESS with unitary efficiency and to 4.7% for the simulation based on a ρ=95% and a BESS with non-unitary efficiency. In both cases the average failure rate for the simulation is close to the expected value of 5%. Moreover, it can be observed that the introduction of a more accurate BESS efficiency model does not provide results considerably different from those obtained for an ideal BESS.

Experiments

The algorithm has been tested experimentally using 720 kVA/560 kWh EPFL BESS described in Section 1.3. Frequency measurements are from an on-site PMU-based metering system [138].

A series of experiments has been carried out, to evaluate the ability of the algorithm to ensure the rated reliability. Experiments have been carried out for T=3h and T=6h and with the α_{max} defined as in section 1.6.2, based on the BESS energy capability. The choice of T=3h and T=6h, although in contrast with the results presented in Table 1.9, is justified by two observations. On one hand, experiments based on T=12h or T=24h would need a considerably long run-time to achieve statistically relevant results. On the other side, for smaller T, an α_{max} computed as in Section 1.6.2 would generate an ineffective regulation, since even for deviations of relatively small magnitude, the BESS power would be limited by its power rating and the regulation signal would not be tracked accurately. For T=3h and T=6h, the power rating of the battery would limit the BESS power from tracking the regulating signal only in the occurrence of large and infrequent frequency deviations (Δf >100mHz). These values of T are therefore suited to the purpose of validating the proposed method, although the consideration of the power ratings should be taken into account in the sizing phase of a BESS designed to perform EFR.

The results of this set of experiments are summarised in Table 1.11 and consist of almost 500 hours of EFR divided in four experiments. Experiments 1 and 2 consist in $H = 23$ consec-

Table 1.11 – Experimental results: reliability and failure rate.

Experiment	Model	T	H	α_{max}	$\hat{\lambda}_T$
		[h]	[$-$]	[kW/Hz]	[%]
1	AR(0)	3h	23	6278	5.7596
2	AR(8)	3h	23	7337	5.9871
3	AR(0)	6h	30	4302	2.8565
4	AR(8)	6h	30	3623	5.5144

utive periods of $T = 3\ h$ each. Experiments 3 and 4 consists in H=30 consecutive periods of $T = 6\ h$ each. In experiments 1 and 3 a AR(0) model has been implemented, while an AR(8) model has been implemented in experiments 2 and 4. The observed failure rates $\hat{\lambda}_T$ for each

experiment are in the neighborhood of the expected value $\tilde{\lambda}_T = 5\%$. Experiment 3 is the one in which $\hat{\lambda}_T$ is the more distant from this value, having a $\hat{\lambda}_T = 2.86\%$. This difference can be explained by the relatively low number of periods H taken into consideration. Longer experiments, not carried out due to time limitations, are expected to provide values that are more close to the theoretical value, the experiments described in this section still present a non-negligible influence of contingent operating conditions.

Figure 1.19 shows the result of "EXP3". The control fails every time the SOE is near to the limits and the battery is not able to implement the set points received from the control logic.
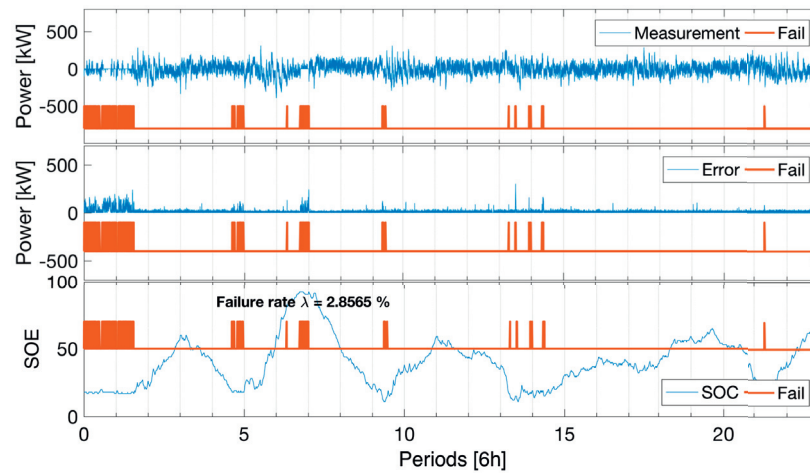
Figure 1.19 – Evaluation of the reliability. Results from experiment 3. Top: power output, middle: absolute error between setpoint and measurement, bottom: SOE.

2 Generic Framework for the provision of multiple simultaneous services

This chapter proposes a generic formulation of the framework developed in Chapter 1, that is with the purpose of providing multiple services simultaneously. First, it provides the motivations and a state of the art summarizing the recent efforts in this direction. Second, it describes a generic framework to optimize the operation of a BESS providing simultaneously several services. Third, it applies this framework to the case of dispatching the operation of a MV feeder and providing simultaneously enhanced frequency response (EFR). Finally it demonstrates via simulations and experiments the validity of such framework.

2.1 Motivations

Chapter 1 presents a set of control algorithms to provide individually several services via a BESS, notably dispatchability, load levelling and frequency regulation. These algorithms are based on a two-stage structure and take into account the uncertainty related to the stochastic quantities considered in the control (the uncontrollable loads and PV generation in the case of the dispatch and load levelling and the frequency deviation signal in the case of frequency regulation). Batteries are normally sized to provide one among said services continuously and reliably. The actual daily deployment of power and exploitation of energy capacity to achieve this result vary due to the uncertainty of the aforementioned stochastic quantities. Therefore, the deployment of such services rarely requires the exploitation of the whole BESS capacity. When a portion of the BESS energy capacity remains unexploited by the deployment of its main service, it could be allocated to a secondary service, to be deployed in parallel. In other words, coupling multiple services together may allow to exploit at best the batteries coupled with stochastic resources.

Figure 2.1 shows a practical example of this concept. The groups of plots indicated by I and II refer respectively to two scenarios (referred hereafter as case I and case II) of BESS utilization to dispatch the operation of a feeder as described in Section 1.4. Subplots I-a) and II-a) show with a blue line the prosumption forecasts computed for the two considered days, with thin gray lines the prosumption scenarios considered for the computation and with thick black
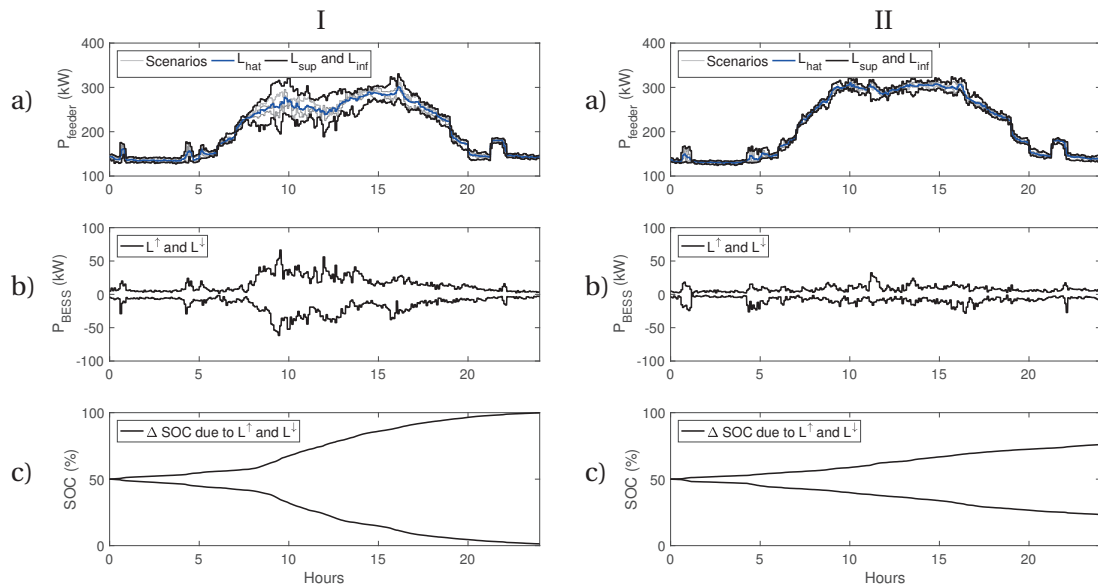
Figure 2.1 – Comparison of the BESS power and energy requirements to dispatch the EPFL MV feeder in two days characterised by high and low uncertainty in the prosumption forecast (plot groups I and II, respectively.).

lines the upper and lower worst case prosumption scenarios taken into consideration. The algorithm developed in 1.4 requires the BESS to be able to compensate for all deviations from the dispatch plan within the worst case scenarios. Subplots I-b) and II-b) show the maximum and minimum active power profiles that could be required to the BESS to satisfy this goal. Subplots I-c) and II-c), finally, show the daily SOC profiles associated to these worst cases. Case I is characterized by higher uncertainty in the forecasts. The power requirements to ensure the dispatchability of the feeder, therefore, are higher than those in case II. The latter, in fact, is characterized by a lower uncertainty in the forecast. This is reflected in the SOC profiles that the BESS would present in the worst cases and, consequently, in the need of energy capacity to operate the BESS in the considered day. In case I the BESS needs its complete SOC range. In fact, at the end of this day, the worst cases generate a BESS SOC that is close to 0 and 100% respectively. In case II, on the contrary, the SOC range necessary to ensure the dispatchability is considerably smaller (about the 50% of the complete range). A BESS is installed to provide exclusively the dispatch service is to be sized to operate in case I, in order to ensure continuous operation. In any day in which the forecast uncertainty is lower (as in case II), the same level of reliability is reached without exploiting a considerable portion of the BESS capacity. Allocating the unexploited capacity to a further service, to be executed simultaneously with the dispatch, would instead constitute an effective exploitation of such device.

60

2.2 State of the art on the simultaneous provision of grid services via BESSs

The relevance of application sinergies for energy storage devices has been pointed out in general terms in [54]. Several works, in the recent literature, propose approaches to provide simultaneously multiple grid services and demonstrate their effectiveness via simulations [33, 47, 81, 82, 111, 116, 135, 162, 183, 184, 191, 193]. These references differentiate themselves from one another for the type of services considered, the control techniques exploited and technical aspects detailed. With respect to the considered services, these can be grouped in three main categories:

1. Energy arbitrage (EA), which consists in generating revenue by buying or selling energy depending on energy market prices;

2. Ancillary services (AS), which are a set of services that batteries can provide to grid operators to enhance the system reliability (e.g. frequency response and regulation). The provision of these services is regulated by specific markets;

3. BESSs can be finally exploited for objectives specific to a location (i.e. local objectives (LO)). Examples of LOs are maximisation of self-consumption, minimisation of PV curtailement, grid constraint management, etc.

The references listed above aim at providing two or more of such services and with regard to such categories, they can be divided as in Table 2.1.

Table 2.1 – Recent literature on clustering of BESS applications in power systems

Services provided	References
EA + AS	[33, 47, 81, 82, 184, 191]
LO + AS	[111, 162, 183]
LO + EA + AS	[116, 135, 193]

In such references, operation scheduling problems for energy storage systems considering multiple services are formulated. These aim at maximising the economic revenue generated for standalone storage systems exploiting multiple revenue streams. This objective is sought after in different pricing contexts and the common result is that by jointly providing multiple services, the BESS economic income is increased. Nonetheless, energy storage systems are often used in two further configurations [82]: *i)* used by system operators to improve system reliability (e.g. [124, 202]) or *ii)* in conjunction with other resources such as distributed generation [3], flexible demand [25] or electric vehicles [159].

Besides the objective of the proposed scheduling problems, the references listed in Table 2.1 focus on different aspects of the control framework needed to provide multiple services

simultaneously. Several references propose specific methods for storage technologies other than BESSs: compressed air energy storage [47], fleets of thermostatically controlled loads [183], or fleets of distributed BESSs [111]. References [183] and [162], besides the formulation of the scheduling problem, describe the real-time control to implement the proposed strategies. References [81, 82, 162] propose a robust optimization approach to deal with uncertainties related to price signals and reserve deployment. Finally [81] analyses how providing multiple services simultaneously affects the BESS lifespan.

2.3 General Problem Formulation

We consider the problem of scheduling the operation of a BESS with energy capacity E_{nom} and maximum power P_{max}, for a time window T. During each time window, the BESS provides J services, each denoted by the subscript $j = 1, \ldots, J$.

2.3.1 Definition of the power and energy budgets

Each service j is characterized by an energy budget $\mathscr{E}_j$ and a power budget $\mathscr{P}_j$. These are the shares of the BESS energy capacity and power necessary along the time window T to deploy the service j. The power and energy budgets $\mathscr{P}_j$ and $\mathscr{E}_j$ necessary for each service are functions of a set of tunable control parameters (composing the decision vector of the scheduling problem and hereafter denoted by x) as well as of variables modelling the uncertainty of the operating conditions related to each service (hereafter θ). The dependency of $\mathscr{P}_j$ and $\mathscr{E}_j$ on θ is introduced to account for the fact that the deployment of the considered services need to be ensured in the occurrence of any scenario of their power demand (practical examples are provided in Section 2.3). We formulate an optimization problem to determine the value of decision vector x (and hence the power and energy budgets $\mathscr{P}_j$ and $\mathscr{E}_j$ for $j = 1, \ldots, J$) that maximizes the portion of BESS energy capacity made available for the provision of the services in J. We discretize the window of duration T in N time steps of duration T/N, each denoted by the subscript k, with $k = 1, \ldots, N$. Formally, the power budget of the service j at time step k is denoted $\mathscr{P}_{j,k}$ and is defined as the interval of the expected power values that the service could require at k. These are between the minimum and maximum expected power realizations for that service, namely in the interval $\mathscr{P}_{j,k} = \left[P_{j,k}^{\downarrow}, P_{j,k}^{\uparrow} \right]$. The power budget along a time period T is defined as the sequence of such intervals:

$$\mathscr{P}_j = \left\{ \left[P_{j,k}^{\downarrow}(x, \theta), P_{j,k}^{\uparrow}(x, \theta) \right], k = 1, \ldots, N \right\}. \tag{2.1}$$

Similarly, the application will require an energy budget

$$\mathscr{E}_j = \left\{ \left[E_{j,k}^{\downarrow}(x, \theta), E_{j,k}^{\uparrow}(x, \theta) \right], k = 1, \ldots, N \right\}. \tag{2.2}$$

An example of energy and power budets is reported in Fig. 2.2. The set of widths of such
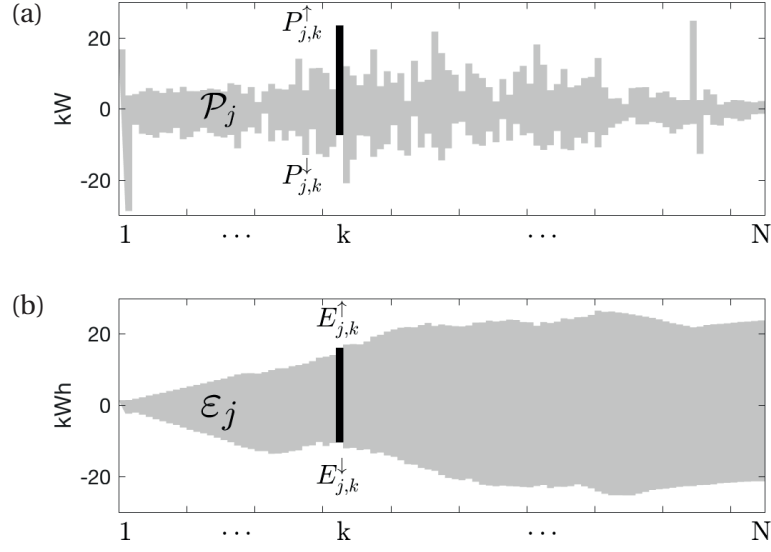
Figure 2.2 – Example of (a) power and (b) energy budgets for a service j.

energy budget trajectory is defined as:

$$w(\mathcal{E}_j(x,\theta)) = \{E^\uparrow_{j,k}(x,\theta) - E^\downarrow_{j,k}(x,\theta), k = 1,\dots,N\}. \tag{2.3}$$

Moreover, we define the operation of sum of budgets of different services (using energy budget as example) as[1]:

$$\sum_j \mathcal{E}_j(x,\theta) =$$
$$= \left\{ \left[\sum_{j=1}^J E^\downarrow_{j,k}(x,\theta), \sum_j^J E^\uparrow_{j,k}(x,\theta) \right], k = 1,\dots,N \right\}. \tag{2.4}$$

2.3.2 Formulation of the optimisation problem

The problem of providing multiple concurrent services with a BESS, while ensuring feasible operation can now be formulated in generic terms. We seek to maximise the set of widths of the energy budget resulting from the sum of the energy budgets $\mathcal{E}_j$ with $j = 1,\dots,J$, within a given time window T, while respecting the BESS power and energy capabilities. The resulting decision problem is:

$$x^o = \arg\max_x \left[w \left(\sum_{j=1}^J \mathcal{E}_j(x,\theta) \right) \right] \tag{2.5}$$

---

[1] Eq. (2.4) can be interpreted as the computation of the overall energy budget within T required by all services J.

subject to:

$$E_{init} + \sum_{j=1}^{J} \mathscr{E}_j(x,\theta) \in [E_{min}, E_{max}] \tag{2.6}$$

$$\sum_{j=1}^{J} \mathscr{P}_j(x,\theta) \in [-P_{max}, P_{max}], \tag{2.7}$$

where E_{min} and E_{max} are the minimum and maximum stored energy and P_{max} the maximum istantaneous power of the BESS. It is worth noting that it is possible to have a different objective function while exploiting the same framework presented here. In Appendix A.3, two variations seeking respectively for the maximisation of the economical revenue and simple feasibility of operation are shown. The same appendix, moreover, proposes a formulation of the day-ahead problem including the load levelling service as well as

2.4 Concurrent dispatch of a MV distribution feeder and provision of EFR

The scheme proposed in Section 2.3 is now applied to control a BESS to dispatch of a MV distribution feeder and to provide EFR to the grid. We have observed that the battery capacity needed to dispatch a MV feeder as in [167] depends on the uncertainty of the forecast of the connected stochastic resources (loads and stochastic distributed generation). Whereas in some cases the full battery capacity is barely sufficient to achieve this goal, in others a considerable portion of the battery capacity remains unutilized when the uncertainty of the prosumption forecast is small. The choice of EFR as a second stacked service is because *i)* large ramping duties of BESSs accomodate the increased demand for fast regulating power in power systems with a high penetration of production from renewables and *ii)* EFR is a "power intensive" application and is well-suited to be coupled with the dispatch service, which is instead "energy intensive".

2.4.1 Day-ahead problem formulation

We want to operate a grid-connected BESS to dispatch the active power flow of a MV distribution system with heterogeneous resources, as in [167], while providing also EFR to the grid. Figure 2.3 shows the main features of this setup. The operation is performed over a T=24 hour period and planned every day for the next calendar day. Following the formulation presented in Section 2.3, we first define the power and energy budgets for the dispatch and EFR, namely $\mathscr{P}_D$, $\mathscr{P}_{FR}$, $\mathscr{E}_D$ and $\mathscr{E}_{FR}$. Based on these budgets, we formulate an optimization problem as in (2.5)-(2.7).

The dispatch service requires the battery to compensate for the mismatch between the aggregated prosumers power flow (denoted by $\mathbf{L}_k = L_1, \dots, L_N$) and a pre-established dispatch plan
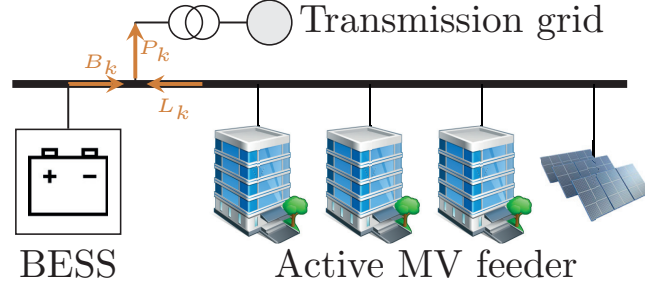
Figure 2.3 – Schematic of the experimental setup. The notation of the power flows refers to the real-time control described in section 2.4.2.

$\hat{\mathbf{P}} = \hat{P}_1, \ldots, \hat{P}_N$, defined at 5-minutes resolution. The dispatch plan is the sum of two terms: the forecasted power profile of the feeder prosumption, $\hat{\mathbf{L}} = \hat{L}_1, \ldots, \hat{L}_N$ and an offset power profile, $\mathbf{F} = F_1, \ldots, F_N$, computed to keep the BESS stored energy within proper limits:

$$\hat{P}_k = \hat{L}_k + F_k \quad \text{for} \quad k = 1, \ldots, N \tag{2.8}$$

We obtain, with a forecasting tool from the literature [167], the daily forecasted profile of the feeder prosumption as well as the deviations from the forecasted profile in the highest and lowest demand scenarios, denoted by $\mathbf{L}^\uparrow = L_1^\uparrow, \ldots, L_N^\uparrow$ and $\mathbf{L}^\downarrow = L_1^\downarrow, \ldots, L_N^\downarrow$ (a detailed definition of the terms above is already provided in Section 1.4 of this thesis). The maximum positive and negative BESS power requirements for the dispatch service are therefore defined as the sum over k of the offset power F_k and of $L_k^\uparrow$ and $L_k^\downarrow$, respectively. With respect to the general definitions of x and θ given Section 2.3, the terms $L_k^\uparrow$ and $L_k^\downarrow$ are input quantities (i.e. $\{\mathbf{L}^\uparrow, \mathbf{L}^\downarrow\}$ are in θ) whereas the offset power $\mathbf{F}$ is a decision variable, determined by the optimization problem defined hereafter (i.e. $\mathbf{F}$ is in x). The power budget is therefore defined as:

$$\begin{aligned}\mathscr{P}_D &= \{\left[P_{D,k}^\downarrow(x,\theta), P_{D,k}^\uparrow(x,\theta)\right], k = 1, \ldots, N\} \\ &= \{\left[F_k + L_k^\downarrow, F_k + L_k^\uparrow\right], k = 1, \ldots, N\}\end{aligned} \tag{2.9}$$

The associated energy budget is:

$$\begin{aligned}\mathscr{E}_D &= \{\left[E_{D,k}^\downarrow(x,\theta), E_{D,k}^\uparrow(x,\theta)\right], k = 1, \ldots, N\} \\ &= \left[\frac{T}{N}\sum_{i=1}^k (F_i + L_i^\downarrow), \frac{T}{N}\sum_{i=1}^k (F_i + L_i^\uparrow)\right]\end{aligned} \tag{2.10}$$

with $k = 1, \ldots, N$.

The EFR service requires the battery to provide a power proportional to the deviation of the frequency from its nominal value $\Delta f_k = f_k - f_n$ [195], with a proportionality coefficient

hereafter denoted by α:

$$P_{FR,k} = \alpha \Delta f_k = \alpha \left(f_k - f_n \right). \tag{2.11}$$

The unit of measurement of α is kW/Hz. The instantaneous requested power cannot be forecasted since frequency deviations are difficult to predict. Therefore, the power budget required by this application will correspond to a constant profile, equal to the maximum power that frequency regulation may require. Since grid codes typically require complete activation of primary reserves for frequency deviations of more than $\Delta f_{max} = 200$ mHz [195], the power budget can be defined as:

$$\begin{aligned}\mathscr{P}_{FR} &= \{\left[P_{FR,k}^{\downarrow}(x,\theta), P_{FR,k}^{\uparrow}(x,\theta)\right], k = 1,\ldots,N\}\\ &= [-0.2\alpha \cdot \mathbf{1}, 0.2\alpha \cdot \mathbf{1}]\end{aligned} \tag{2.12}$$

Where $\mathbf{1}$ is the all-one vector of length N. The energy budget necessary to ensure feasible operation for this service within a given time interval can be inferred statistically. In particular, we examined grid frequency data of the European grid from the last 2 years. Data have been collected by a PMU-based metering system installed on the EPFL campus [138]. Since frequency regulation requires the injection of a power $P_k = \alpha \Delta f_k$, the energy required by the grid during a given time window T is:

$$\begin{aligned}E_{FR,k} &= \frac{T}{N}\sum_{i=0}^{k} P_{FR,i} = \frac{T}{N}\sum_{i=0}^{k}(\alpha \Delta f_i)\\ &= \alpha \left(\frac{T}{N}\sum_{i=0}^{k} \Delta f_i\right) = \alpha W_{f,k}\end{aligned} \tag{2.13}$$

for $k = 1,\ldots,N$ and where $W_{f,k}$ denotes the integral of frequency deviations over a period of time and it is to be interpreted as the *energy content* of the signal given by the frequency deviation from its nominal value. The upper and lower bounds for $W_{f,k}$ for $k = 1,\ldots,N$ can be inferred from a statistical analysis of historical frequency deviation time-series,reported in Appendix A.4). These are defined hereafter as $\mathbf{W}_f^{\uparrow} = W_{f,1}^{\uparrow},\ldots,W_{f,N}^{\uparrow}$ and $\mathbf{W}_f^{\downarrow} = W_{f,1}^{\downarrow},\ldots,W_{f,N}^{\downarrow}$. With regard to the general definitions of x and θ given in Section 2.3, the terms $W_k^{\uparrow}$, $W_k^{\downarrow}$ (as well as Δf_{max} in (2.12)) are input quantities (i.e. $\{\mathbf{W}^{\uparrow}, \mathbf{W}^{\downarrow}, \Delta f_{max}\}$ are in θ) whereas α is a decision variable, determined by the optimization problem defined hereafter (i.e. α is in x). The energy budget for frequency regulation is then defined as:

$$\begin{aligned}\mathscr{E}_{FR} &= \{\left[E_{FR,k}^{\downarrow}(x,\theta), E_{FR,k}^{\uparrow}(x,\theta)\right], k = 1,\ldots,N\}\\ &= \{\left[\alpha W_{f,k}^{\downarrow}, \alpha W_{f,k}^{\uparrow}\right], k = 1,\ldots,N\}.\end{aligned} \tag{2.14}$$

Relying on the definitions given in Section 2.3, it is $x = [\alpha, \mathbf{F}]$ and $\theta = [\Delta f_{max}, \mathbf{W}_f^{\downarrow}, \mathbf{W}_f^{\uparrow}, \mathbf{L}^{\downarrow}, \mathbf{L}^{\uparrow}]$

and the objective function in (2.5), corresponds therefore to:

$$
\begin{aligned}
w\left(\sum_j \mathcal{E}_j\right) &= w\left(\mathcal{E}_D + \mathcal{E}_{FR}\right) \\
&= \left(\frac{T}{N}\sum_{i=0}^{k}(F_i + L_i^{\uparrow}) + \alpha W_{f,k}^{\uparrow}\right) + \\
&\quad -\left(\frac{T}{N}\sum_{i=0}^{k}(F_i + L_i^{\downarrow}) + \alpha W_{f,k}^{\downarrow}\right) \\
&= \left(\frac{T}{N}\sum_{i=0}^{k}(L_i^{\uparrow}) - \frac{T}{N}\sum_{i=0}^{k}(L_i^{\downarrow})\right) + \alpha\left(W_{f,k}^{\uparrow} - W_{f,k}^{\downarrow}\right)
\end{aligned}
\tag{2.15}
$$

with $k = 1, \ldots, N$.

Since α is the only control variable in the above expression, the objective to maximize $w\left(\sum_j \mathcal{E}_j\right)$ in (2.5) reduces to maximizing α, subject to (2.6)(2.7). The problem (2.5)-(2.7) is as:

$$
\left[\alpha^o, \mathbf{F}^o\right] = \underset{\alpha \in \mathbb{R}^+, \mathbf{F} \in \mathbb{R}^N}{\arg\max}\ (\alpha)
\tag{2.16}
$$

subject to:

$$
E_{init} + \mathcal{E}_D(x,\theta) + \mathcal{E}_{FR}(x,\theta) \in [E_{min}, E_{max}]
\tag{2.17}
$$

$$
\mathcal{P}_D(x,\theta) + \mathcal{P}_{FR}(x,\theta) \in [-P_{max}, P_{max}]
\tag{2.18}
$$

By expressing explicitly the dependency of the power and energy budgets on the parameters and control variables, the problem (2.16)-(2.18) becomes:

$$
\left[\alpha^o, \mathbf{F}^o\right] = \underset{\alpha \in \mathbb{R}^+, \mathbf{F} \in \mathbb{R}^N}{\arg\max}\ (\alpha)
\tag{2.19}
$$

subject to:

$$
E_{init} + \frac{T}{N}\sum_{i=1}^{k}\left(F_i + L_i^{\uparrow}\right) + \alpha W_{f,k}^{\uparrow} \leq E_{max}
\tag{2.20}
$$

$$
E_{init} + \frac{T}{N}\sum_{i=1}^{k}\left(F_i + L_i^{\downarrow}\right) + \alpha W_{f,k}^{\downarrow} \geq E_{min}
\tag{2.21}
$$

$$
F_k + L_k^{\uparrow} + 0.2\alpha \geq P_{max}
\tag{2.22}
$$

$$
F_k + L_k^{\downarrow} + 0.2\alpha \geq -P_{max}
\tag{2.23}
$$

with $k = 1, \ldots, N$.

The notion of battery round-trip efficiency is incorporated in the decision problem (2.19)-(2.23) with an empirical two-stage approach by enforcing conservative limits for the battery

stored energy. This process is explained in the following. First, the problem (2.19)-(2.23) is solved implementing the nominal battery state-of-energy limits (i.e. $E_{max} = E_{nom}$ and $E_{min} = 0$). Second, the following finite impulse response model [62, 167]:

$$E_k = E_0 + \frac{T}{N} \sum_{i=1}^{k} \eta_i B_i, \qquad \eta_i = \begin{cases} \beta & B_i \geq 0 \\ 1/\beta & B_i < 0 \end{cases}, \qquad (2.24)$$

where B_i is the total power injected or absorbed by the BESS at time i and η_i the BESS efficiency, is used to model the stored energy E_k of a non ideal BESS for the set of simulation scenarios presented in Section 2.5.1. The energy stored at the end of each day in a BESS modeled as ideal ($\eta = 1$) and non ideal ($\eta = 0.97^2$) are compared and the largest difference over the all set of simulations is used to impose a conservative bound to the minimum stored energy constraint (2.21). For example, in the case proposed in Section 2.5.1, the largest difference is 4% of E_{nom}, therefore we adopt $E_{min} = 0.05E_{nom}$. It is worth noting that this approach allows to define the energy budgets independently for each service and sum them as in (2.15). In other words, it achieves a separation of concerns between services, which can be designed independently from each other and stacked together at the end of the process. Also, it is worth noting that the round-trip efficiency of modern Li-ion based BESS is generally above 90% [28, 60, 148].

Appendix A.3 proposes a formulation of the day-ahead problem including the load levelling service, besides the dispatch and EFR already discussed here. It is also to be noted that applying the proposed generic formulation to provide only one service, would result in problem formulations very similar to those presented in Chapters 1.4 and 1.6 for dispatch and EFR respectively. In fact, removing α, $\mathbf{W}_f^{\uparrow}$ and $\mathbf{W}_f^{\downarrow}$ from the Problem in (2.19)-(2.23), would determine an offset profile $\mathbf{F}$ that ensures the feasibility of the dispatch. Such $\mathbf{F}$, summed to the prosumption forecast $\hat{\mathbf{L}}$, provides the dispatch plan $\hat{\mathbf{P}}$. On the contrary, removing the terms $\mathbf{L}^{\uparrow}$ and $\mathbf{L}^{\downarrow}$ (but keeping $\mathbf{F}$, as degree of freedom to manage the BESS state of energy) would determine the maximum value of the droop coefficient α that can be exploited by a BESS providing exclusively EFR.

2.4.2 Real-time control

The proposed algorithm consists in two phases: *i)* the solution of a planning problem for the next calendar day of operation, determining the values of the coefficient α^o and of the offset profile $\mathbf{F}^o$ and *ii)* a real-time control problem. The latter determines, with higher time resolution, the setpoint to be requested to the BESS. In the case of the dispatch (see Section 1.4.2), this was done via a the solution of a MPC problem. In the case of frequency regulation, the power setpoint was the sum of an offset power computed to manage the state of energy and a regulating power, proportional to the frequency deviation (see Section 1.6.2). The formulation of a real-time control for the joint deployment of these two services is detailed hereafter, and illustrated in Figure 2.4. The time resolution of this control is of 1 second. The

---

[2]the value of $\eta = 0.97$ has been determined experimentally for the 560 kWh/720 kVA BESS used in this work.
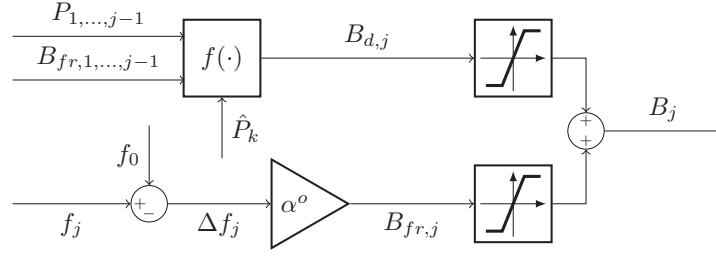
Figure 2.4 – Scheme of the BESS real-time control, $f(\cdot)$ corresponds to Equations 2.26 and 2.27.

index $j = 0,\ldots,299$ denotes hereafter the 1-second time steps within each 5 minutes interval k defined in the day-ahead phase. The real-time control determines here the battery active power setpoint B_j as the algebraic sum of the setpoints $B_{d,j}$ and $B_{fr,j}$ determined respectively for the dispatch and the EFR by two independent control loops:

$$B_j = B_{d,j} + B_{fr,j}. \tag{2.25}$$

The power setpoint $B_{d,j}$ is to compensate the tracking error ϵ_j, which is the difference between the objectve feeder power $\hat{P}_k$ (from the dispatch plan, with 5 minutes resolution) and the mean deviation from this value within the 5 minutes interval. This deviation is the sum of two terms. The first is the mean of the feeder power measurements P_i in the instants i from the beginning of the current 5-minutes period to the present instant j, filtered out of the power requests due to the EFR, $B_{fr,i}$. The second is a short-term forecast of the load $\hat{L}_i$ over the remaining five minutes interval (i.e. with $i = j,\ldots,299$):

$$\epsilon_j = \hat{P}_k - \frac{1}{300}\left(\sum_{i=0}^{j-1}(P_i - B_{fr,i}) + \sum_{i=j}^{299}\hat{L}_i\right). \tag{2.26}$$

The expression above is an energy objective over a 5 minutes horizon and the power setpoint to respect it is therefore defined as:

$$B_{d,j} = \frac{1}{300 - j} \cdot \epsilon_j. \tag{2.27}$$

The power setpoint for the frequency regulation $B_{fr,j}$ is calulated as:

$$B_{fr,j} = \alpha^o \cdot (f_j - f_n). \tag{2.28}$$

In order to comply with the constraints imposed by the day-ahead policy, both setpoints are constrained within saturation thresholds, which are, notably, equal to $\pm 0.2\alpha^o$ for $B_{fr,j}$ and $\pm(P_{max} - 0.2\alpha^o)$ for $B_{d,j}$. The latter threshold is set such that the dispatch can require, instantaneously, all the power not reserved by the frequency regulation. It remains, nevertheless,
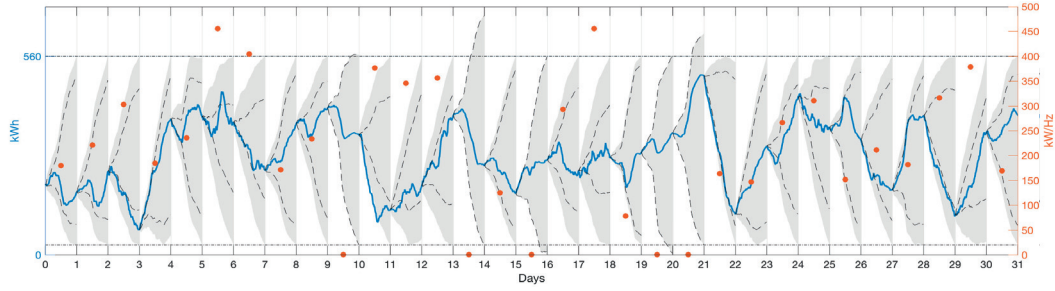
Figure 2.5 – Simulation results of 31 consecutive days of operation. Blue line: BESS stored energy; Grey area: total daily energy budget $\mathscr{E}_D + \mathscr{E}_{FR}$; Black dashed lines: bounds of the daily energy budget reserved to the dispatching service $\mathscr{E}_D$; red dots: daily values of α^o (referred to the right-hand y-axis).

that the dispatch power averaged over a 5 minutes period is expected to remain between $\mathbf{L}^\uparrow + \mathbf{F}^o$ and $\mathbf{L}^\downarrow + \mathbf{F}^o$.

2.5 Results

The proposed planning and control strategy has been validated by simulations and experiments in a real-life grid. The goal of this validation effort is double. The simulations demonstrate the effectiveness of the proposed control architecture in the determination of the coefficient α^o and the offset profile $\mathbf{F^o}$. The values found for such quantities allow to maximise the battery exploitation, while respecting the battery operational limits and therefore allowing for the continuous operation for a month. The experimental results validate the assumptions made in the control design and in the simulations and they demonstrate the practical relevance and deployability of the proposed control architecture.

Both simulations and experiments are based on the setup with a 560 kWh/720 kVA Lithium-ion BESS installed at the EPFL campus in Lausanne and described in Section 1.3.

2.5.1 Simulations

Thirty-one consecutive days of operation are simulated. These 31 days are characterized by different initial SOE values[3], ranging from 12% to 90%, and determined by the operation of the previous days (the first day of the simulation the initial SOE has been set to 35%).

Figure 2.5 reports the profile of the energy stored in the battery along the 31 days and the daily energy budget for the dispatching service $\mathscr{E}_D$ and the total daily energy budget ($\mathscr{E}_D + \mathscr{E}_{FR}$), calculated as a function the stochastic forecasting model of the demand and frequency (i.e. on the basis of $[\mathbf{L}^\uparrow, \mathbf{L}^\downarrow, \mathbf{W}_f^\uparrow, \mathbf{W}_f^\downarrow]$). Figure 2.5 shows as well the values assumed daily by α^o. It

---

[3]The SOE is here defined as the amount of stored energy normalized over the BESS nominal energy capacity E_{nom}.

Table 2.2 – Simulation results

	SOE_0 [%]	α^o [kW/Hz]	F_{avg} [kW]	$SOE_{min}|_T$ [%]	$SOE_{max}|_T$ [%]
Mean	50.8	216.6	0.5	37.4	64.9
Max	90.3	455.7	10.0	61.6	90.7
Min	12.5	0.0	-9.3	12.4	36.0

can be observed that the total daily energy budgets (grey areas) hit the BESS operational limits (SOE=5% and SOE=100%) in all days except for day 10, 14, 16, 20 and 21. This denotes that the day-ahead planning problem is able to schedule efficiently the offset profile $\mathbf{F}^o$ and the value α^o to exploit the full battery energy capacity accounting for the stochastic behaviour of frequency and demand. On the other hand, in the five days mentioned above, the grey area exceeds the SOE limits. This is because the uncertainity related to the demand (reflected by the sequences $\mathbf{L}^\uparrow$ and $\mathbf{L}^\downarrow$) prevents the feasibility of problem (2.16)-(2.18). In such days, the solution of (2.16)-(2.18) provides an α^o equal to zero, i.e. no frequency regulation is performed. In all cases, the activated constraint in the solution of (2.16)-(2.18) has been the one on the energy budget sum.

Quantitative results from the simulations are collected in Table 2.2: SOE_0 is the daily initial SOE in percentage, α^o the daily coefficient for EFR in kW/Hz, F_{avg} the mean value of the offset profile and ΔSOE the overall SOE variation during the day due to the simultaneous deployment of the two services. Table 2.2 shows the average, maximum and minimum values of such quantities over the 31 days simulation period. The average daily value of α^o is of 216.6 kW/Hz. This corresponds to the provision of up to 43 kW for EFR (considering Δf_{max} = 200 mHz). In comparison to the control scheme described in Section 1.4 of this thesis, where the control of the BESS aims exclusively at dispatching the operation of a MV feeder, we are able to provide power both for the dispatch and for EFR, while still ensuring the respect of the BESS operational constraints. This is done by taking advantage of the BESS capacity that remains unexploited by the dispatching operation, due to the daily variation of the uncertainty set of the prosumption defined by $\left[L_k^\downarrow, L_k^\uparrow \right]$ for $k = 1, \ldots, N$. The black dashed lines in Figure 2.5 delimit the energy budget reserved to the dispatching service $\mathcal{E}_D$. The width of this budget in days characterized by low uncertainty in the feeder prosumption forecast (e.g. days 5 or 17) is rather narrow and the unexploited battery capacity is therefore allocated to provide EFR (a high value of α^o is found). In days in which such uncertainty is high (e.g. days 18 to 20) almost all (or more than all) the battery capacity is needed to perform the dispatch, resulting in a very wide $\mathcal{E}_D$ and in a very low value of α^o.

2.5.2 Experimental validation

The described algorithm has been implemented in the controller of the 560 kWh/720 kVA Lithium-ion BESS. The results of 2 days of experiments are reported in this section.
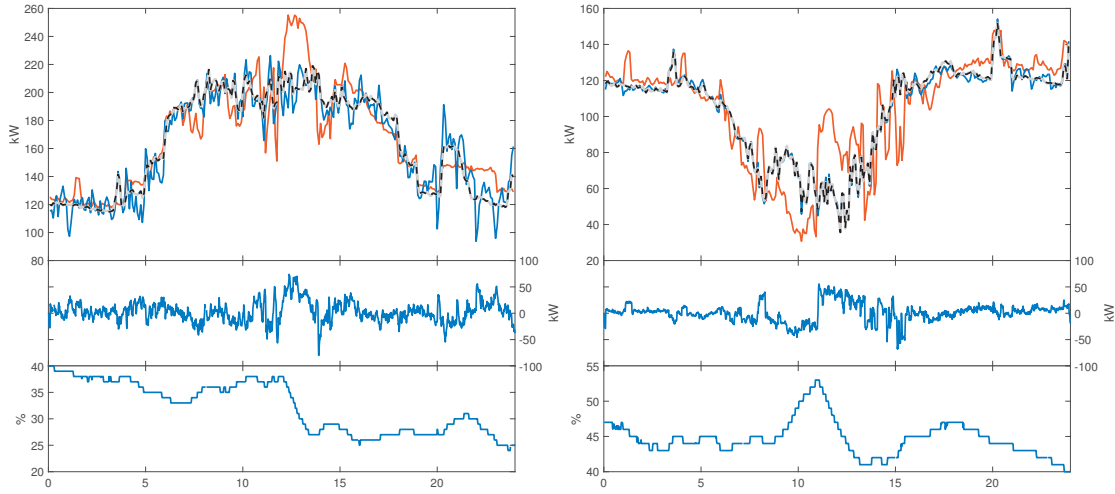
Figure 2.6 – Experimental results, **left:** day 1, **right:** day 2. **Upper plots -** feeder power profiles. Thick grey line: dispatch plan, red line: feeder prosumption, dashed black line: feeder real power (excluded the EFR power injection), blue line: feeder real power (with the EFR). **Middle plots -** BESS power injection. **Lower plots -** BESS SOE evolution.

Table 2.3 – Experimental Results

	SOE_0 [%]	α^o [kW/Hz]	F_{avg} [kW]	$SOE_{min}|_T$ [%]	$SOE_{max}|_T$ [%]
Day 1	40	584	0.84	24	40
Day 2	47	127	-0.56	40	53

Figure 2.6 shows the power and SOE profiles for two days of operation, an intra-week day and a weekend day (hereafter referred to as Day 1 and Day 2). Numerical results are summarized in Table 2.3 and Table 2.4. In Day 1, the day-ahead optimization procedure has determined a value of α^o of 584 kW/Hz and an offset power of 0.84 kW on average. In Day 2, the α^o has been found equal to 127 kW/Hz and the average offset power equal to -0.56 kW. These values of α^o allow to exploit a portion of the battery capacity that would remain unexploited when providing power only to dispatch the operation of the MV feeder, as in [167]. In this case, the maximum amplitude of the energy budget that needs to be reserved for the dispatch, calculated as in (2.10) on the basis of the upper and lower worst case scenarios of the feeder prosumption ($L_k^{\downarrow}$ and $L_k^{\uparrow}$, with $k = 1, \ldots, N$, using the nomenclature introduced in Section 2.4.1), is of about the 54% of the BESS nominal capacity for Day 1 and of about the 10% for Day 2. The remaining capacity is fully exploited by the EFR application, thanks to the computation of a proper value of α^o, by means of (2.16)-(2.18).

Table 2.4 collects the relevant metrics to evaluate the performance of the dispatch application when performed in conjunction with frequency regulation, i.e. the mean, RMS and maximum absolute values of the tracking error in these two days. The RMS value of the tracking error is about 0.5 kW over a feeder prosumption of about 130 kW on average.

Table 2.4 – Dispatch performance metrics (in kW)

	ϵ_{mean}	ϵ_{rms}	ϵ_{max}
Day 1	-0.03	0.52	4.45
Day 2	0.02	0.5	6.83

We note that, in both these two days, the energy demand for the two applications has been of opposite sign. For istance, in Day 1 the daily energy requested for the dispatch operation is of about 89 kWh, whereas the average power requested for the frequency regulation is of -24 kWh. The simultaneous deployment of these two services in this case generates a SOE drift that is lower than the one the dispatch alone would generate. It is worth noting that, when simultaneously providing multiple services, the saturation (or depletion) of the battery energy capacity would occur only if the power requests of all services corresponded to the upper (or lower) bounds of their budgets. If the uncertain processes related to the services are uncorrelated, as in the case of the dispatch and frequency regulation, the occurrence of this condition is reduced. Providing multiple services simultaneously, in this regard, may ensure more reliable operation, in the sense that failure due to complete depletion or saturation of the battery capacity would be less likely to occur. The downside of this is of course that an eventual failure would be more deleterious since multiple services would stop at once. This could be addressed by implementing strategies to prioritize the services in contingency situations, e.g. by selecting, before hitting the operational limits, which service is to drop and which to maintain.

3 Inclusion of ageing policies in the control of a grid-connected BESS

This Chapter focuses on a further fundamental aspect to take into account in the development of effective control strategies for BESS. This is the degradation over time of the performances of such devices, i.e. their ageing. It provides, first, few important definitions and a state of the art on the methods to empirically assess and account for ageing in BESS control. Second, it proposes the improvement of one of such methods - the energy throughput - by weighting the effect that different C-rates have on the ageing of a BESS. Third, it applies the proposed method to the case of using a BESS to achieve the load levelling of a distribution feeder. It assesses the ageing generated by this service and shows how integrating the proposed model in BESS control can limit the rate of this process, thus increasing the BESS lifetime.

3.1 Definitions and state of the art

Battery performances degrade over time. From a macroscopic point of view, the factors that determine the magnitude of this degradation are the value of charging and discharging currents, the depth of discharge (DOD) reached during operation, the temperature of the cells and their SOC. The first two factors come into play when the battery is used, i.e. during charges and discharges. On the contrary, the temperature and SOC of the cell affect the degradation rates regardless of the operating condition of the battery, i.e. also in "resting" phases. This distinction led to the definition of two distinct terms to describe the degradation of battery performances, i.e. **calendar** and **cycle ageing**. Calendar ageing describes the degradation of battery performances that is independent from the way the battery is operated or cycled and therefore independent of its usage patterns. It is related to battery "shelf life" and it is used to describe the effect of the temperature and SOC at which the battery is kept. Cycle ageing, on the contrary, models the degradation of the battery due to its operation. It represents the irreversible degradation associated to charging and discharging events. This type of degradation occurs only when operating the battery and can be avoided by not operating it. The main factors that are taken into account by cycle ageing are the C-rate and DOD characterizing the BESS operation. Despite this classification, typically, all the above mentioned degradation

factors come into play simultaneously, and interact with each other in a complex manner[1].

Regardless of the triggering factor, the degradation of battery performances consists in two main macroscopic effects. The first is the **capacity fade**. This is the decrease of the capacity of the battery, i.e. the fact that the battery can store less energy. This is due - microscopically - to the irreversible consumption of active material. The second is the **impedance rise**. This is the increase of the battery internal impedance (and internal resistance in particular). The main practical effect of the impedance rise is a decrease of the capability of the battery to provide power. This is due - microscopically - to the accumulation of inert material within the battery electrodes and electrolyte. This is a side product of the reactions that consume the active material.

The **end of life** of a battery is the moment, quantified in years from the beginning of its operation, in which the BESS is shut down and dismantled, due to the fact that its performance is no more sufficient to provide services effectively. Typically this moment is assumed to be when the capacity of the battery fades at 80% of its original value. The **state of health (SOH)** of a battery is a quantity, expressed in percentage (or in per unit) that indicates the condition of a battery with respect to its initial condition. Typically, it is defined based on the capacity at current time with respect to the initial batter capacity: $SOH = \frac{Q_{actual}}{Q_{initial}} \times 100\%$. However, this definition is not univocal. The SOH is also defined, often, based on the rise of internal resistance rather than loss of capacity [5].

The literature concerning the assessment of degradation of Li-ion batteries and its consideration in the control of BESS covers several objectives and rely on two main classes of methods. The research objectives are *i)* the online estimation of the SOH, *ii)* the development of ageing models to be used in the planning phase and in the a-posteriori analysis of application and control strategies of BESSs and *iii)* the usage of ageing models to determine operation schedules or control actions taking ageing into account directly in the control and/or scheduling problems. The latter objective is of our interest. The online estimation of the SOH concerns the lower level of control (as, for instance, functionalities of battery management systems - BMSs), while the second and third do apply similar models. We focused on the third, since it is directly related to the applications developed in Chapters 1 and 2 of this thesis. These applications, in fact, are structured in a period-ahead scheduling phase and in a real-time control. Both of these two phases determine the power that the battery should provide (scheduling) or provides (real-time control) and this decision can take into account considerations related to ageing.

A further distinction in the scientific literature is about the methods used to assess these phenomena. The two main classes are *i)* empirical and heuristic models and *ii)* physics-based models. The first family of methods uses rather extensive experimental data to fit empyrical models of ageing. These are simpler to use in planning methods and integrate in control

---

[1]The difficult task of characterizing macroscopically these complex interactions is, in fact, one of the motivations to adopt physics-based approaches to model battery degradation, as discussed in the second part of the thesis.

algorithms. However, they require extensive, long and expensive experiments, and have a validity limited to the operating conditions in which these experiments are carried out. Moreover, these do not provide insight in the physics behind the degradation phenomena that lead to battery ageing. These methods rely on data - often provided by manufacturers such as those shown in Figures 3.1 or 3.2. Notably, 3.1 shows how many cycles (at a given C-rate) can a battery withstand before reaching its end of life. This is usually achieved by long term experiments made by manufacturers, that cycle the battery with standard cycles and for thousands of times (i.e. for several years). A second example of data usually provided by the battery manufacturer is usually that shown in Fig. 3.2. This shows, for various levels of DOD how many cycles the battery can withstand before reaching end of life (EOL).
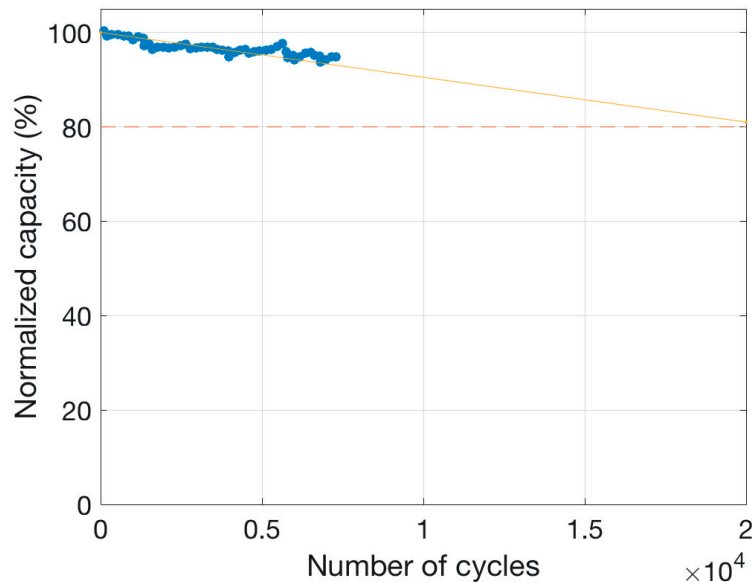
Figure 3.1 – Li-ion cell capacity vs. number of full cycles curve. The curve is for a 30Ah LTO-NCA cell.

The Li-ion cell physics-based models describe battery dynamics via a set of first principle partial differential equations (PDEs) and algebraic non-linear equations. The degradation phenomena taking place within Li-ion cells, can then be described as functions of the states of such models. These models can be quite accurate and are in general valid for a wide range of operating conditions. However, the development, identification and exploitation of such models is typically too complex to be practically exploited in the operation and control of BESSs. Efforts in this sense have been made in the recent literature. These, together with the contributions of this thesis in this respect will be discussed in Chapters 4 and 6. In this chapter we will focus on the first class of methods (i.e. empirical and heuristic models). In the remainder of the chapter, a method - the weighted energy throughput - is presented. We summarize here some works in the recent literature that can be compared to it.
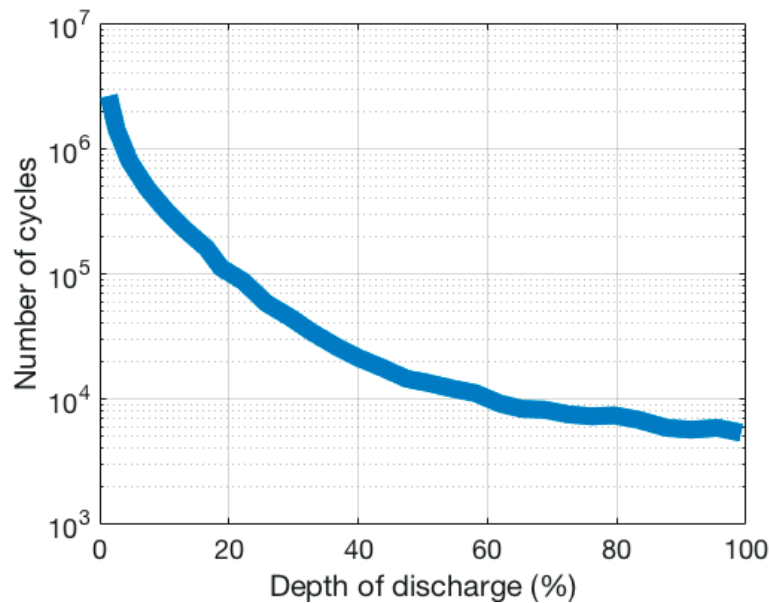
Figure 3.2 – Achievable cycle count (ACC) vs. DOD characteristic.

Typically, the methods that exploit the manufacturer's data are those used to consider ageing limitations in control. Notably, since battery operation is a complex sequence of charges and discharges, methods to reconduct these complex usage patterns to the test conditions represented by figures 3.1 and 3.2 are developed. A set of methods relies on the so called **charge throughput**. It assumes that the charge that can be absorbed *and* provided by a battery is fixed. By consequence, there is an equivalent depletion of lifetime between a test composed by the regular sequence of cycles (as that shown in figure 3.1) and a complex usage pattern whose throughput is the same. This method has been first introduced in [19] and has been enriched with the consideration of weighting factors [156] that assign higher weight to more severe events or by proposing a similar method based on energy thorughput [68, 100] rather than current (the former being the quantity more commonly used in power system problems). A second common method is the so called **rainflow cycle counting**. It consists in grouping charge and discharge events so to obtain a certain number of equivalent cycles. Such method is exploited, for instance in [128] of state-of-health estimation for electric vehicles or in [161, 163] in the control of a BESS for the provision of ancillary services (check reference). Further methods rely on empirical functions of various parameters. [79] and [114], for instance, propose sets of empirical function to describe cycling and calendar ageing dependence on SOC, DOD, temperature and charge rate. [93] proposes using an empirical model accounting for both calendar and cycle ageing when dispatching the operation of a PV power plant. It proposes to model capacity loss due to calendar ageing as a parabolic function of SOC and temperature and capacity loss due to cycle ageing as a linear function of used power. [59] proposes the joint exploitation of an approximation derived from physical laws and empiric functions to integrate the degradation process in an MPC method. [135] proposes a heuristic

event-based method to characterize the cycling behavior of a BESS and infere its degradation. The common denominator of these methods is the reconstruction of cycles that are then assumed equivalent to reference cycles executed in controlled conditions by manufacturers and assign therefore a quantity of degradation.

These models are used in scheduling problem as well as real-time control algorithms. For instance, [49] proposes a scheduling algorithm for power plants with storage, in which a constraint is added so to limit the degradation generated by a given schedule. Similarly, [70] proposes an optmisation problem to determine the operation of a BESS to provide frequency regulation in cooperaton with wind power. This includes constraints based on the aforementioned methods to limit the degradation of BESSs. Instead of constraining ageing to a given threshold during a scheduling horizon, [196] proposes the formulation of a penalty function to be added to the objective of a scheduling problem formulated to provide regulation response.

3.2   The Weighted Energy Throughput method

The method here described relies on the principle that an eletrochemical cell can exchange a finite amount of charge during its lifespan, as described in [156]. This value can be assessed through cycling tests and calculated as the charge that pass through a cell during a complete discharge-charge cycle (i.e. $2C_{rated}$) multiplied by the total number of cycles that a battery can perform before depletion. This method, known as charge throughput, has the advantage of relying only on values that are most often given by the manufacturers (rated capacity and number of cycles). It has to be noted that the depth of discharge (DOD) of the cycles is implicitly taken into account in a linear fashion, as a cycle with lower DOD has also proportionally lower charge throughput. Assessment methods relying on physical models of the cells and of their degradation phenomena, such as the one proposed in [154] may provide more precise results, but requires the development and validation of complex models and the knowledge of a set of physical parameters usually not available to the end-user. The charge throughput, on the contrary, while being rather simple, neglects a series of factors, such as the influence of the C-rate on the cycle ageing or the calendar ageing. We propose a method that is similar, conceptually, to the charge throughput and that we call *weighted energy throughput*. With respect to the former, this presents two relevant features that improve its accuracy and its applicability to problems related to operation planning and control of BESSs. First, it consists in assessing the *energy throughput* rather than the charge one. Most of the problems concerning the planning of the operation of BESSs (included the day-ahead problems formulated in the previous Chapters of this thesis) have the battery power as decision variable. It is therefore more convenient to used power (opposed to current) in the ageing assessment as well. This results in the assessment of an energy (opposed to charge) throughput, that can be treated with the same assumptions made for the more conventional charge throughput. Second, the proposed method introduces a set of weighting factors to take into account the fact that operating the BESS at higher rates provokes more severe ageing. These are determined based

solely on data provided my the manufacturer and available on manufacturer's cell data-sheet.

We consider a finite interval T in which a BESS is operated with a complex pattern of charges and discharges. Discretizing this interval in $k = 1,\ldots,N$ steps of duration ΔT, we define the energy exchanged by the BESS in this interval, $E_{exch}(T)$, as:

$$E_{exch}(T) = \Delta T \sum_{k=1}^{N} |w(k)B(k)| \tag{3.1}$$

where $B(k)$ is the BESS power at step k and $w(k)$ is a weighting factor related to the magnitude of $B(k)$. The exact definition of the weights is provided in the next paragraph of this section. The ratio between $E_{exch}(T)$ and the energy exchanged during a complete cycle by the cell, i.e. $2E_{batt}(T)$, defines the number of *equivalent cycles* that the cell has performed in T:

$$N_c(T) = \frac{E_{exch}(T)}{2E_{batt}(T)} \tag{3.2}$$

It is to be noted that the denominator of Eq. (3.2) evolves with time, since the energy exchanged during a complete cycle depends on the current energy capacity, which decreases as the cell ages. Defining the index $j = 0,\ldots,T-1$, that covers all operating periods since the beginning of the BESS operation, it is:

$$E_{batt}(T) = E_{rated} \left(1 - \frac{\sum_{j=0}^{T-1} N_c(j)}{N_M} \right) \tag{3.3}$$

where E_{rated} is the rated energy capacity of the cell and N_M is the nominal number of cycles that the cell can endure. Both these quantities are usually indicated on cell data-sheets. In the case of the cells under analysis, it is $N_M = 20\,000$ cycles, this value being defined as the number of cycles at 4C after which the cell capacity falls below 80% of its initial value. Comparing N_c with the maximum number of cycles for the cell N_M, a time in years until the cell end of life (EOL) can be defined as:

$$EOL = \frac{N_M}{N_c} \frac{1}{365} \tag{3.4}$$

Definition of the weights $w(k)$

The cells used for the here proposed analysis are 30 Ah lithium-titanate batteries, whose expected cycling life-time is of 20 000 cycles. The weights are calculated from cycling data provided by the cell manufacturer on their cell data-sheet. Fig. 3.3 shows the evolution of the state of health (SOH) of the cell, defined as the cell capacity after a certain time of operation normalized with its initial one, with the number of cycles and with different current rates. Notably, the blue dots and line refer to a cycling performed at 4C, whereas the red ones refer to a 1.5C cycling.
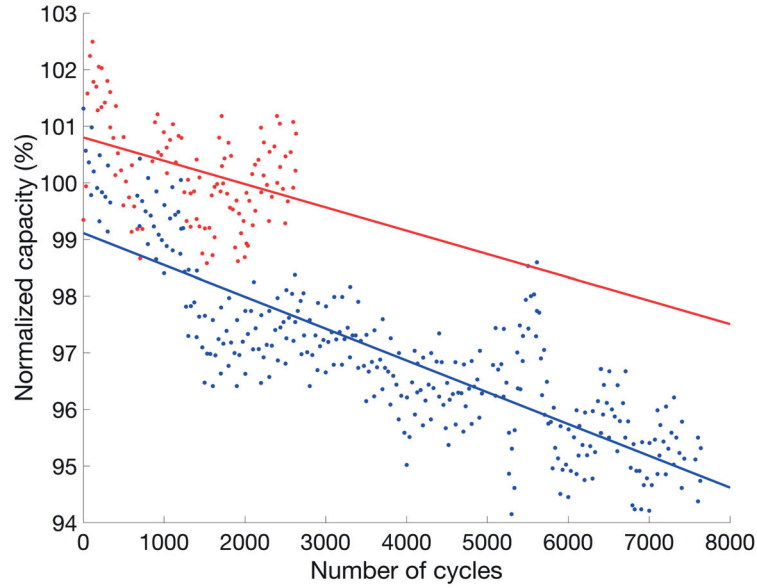
Figure 3.3 – Experimental data from cycle ageing test at 4C (blue) and 1.5C (red).

Table 3.1 – Weighting factors for the C-rates in Fig. 3.3

C-rate	SOH_0	$m(10^{-4})$	w
4C	100.8	5.617	1
1.5C	99.11	4.117	0.73

The data points in Fig. 3.3 are the normalized capacity measured values for different number of cycles. The lines, are obtained through linear interpolation of the measured data. Their slopes can be used to define the weights for the energy throughput calculation, and are shown in Table 3.1. In fact, it can be seen that for a higher rate, a higher slope is present (in agreement with the fact that cycling at higher rate causes faster degradation of the cell).

The interpolated lines are defined as:

$$SOH(NoC) = SOH_0 - m * NoC \tag{3.5}$$

where NoC is the number of cycles, $m = f(C_{rate})$ is the rate of decrease of the state of health, and is function of the C_{rate} at which the cycles are performed. In Fig. 3.3, notably, the behaviors for the experimental data and the cycling trends of 1.5C and 4C are represented. The weights w are finally obtained by normalizing the values of m on the value at 4C, given that the maximum number of cycles for the examined cell is defined at this particular rate.

The above data allow to extract a trend line for the weights at current rates different from the ones at which the experiments have been performed by the manufacturer. Through linear

interpolation it is obtained that:

$$w(C_{rate}) = 0.57 + 0.11 * C_{rate} \tag{3.6}$$

In equation 3.6, the constant term is relative to a degradation process independent from the cycling rate whereas the effect of C-rate is found in the second term. This method allows to obtain a weighting factor for any cycling condition encountered in the operation of the BESS.

3.3 Results based for a BESS providing load leveling services

This section applies the method developed above to the operation of a utility scale BESS. First, Section 3.3.2 applies the proposed method to assess how a load leveling strategy [127] [133] [101], implemented with this BESS, affects the degradation of the cells. Second, Section 3.3.3 shows how an additional constraint can be added to this strategy to limit ageing and achieve a desired lifetime for the BESS.

The load leveling used as a case study is operating in 24 hours periods and formulated as described in Section 1.5. We recall here the main features of the method. The feeder forecasted load profile is defined the day ahead of operation through data-driven forecasting. The BESS power injection is then defined so that the overall feeder power profile is leveled. The MV feeder power profile is then dispatched through an intra-day operation of the BESS. The control strategy for the BESS aims at reducing the deviation of the load profile of a MV feeder $\hat{L}$ from its mean power value $\hat{L}_{avg}$, through the utilization of the BESS power B. For the BESS it is therefore determined the profile of the power injections along a 24h period, with a resolution of 5 minutes. The load profile is built through the averaging of forecast scenarios composed by historical data and the problem is solved the day ahead of the operation.

$$\underset{B_i}{\arg\min} \sum_{i=1}^{N=288} \left(\left(\hat{L}_i - \hat{L}_{avg} \right) - B_i \right)^2 \tag{3.7}$$

Subject to:

$$|B_i| < B_{\max} \tag{3.8}$$

$$|P_i| < P_{\max} \tag{3.9}$$

$$0 < SOE_i < 1 \tag{3.10}$$

The constraints for this problem, without taking into account for ageing limitations, bound the battery power B_i, the power absorbed by the feeder $P_i = B_i + L_i$ and the battery state of energy SOE_i [107] built as:

$$SOE_i = SOE_0 + \frac{\Delta T}{C_{nom}} \sum_{j=0}^{i} B_j, \tag{3.11}$$

where C_{nom} is the nominal capacity of the BESS. The energy throughput is calculated on the BESS usage defined in the day-ahead problem and the constraint imposed on the BESS usage described in section 3.3.3 limits the load-leveling objective of the control strategy.

3.3.1 Case Study Setup

The methodology described in the previous section has been deployed with a lithium-titanate BESS of 280 kWh[2], connected to a 20 kV active distribution network characterized by a peak load of about 300 kW and embedding 100 kWp of PV generation [138]. The BESS performs the leveling of the feeder load. The battery power, current and state of charge are measured in real time by a tailored battery management system (BMS) with a sampling rate of one second.

3.3.2 Ageing Assessment of the Unconstrained Load Leveling Strategy

In this section the weighted energy throughput method described and characterized above is used to assess the ageing resulting from the load leveling strategy[3]. Several scenarios obtained from historical data of the power consumption of the targeted feeder are considered. Fig. 3.4 shows the power and stored energy profiles of the BESS during 24h from one of the scenarios taken into account. In the upper image we can see the behavior of the power of the MV feeder without and with the contribution of the BESS. In the middle figure we can see the daily profile of the BESS power and in the lower figure we can see the daily evolution of its stored energy. The power profiles are discretized in 5 minute intervals. The exchanged energy of the BESS can be therefore calculated as the sum of battery power absolute values within 24h, weighted with the w factors defined in section 3.2. This energy can then be compared with the rated energy of a complete cycle to obtain an equivalent number of cycles per day and from this value an estimation of the battery duration before depletion, if in use with this specific control strategy. Table 3.2 collects the ageing data obtained for several days of load leveling operation, taken in various moment of the year and of the week.

It can be seen how, for this specific battery chemistry and this specific application, the EOL values are very high, i.e. the ageing of the battery due to its cycling takes place in a very long period. These values are especially high when compared to the calendar lifetime of these devices, which, for this specific BESS is of 20 years. The BESS itself, in such a long time span can incur in ageing from many and various causes, such as calendar and mechanical ageing, defects of individual parts of the BESS or disruptive events. The above analysis, nevertheless,

---

[2]The BESS model used in this Section has a capacity that is half of the EPFL BESS, used in most experiments and simulations throughout the thesis. The reason for this is that we observed that for the cell technology of this BESS, Lithium titanate, the cycling effect on ageing is really minimal, due to the extremely high number of cycles it can withstand. We chose therefore to model a BESS having a smaller capacity and therefore injecting power at higher rates to provide the same services considered in the previous chapters. This BESS, while having ratings that are still pretty common (see e.g. [88]), constitutes a more interesting case study for the assessment and limitation of ageing. It holds that the methods described here are general and can be of much higher value for BESSs based on other - more conventional - types of Li-ion chemistries.

[3]In Appendix A.5 a similar assessment for other services described throughout this thesis is provided.
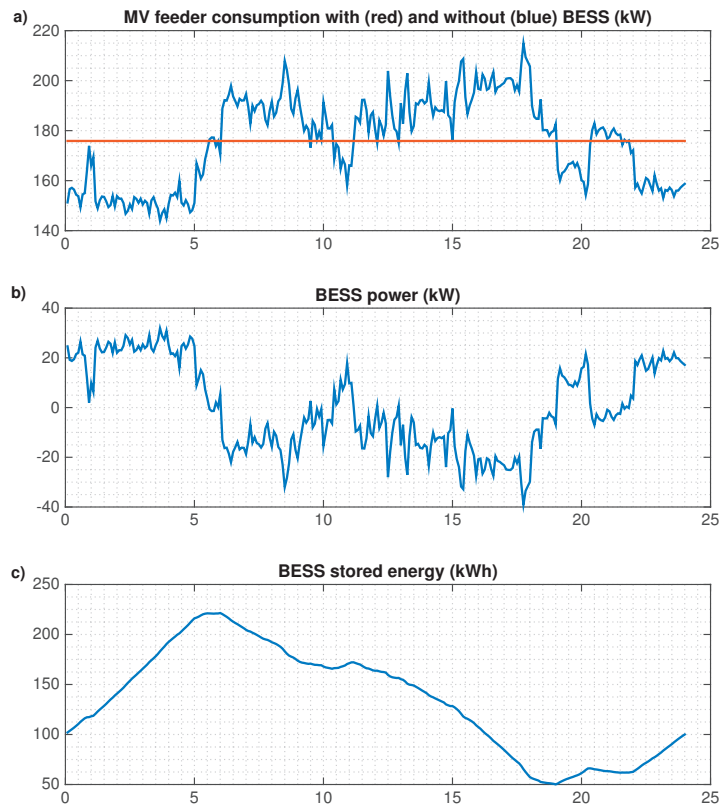
Figure 3.4 – BESS operation in a 24h scenario: a) profile of the feeder consumption without the BESS (red) and with the BESS (blue); b) Power injection of the BESS c) Energy stored in the BESS.

remains extremely important, as it assess the ageing that is directly linked to the battery operation and it assess therefore, if and how the control strategies developed for the BESS need to be aware of this process.

Table 3.3 reports the average daily values for several relevant metrics, obtained from a simulation of 5 years of operation of the BESS. Notably, $var(L)$ and $var(P)$ are the variances of the feeder consumption and of the total power absorption including the BESS contribution. These values measure the performance of the load leveling objective: it can be seen how $var(P)$ is several times smaller than the variance of the consumption profile $var(L)$. Table 3.3 reports as well the values obtained for the average daily exchanged energy E_{exch}, number of equivalent cycles N_c and the expected EOL for the case analyzed. The expected cycling related battery lifetime for the proposed load leveling strategy is of about 40 years.

This number is considerably higher than the calendar lifetime of the cells, i.e. 20 years, meaning that, for the considered application and cell chemistry, the cycle ageing is not the

Table 3.2 – Ageing assessment for a load leveling strategy with different scenarios

E_{exch}	N_c	EOL
433.18 kWh	1.36	40.36 years
477.08	1.49	36.68
505.91	1.58	34.58
513.19	1.61	34.09
313.34	0.98	55.82
525.7	1.65	33.29
337.03	1.06	51.92
505.54	1.58	34.59
437.79	1.37	39.95

Table 3.3 – Performances for unconstrained BESS operation employing cells with 20000 cycles

Metric	Value
$var(L)$	$1.79 \cdot 10^3 \ kW^2$
$var(P)$	$396.15 \ kW^2$
E_{exch}	$789 \ kWh$
average N_c	1.41
expected EOL due to cycling	$40.1 \ years$
expected calendar EOL	$20 \ years$

main source of ageing. In such a case, therefore, there is no need to limit with respect to this aspect the load leveling operation of the BESS, in order to reach the expected calendar lifetime of 20 years.

3.3.3 Implementation of an additional constraint in the BESS control strategy

The results in the previous section refer to a BESS composed by Lithium-titanate cells, characterised by a very high cycle life. We've shown how for such BESS cycle ageing is not a major concern. For BESSs based on more common Li-ion cell chemistries, however, it may be useful or even necessary to take into account cycle ageing in their operation. In order to do so, and for the case of a BESS operated to provide load levelling, the following constraints, which bounds the exchanged energy E_{exch} of the BESS, can be added to the control problem described by Eq. 3.7-3.10:

$$\frac{1}{2E_{batt}} \frac{\Delta T}{3600} \sum_{j=0}^{i} |w_j B_j| < N_M, \qquad i = 1, \ldots, 288, \tag{3.12}$$

where N_M is a number of cycles per day chosen in relation to a desired end of life time EOL in years.

Table 3.4 – Performances for unconstrained BESS operation and employing cells with 3500 cycles

Metric	Value
$var(P)$	415.81 kW^2
E_{exch}	789 kWh
N_c	1.41
expected EOL due to cycling	7 $years$
expected calendar EOL	10 $years$

Table 3.5 – Performances for BESS operation constrained to a lifetime of 30 years and employing cells with 3500 cycles

Metric	Value
$var(P)$	685.83 kW^2
E_{exch}	401 kWh
N_c	0.96
expected EOL due to cycling	10 $years$
expected calendar EOL	10 $years$

To quantify the usefulness of the additional constraint, we consider a cell chemistry having a cycling lifetime of 3500 cycles and a calendar lifetime of 10 years, these values being typical for classical li-ion cell chemistries. We compare the simulation results obtained operating the battery while disregarding the ageing limitation and then considering it. Figure 3.5 reports the feeder consumption profiles, BESS power injection and BESS stored energy for a day of operation without the contribution of the BESS and in the two considered cases. By measuring the exchanged energy and average equivalent cycles per day, we see how with such cells, the expected EOL of the BESS is reached after 7 years. This case illustrates the importance to integrate the cycle ageing into the control strategy, as the EOL is reached before the calendar lifetime declared by the manufacturer. Table 3.4 reports the relevant metrics for this case. We set then an additional constraint to the load leveling minimization algorithm, such that the battery EOL occurs after 10 years. We can see in Table 3.5 that by applying this constraint the performances with regard to load leveling are worsened, but the lifetime goal is reached.

3.3.4   Conclusive remarks

This Chapter proposed an empirical method to asses the cycle ageing of a BESS controlled to level the load of a distribution feeder. Based on this assessment, several key conclusions can be made. First, cycle ageing is a minor concern for BESSs based on LTO cell technology. Second, cycle ageing plays instead a role in determining the end of life for BESSs using more common Li-ion battery technologies. Third, based on the proposed method, it is possible to extend the control frameworks provided in Section 1.5 to host ageing-limiting constraints, so
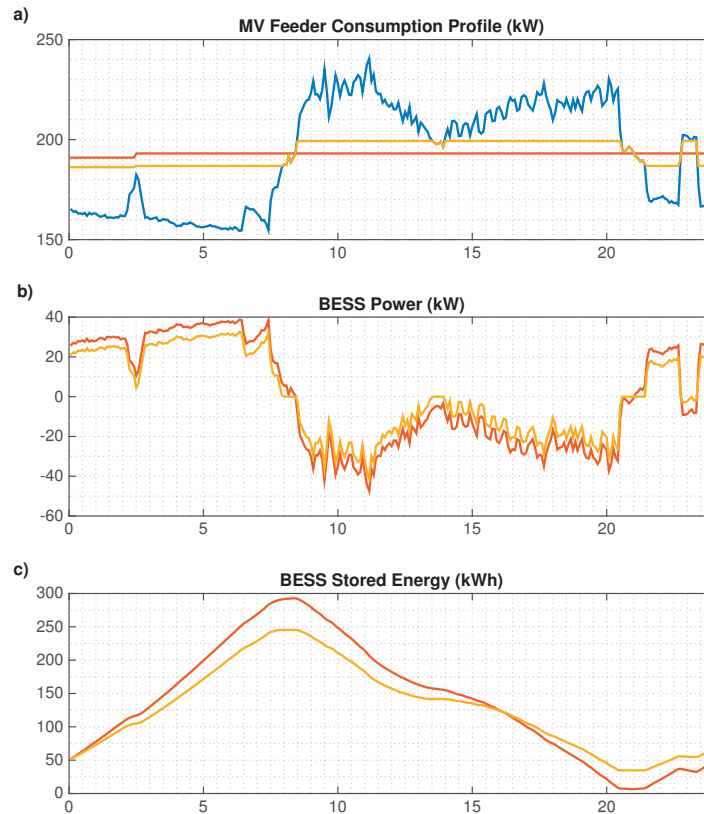
Figure 3.5 – Comparison of a load leveling daily profile without BESS operation (blue), with BESS operating without ageing constraint (red) and with BESS operating with EOL constrained to 30 years (yellow).

to ensure the achievement of a specific BESS lifetime.

With respect to the method itself, we observe how this relies on data commonly provided in battery datasheets and is rather simple to use for ageing assessment and control. However, it relies on the rather heavy assumption that the degradation due to a complex cycling pattern is the same as the one due to a regular cycling profile characterized by the same energy throughput. This assumption allows for a easy although approximate accounting for battery ageing. In order to remove it and account for battery degradation more accurately, the physical phenomena occurring in Li-ion cells should be modeled explicitly. This latter approach, however, is considerably more complex than the methods presented in this Chapter and is discussed throughout the second part of this thesis.

PART II

ON THE INTEGRATION OF ADVANCED BATTERY MODELS IN BESS CONTROL

4 On the Evolution of BESS control including advanced Li-ion cell models

In the first part of the thesis, an equivalent circuit model and a empirical degradation model have been used within an MPC framework and to assess cycling ageing of a BESS respectively. This second part of the thesis aims at substituting these conventional models with advanced physics-based models.

Circuit models mimic cell dynamics via networks of electrical components. They are efficient to predict cell voltage and estimate the cell state of charge with low computational burden. However, they have limited accuracy and capacity to describe the cell behaviour over a wide set of operating conditions. Similar issues affect the empirical ageing models introduced in Chapter 3 of this thesis. Recent research efforts have tried to substitute both ef these with advanced physics-based models. These are electrochemical models that describe in detail (rather than mimicking) Li-ion cell behaviour. They have been initially developed with the purpose of designing the cells and studying their microscopic behaviour. Only recently, from the late two-thousands, researchers have tried to use them in control applications.

This chapters provides first an overview on the various classes of battery models and, second, analyzes the challenges and potential advantages of using physics-based models in the control of BESS.

4.1 Definitions on Li-ion cells

A Li-ion cell is the constitutive element of a BESS. Li-ion cells store electrical energy through reversible electrochemical reactions and are connected in series and in parallel in BESSs. Each cell is composed by two electrodes (the positive one being the cathode and the negative being the anode), immersed in an electrolyte and isolated electronically by a separator layer (see Fig. 4.2-a). The electrodes are composed by intercalation materials and have a porous structure. Typically, the anode is in carbon, although novel materials have been used in specific applications. For instance, the BESS used in this thesis has an anode composed by Lithium titanate oxide ($Li_4Ti_5O_{12}$, or LTO).). The cathode can be composed by various metal

oxides. Examples are Lithium iron phosphate ($LiFePO_4$, or LFP), Lithium cobalt oxide ($LiCoO_2$, or LCO) or Lithium Nickel Cobalt Aluminum Oxide ($LiNiCoAlO_2$, or NCA). The electrodes are conductive electronically and connected via metallic connectors to the the exterior of the cell (and eventually to the external electrical circuit) and can intercalate or de-intercalate Lithium ions within their lattice structure[1]. The electronic insulation between the two electrodes is ensured by a separator layer. All these three components are then immersed in an electrolyte. This is typically composed by a Lithium salt in an organic solvent and allows the movement of Lithium ions within the cell.

A typical reaction occuring in a Li-ion cell, having graphite (C) as anode material and a generic metal oxide (MO_2) as cathode material, can be espressed as follows: The rightwards arrows

$$
\begin{aligned}
\text{Cathode:} \quad & LiMO_2 \rightleftarrows Li_{1-x}MO_2 + Li^+ + xe^- \\
\text{Anode:} \quad & C + yLi^+ + ye^- \rightleftarrows Li_yC \\
\text{Overall:} \quad & LiMO_2 + x/yC \rightleftarrows x/yLi_yC + Li_{1-x}MO_2.
\end{aligned}
$$
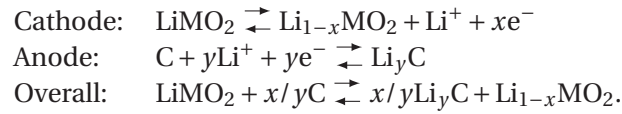
($\rightarrow$) refer to the charging process, while the leftwards arrows ($\leftarrow$) refer to discharge. x and y indicate the quantity of Lithium ions that are intercalated respectively in the anode and cathode materials normalized over their maximum insertion capacity. When charging the cell, an electric current is injected by a source to the positive electrode of the cell. This corresponds to electrons flowing out of the positive tab of the cell, through the external circuit and into the negative tab of the cell. At the same time, within the cell, Lithium ions ($Li+$) deintercalate from the active material of the cathode, flow through the electrolyte and intercalate in the anode active material.

4.2 State of the art on Li-ion cell models

This section briefly discusses the models of battery dynamics that can be used in BESS control. There are three main classes of models, in order of increasing complexity. The first includes "bucket" models, that trivially represent batteries as integrators of charge, eventually with the consideration of their efficiency. The second, equivalent circuit models, represent the voltage and SOC dynamics via an abstract equivalent network of electric components. The third, electrochemical models, faithfully represent the cell internal dynamics and phenomena. While the first two classes are commonly used in a wide set of applications (the primal example being first part of this thesis), the application of the latter in control applications is subject of ongoing research. Hereafter we describe the main features of these classes of models, describe their advantages and flaws. It is not the objective of this Chapter to provide a complete review of Li-ion cell and battery models, but rather to provide the key points to highlight the potential benefits of integrating advanced (i.e. electrochemical) models in control. Extensive reviews of battery models are provided in [78, 155].

---

[1]Intercalation is the process of insertion of a molecule (in this case of a Lithium ion) within the layered structure of a material (in this case the electrode active materials).

Models of Li-ion cells of increasing complexity and accuracy exist and are used depending on the application and context. The simplest possible approach is to model a Li-ion cell as a current integrator. The charge Q stored in the cell, will be a function of its current i:

$$Q(t) = Q(t_0) + \int_{t_0}^{t} i(t) dt. \tag{4.1}$$

This provides a tool to predict the state of charge. This approach is typically used in planning and scheduling problems where, given the long time horizons involved and the impossibility to predict the exact operation of the battery with such advance, an approximate state of the battery is sufficient for the purposes of such problems. This type of model is used in the day-ahead problems described in the first part of this thesis, as well as, for instance, in [82,162].

4.2.1 Equivalent circuit models

Increasing in complexity and accuracy, the equivalent electrical circuit models of Li-ion cells are able to represent the dynamics of external voltage of the cell as a function of the input current and of a set of model states (typically the battery state of charge and (see for instance the model represented in Figure 1.6, in Chapter 1) the voltages on the RC branches of the model). In Section 1.4.2, one of such models has been casted in a MPC framework. Here we provide a general description of these models in order to be able to highlight, in the remainder of the chapter, the differences between them and the more complex electrochemical models. Fig. 4.1-a reports the typical structure of the equivalent circuit model. This is composed by a voltage source, representing the equilibrium voltage of the cell and by a set of other components, representing its dynamic behavior. The voltage source is most often a non-linear function of the state of charge [73]. Among the additional elements, typically, a series resistance (fig. 4.1-b) is always present, to capture the ohmic losses and the instantaneous voltage drop that a current generates in the cell. A number of parallel RC branches (fig. 4.1-c) is then used to represent the diffusive phenomena taking place in the cell. These cause the cell voltage to stabilize only after a given time after exciting the cell with a current. In principle, a very high number of such branches is necessary to model accurately diffusive phenomena [180]. However, this makes the model less tractable and in the literature, models with one [98], two [48] or three [6] branches are typically used[2]. Finally, further elements (fig. 4.1-d) can be added to model specific aspects of the battery behavior. For instance [141] proposes to use a non-linear function to model voltage hysteresis (i.e. the fact that, for some chemistries, the cell can have different open circuit voltages for a same state of charge, depending on the cycling path to reach that state[3]).

The usage of such models for Li-ion BESS simulation and control purposes is well-established

---

[2]In Section 1.4.2, we showed that, for the EPFL BESS and for a real-time control operating at 10 seconds resolution, a model with two RC branches provides satisfactory results.

[3]Ref. [12] quatifies this phenomenon and finds that it is rather important in LiFePO$_4$ cells, whereas it is less relevant in LTO-based cells.
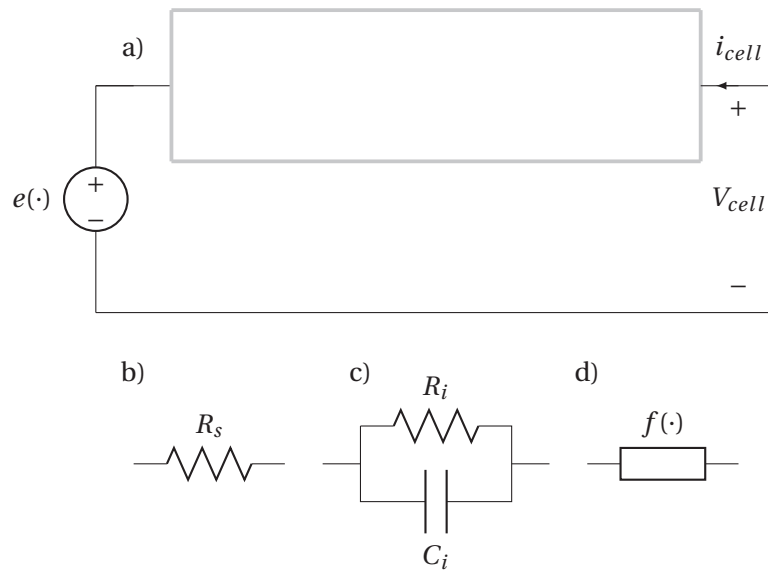
Figure 4.1 – Generic structure of an equivalent circuit model of a Li-ion cell.

in the scientific literature and a comprehensive review and comparison of the various circuit models is presented in [73].

In the context of Li-ion cell state estimation and in general control, the exploitation of such models is widespread, due to their simplicity and tractability. However, a major disadvantage of these models is the lack of representativeness of the physical phenomena happening within the cells. A direct consequence is that a model that performs well in given operating conditions, may perform poorly in others. Similarly, since parameters of circuit model don't have specific physical meaning, their change due to degradation and ageing of the BESS cannot be predicted via laws and can only be fitted by using large - and hard to obtain - datasets, as discussed in Chapter 3.

4.2.2   Electrochemical models

Electrochemical models describe in detail the physical phenomena happening within the cells. These have been originally developed by electro-chemists to design such cells and analyse their physical and chemical properties. For instance, [39] compares the performances of Lithium titanate to graphite anodes, [4] describes the behavior of several cathode materials, [35, 38] describe cell degradation mechanisms as solid-electrolyte interphase (SEI) formation and fractures due to material stress.

The main electrochemical model used in the literature to describe Li-ion cells is the one developed by Newman in the mid-nineties, based on his porous electrode theory [122] and described in the seminal papers [46] and [63]. This is referred in the literature as the pseudo-2-

dimensional (P2D) model or the Doyle-Fuller-Newman (DFN) model, following the names of the authors of [46].

The P2D model describes the main phenomena taking place within the cells. These are:

1. the intercalation and de-intercalation of Lithium ions in the active material of the electrodes. This corresponds to the exchange of Lithium between the solid phase (i.e. the lattice structure of the electrodes) and the liquid phase (i.e. the electrolyte);

2. the movements of ions both in the electrolyte and electrode active material, due to diffusion (i.e. movement driven by concentration gradient) and migration (i.e. movement driven by electric potential gradient);

3. the conduction and creation of gradients of electric potential both in the electrodes and electrolyte.

The mathematical description of these simultaneous and interconnected phenomena, is done by exploiting the porous electrode theory. Following this theory [122], the electrolyte-impregnated porous structure of the electrodes is modeled as the superposition of two continua, representing the solid and liquid phase respectively. A Li-ion cell is composed by three layers of finite area and thickness, each presenting these two continua: an anode, a separator and a cathode. Referring to the coordinates in figure 4.2-a, it is assumed that the behavior of the cell is uniform along y and z. The only coordinate in the orthogonal space necessary to characterize the cell behavior is the one along x that describes the cell states along its thickness.

At any position along x, and for a time t, the following quantities are defined:

- the ion concentration in the electrolyte $c_e(x, t)$;

- the potential of the electrolyte $\phi_e(x, t)$ and of the electrodes' active materials $\phi_s(x, t)$;

- the current flowing in the electrolyte $i_e(x, t)$ and in the electrode active materials $i_s(x, t)$;

- the intercalation current density $j^{Li}(x, t)$, describing the exchange of ions between the electrode active material and the electrolyte;

Moreover, for each step along x a further problem is formulated to describe the diffusion of ions within the electrode solid particles. This is defined in the radial coordinate r and determines the value of the concentration of ions within said particles, $c_s(x, r, t)$ (see Figure 4.2-b). The corresponding partial differential equation (PDE) is solved in r for every step in x and is related to the system of equations in x through the exchange current density, which is defined as a non-linear function of $c_e(x, t)$ and $c_s(x, r, t)|_{r=R}$. This system is described by Equations (4.2)-(4.10), reported from [21]. Such equations describe the behavior of one layer

and are to be replicated for all three layers composing a cell (adapting the boundary conditions and considering that in the separator only the equations related to the electrolyte hold). The meaning of all parameters used in this set of equations is provided in Table 4.1.
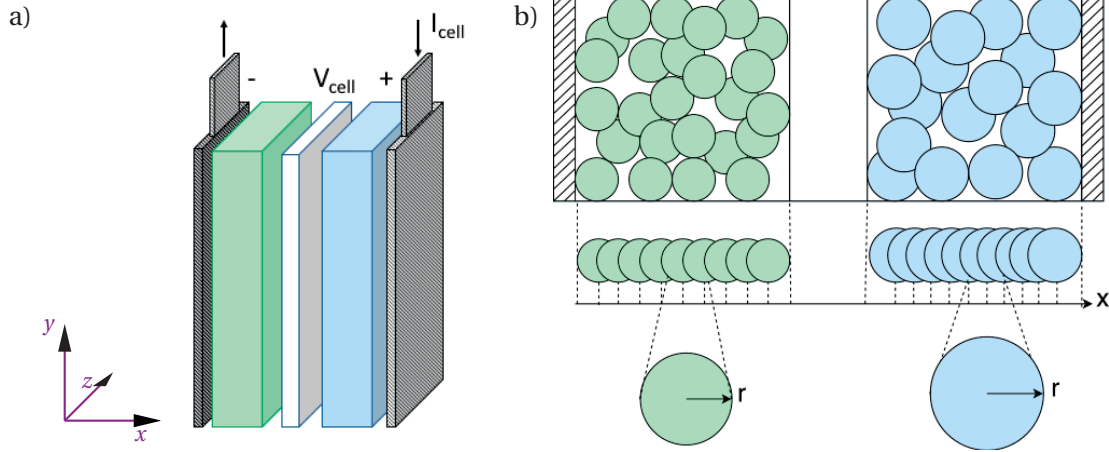
Figure 4.2 – Schematics for the representation of the P2D model of a Li-ion cell: a) 3-D representation, b) section showing the spatial coordinates considered in the model.

Solid radial diffusion:

$$\frac{\partial c_s}{\partial t} = \frac{1}{r^2} \frac{\partial}{\partial r} \left(r^2 D_s \frac{\partial c_s}{\partial r} \right) \tag{4.2}$$

$$\text{with: } \frac{\partial c_s}{\partial r}\Big|_{r=0} = 0, \ \frac{\partial c_s}{\partial r}\Big|_{r=R_s} = \frac{-j^{Li}}{a_s F} \tag{4.3}$$

Charge transfer between solid phase and electrolyte:

$$j^{Li} = a_s i_0 \left[e^{\frac{\alpha_a F}{RT} \eta} - e^{\frac{-\alpha_c F}{RT} \eta} \right], \tag{4.4}$$

$$\text{where: } i_0 = kF \left(c_s^{max} - c_s|_{r=R_s} \right)^{\alpha_a} \left(c_s|_{r=R_s} \right)^{\alpha_c} (c_e)^{\alpha_a}, \tag{4.5}$$

$$\text{and where: } \eta = \phi_s - \phi_e - U_{eq}(c_s|_{r=R_s}) \tag{4.6}$$

where U_{eq} is the equilibrium voltage of the electrode and is typically a non-linear function of the ion concentration on the surface of its solid particles, $c_s|_{r=R_s}$.

Electrolyte linear diffusion:

$$\epsilon_e \frac{\partial c_e}{\partial t} = \frac{\partial}{\partial x} \left(D_e^{eff} \frac{\partial c_e}{\partial x} \right) + \frac{1 - t_+^0}{F} j^{Li} \tag{4.7}$$

Parameter	Meaning
D_s	solid diffusivity $[m^2 \cdot s^{-1}]$
R_s	radius of electrode's solid particles $[m]$
a_s	specific surface $[m^2 \cdot m^{-3}]$
α_a, α_c	anodic/cathodic transfer coefficients [-]
T	temperature [K]
k	reaction rate constant $[m^{2.5} mol^{-0.5} s^{-1}]$
ϵ_e	porosity of the material [-]
D_e^{eff}	electrolyte diffusivity $[m^2 \cdot s^{-1}]$
t_+^0	transference number [-]
k_D^{eff}	diffusional conductivity []
σ^{eff}	electrode conductivity $[S \cdot m^-1]$
R	Universal gas constant ($8.31\ J \cdot K^{-1} \cdot mol^{-1}$)
F	Faraday constant ($9.65 \cdot 10^4\ s \cdot A \cdot mol^{-1}$)

Table 4.1 – Paramaters of a P2D model

Ohm's Law in electrolyte:

$$k^{eff} \frac{\partial \phi_e}{\partial x} - k_D^{eff} \frac{\partial \ln c_e}{\partial x} + i_e = 0 \tag{4.8}$$

$$k_D^{eff} = \frac{RT}{F} \left(1 - 2t_+^0\right) k^{eff} \tag{4.9}$$

Ohm's law at the surface of the particles:

$$\sigma^{eff} \frac{\partial \phi_s}{\partial x} + i_s = 0 \tag{4.10}$$

This model constitutes the cornerstone of a set of physics-based models of Li-ion cell, both more complex (e.g. integrating thermal dynamics [56], variable parameters [4], degradation laws [150] etc.) and simpler than their predecessor. Examples of the latter are [67], where electrolyte dynamics are neglected, or [172] where a parabolic algebraic function, rather than a PDE, is used to represent solid diffusion.

4.2.3 First-principle models of Li-ion cell ageing phenomena

Chapter 3 of this thesis, describes a method to characterize ageing of a BESS from a macrosopic point of view. This, however, is the effect of microscopic processes, altering irreversibly the materials composing the cells. The electrochemical models described above allow for a precise description of such mechanisms. Among the most common processes that generates degradation in Li-ion cells, there are the growth of the solid-electrolyte interphase (SEI) layer, electrolyte decomposition, cathode dissolution, dendrite formation, lithium plating, etc. [182]. The most common degradation mechanisms of Li-ion cells are listed, together
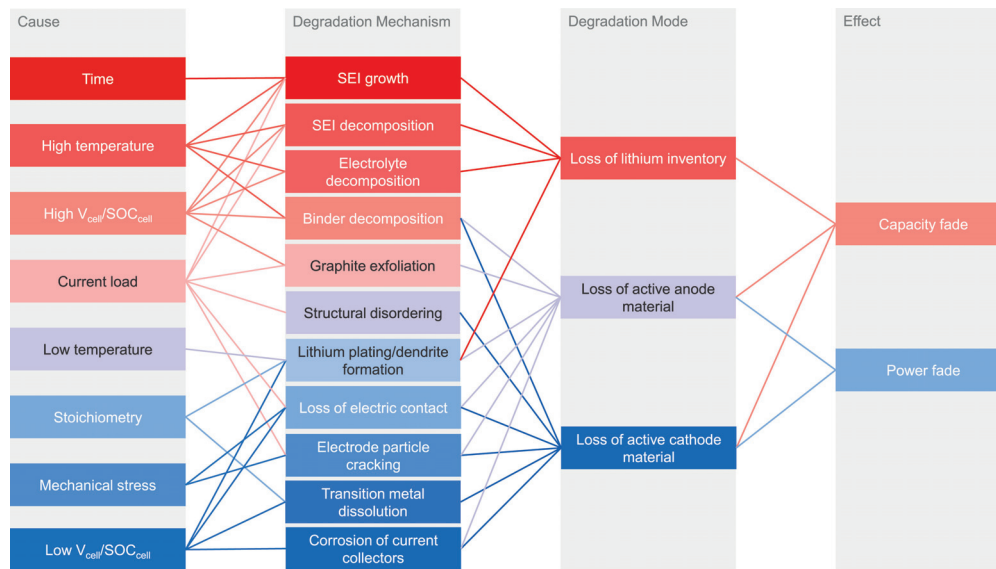
Figure 4.3 – Main degradation mechanisms of Li-ion cells, from [20]

with their causes and effects, in Figure 4.3, while a thorough review of such processes is provided in [182] or [14]. Most of these degradation mechanisms can be described referring to the porous electrode theory and exploiting the models based on it. In fact, the rate at which these mechanisms proceed is determined by the internal state of the cells (i.e. the variables of the models described in Section 4.2.2) and generate changes in the values of the parameters of these same models. As an example, we can use the growth of the SEI layer and the corresponding electrolyte decomposition [150]. This phenomenon is enhanced by high values of ion concentration in the solid particles of the anode and by high current rates (i.e., with respect to equations (4.2)-(4.10) when, in the anode, $c_s \rightarrow c_{s,max}$ and $(\phi_s - \phi_e)$ is high). This example will be described more in detail in Chapter 6 of this thesis.

The utilization of electrochemical models to explicitly model, visualize and eventually integrate in the battery control these physical processes is proposed by several references. As for the case of electrochemical models to represent cell dynamics, the integration of degradation processes in these models has been first performed by researchers in electro-chemistry [35, 125, 150]. These papers show how some of the most common ageing phenomena, i.e. electrolyte decomposition and growth of the SEI layer, can be integrated in an electrochemical model based on porous theory. Similarly, [34, 37, 38] describe material stress due to intercalation and de-intercalation of Lithium ions in the cell electrodes. Further works, such as [36, 42, 147] have then exploited this approach to predict the cycle life, capacity fade and impedance rise of a battery. Finally, [119, 137, 151] have proposed reduced-order formulations to use such models in real-time control applications.

4.3 The uses of Li-ion cell models in the control of BESS

A first usage of battery models is to simulate battery behavior so to determine the necessary characteristics of the batteries themselves and related systems (e.g. electronics or control loops). This is for example the aim of the model developed in [32]. Battery models are then used within algorithms to plan BESS operation over time horizons of considerable length. This is the case, for example, of the day-ahead problems developed in the first part of this thesis, where an integrator (including a model of the BESS round-trip efficiency) was used. Problems characterized by such long time-horizons (24 hours) and by such coarse resolution (5 minutes), in fact, do not require the exact modeling of all battery dynamics.

The following two subsections focus on those control problems where a detailed modeling of Li-ion cell is instead beneficial or even necessary.

4.3.1 Cell state estimation

Cell state estimation consists in determining an estimate of quantities (states) that are relevant to cell operation but un-observable (the battery SOC is the most typical example). Knowledge of such quantities is important to determine the instantaneous power that can be required from the cell, as well as the available energy and the charge and discharge runtime. Model-based state estimation is a widespread technique[4] to determine the state of Li-ion cells used in energy storage applications. It is performed by observer and filters that rely on models of various complexity. The seminal work in this respect is presented in the series of paper [140–142] by Plett. These formulate and demonstrate the effectiveness of the usage of an extended Kalman filter (EKF) exploiting an equivalent circuit model for LiPB-based battery packs. Examples of other works in this directions are [143, 144, 173] in which unscented Kalman filters are presented, or [21] that exploits an electrochemical model, rather than an equivalent circuit one, within an EKF.

4.3.2 Predictive control of BESS

A function that is closely related to SOC estimation and that is fundamental in the management of Li-ion cell is the determination of the maximum charge and discharge power for any given point of operation. This is a fundamental function of BMSs also typically done via models [146]. Exploiting the information about the current state and a model of the battery, it is possible to predict what would be the final cell voltage when requesting a given power for a given duration. Knowing the maximum and minimum cell voltages, it is therefore possible to assess the values of the maximum charge and maximum discharge powers.

Recent works, such as [74] or [192] propose to identify, rather than simply the power limit

---

[4]Simple methods, not relying on models, can be used but are limited in applicability and accuracy. Coulomb counting, for example, is affected by sensor biases and its estimate may drift in time from the real cell state, while the OCV-SOC curve provides an accurate estimate only for operation at quasi-equilibrium conditions [194].

within an interval, the optimal charging/discharging profile within this same interval, by means of predictive algorithms. These exploit circuit models within optimization algorithms. A similar concept is also used in Chapter 1 of this thesis to determine the optimal operation of the BESS to satisfy the tracking objective of the dispatching service with a 5-minutes horizon.

4.4 Potential advantages of the integration of advanced models in BESS control

Integrating advanced physics-based models in the control of BESSs and using them in the same (or at least in a similar) way as circuit models are used nowadays is object of a consistent - although recent - amount of research.

A consistent - although recent - amount of research aims at integrating advanced physics-based models in the control of BESSs and using them as nowadays circuit models are being used. In this section we list and discuss the advantages that this is expected to bring, whereas in section 4.5, we discuss the challenges that need to be addressed to reach these goals.

4.4.1 Increased accuracy in state estimation, prediction and simulation

A comprehensive comparison of the prediction performances of equivalent circuit and electrochemical models does not exist in the scientific literature (we found however a coarse comparison in [158]). This is due to the fact that these two classes of models are different in nature and while equivalent circuit models can be extended arbitrarily to represent any dynamic but have states with no physical meaning, electrochemical models have a predetermined and rather stiff structure but provide a deeper insight in the actual cell dynamics. This increased observability is another important advantage of electrochemical models, described in the following section. A comparison between an equivalent circuit and an electrochemical model would therefore be limited in validity to the specific structure of the former and to the specific operating conditions considered. However, few considerations concerning the accuracy in the voltage predictions and simulations attainable with these two classes of models can be made:

- first, as mentioned, equivalent circuit models are fitted so to predict/simulate battery behavior with most accuracy around a given operating point rather than in its whole operating range. On the contrary, the validity of electrochemical models is not limited to a more or less narrow operating range, but holds for any operating conditions in which the same phenomena are occurring and the same physical laws apply;

- diffusive processes take place in the electrode as well as in the electrolyte. Circuit models typically try to capture these phenomena via a series of RC branches. However, in order to have an accurate representation of such phenomena a very high number of branches is needed [180]. On the contrary, electrochemical models solve the exact PDEs governing diffusive phenomena, and represent therefore more precisely the associated dynamics.

- it is generally accepted that electrochemical models are more accurate than equivalent circuit models. Several works in the literature (e.g. [60, 149]) use an electrochemical model rather than experimental data as a reference to identify the parameters and assess the performances of simpler models.

4.4.2 Observability of cell dynamics and states

The equivalent circuit model used in Chapter 1 of this thesis is used to estimate the state of charge of a BESS as well as other "virtual" states (i.e. the voltages across the RC branches of the circuit). Among these, the SOC is the only relevant information about the actual internal physical state of the Li-ion cell. Although this may be sufficient for some purposes (e.g., the predictive constraints in the real-time control algorithm presented in Section 1.2), the SOC is a poor indicator of the processes occurring within a Li-ion cell during its cycling. As it is discussed in Section 4.2.2 and in more detail in Chapter 5, potentials and ion concentration assume non-uniform distributions in the various parts of Li-ion cells. The SOC and the external voltage are instead lumped quantities that fail to capture these inhomogeneities. On the contrary, electrochemical models allow to explicitly estimate ion concentrations and potentials in the various parts of Li-ion cells, thus gaining insight into these unbalances. This insight is extremely helpful, since it allows for a more efficient exploitation of the cells (see Section 4.4.3) and for the explicit consideration of most ageing phenomena (see Section 4.4.4).

4.4.3 Enhanced operating domain

A key challenge related to the reliable operation of BESS is the development of control strategies capable to account for both their physical operational constraints and aging factors with the main objectives of reducing fault occurrences, thermal runways and the magnitude of degradation phenomena in the cells. The magnitude of these phenomena depends on the evolution of the cells internal states and, in particular, overpotentials and ion concentrations in the various parts of the cell. Therefore, the knowledge of these quantities allows to implement efficient battery control policies that avoid electrochemical degradation while exploiting the full battery potential [30, 45, 118, 136, 164]. Since these quantities are not directly measurable, the operational constraints are normally defined on variables that are directly measurable (i.e.the battery terminal voltage and the current) or lumped states as the cell SOC [72, 177]. These quantities, however, are related to the physical states of the cell in a rather complex (nonlinear and time-dependent) way. In order to operate the BESS in a safe domain by imposing operational limits on these externally-available and/or lumped quantities, one should therefore choose conservative constraints. These, besides avoiding operation in unsafe conditions, may prevent to operate the BESS in non-harmful conditions [136], thus unnecessarily limiting the performances of Li-ion cells. In other words, these limits reduce the power and energy capability of a BESS (Fig. 4.4 provides a qualitative representation of this concept). Estimating the exact physical state of Li-ion cells via an electrochemical model can avoid this issue: it allows, in fact, to set the operating limits based on these estimated
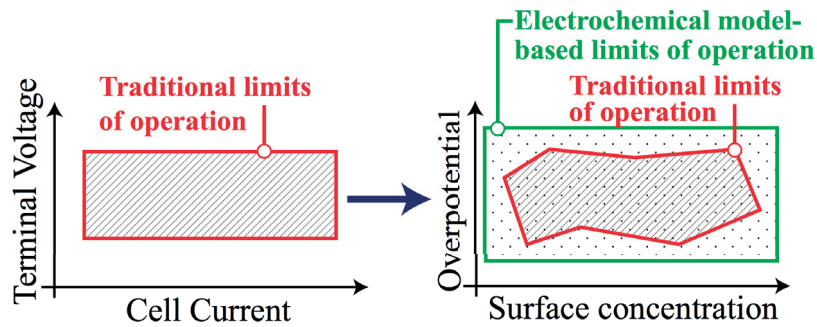
Figure 4.4 – Qualitative comparison of the traditional operational constraints for a Li-ion cell, based on measurable quantities (left) and allowed by the knowledge of actual cell physical states (right) [118].

quantities so that only operating conditions that are actually harmful to the cells are avoided. Moreover, as Li-ion batteries age, their behavior evolves. Constraints set on measurable and lumped quantities that are valid for new non-cycled cells may not ensure safe operation for an aged ones. This problem can be avoided by imposing limitations on the states estimated via electrochemical models.

4.4.4 Accounting of ageing via explicit modelling of degradation phenomena

As of today, ageing is taken into account in the control through macroscopic indicators, such as impedance rise and capacity fade (as detailed in Chapter 3). However, since the relation of degradation with operating pattern is rather complex, the same capacity fade or impedance rise could be reached via different patterns or operating strategies. Such indicators, therefore, are not sufficient to identify the optimal control strategy to operate a BESS (if not in an approximate way). Physical models provide the basis to enhance the assessment and limitation of ageing in BESS control, since the intensity of the degradation phenomena can be quantified on the basis of the cell physical states. These considerations are object of few recent works. The references [137, 151], for instance, propose to track specific physical quantities (such as the intercalation current density and ion surface concentration in the anode) rather than macroscopic ones.

Chapter 6 will provide a practical proof of concept on the advantages described in sections 4.4.2, 4.4.3 and 4.4.4 of using a physics-based model in the control of a BESS.

4.5 Challenges for the integration of advanced Li-ion cell models in BESS control

Three main challenges can be identified for the implementation of advanced, physics-based models. First, these are, in their original formulation, computationally demanding, and

hence not suited for real-time applications. Second, they rely on numerous and hard-to-get parameters. Third, these models represent the behavior of individual Li-ion cells and they need therefore to be scaled to be used in BESS control. Hereafter we provide few details on each of these challenges.

4.5.1 Computational complexity

The computational complexity of the P2D model and its "relatives" lies in their complex structure, where non-linear algebraic equations (such those modeling the charge tranfser) are coupled to a set of partial differential equations (modeling diffusion). Notably, the solid diffusion process need to be solved, on the r coordinate, for each x coordinate that lies within the electrodes (see Section 4.2.2). Due to this complex structure, iterative processes are necessary to solve the equations of these models.

This has been addressed and mostly solved by reduced order modeling techniques. Reduced order models (ROMs) rely on mathematical methods to identify models with a lower number of states from the "full" models, while maitaining the representativity of a number of physical states. For instance, [27] exploits proper orthogonal decomposition to build a ROM that present good agreement with the respective full electrochemical model, while requiring about one tenth of its computation time. [57] linearizes the model's algebraic equations and approximates the spherical diffusion PDEs via Padé approximations, greatly reducing its number of states. [95] derives a discrete-time state-space model from a P2D model by relying on the Ho-Kalman algorithm. Other approaches rely on simplifications such as neglection of electrolyte dynamics (see for instance [67], as well as Chapters 5 and 6 of this thesis) or the approximation of solid diffusion dynamics via analytical parabolic functions [172]. Such methods have successfully lightened the computational burden of physics based models, while preserving their representativity. This thesis, therefore, does not address this issues but rather focuses on another fundamental challenge, described in the following subsection.

4.5.2 Parameter identification

Besides having a complex structure, physics-based models rely on many parameters. The seminal P2D model described in [46, 63] and implemented in the DUALFOIL fortran program, for instance, relies on 74 parameters to completely characterize a Li-ion cell. To run such a model for a new cell chemistry, each of them need to be known or estimated with reasonable confidence. Even a much simpler single particle model, such the one described in [67], still needs 14 parameters, as well as the two open-circuit potential curves to be identified. On the contrary, a similar problem does not exist for circuit models. Their parameter set, besides being smaller, does not represent any specific physical phenomena and can therefore be identified aiming solely at the minimization of the model prediction or simulation error. Since parameters of physics-based models represent specific properties of the cell, these need to be identified accurately to correctly represent their dynamics. Typically, these parameters can be

known by cell designers or can be inferred by cell tear-down and electrochemical and physical testing. The latter, however, are costly and require specific equipment and competences and therefore may not be viable methods in most laboratories. Moreover, it may not be possible to measure all parameter values and some may still need to be fit through an optimization process [77].

Few papers address the challenge of identifying the parameters of a physics based model via cycling and, in general, methods that can be executed by control and electrical engineers with standard laboratory equipment. These are [22, 58, 77, 157]. [58] employs a computational cluster for several days, to identify the 88 parameters of a P2D model. While this being the more complex model successfully identified based only on cycling experiments, the computational requirements for the proposed method are still prohibitive for most cases. [77] and [22] identify respectively a reduced order P2D model and a SPM by clustering specific sets of parameters to specific tests. In order to identify the parameters related to diffusive phenomena, however, these rely on electrochemical impedance spectroscopy (EIS) which is a technique that requires specific and not-so-widespread equipments. Finally, [157] does use only cycling tests to identify a SPM, although it does not describe specific cycles optimized for identifiability, but rather analyses the identifiability of parameters from the available cycles based on a Fisher-information matrix approach.

4.5.3 Scaling from cell to system models

Finally, the question arises, whether and to what extent cell models can be exploited in the control of BESS composed of hundreds or thousands of such cells. This is not a concern for state estimation, where the state of each cell needs to be estimated. However, this is a relevant question for the case of model predictive control, where, as shown in Chapter 6 of this thesis, physics-based model may bring relevant performance improvements. However, including the models of hundred or thousand cells in the predictive control framework is prohibitive.

The Chapter 6 of this thesis, as well as for instance [134], assumes that all cells are equal and their states evolve coherently. This assumption allows to consider the cell voltage V_{cell} and current I_{cell} as proportional to the BESS ones (V_{BESS} and I_{BESS}):

$$V_{cell} = V_{BESS}/n_s \tag{4.11}$$
$$I_{cell} = I_{BESS}/n_p \tag{4.12}$$

where n_s and n_p are respectively the number of cells in series and in parallel in the BESS. This assumption, however, is not true in general, since the parameters of Li-ion cells vary. [152] studied a set of 1100 fresh Li-ion cells, in order to quantify the dispersion of the values of several cell parameters. The results show that the capacity and impedance of the cells present a relative variation of 0.28% and 0.72% respectively[5].

[5]Such values concern fresh cells, i.e. do not take into account changes in the parameters due to ageing and to faults. It is reasonable to assume that these variations will gradually increase during BESS operation
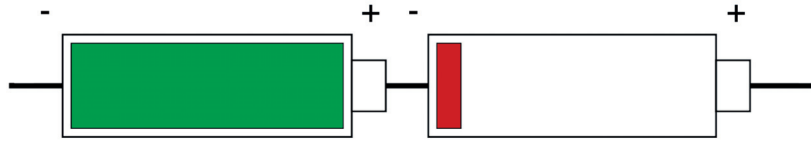
Figure 4.5 – Overemphasized representation of a battery pack composed by two cells in series having different SOC.

Assuming all cells' states evolve homogeneously and using an aggregate state to represent them may cause issues in their control, since the limits of operation of a battery pack are determined by the "weakest" cells, i.e. those cells that are more distant from the average state. An overemphasized example is provided in Fig. 4.5. Here, a battery pack is composed by two cells in series and one is completely full, while one is empty. Considering exclusively the pack capacity and the stored charge, the pack SOC could be said to be 0.5. However, since one cell is full, the pack cannot be charged (is then the pack SOC equal to 1?) and since one cell is empty, the pack cannot be discharged (is then the pack SOC equal to 0?)[6]. This emphasized case shows how the individual states of all cells should be considered, in a truly efficient control. This, however, is a challenging problem, due to the high number of cells present in BESSs and the consequent dimension of the estimation and/or control problems. Few papers address the issue of the efficient estimation of Li-ion battery packs. [145] proposes to estimate the states of such systems via the so called *bar-delta filtering*. It consists in estimating an average (*bar*) state of the pack via an extended Kalman filter (precise and executed with a fast sampling time) and estimating the variations (*deltas*) of individual cells from this average through simpler and slower-paced filters. [96] aims at identifying, within a pack, the two cells that impose the charge and discharge limits, rather estimating the states of all cells. While these papers proposes promising approaches for the state estimation of Li-ion cell packs, they do not address the issue of how to exploit such information in a predictive control framework.

Of the three challenges listed above, we consider the first (i.e. the computational complexity) as being mostly solved by recent research efforts. In this Thesis, Chapter 5 proposes a novel approach to tackle the second (i.e. the parameter identification). The third (the coupling of cell models and BESS control) is relatively unexplored yet and, in the conclusion of this thesis, few considerations are made about possible approaches to tackle this issue.

---

[6]In fact, many works on BESS operation, scheduling and control, use a unique SOC value to represent the state of the BESS (e.g. [113]). This quantity is not the same as the SOC defined in the works on SOC estimation of Li-ion cells, where the estimation is performed on single cells. The usage of a BESS SOC in these works is related with the "proper" definition of SOC only if it is assumed that (4.11) and (4.12) are valid. This assumption, however, is not true in general.

5 Parameter identification of a Li-ion cell single particle model

This chapter addresses one of the challenges related to the integration of battery physics-based models in control described in Chapter 4: the parameter identification of Li-ion cell electrochemical models. Specifically, this chapter considers a Li-ion cell single particle model (SPM). First, it proposes a model reformulation that reduces the number of parameters necessary to describe the cell dynamics. Second, it proposes a set of experimental tests to identify separately given subsets of parameters. Third, it demonstrates, via simulations and experiments the effectiveness of the proposed approach.

5.1 The single particle model

The SPM formulation upon which this Chapter is based is first introduced in [67]. The SPM describes the main phenomena taking place in a Li-ion cell: solid state diffusion, intercalation and de-intercalation and conduction. It neglects the diffusion in the electrolyte. This simplification allows for a considerable simplification in the model structure and dimension and is generally considered to be acceptable as long as the current rates are low and electrodes are thin and highly conductive. Following this assumption, diffusion and intercalation phenomena occur uniformly in all the anode and cathode volume and the two electrodes can be therefore modeled by two spherical particles. The model structure and the relevant phenomena occurring within the cell and modeled by an SPM are represented in Fig. 5.1. The physical phenomena modeled are: *i)* the diffusion in the anode active material; *ii)* the intercalation at the anode-electrolyte interface; *iii)* ionic conduction in the electrolyte; *iv)* intercalation at the cathode-electrolyte interface; *v)* diffusion within the cathode active material. This model can incorporate a detailed physical description of ageing processes [125] and a physical description of thermal behavior [67] of the cells and can be used in SOC estimation algorithms [43]. We report here the governing equations for the diffusion processes in the two electrodes and the equation describing the cell voltage. The diffusion within the electrode active material is modeled through two radial diffusion partial differential equations (PDEs) such as (5.1). In (5.1)-(5.4), the subscript $i = (p, n)$ indicates the electrode, with p standing for positive and n for negative electrode. c_i is the ion concentration within the single particle,
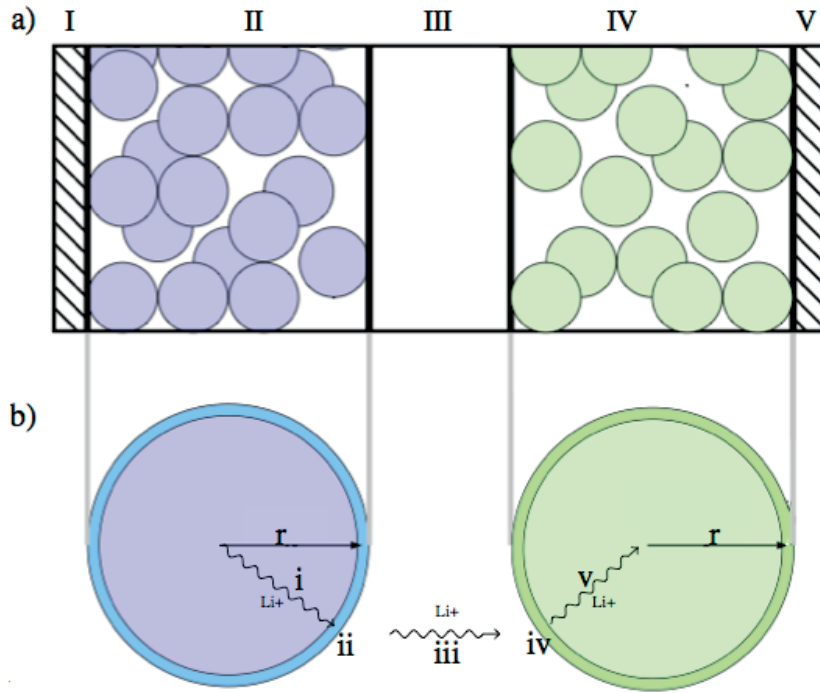
Figure 5.1 – a) Structure of a Li-ion cell: I) negative current collector; II) anode; III) separator; IV) cathode; V) positive current collector. b) single-particle model schematic.

as a function of time t and radial coordinate r. D_i indicates the diffusion coefficient of the electrode, S_i its total active surface area, R_i the radius of the particles composing the active material, V_i the total electrode volume and ϵ_i its porosity. Finally, I_{app} is the current applied to the cell and F the Faraday constant.

$$\frac{\partial c_i(r,t)}{\partial t} = \frac{D_i}{r^2} \frac{\partial}{\partial r}\left(r^2 \frac{\partial c_i(r,t)}{\partial r}\right) \tag{5.1}$$

with boundary conditions:

$$D_i \frac{\partial c_i}{\partial r}\big|_{r=0} = 0, \qquad D_i \frac{\partial c_i}{\partial r}\big|_{r=R_i} = -J_i(t) \tag{5.2}$$

and where:

$$J_i(t) = \pm \frac{I_{app}(t)}{FS_i}, \tag{5.3}$$

$$S_i = \frac{3\epsilon_i V_i}{R_i}. \tag{5.4}$$

In (5.3), the positive sign is for the positive electrode and the negative sign is for the negative one. These equations define the ion concentration within the two electrodes. The external voltage of the cell V_{cell} is then computed as a sum of several terms, as in (5.5). U_p and U_n are the open-circuit potential (OCP) of the cathode and anode respectively and are functions of

108

the ion concentration in the two electrodes. The three remaining terms are the voltage drops respectively due to *i)* the intercalation in the cathode, *ii)* the intercalation in the anode and *iii)* the ohmic losses in the electrolyte and the electrodes. The expressions for the voltage drops due to intercalation processes are obtained by reversing the Butler-Volmer equation for the intercalation current density, as defined in [181]. In (5.5) and (5.6), R is the gas constant, T is the absolute temperature, k_i is the reaction rate constant for the electrode i, c_e is the ion concentration in the cell electrolyte, $c_{i,max}$ the maximum ion concentration possible for an electrode and $c_{i,surf}$ the surface concentration of the electrode single particle.

$$
\begin{aligned}
V_{cell} = \quad & U_p(z_{p,surf}) - U_n(z_{n,surf}) + \\
& + \frac{2RT}{F} ln\left(\frac{\sqrt{m_p^2 + 4} + m_p}{2}\right) + \\
& + \frac{2RT}{F} ln\left(\frac{\sqrt{m_n^2 + 4} + m_n}{2}\right) + I_{app}R_{cell}
\end{aligned}
\tag{5.5}
$$

$$
m_i = \frac{I_{app}}{Fk_i S_i c_{i,max} c_e^{0.5}\left(1 - x_{i,surf}\right)^{0.5} x_{i,surf}^{0.5}},
\tag{5.6}
$$

where $z_{i,surf} = \frac{c_{i,surf}}{c_{i,max}}$. We report in Table 5.1, the parameters needed to fully characterize the model. This formulation of the SPM needs 14 parameters and the two analytical functions $U_p(z_{p,surf})$ and $U_n(z_{n,surf}$ for the two equilibrium potentials to fully describe the cell behavior.

Table 5.1 – Parameters of a full SPM

Parameter	Unit	Meaning
D_p	$m^2 s^{-1}$	Cathode solid diffusion coefficient
D_n	$m^2 s^{-1}$	Anode solid diffusion coefficient
ϵ_p	-	Cathode porosity
ϵ_n	-	Anode porosity
R_p	m	Cathode Particle radius
R_n	m	Anode particle radius
V_p	m^3	Cathode volume
V_n	m^3	Anode volume
$c_{p,max}$	$mol\ m^{-3}$	Cathode maximum solid concentration
$c_{n,max}$	$mol\ m^{-3}$	Anode maximum solid concentration
k_p	$m^{2.5} mol^{-0.5} s^{-1}$	Cathode reaction rate constant
k_n	$m^{2.5} mol^{-0.5} s^{-1}$	Anode reaction rate constant
R_{cell}	Ω	Cell resistance
c_e	$mol\ m^{-3}$	Electrolyte ion concentration

5.2   Reformulation of the SPM to reduce the number of parameters

It is to be noted that some of the model parameters are always present and only *grouped* with other parameters. Examples are the electrode porosities ϵ_i or the ion concentration in electrolyte c_e in (5.1) and (5.6) respectively. The isolation and identification of these as independent parameters, therefore, does not bring any information relevant to the modeling of the cell dynamics. We define new parameters by lumping those that appear only grouped and by normalizing the variables in the diffusion equation (5.1). This allows the definition of an SPM that has exactly the same accuracy and generality as the one in [67] while relying on the identification of only half of its parameters. Eq. (5.1) can be reformulated, by defining the normalized coordinate $x = \frac{r_i}{R_i}$ and the normalized concentration $z = \frac{c_i}{c_{i,max}}$. Substituting these newly defined terms in Eq. (5.1) and defining a normalized diffusivity as $D_i^* = \frac{D_i}{R^2}$ and an equivalent electrode capacity as $Q_i = FR_iS_ic_{i,max}$, the diffusion processes in the two electrodes can be described by the equation:

$$\frac{\partial z}{\partial t} = D_i^* \frac{1}{x^2} \frac{\partial}{\partial x}\left(x^2 \frac{\partial z}{\partial x}\right)$$

with boundary conditions: $\hspace{10em}$ (5.7)

$$D_i^* \frac{\partial z}{\partial x}\Big|_{x=0} = 0, \qquad D_i^* \frac{\partial z}{\partial x}\Big|_{x=1} = \frac{I_{app}}{3Q_i}$$

The description of diffusion in an electrode, depends therefore only on two parameters, D_i^* and Q_i. The parameters in (5.6) can also be grouped in a similar way. By defining $k_i^* = \frac{k_i c_e^{0.5}}{R_i}$ and using the Q_i defined above, it can be obtained that:

$$m_i^* = \frac{I_{app}}{3Q_i k_i^* (1 - z_{i,surf})^{0.5} z_{i,surf}^{0.5}}$$
$\hspace{30em}$ (5.8)

The resulting set of parameters is shown in Table 5.2. The dynamics of each electrode, with this novel SPM formulation are fully described by: *i)* a capacity Q_i, *ii)* a diffusivity D_i^*, *iii)* a reaction rate k_i^*. The additional resistive term R_{cell} takes into account the ohmic voltage drop in the electrolyte and electrodes. Globally, the SPM, reformulated as proposed, can describe the cell dynamics while relying only on 7 parameters. It is to be stressed that the newly defined parameters are dependent on those of the original formulation, through the relations described above. A different value of the electrode active material porosity ϵ_i, for example, will emerge in a different value of Q_i. In spite of this, as long as the goal of the modelling effort is to describe the dynamics of the cell, the newly defined parameters are sufficient: once these are known, the model equations providing the model state variables and the cell output voltage are parametrised completely. If one seeks instead a more detailed characterisation of the cell, and thus the identification of all the parameters of the original model, further tests beyond those proposed in the present work are needed. With the reformulation presented above, Eq. 5.5 holds for the cell voltage. The cell SOC can be calculated from the relative ion concentration in one of the two electrodes. Defining the average ion concentration in the

Table 5.2 – Parameters of the reformulated SPM

Parameter	Unit	Definition
D_p^*	s^{-1}	Cathode normalized diffusivity
D_n^*	s^{-1}	Anode normalized diffusivity
Q_p	C	Cathode capacity
Q_n	C	Anode capacity
k_p^*	s^{-1}	Cathode reaction rate constant
k_n^*	s^{-1}	Anode reaction rate constant
R_{cell}	Ω	Cell resistance

single particle as $\bar{z}_i$, it is:

$$
\begin{aligned}
SOC(t) &= \frac{\bar{z}_n(t) - z_{n,min}}{z_{n,max} - z_{n,min}} \\
&= 1 - \frac{\bar{z}_p(t) - z_{p,min}}{z_{p,max} - z_{p,min}}
\end{aligned}
\tag{5.9}
$$

5.3 Parameter identification procedure

5.3.1 Clustering of parameters based on physical phenomena

The parameters described above can be divided in three groups, each one related to a given characteristic of the electrodes. Each one of these groups of parameters can be identified by a specific test, crafted to isolate the relevant phenomena and to be performed on a commercial cell with non-invasive techniques:

1. Q_p and Q_n are the capacities of the electrodes and can be found through low-rate tests. With low-rate tests we mean here a full discharge followed by a full charge of the cell carried out at constant and low current rate. Such experiment allows to determine the capacity of the whole cell and its open-circuit voltage characteristic. These elements are then used to compute the capacities of the two individual electrodes;

2. the subset $\theta_{pt} = [k_p^*, k_n^*, R_{cell}]$ can be identified by performing a series of pulse tests at various SOCs and with various current rates. Every current pulse is characterized by a given couple of values of SOC and current rate. By fitting the values of the instantaneous voltage drops during the pulses, it is possible to identify the triplet θ_{pt};

3. the subset of parameters related to diffusive phenomena $\theta_{GITT} = [D_p^*, D_n^*]$ can be identified by performing a series of galvanostatic intermittent titration technique (GITT) cycles at various SOCs. Every GITT cycle is composed by a constant current discharge of limited duration followed by a resting phase. The voltage values before the discharge, at the end of the discharge and after the resting phase provide the experimental data used to identify θ_{GITT}.

This set of tests allows for a complete characterization of the SPM of a Li-ion cell. The only prior knowledge needed is the materials of the two electrodes, as this provides information about their OCP curves. The results of the first test are necessary to proceed to the following two, whereas these are independent from each other. The low rate test identifies the equilibrium properties of the two electrodes, thus allowing to determine the relative ion concentration and open-circuit potential of the two electrodes for any equilibrium condition of the cell. The identification of θ_{pt} and θ_{GITT} relies on this knowledge, since the electrodes concentrations at equilibrium and the relative open-circuit potential values are used as data in the analytical functions used for the fitting problems (5.17) and (5.21). The identification problems for the three subsets θ_{ocv}, θ_{pt} and θ_{GITT} are formulated as non-linear least-squares fitting problems. Since these are in general non-convex, multiple runs have been carried out of each of them, with different starting points, in order to minimize the possibility of being trapped in local minima. The identification procedure took overall a computational time in the order of few tens of seconds on a standard laptop.

In the following subsections, the three tests composing the identification procedure are described in detail.

5.3.2 Identification of the electrode capacities and OCP curves

A low-rate test consists in a constant current (CC) complete discharge at very low rate followed immediately by a CC complete charge at the same rate. In such experiment, it is assumed that the reactions at the two electrodes happen in an equilibrium state. Ideally, no diffusion nor voltage drop due to charge transfer or ohmic losses occur. This experiment is therefore suited to identify the capacity terms of the two electrodes and the open-circuit voltage (OCV) curve of the cell as a function of the SOC.

Knowing the materials of the two electrodes, it is possible to determine from the literature the open-circuit potential curves as functions of the ion concentration in the two materials. Now, in a commercial cell, these curves are not totally *exploited*, i.e. the maximum and minimum cell voltage may be reached when at an electrode the ion concentration is lower (or higher) than its maximum (minimum) theoretical value. Our aim is to find the maximum and minimum concentration of the individual electrodes such that the open-circuit voltage curve measured during the low rate experiment fits at best with the theoretical functions of the two materials. This can be done by fitting the OCV curve obtained from the two OCP curves from the literature to the measured one. Formally, we define the parameter vector $\theta_{ocv} = [z_{p,max}, z_{p,min}, z_{n,max}, z_{n,min}]$. The analytical curve $O\hat{C}V$ is then found as:

$$
\begin{aligned}
O\hat{C}V(\theta_{ocv}) = & + OCP_p(z_{p,max}, z_{p,min}) + \\
& - OCP_n(z_{n,min}, z_{n,max})
\end{aligned}
\tag{5.10}
$$

The optimal value θ_{ocv}^o can be found solving the following least-squares problem:

$$\min_{\theta_{ocv}} \sum_{j=1}^{N} \left(OCV_j - O\hat{C}V_j(\theta_{ocv}) \right)^2 \tag{5.11}$$

where N is the number of equally spaced points (in terms of SOC) in which both the experimental and analytical curve are discretized [1].

Having obtained the limit values of concentration for the two electrodes we are able to calculate their capacity. The cell capacity is inferred through the experiment by current integration. As we have performed both a complete charge and a complete discharge, we calculate the cell capacity Q_{cell} as the average of the two values obtained during the charge and discharge respectively. With this value and the values of the elements of θ_{ocv}^o, we can determine the capacity of the two individual electrodes as follows:

$$Q_p = \frac{Q_{cell}}{z_{p,max} - z_{p,min}}, \quad Q_n = \frac{Q_{cell}}{z_{n,max} - z_{n,min}} \tag{5.15}$$

5.3.3 Identification of the resistive terms of the SPM

Once the capacities of the two electrodes are identified, we seek the identification of the parameters in the terms of Eq. 5.5 related to intercalation and conduction. We do so through a series of pulse tests. A pulse test is here defined as a test in which the cell is in equilibrium condition and is subjected to a pulse of current, of a given amplitude and for a short duration. In such a test, the ion concentrations in the electrodes (and thus their OCPs) do not change considerably as the drained charge is very small, due to the short duration of the pulses. Additionally, diffusive phenomena does not take place, as these need some time to be activated. The instantaneous voltage drop ΔV_{pt} occurring when a current pulse is applied is therefore proportional only to the three latter terms of Eq. 5.5, which are dependent exclusively on k_n^*,

---

[1]The proposed method can be extended to take into account hysteretic behaviour of OCP curves. If, for example, the anode material has different OCP curves for charge and discharge, one can seek the identification of θ_{ocv}^o through the solution of the following optimisation problem, adapted from (5.10),(5.11):

$$\min_{\theta_{ocv}} \left(\sum_{j=1}^{N} OCV_{ch,j} - O\hat{C}V_{ch,j} \right)^2 + \left(\sum_{j=1}^{N} OCV_{d,j} - O\hat{C}V_{d,j} \right)^2 \tag{5.12}$$

where:

$$O\hat{C}V_{ch}(\theta_{ocv}) = + OCP_p(z_{p,max}, z_{p,min}) +$$
$$- OCP_{n,ch}(z_{n,min}, z_{n,max}) \tag{5.13}$$
$$O\hat{C}V_d(\theta_{ocv}) = + OCP_p(z_{p,max}, z_{p,min}) +$$
$$- OCP_{n,d}(z_{n,min}, z_{n,max}) \tag{5.14}$$

and where the subscripts *"ch"* and *"d"* are to differentiate the OCP curves in charge and discharge.
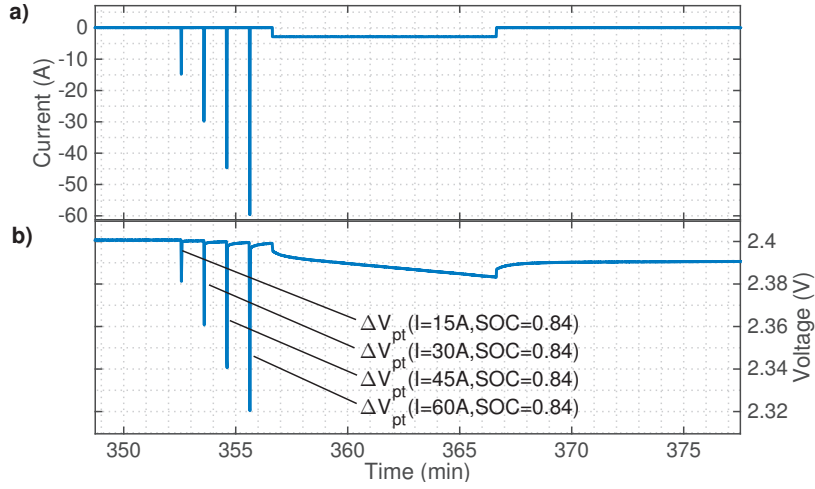
Figure 5.2 – Experimentally measured current and voltage profiles (a) and b) respectively) during a pulse test for a 30 Ah Lithium-titanate cell.

k_p^* and R_{cell} and on the already identified Q_n and Q_p:

$$\Delta V_{pt} = + \frac{2RT}{F} ln\left(\frac{\sqrt{m_p^{*2}+4}+m_p^*}{2} \right)$$
$$+ \frac{2RT}{F} ln\left(\frac{\sqrt{m_n^{*2}+4}+m_n^*}{2} \right) + I_{app}R_{cell} \tag{5.16}$$

With m_p^* and m_n^* function of I_{app} and $z_{p,surf}$ and $z_{n,surf}$ respectively and given by Eq. 5.8.

The experimental protocol for the proposed tests is as follows: *i)* the cell is completely charged and in equilibrium conditions; *ii)* it is subjected to a train of pulses each one with a different current; *iii)* it is then discharged of a given ΔSOC and it rests for few hours so that it reaches equilibrium conditions again; *iv)* a new set of pulses is performed and the procedure is repeated until $SOC = 0$. In this way, a matrix of experimental values for ΔV_{pt} at different SOCs and current rates is collected. In Fig. 5.2, a detail from such test, carried out on the cell described in section 5.5, is shown.

Parameters k_n^*, k_p^* and R_{cell} can be identified by fitting the resulting ΔV_{pt} data. Formally, we define $\theta_{pt} = [k_n^*, k_p^*, R_{cell}]$ and we find its optimal value θ_{pt}^o by solving:

$$\min_{\theta_{pt}} \sum_{j=1}^{N} \left(\Delta V_{pt,j} - \hat{\Delta V}_{pt,j}(\theta_{pt}) \right)^2 \tag{5.17}$$

where N is the overall number of pulses, and the circumflex symbol denotes the values found analytically through Eq. 5.16.
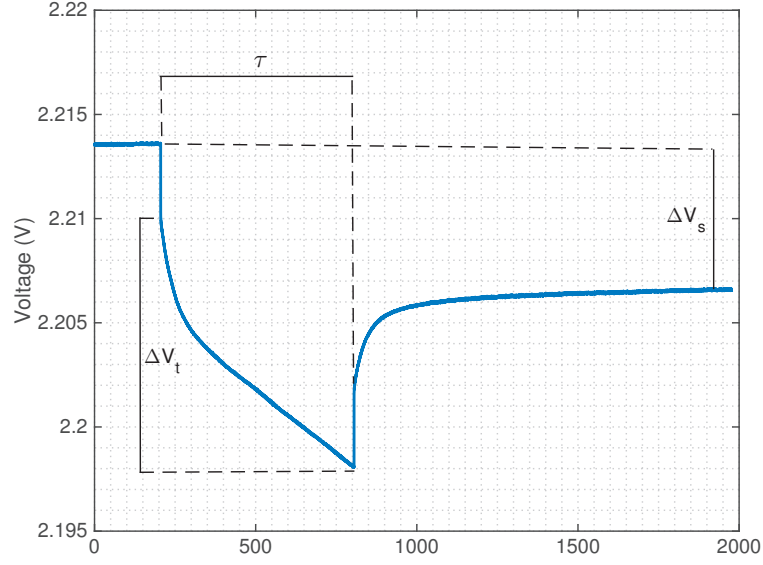
Figure 5.3 – Experimentally measured voltage profile during a GITT discharge for a 30 Ah Lithium-titanate cell.

5.3.4   Identification of the diffusive terms of the SPM

The values of the two diffusivities can be found by means of a series of GITT tests. This technique is commonly used to determine solid diffusion coefficients for single electrodes [160]. It consists in submitting the targeted cell to a sequence of CC discharge pulses at low C-rate, followed by resting phases that bring the cell back to equilibrium. In Fig. 5.3 we see the detail of the voltage profile during one of such pulses, carried out on the cell described in section 5.5.

The general equation for the diffusion coefficient calculation of a half cell electrode from GITT measurements, is:

$$D_i = \frac{4}{\pi\tau}\left(\frac{R_i}{3}\right)^2\left(\frac{\Delta V_s}{\Delta V_t}\right)^2 \tag{5.18}$$

Where R_i is the radius of the active material particles, τ is the duration of the pulse (set by the experimenter) and ΔV_s and ΔV_t are experimentally measured values (see Fig. 5.3). Eq. 5.18 is directly derived from the approximation of the analytical solution of Eq. 5.1, for the case of a discharge pulse of small duration (such that $\tau << R_i^2/D_i$) as shown in [187]. In the case of complete cells, an analytical solution is impossible because it is impossible to discern the contribution of the two individual electrodes to ΔV_s and ΔV_t. We propose instead to proceed through the minimization procedure detailed hereafter.

A series of GITT discharge pulses can be perfomed, in order to obtain a set of experimental values for τ, ΔV_s and ΔV_t at various SOC levels. As ΔV_s is a difference between two open-circuit potentials, we can determine the values for the individual OCP differences of the two

electrodes $\Delta V_{s,p}$ and $\Delta V_{s,n}$, thanks to the tests performed to identify the electrode capacities. $\Delta V_{t,p}$ and $\Delta V_{t,n}$ can be then expressed as follows:

$$\Delta V_{t,i} = \sqrt{\frac{4}{\pi \tau} \frac{1}{9} \frac{1}{D_i^*}} \Delta V_{s,i} \tag{5.19}$$

with $i = p, n$ and where D_i^* are the diffusivities reformulated as described in section 5.3.1. Finally we have:

$$\Delta V_t = \Delta V_{t,p} + \Delta V_{t,n} \tag{5.20}$$

We see that ΔV_t can be expressed as a function of known experimental values and of the set of parameters $\theta_{GITT} = [D_p^*, D_n^*]$. We can therefore identify the two diffusivities by solving the following least-squares problem:

$$\min_{\theta_{GITT}} \sum_{j=1}^{N} \left(\Delta V_{t,j} - \Delta \hat{V}_{t,j}(\theta_{GITT}) \right)^2 \tag{5.21}$$

where N is the overall number of GITT pulses and the circumflex symbol denotes the values found analytically via Eq. 5.20.

For any individual value of ΔV_t, multiple different values of θ_{GITT} may generate a good fit: since one equation is available for the determination of two unkowns, the resulting system is underdetermined. On the contrary, the system of nonlinear equations obtained by imposing $\Delta V_t - \Delta \hat{V}_t(\theta_{GITT}) = 0$ to a set of ΔV_t values at various SOCs is an overdetermined system, if the resulting equations are independent. This is the case whenever at least one of the two electrodes presents a non-linear OCP curve (as is often the case for Li-ion cells). A solution to this problem is provided by the least-squares method, that identifies a likelihood estimate of the values of the two diffusivities. Intuitively, provided that at least one electrode OCP curve is non-linear, the relative weight of $\Delta V_{t,n}$ and $\Delta V_{t,p}$ in the cell ΔV_t will be a function of the SOC. This non-linearity and SOC dependency allows to discern the contribution of each electrode to the cell ΔV_t values and therefore the value of the two diffusivities. This is exemplified in Fig. 4. We report in blue the values of ΔV_t obtained with the optimal set θ_{GITT}^o for a MCMB-LiCoO$_2$ cell (whose complete parameter identification is discussed in section 5.4). We show in red the values of ΔV_t in the case in which D_n^* is arbitrarily set to 100 s^{-1}. A very high value of D_n^* results into a very fast diffusion in anode solid particles. The consequence is that this electrode reaches the equilibrium condition very fast and its contribution to the overall ΔV_t is minimised. The red curve, therefore, shows the contribution of the cathode alone to the cell ΔV_t. Equivalently, in yellow, we show the results in the case of $D_p^* = 100$ s^{-1}, i.e. the contribution of the anode alone to the overall ΔV_t. It emerges that the peak in the ΔV_t values at low SOC is due to the anode, the peaks at $SOC \simeq 0.8$ are due to the cathode, whereas the peak at $SOC \simeq 0.5$ is due to both electrodes. Therefore, while values of θ_{GITT} different from θ_{GITT}^o may result in a good fit for certain ΔV_t values, only the latter ensures it across the complete SOC range.
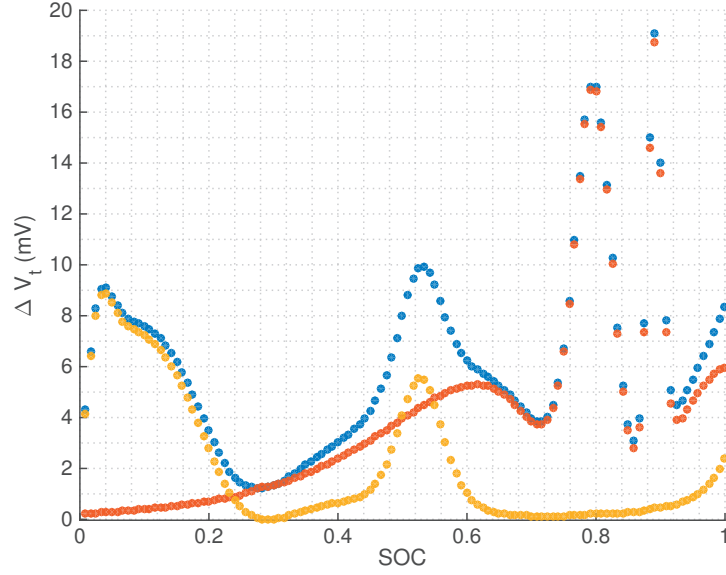
Figure 5.4 – Values of ΔV_t obtained for a MCMB-LiCoO$_2$ cell and for various values of diffusivities. Blue dots: $D_n^* = 0.38 \cdot 10^{-3}\ s^{-1}, D_p^* = 0.79 \cdot 10^{-3}\ s^{-1}$, red dots: $D_n^* = 100\ s^{-1}, D_p^* = 0.79 \cdot 10^{-3}\ s^{-1}$, yellow dots $D_n^* = 0.38 \cdot 10^{-3}\ s^{-1}, D_p^* = 100\ s^{-1}$.

Diffusion coefficients variable with the SOC

Several electrode materials present diffusion coefficients that are dependent on the SOC. In the case of the Lithium-titanate cell used in section 5.5 of the present work, for example, we know from the literature that the diffusion coefficient of the $LiNiCoAlO_2$ (NCA) cathode is variable with the ion concentration [4], with a trend as:

$$D_p^* = p_1 \cdot [(1 + \tanh(-p_2(z_p - p_3))) + p_4] \tag{5.22}$$

The diffusion coefficient of the titanate anode is considered constant, in accordance to [39] and [94]. The procedure described above can be therefore adapted in order to incorporate this dependency. The experimental test and the fitting problem remain unchanged, but we seek the identification of the parameter subset θ_{GITT} composed as $\theta_{GITT} = [D_n^*, p_1, p_2, p_3, p_4]$.

5.4 Validation of the proposed method against a reference model

A first validation of the proposed procedure has been carried out through a controlled "virtual" experiment, in which the proposed tests and validation cycles have been carried out on the detailed P2D model of a 30 Ah MCMB-LiCoO$_2$ cell. All the state variables and the parameters associated to this simulated cell are henceforth referred as *true*. The SPM parameters have been identified from the synthetic noiseless voltage and current measurements resulting from this simulation. This controlled experiment setup provides prior knowledge of the true cell

117

parameters and the access to the true cell states during cycling (which are not accessible in the case of real cells). Therefore, we are able to compare the SPM parameters obtained through the proposed identification procedure with the true ones as well as the profiles of the internal states as simulated via the SPM and the true ones, i.e. those from the reference P2D model.

The reference model used in this section and its parameters are from [136][2].

In Table 5.3 the true parameters and those identified via the proposed procedure are reported. Notably, the set of parameters on the left side of the table is obtained by applying the reformulation described in section 5.3.1 to the original set of parameters of the P2D model. The parameters on the right are obtained via the identification procedure described in sections 5.3.2 to 5.3.4. It can be observed that the parameters of subset θ_{ocv} are identified extremely well, with a mean relative error of 0.02%. Parameters k_p^*, k_n^* and D_n^* are identified with a relative error below 10%, whereas only D_p^* is identified with a relative error of about 21%.

Table 5.3 – Parameters of the MCMB-LiCoO$_2$ cell

	True	Identified
Q_p	$2.4709 \cdot 10^5 \ C$	$2.4703 \cdot 10^5 \ C$
Q_n	$1.4463 \cdot 10^5 \ C$	$1.4464 \cdot 10^5 \ C$
k_p^*	$0.9833 \cdot 10^{-5} \ s^{-1}$	$0.9567 \cdot 10^{-5} \ s^{-1}$
k_n^*	$0.3277 \cdot 10^{-3} \ s^{-1}$	$0.3005 \cdot 10^{-3} \ s^{-1}$
R_{cell}	[-]	$3.497 \cdot 10^{-4} \ \Omega$
D_p^*	$1 \cdot 10^{-3} \ s^{-1}$	$0.7857 \cdot 10^{-3} \ s^{-1}$
D_n^*	$0.39 \cdot 10^{-3} \ s^{-1}$	$0.3777 \cdot 10^{-3} \ s^{-1}$

Figures 5.5 to 5.7 show the outcomes of the three tests composing the proposed identification procedure. Figures 5.5-a and 5.5-b show the portions of the analytical OCP curves of the electrodes obtained with the estimated set θ_{ocv}^o. Fig. 5.5-c shows the real OCV curve (blue line) and the one obtained by using θ_{ocv}^o (dashed red line). The two curves match very closely, with a maximum error below 3 mV and an RMSE of about 0.03 mV. Fig. 5.6 shows the results of the pulse tests. The blue dots are the values of ΔV_{pt} obtained for various C-rates and SOCs by exciting the reference model with the profile described in section 5.3.3 whereas the red dots are the values obtained analytically with the optimal set of parameters θ_{pt}^o, obtained by solving Eq. 5.17. Maximum error and RMSE are respectively of 0.4 mV and 0.17 mV. Finally, Fig. 5.7 shows the values of ΔV_t at various SOCs as obtained with the reference model and analytically with the optimal subset of SPM parameters θ_{GITT}^o. The maximum error is of 1.41 mV and the RMSE is of 0.59 mV.

The reference model and the SPM with the parameters as in the right side of Table 5.3, have been excited with two current profiles, respectively from a grid-level application and from an EV cycling test. The first consists of a sequence of constant current steps of the duration of 15 seconds each and variable amplitude. The duration of a complete test is 24 h and

---

[2]At the moment of writing this thesis, April 2018, this is available online at *https://github.com/scott-moura/*
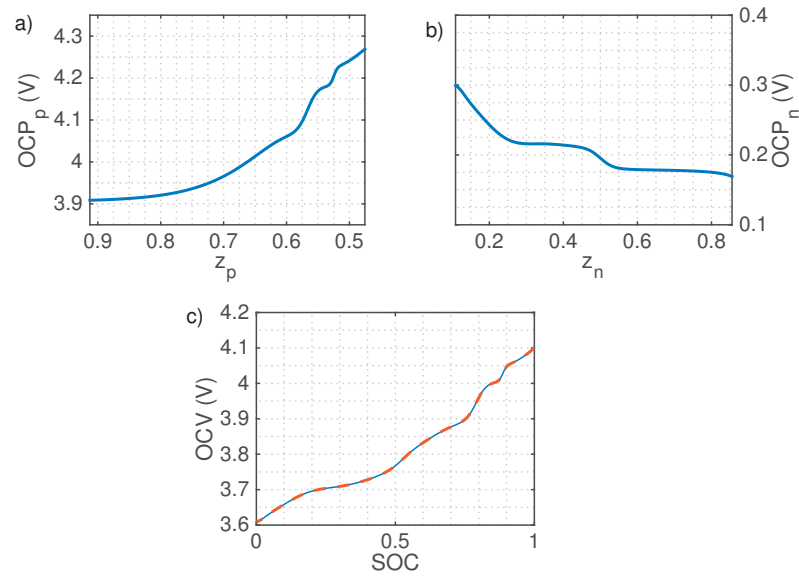
Figure 5.5 – Results of the low rate test for the MCMB-LiCoO$_2$ cell. a) cathode OCP curve, b) anode OCP curve, c) experimental OCV curve (blue) versus OCV curve corresponding to the optimal set of parameters θ_{ocv}^o (dashed red).
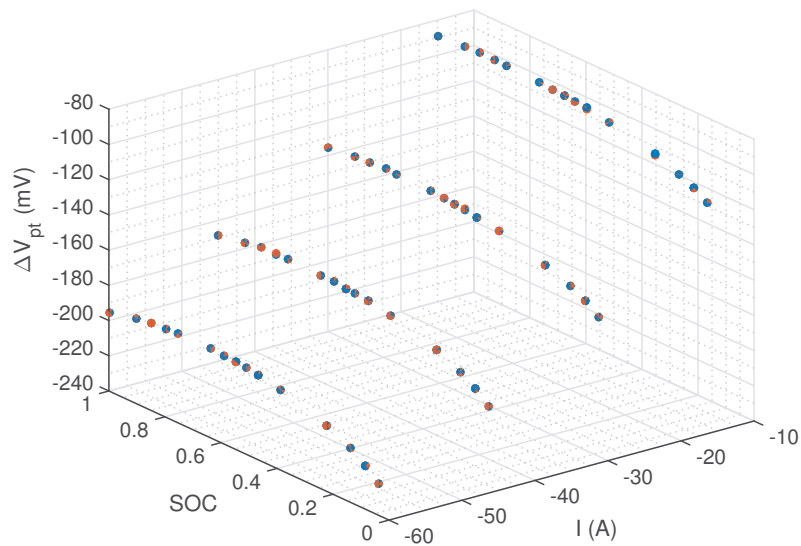
Figure 5.6 – Results of pulse experiments. The blue dots are the values of the istantaneous ΔV_{pt} from the reference model. The red dots are the values of ΔV_{pt} obtained through simulation and with the optimal set of parameters θ_{pt}^o.
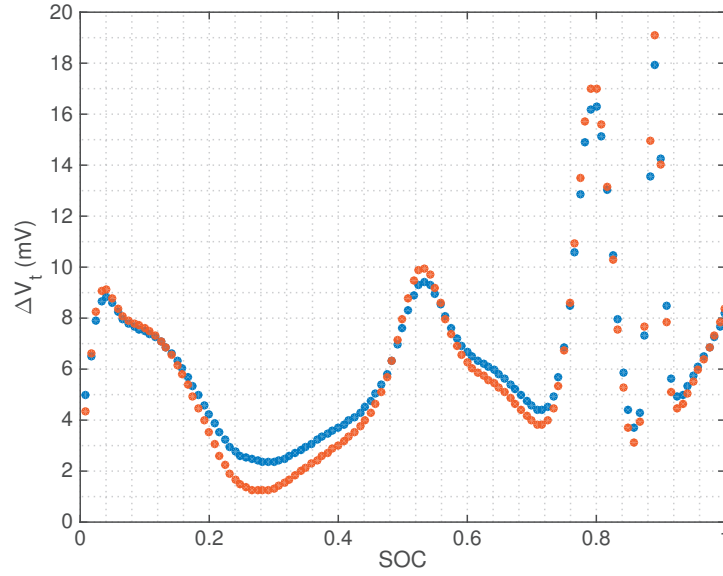
Figure 5.7 – Results of GITT experiments. The blue dots are the ΔV_t experimental values. The red dots are the ΔV_t values obtained through simulation and with the optimal set of parameters θ^o_{GITT}.
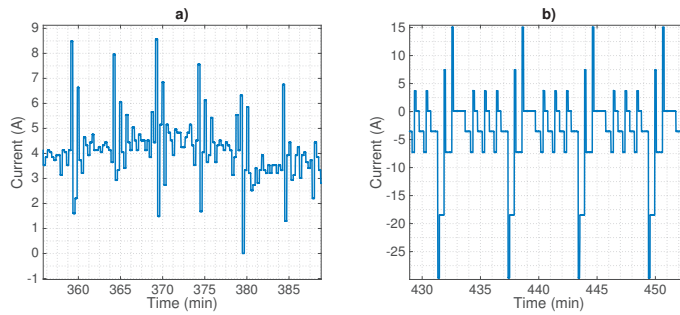
Figure 5.8 – Detail of the experimental current profiles used as validation dataset: a) current profile from a real BESS application [167]; b) cycle composed by a sequence of DST profiles.

the maximum current is 18 A (0.6C). This profile and this value have been determined by scaling down to the cell level the actual current profile during a day of operation of a 560 kWh BESS composed of 8100 cells identical to that used in this study. The BESS has been used to dispatch the operation of a medium voltage feeder [26]. The current profile results in the cell charging with variable current for the first part of the day from a medium to a high SOC and the discharging again to a lower SOC in the second part of the day. A detail of this cycle is shown in Fig. 5.8-a. A second validation cycle has been performed by stressing the cell to a series of DST cycles [35] such that from a condition of SOC = 1 the cell has been discharged untill SOC = 0.1. The maximum current has been chosen equal to 30 A (1C). Fig. 5.8-b shows a detail of the current of this second validation cycle.

The profiles of voltage and internal variables (i.e. the ion surface concentration in the two electrodes) have been compared to those obtained via the reference model for these two
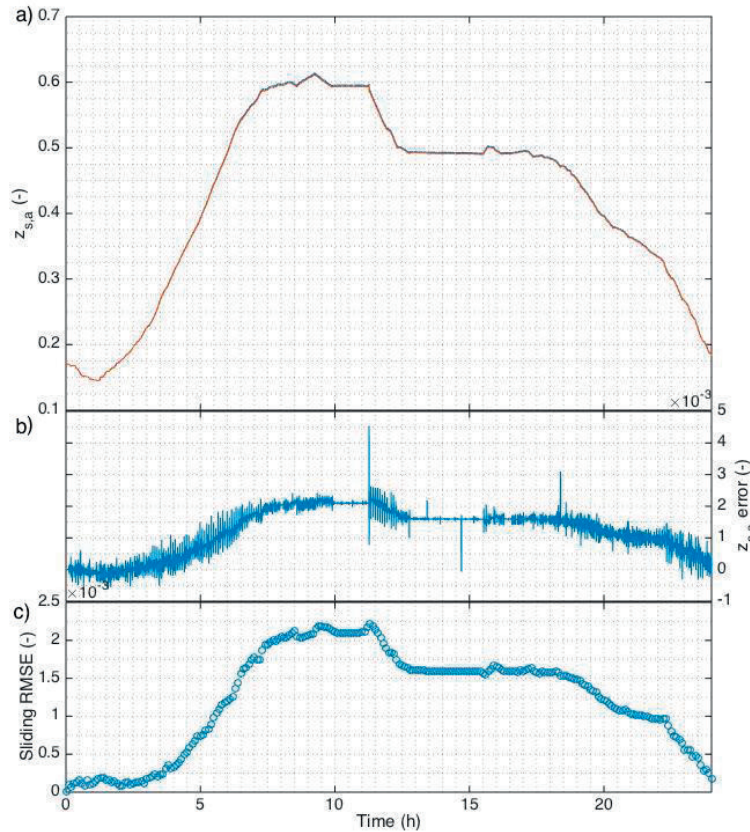
Figure 5.9 – Profiles for the cell submitted to a 24 h current profile from the BESS application of [167]: a) Reference model (red) and SPM (blue) anode surface concentration profiles, b) instantaneous error, c) sliding RMSE.

cycles. Fig. 5.9-a) shows the behaviour of the anode surface concentration for the profile from the power system application for the reference model and for the SPM. Plots 5.9-b) and 5.9-c) show respectively the instantaneous voltage error and the sliding root-mean-square error (sRMSE). The sRMSE is computed as the root-mean-square error (RMSE) of the data over a sliding time window of 6 minutes. The duration of the sliding window is consistent with the duration of a DST cycle and similar results can be obtained for other sliding window lengths. Similar results are obtained for the cathode surface concentration and the output voltage and for these same quantities in the simulation of the DST profile. Fig. 5.10 shows a magnified detail of the curves shown in Fig. 5.9-a. In Table 5.4 the maximum, mean and root-mean-square error (RMSE) for these quantities are reported.

It can be observed that the SPM, identified through the proposed procedure, performs extremely well. The voltage simulated with it presents an RMS error below the 0.4% with respect to the voltage simulated with the reference model. Most importantly, it is worth noting that the RMS error is extremely low also in the case of the surface concentration profiles. These have an RMS error below 0.5% in all cases. This last information is very relevant. In fact, in the
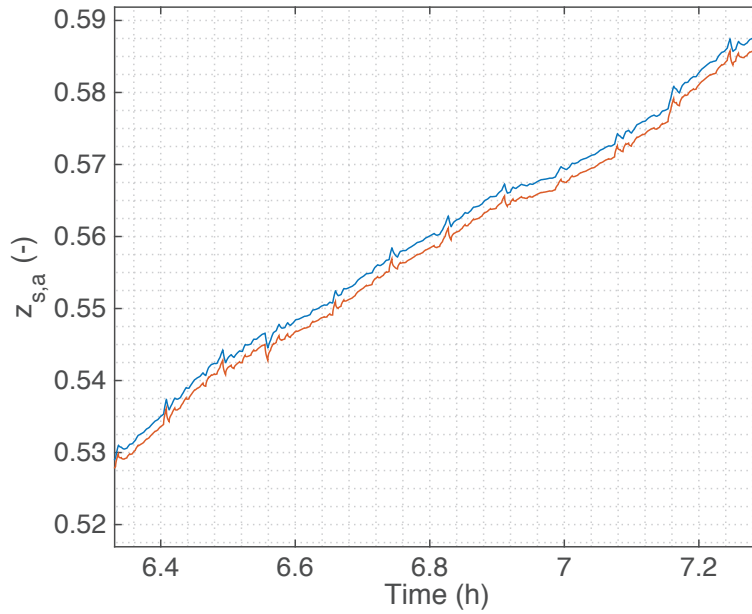
Figure 5.10 – Detail of the anode surface concentration profiles shown in Figure 5.9-a: reference model (red) and SPM (blue).

Table 5.4 – Errors of the SPM with respect to the reference P2D model.

	RMS (%)	Mean (%)	Max (%)
Realistic profile			
V_{cell}	0.11	0.08	0.96
$z_{s,a}$	0.33	0.29	1.09
$z_{s,c}$	0.12	0.10	0.27
DST profile			
V_{cell}	0.37	0.24	1.57
$z_{s,a}$	0.46	0.37	1.61
$z_{s,c}$	0.11	0.09	0.27

case of real Li-ion cells, these quantities cannot be measured. Therefore, it is quite important to know that these can be effectively determined through the reformulated SPM proposed in this Chapter.

5.5 Validation against experimental data

The proposed procedure has then been used to infer the parameters of an SPM of a 30 Ah LTO-NCA cell. The relevant open-circuit potential curves for these two materials can be found in [39, 41, 94]. We describe hereafter the test bench used to perform the identification, then we show the results of the identification itself and finally we show how the model performs in the simulation of realistic charging profiles through the comparison of the simulated voltage profiles with experimental data.

5.5.1 Experimental setup

The experimental test bench is composed of four main elements: (i) a climatic chamber hosting the targeted cells and keeping a constant temperature at 25 °C; in steady state conditions the temperature ripple is of 0.2 °C; (ii) a power source working in the following V/I ranges: 0-80 V, 0-120 A; (iii) an electronic load working in the following V/I ranges: 0-80 V, 0-200 A; (iv) a control PC where a suitable realized software developed using the LabView programming environment is able to perform the monitoring and control of the whole system. The electronic load and the power supply were characterized by an overall bandwidth from DC to 1 kHz. The cell voltage was directly sampled using an analog-to-digital converter operating at a 16-bit resolution with a maximum sampling frequency of 100 kHz and characterized by a bandwidth from DC to 100 kHz (3 dB) with an overall accuracy of 1.5 mV. The cell current was measured using a dedicated Hall-effect sensor characterized by a bandwidth from DC to 100 kHz (3 dB) and an overall accuracy of less than ±0.5% of the measured current. Voltage and current signals are oversampled and averaged in order to increase the resolution of the measurement and increase the signal-to-noise ratio. In particular, the dynamics of these quantities for electrochemical cells are in the range of few Hz and we sample them at 10000 samples/seconds with average over a 100 milliseconds windows. A representation of the experimental test bench is provided in Figure 5.11.

The low-rate test has been carried out at C/20. Since we have experimentally observed that even at very low rates the equilibrium condition is not reached for this cell, the OCV curve has been determined by averaging the two curves obtained through low rate complete CC discharge and low rate complete CC charge. The pulse tests are performed at C/2, 1C, 3/2C and 2C at SOC intervals of 1.5%. The current pulses have a duration of 2 seconds. However, the voltage samples used for the calculation of the experimental values of ΔV_{pt} are those at 100 milliseconds after the occurrence of the current step, i.e. as close as possible to the step compatibly with the experimental test bench described above. Finally, the GITT discharge pulses have a duration of 10 minutes followed by a relaxation time of 20 minutes and a constant current value of 3 A ($C/10$).
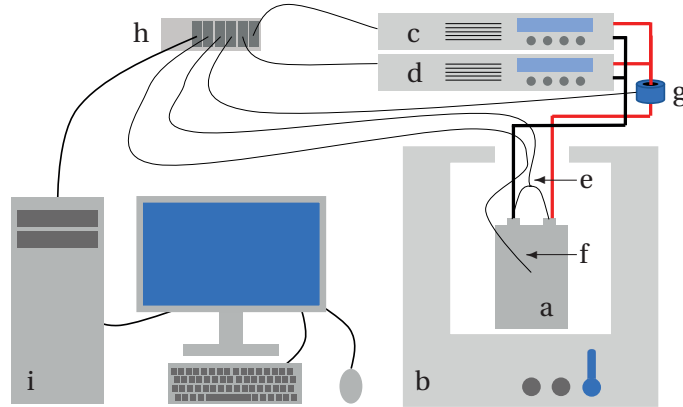
Figure 5.11 – Graphical representation of the test bench used to carry out the experiments described in this chapter: a) cell, b) climatic chamber, c) power supply, d) electronic load, e) voltage sensor, f) temperature sensor, g) current sensor, h) test automation and data acquisition interface, i) desktop PC.

5.5.2 Cycling tests results

The identification procedure described in section 5.3 has been applied to experimental data obtained on a 30 Ah LTO-NCA cell. The resulting parameters are listed in Table 5.5.

Table 5.5 – Parameters identified for the LTO-NCA cell

Parameter	Value
Q_p	$2.266 \cdot 10^5$ C
Q_n	$1.501 \cdot 10^5$ C
k_p^*	$6.23 \cdot 10^{-5}$ s^{-1}
k_n^*	$1.403 \cdot 10^{-3}$ s^{-1}
R_{cell}	$3.048 \cdot 10^{-4}$ Ω
D_p^*	see Eq. 5.23
D_n^*	0.0011 s^{-1}

$$D_p^* = +8.738 \cdot 10^{-5} * [(1+ \\ + \tanh(-74.04 \cdot (z_p - 0.897))) + 1.51 \cdot 10^{-7}] \tag{5.23}$$

Figures 5.12-a and 5.12-b show the cathode and anode OCP curves respectively, obtained with the optimal subset of parameters θ_{ocv}^o. Fig. 5.12-c shows the OCV curve obtained experimentally (blue line) and via the model parametrised with the subset θ_{ocv}^o (dashed red line). The root-mean-square error (RMSE) between the two curves is of 18 mV, the mean error is of 16 mV and the maximum error is in absolute value of 46 mV for a SOC close to zero. It is important to observe how the best fit of the experimental curve is obtained by considering
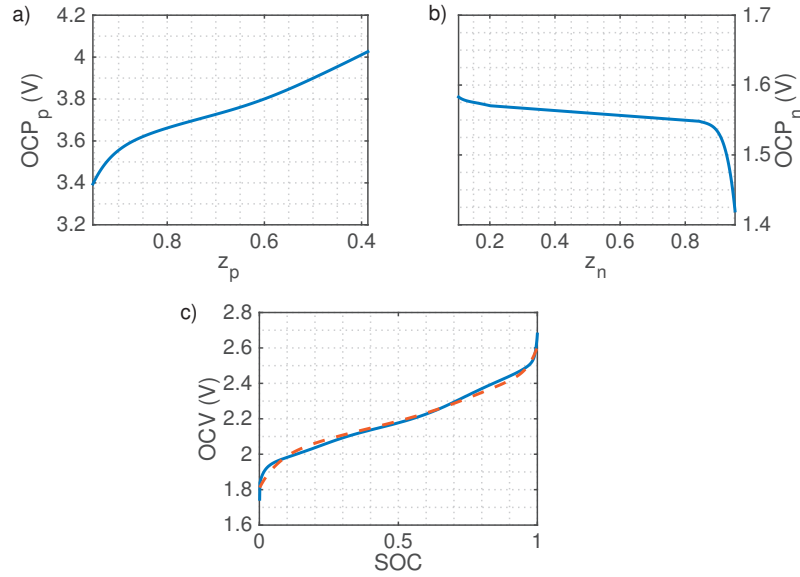
Figure 5.12 – Results of the low rate test for the LTO-NCA cell. a) and b) are the cathode and anode OCP curves respectively. c) Experimental OCV curve (blue) versus OCV curve corresponding to the optimal set of parameters θ_{ocv}^o (dashed red).

a range of the LTO OCP curve including the nonlinear regions for very low and very high ion concentrations (as can be seen in Fig. 5.12-b, for $z_n > 0.8$ and, to a lesser extent, for $z_n < 0.2$). As the LTO OCP curve is almost completely flat in its central part, a precise identification of the subset θ_{ocv} would have been problematic for a cell in which only this flat part of the curve is exploited. Fig. 5.13 shows (in blue) the experimental values of the instantaneous voltage drops obtained submitting the cell to current pulses of different amplitudes and at different SOCs over its complete range. The values of the same voltage drop, calculated through the analytical function in Eq. 5.16 using the optimal set of parameters θ_{pt}^o are shown in red. The root-mean-square error (RMSE) between the two sets of values is of 14.1 mV, the mean error of 2.3 mV and the maximum error in absolute value of 56.2 mV. Fig. 5.14 shows (in blue) the experimental ΔV_t values obtained submitting the cell to GITT cycles at various SOCs over its complete range. The red points represent the same ΔV_t obtained applying Eq. 5.19 and 5.20 with the optimal set of parameters θ_{GITT}^o. The RMSE between the two sets of values is of 4.8 mV, the mean error of 3.3 mV and the maximum error in absolute value of 14.7 mV.

A validation of the SPM and of the identification procedure has finally been carried out through the comparison of experimental and simulated voltage profiles for the cell submitted to the dynamic cycles already described in section 5.4. The experimental and simulated voltage profiles for these two validation cycles are shown respectively in Fig. 5.15 and 5.17. The plot a) shows experimental data in blue and the simulated voltage profile in red, plots b) shows the instantaneous voltage error and plot c) the sRMSE, as defined in section 5.4. Figures 5.16 and 5.18 show a magnified detail of the measured and simulated voltages, again in blue and red respectively. In the case of the realistic profile for a BESS application, the root-mean-square and maximum error for a period of 24 h are respectively 12 mV (0.78% in relative terms) and of
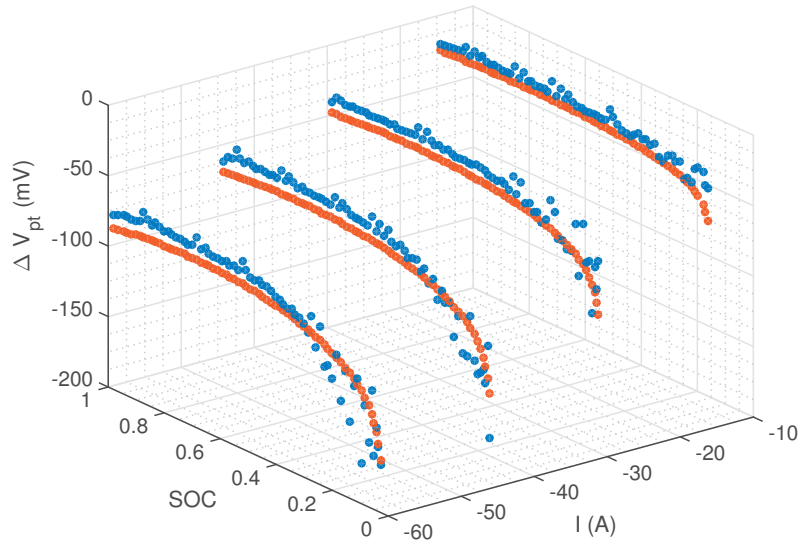
Figure 5.13 – Results of pulse experiments. The blue dots are the instantaneous ΔV_{pt} obtained experimentally. The red dots are the values of ΔV_{pt} obtained through simulation and with the optimal set of parameters.

35 mV (1.8%). In the case of the discharge through DST cycling, the root-mean-square and maximum errors are 11 mV (0.73%) and 45 mV (2.3%). Table 5.6 reports the root-mean-square, mean and maximum error in the voltage prediction for these two profiles and for the profile obtained through the GITT experiment. The validation of the SOC provided by the model

Table 5.6 – Errors of the model in voltage simulation

Experiment	RMS (%)	Mean (%)	Max (%)
GITT profile	0.38	0.19	1.54
realistic profile	0.78	0.34	1.84
DST cycling	0.73	0.41	2.28

has been performed against the SOC value computed through the integration of the current. Fig. 5.19 shows such validation performed with data from the DST cycle. It can be seen that the values given by the model match closely the SOC values provided by the integration. The maximum discrepancy is found at SOC = 0.1 and is of 1.91%.

5.6   Conclusive remarks

Chapter 4 discussed the potential advantages and the challenges of integrating advanced physics-based models in the control of BESSs. This chapter proposes an approach to address the second of these challenges, i.e. the parameter identification of Li-ion cell physics-based models.

Notably, it proposes a methodology to identify the parameters of a SPM and demonstrated
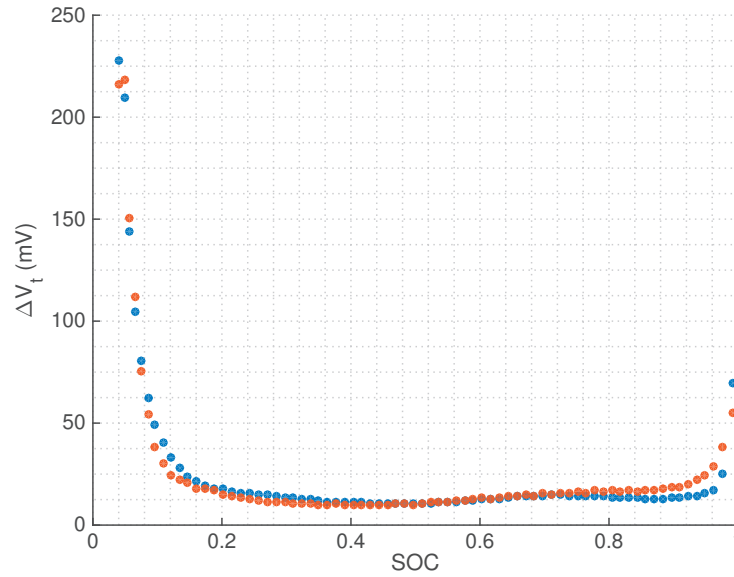
Figure 5.14 – Results of GITT experiments. The blue dots are the ΔV_t experimental values. The red dots are the ΔV_t values obtained through simulation and with the optimal set of parameters.

its effectiveness by applying it to a reference model as well as to a 30 Ah Lithium-titanate cell. The proposed methodology relies solely on a set of cycling experiments, that can be carried out with the standard equipment of an electrical engineering laboratory. It does not require cell tear-down, specific equipment for electrochemical testing nor in-depth knowledge and skills in chemistry.

The proposed procedure can successfully identify the parameters of an SPM. The identified model achieves voltage RMSEs below 0.5% and 0.75% with respect to a reference model and to experimental data respectively. Considering its relative simplicity and its experimental validation, this method is possibly an important contribution to the efforts aiming at integrating advanced Li-ion cell models in the control of BESSs.
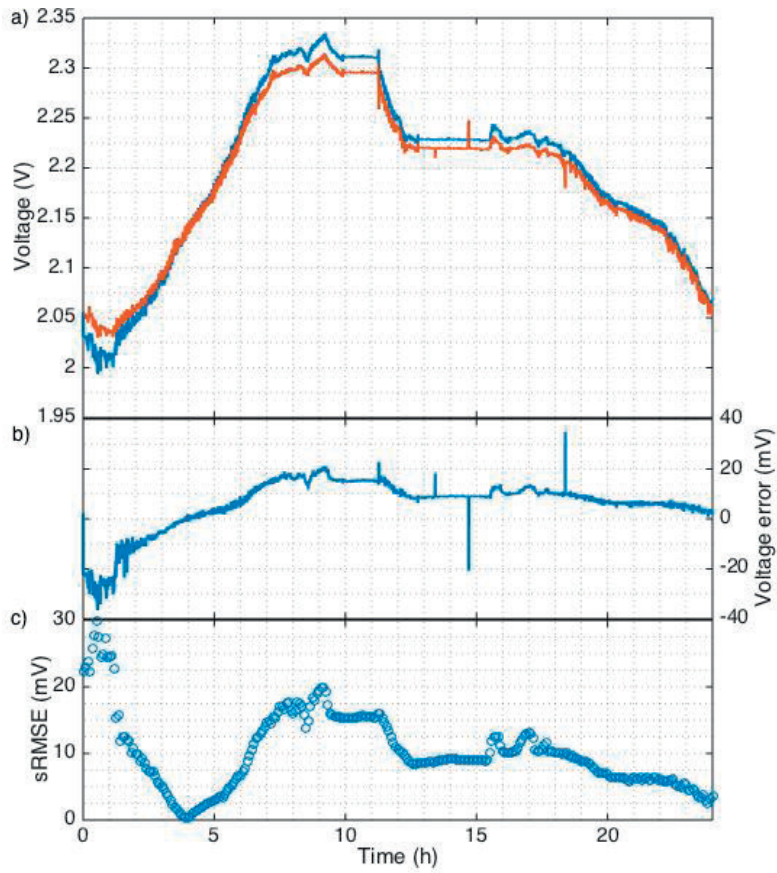
Figure 5.15 – Profiles for the cell submitted to a current profile from a BESS application: a) Experimental (red) and simulated (blue) voltage, b) instantaneous voltage error, c) sRMSE.
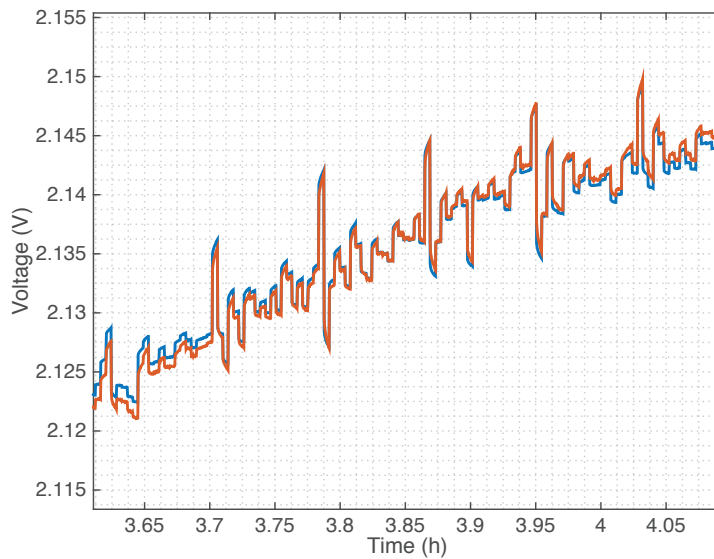
Figure 5.16 – Detail of the Experimental (red) and simulated (blue) voltage profiles shown in Figure 5.15.
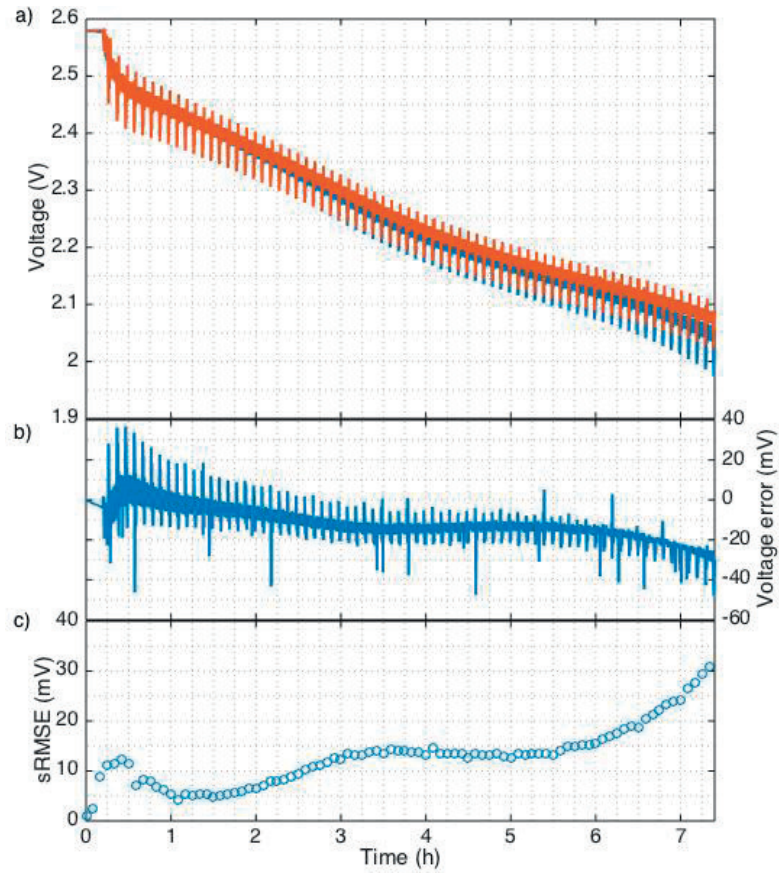
Figure 5.17 – Profiles for the cell submitted to a train of DST cycles: a) Experimental (red) and simulated (blue) voltages, b) instantaneous voltage error, c) sRMSE.
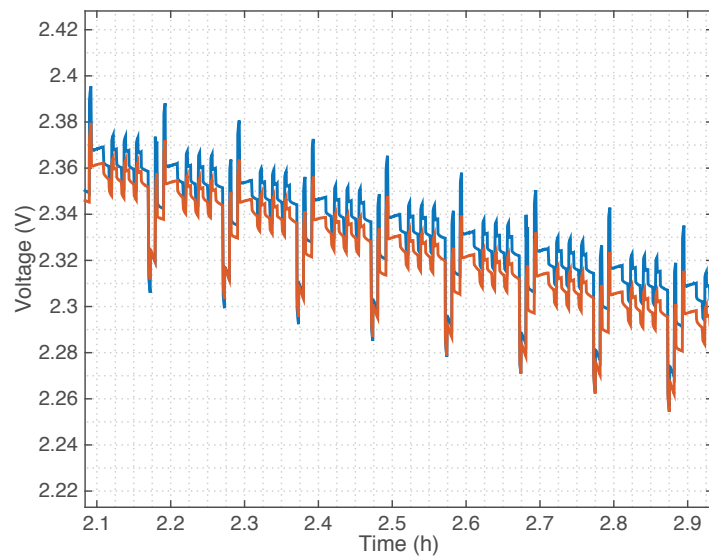
Figure 5.18 – Detail of the Experimental (red) and simulated (blue) voltage profiles shown in Figure 5.17.
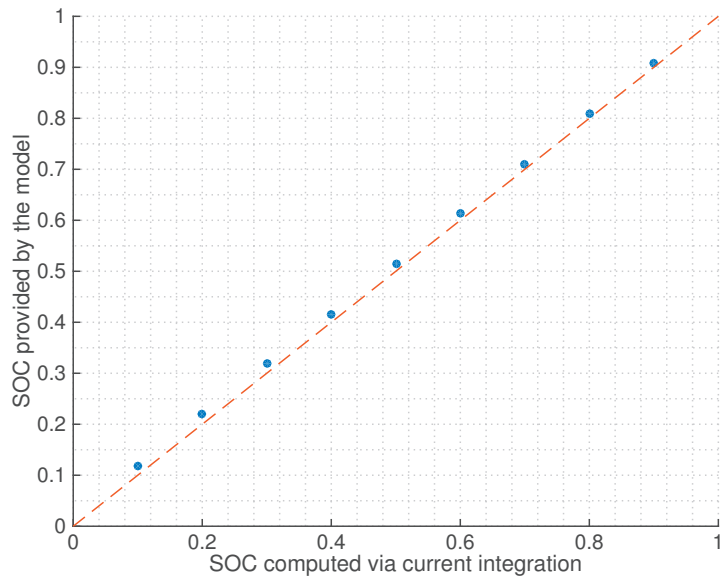
Figure 5.19 – Comparison of the SOC computed through the model equations (y axis), with the SOC computed through current integration (x axis), (the red dashed line has slope equal to one).

6 Predictive control of a BESS using a single particle model

This chapter describes the integration of an advanced Li-ion cell model into the real-time control of a BESS. This is the real-time control stage of the framework described in Chapter 1. It is based on model predictive control and relies -in its original formulation- on an equivalent circuit model. This chapter proposes to substitute the latter with a single particle model. It describes the formulation developed to achieve this goal. Then, it assesses the differences in the performances obtained using these two battery models in the real-time phase of the control of a BESS dispatching the operation of an active distribution feeder.

6.1 Recall to the previous chapters

This chapter aims, essentially, to demonstrate some of the advantages of integrating advanced models in the control of BESSs, discussed in Chapter 4. To this end, we first recall few fundamental concepts about the SPM (extensively described in Chapter 5), and about the MPC framework for the real-time control of a BESS introduced in Chapter 1 of this thesis.

6.1.1 The single particle model

The model used in this Chapter is the so-called single particle model (SPM), extensively described in Chapter 5 and based on [67]. The SPM describes the intercalation dynamics of a Lithium ion cell and its charge transfer phenomena. The two electrodes of a Li-ion cell are modeled by two spherical particles. The model structure and the relevant phenomena occurring within the cell and modeled by a SPM are represented in Fig. 5.1. The modeled physical phenomena (and in parentheses the respective contribution to external voltage) are: i) the mass transfer (i.e. the diffusion of Lithium ions) within anode active material (anode equilibrium potential); ii) the charge transfer at the electrode electrolyte interface (anode charge transfer polarization); iii) the ionic conduction in the electrolyte (ohmic voltage drop); iv) the charge transfer at the electrode electrolyte interface (cathode charge transfer polarization); v) the mass transfer within cathode active material (cathode equilibrium potential).

We report here the governing equations for the diffusion processes in the two electrodes and the equation describing the cell voltage. Let the subscript $i = p, n$ denote the electrode (p and n respectively refers to the positive and negative), c_i denote the ion concentration within the single particle as a function of time t and radial coordinate r, D_i denote the diffusion coefficient of the electrode, S_i denote the electrode total active surface and R_i denote the radius of the particles composing the active material. Finally, I_{app} is the current applied to the cell, and F is the Faraday constant. The diffusion within the electrode active material is modeled through two radial partial differential equations:

$$\frac{\partial c_i(r,t)}{\partial t} = \frac{D_i}{r^2}\frac{\partial}{\partial r}\left(r^2\frac{\partial c_i(r,t)}{\partial r}\right) \tag{6.1}$$

with boundary conditions:

$$D_i\frac{\partial c_i(r,t)}{\partial r}\Big|_{r=0} = 0, \qquad D_i\frac{\partial c_i(r,t)}{\partial r}\Big|_{r=R_i} = \frac{I_{app}}{FS_i}, \tag{6.2}$$

These equations define the concentration of Lithium ions within the two electrodes. The external voltage of the cell V_{cell} is then computed as a sum of several terms:

$$\begin{aligned} V_{cell} = &+ U_p(c_p|_{r=R_p}) + \eta_p(I_{app}, c_p|_{r=R_p}) \\ &- U_n(c_n|_{r=R_n}) + \eta_n(I_{app}, c_n|_{r=R_n}) \\ &+ I_{app}R_{cell}. \end{aligned} \tag{6.3}$$

U_p and U_n are the open circuit potential (OCP) of the cathode and anode, respectively, and are functions of the ion concentrations. η_p and η_n are the overpotentials due to the charge transfer in the cathode and anode respectively and are given by algebraic functions of the applied current and of the ion concentrations (5.5)-(5.6). $I_{app}R_{cell}$ describes the ohmic losses in the electrolyte. The equations and their terms are described in detail in Section 5.1.

6.1.2   The real-time control of a BESS via model predictive control

We consider the problem described in Section 1.4.2 of this thesis. It consists in controlling a BESS with the objective of achieving an assigned energy throughput in a given time horizon. This is a common application in the context of BESS energy management, see for example [2, 109]. Remarkably, by taking advantage of the fact that the objective is achieving an integral quantity, one could think of implementing a MPC algorithm. MPC consists in determining the control action for a given system by solving at each time step an optimization problem with updated information, where the system constraints are enforced by implementing prediction models in the optimization problem. In the case of the BESS considered here, the algorithm consists in determining an optimal current trajectory that, within the available time horizon, satisfy the control objective while obeying to constraints imposed by the battery model.

6.2 The integration of the SPM in the MPC algorithm

BESS operational limits are enforced in the MPC by the SPM model described in Section 6.1.1. The following two subsections describe how the SPM is linearized in order to be casted in the MPC optimization problem, and the resulting physics-based MPC formulation.

6.2.1 Reformulation of the SPM

For the integration in such context, the SPM is linearized and expressed as the following state-space form:

$$x_{k+1} = Ax_k + Bu_k \tag{6.4}$$
$$y_{k+1} = Cx_{k+1} + Du_k \tag{6.5}$$

The state vector x_k is composed by the ion concentration profiles in the two electrodes, c_n and c_p, provided by the diffusion equations and by the electrode overpotential values η_n and η_p. The input u_k is the current applied to the cell I_{app}, and the output y_k is the cell voltage V_{cell}. With regard to the SPM equations, diffusion PDEs in (6.1) are discretized through a forward Euler scheme. The resulting discrete equations are linear and provide the ion concentrations in the electrodes at each time step and at equally spaced positions along the particle radial coordinate r. The electrode overpotentials η_n and η_p and the external voltage are nonlinear algebraic functions of the applied current I_{app} and the c_n and c_p values in the two electrodes at $r = R$ (see (6.3)). These functions are therefore linearized with a first-order Taylor approximation around the operating point at each time step, i.e. at each time step the system matrices of (6.4)-(6.5) are recomputed on the basis of the last known values of the SPM states.

6.2.2 MPC Formulation

We consider a MPC to achieve an assigned energy throughput in a available time horizon. Let $(1, 2, \ldots, \overline{k})$ be the time horizon (of length $\overline{k}$ and discretized at T_s seconds) for which the control trajectory is to determine, $k = 1, \ldots, \overline{k}$ rolling index denoting the current time interval, e_k the reference BESS energy throughput to achieve by the end of the time window, and $\boldsymbol{i}_{k|k} = (i_{k|k}, i_{k+1|k}, \ldots, i_{\overline{k}|k})$ sequence of BESS current values considered at time k. At time k, the optimization problem underlying the adopted MPC is given by seeking the current profile to minimize the distance between the battery energy throughput and its reference tracking error at the end of the control horizon, while subject to constraints on the current magnitude and concentration. Formally, it is:

$$\boldsymbol{i}_{k|k}^o = \arg\min_{\boldsymbol{i}_{k|k} \in \mathbb{R}^{(\overline{k}-k)}} \left\{ \left(\sum_{j=k}^{\overline{k}} (P_{j|k}) - e_k \right)^2 \right\} \tag{6.6}$$

subject to

$$P_{j|k} = v_{j|k} \cdot i_{j|k}, \qquad\qquad\qquad j = k,\dots,\overline{k} \qquad\qquad (6.7)$$

$$\boldsymbol{v}_{k|k} = f(x_{k|k}, \boldsymbol{i}_{k|k}) \qquad\qquad\qquad\qquad\qquad\qquad (6.8)$$

$$\boldsymbol{x}_{k|k} = g(x_{k|k}, \boldsymbol{i}_{k|k}) \qquad\qquad\qquad\qquad\qquad\qquad (6.9)$$

$$c_{i,j|k} \subset x_{j|k} \qquad\qquad\qquad\qquad j = k,\dots,\overline{k} \qquad\qquad (6.10)$$

$$\eta_{i,j|k} \subset x_{j|k} \qquad\qquad\qquad\qquad j = k,\dots,\overline{k} \qquad\qquad (6.11)$$

$$c_{i,min} \le c_{i,j|k} \le c_{i,max} \qquad\qquad\quad j = k,\dots,\overline{k} \qquad\qquad (6.12)$$

$$\eta_{i,min} \le \eta_{i,j|k} \le \eta_{i,max} \qquad\qquad j = k,\dots,\overline{k}. \qquad\qquad (6.13)$$

Eq. (6.7) states that the BESS power output $P_{j|k}$ is the product between voltage $v_{j|k}$ and current $i_{j|k}$. Eq. (6.8) corresponds to the BESS voltage linearized model and, together with (6.9) composes the linearized state-space SPM. Equations (6.10) and (6.11) simply denote that the ion concentrations and the overpotentials in the electrodes are extracted as subsets of the state vector. Finally, (6.12) and (6.13) constrain concentrations and the overpotentials in the allowed ranges, denoted by $(c_{i,min}, c_{i,max})$ and $(\eta_{i,min}, \eta_{i,max})$[1]. The former is imposed to avoid oversaturation or depletion of Lithium in the active material of the two electrodes, while the latter bounds the overpotentials in each electrode, since excessive values would lead to the occurrence of degradation. At each step k, the optimization problem is solved on a shrinking horizon k to $\overline{k}$ and only the first portion of the optimal control $\boldsymbol{i}_{k|k}^o$ law is actuated. The computation of the evolution of the state vector requires the knowledge on the full state, which is reconstructed by applying a Kalman filter by using the measurements of the BESS DC voltage.

6.3   Simulation setup

We consider a setup where a BESS is required to compensate for the mismatch between a dispatch plan at 5 minute resolution and the realization of a group of stochastic prosumers. The tracking problem is performed with the MPC described in Section 1.4.2, which is augmented with the electrochemical predictive constraints (6.12)-(6.13). The mismatch enters in the problem as the input variable e_k, $\overline{k} = 5$ min and $T_s = 10$ s. The considered BESS is a 560 kWh unit, modelled as composed of $N_p = 18$ parallel branches, each with $N_s = 300$ Li-ion cells in series. These are 30 Ah MCMB-LiCoO$_2$ cells[2], with operating voltage between 3.6 and 4.1 V. At this stage, we assume that all the cells are balanced and have same physical properties[3]. For such setup, and for each scenario detailed in the following sections, we perform two simulations. The first is based on an MPC in which the constrained quantities are

---

[1]We recall than in Eqs. (6.10) to (6.13) the first index in the subscript is $i = n, p$, denoting the negative and positive electrodes of the cell.

[2]These cells have been preferred to the LTO cells composing the actual EPFL BESS, because for the former all the parameters for both the SPM and the reference P2D model are available in [118].

[3]This allows to define the BESS voltage v and BESS current i as $v = V_{cell} * N_s$ and $i = I_{app} * N_p$, respectively.

the cell output voltage and current. In the second, we constrain the ion concentrations and electrode overpotentials instead. In both cases the prediction of the constrained quantities is based on the SPM described in section 6.1.1[4]. In both cases, at each simulation time step, the following actions are performed: *i)* a SPM-based Kalman filter reconstructs the state starting from measured current and voltage values, *ii)* based on the full knowledge of the state, the MPC optimization problem is solved and the first portion of the computed control action is chosen for being actuated, *iii)* BESS behavior as a function of the actuated current set-point is simulated through a detailed electrochemical model (described in [118]) at 500 ms resolution. The cell parameters of both the SPM used in the control and the detailed cell model used to simulated the battery behavior are from the literature [118].

6.4 Results

6.4.1 Qualitative observation of the increased operational domain

In order to achieve a fair comparison between concentration and voltage limits, these have been selected in the following way. Concentration limits $c_{n,min}$, $c_{n,max}$, $c_{p,min}$ and $c_{p,max}$ are given as parameters of the model, i.e. they are the maximum and minimum Lithium stoichiometry achievable in the electrodes. Voltage limits V_{max} and V_{min} are chosen to be equal to the open circuit voltages in correspondance of the extreme concentration conditions. Formally, it is $V_{min} = V_{oc}(c_{n,min}, c_{p,max})$ and $V_{max} = V_{oc}(c_{n,max}, c_{p,min})$. This is because the relation between voltage and concentrations is not time-invariant. The selected voltage limits are chosen so that concentration limits (where the concentration is the quantity that we *really* want to constrain) are not violated in any condition, i.e. for any shape of input current profile. For a fast charge, for example, the instantaneous voltage will be higher than the open circuit voltage of the cell corresponding to a given set of concentrations. Thus, a voltage limit will be conservative compared to the concentration limits. For a very slow charge, the instantaneous voltage will be almost equal to the open circuit voltage and the voltage limit will represent well the cell concentration limitations.

Figure 6.1 is useful to understand this relationship. It shows the current, voltage and anode surface ion concentration in a trivial scenario in which the controller requires the cell to be charged as much as possible at a constant current rate. Red lines refer to the case in which, in the MPC problem formulation, voltage and current are constrained. A constant-current charge is interrupted at t' and a constant-voltage charge takes place. The blue lines refer to the case in which concentrations and overpotentials are constrained. The constant-current charge can therefore continue even for voltages that are higher than the threshold

---

[4]The quantities constrained in the conventional MPC (voltage and current), can be predicted both via equivalent circuit and electrochemical models. In this Chapter, we use an SPM, so that the conventional MPC and the physics-based control are based on models having exactly the same prediction performances so that the comparison between the two results is "fair". It is understood that since equivalent circuit models allow only for the conventional MPC, the proposed comparison implicitly compares the usefulness of equivalent circuit and electrochemical models

135
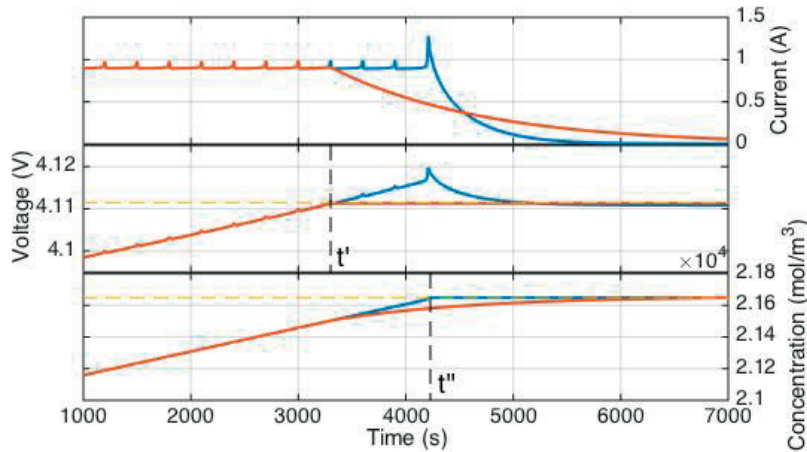
Figure 6.1 – Battery charge with a fixed power set-point. **Top:** cell current, **middle:** cell voltage, **bottom:** anode surface ion concentration. The red lines refer to an MPC based on I-V limits, the blue lines refer to a physics-based MPC. The yellow dashed lines in the middle and bottom plots represent the tresholds for the voltage and anode concentration respectively.

of the previous case, as concentration limits are not violated. When these are reached, at t'', a constant-concentration charge takes place. It can be seen, the constant voltage and constant concentration charges lead to the same cell state for long charging times. The current decreases and the charge continues closer and closer to an equilibrium condition, at which the two limits coincide. Nevertheless, it is also evident that in the case where the constrained quantities are the concentrations rather than the voltage, the constant-current charge can continue longer. This is an actual improvement in the cell performances, since the range in which the cell can provide the desired current is expanded.

6.4.2   Increased performance in the charge of the BESS

We first run a set of simulations such the one in Fig. 6.1 for a set of power values, in order to assess the performances of the new control paradigm at various power rates. For any power setpoint we run both a simulation using an MPC based on current and voltage (I-V) limits and one based on the electrochemical constraints defined above. For each couple of simulations the metrics chosen to perform the comparison are the following: *i)* ΔT: the delay, in minutes, between the constraint activation in the case of physics-based control and in the case of MPC based on I-V limits; *ii)* ΔE: the increase the energy delivered at the desired power (i.e. in unconstrained operation), with respect to the cell nominal capacity; *iii)* oV: the cell overvoltage in mV, reached in the case of physics-based control, with respect to the corresponding case with traditional control; *iv)* C_ratio: anode surface ion concentration reached at constraint activation with traditional I-V limits (relative to the case of physics-based control). Table 6.1 shows the results of such simulations for a set of charge values. For all power rates, the constraints of the physics-based control problem are activated considerably later than in the case of traditional I-V limits. The energy delivered at the desired power rate,

therefore, is greater for the case of physics based control. The difference between the two cases is low/negligible at low power rates (e.g. it is just above 2% at 0.1 p.u.) but becomes quite important at higher power rates, being of more than the 20% at 1 p.u. of power. It can also be observed that constraining concentration levels rather than the output voltage results in oV values of magnitude increasing with the power rate. On the contrary the control based on I-V constraints results in an anode surface concentration reached at constraint activation lower than in the case of physics based control. This corresponds to a sub-optimal operation of the BESS, and it can be observed that this effect increases with higher power rates (as shown by the decreasing values of C_ratio).

Table 6.1 – Comparison metrics for BESS charge

Power (p.u.)	ΔT (min)	ΔE (%)	oV (mV)	C_ratio
0.01	10.2	0.12	1.07	1
0.02	14.8	0.41	2.67	1
0.04	15.5	1.03	5.91	0.99
0.06	15	1.3	8.67	0.99
0.08	15.5	2	12.29	0.99
0.1	15.3	2.43	14.84	0.98
0.15	14.8	3.59	18.44	0.98
0.2	14.2	3.63	22.68	0.97
0.3	15	7.24	35.37	0.95
0.4	17.7	11.03	47.54	0.92
1	10	20.64	81.54	0.9

6.4.3   Results in a representative day of operation

Finally, we simulate a realistic daily scenario of BESS operation, considering the application described in Chapter 1. The MPC control framework with I-V limits has been used to control a grid-connected BESS in order to dispatch the operation of a distribution feeder according to a trajectory with 5 minutes resolution, established the day before the operation. The data used for this simulation are from the operation of the 15th of January 2016. In such day, the tracking of the objective dispatch plan failed due to the BESS hitting its upper voltage limits.

We show in this section the results obtained simulating the operation of the BESS, controlled via an MPC in which classical I-V limits are implemented and one based on a physics-based control. Notably, Fig. 6.2 shows the tracking performances of the two MPCs. Both achieve perfect tracking for most of the analysed day. Nevertheless, due to considerable charing demand in the first part of the day, around midday both control approaches fail in their objective. Table 6.2 shows the performances relative to the two constrained control implementations. We observe that, while the BESS fails to track the dispatch plan along the whole day in both cases, in the case of physics-based control the time interval during which the tracking objective is not respected decreases. Most importantly, the cumulated tracking error along the day decreases considerably (of about the 35%), i.e. even when the tracking fails, the tracking error

Table 6.2 – Comparison of the two control approaches for a day of operation

I-V limits		
Tracking fails during:	21	min
Cumulated tracking error:	17.88	kWh
Physics-based control		
Tracking fails during:	18	min
Cumulated tracking error:	11.59	kWh
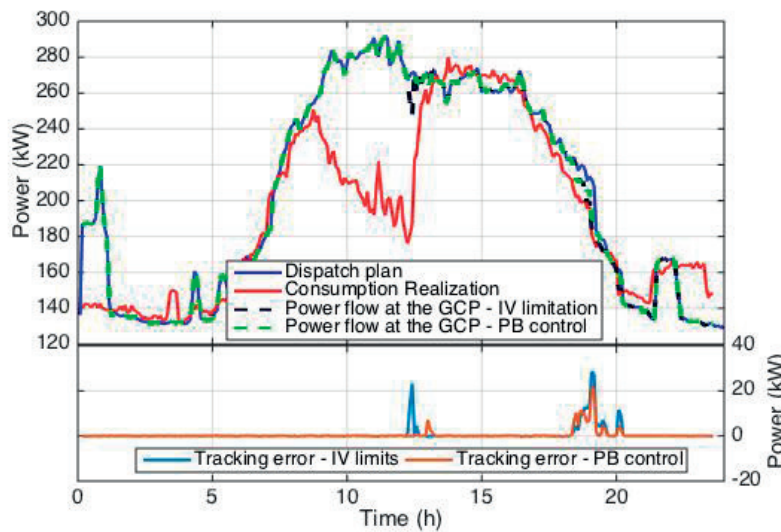
Figure 6.2 – **Top:** 5-minutes resolution profiles of reference power profile, power realization and corrected power profile (both conventional and physics-based MPC). **Bottom:** Tracking error.

achieved by the physics based control is reduced. Fig. 6.3 shows in the first two panels the simulated current and voltage profiles during 24 hours of operation (for the case of physics-based MPC). In the third panel of Fig. 6.3 it is shown the voltage prediction error. It can be seen that the SPM achieves a good performance in voltage prediction, with a relative maximum error well below 0.5%. Summarizing, Table 6.2 shows how, for a real-world BESS application and a realistic scenario, physics-based control can achieve better performances compared to standard approaches. The advantage of the proposed approach is particularly important for higher power rates (as shown in Table 6.1) which may provide a considerable advantage in high-power BESS applications.

6.4.4 Assessment of BESS ageing due to solid-electrolyte interphase (SEI) formation

Fig. 6.4 shows, in the top panel, the profile of the ion concentration on the surface of the anode particle together with its respective constraints, and, in the bottom panel, the current
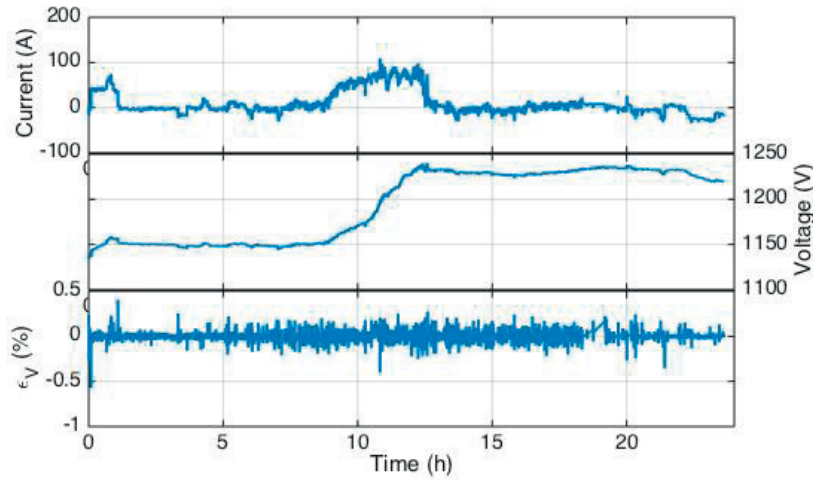
Figure 6.3 – **Top:** BESS current profile simulated through the detailed electrochemical model. **Middle:** BESS simulated voltage profile. **Bottom:** One-step-ahead prediction error of the voltage predicted through the SPM.

density of the side reaction leading to SEI formation. The latter has been calculated based on the quantities estimated through the SPM and by implementing the model in [151]. This is of definite importance because it allows for the inclusion in the MPC of anti-ageing policies based on the accurate and explicit modelling of degradation phenomena. Knowledge of ion concentrations and potentials within the cells, besides allowing for their direct limitation, allows to limit explicitly the magnitude of side reactions that induce capacity fade and increase in the equivalent series resistance. The magnitude of these side reactions is in fact dependent on the values of the internal states provided by the physics-based model. Therefore leaning on a physics-based model, one can as well integrate explicit models of these side reaction, rather than relying on heuristic approaches to limit degradation. As an example, we discuss hereafter SEI formation, which is one of the most common of such degradation mechanisms.

SEI formation consists in the irreversible consumption of cyclable Lithium via a side reaction between Lithium and solvent species present in the electrolyte. This takes place at the surface of the anode active material particles and form compounds such as Li_2CO_3, LiF, Li_2O depending on the nature of the solvent. In general, referring to the solvent with S and to the side reaction byproduct with P, this irreversible side reaction can be generalized as $S + 2Li^+ + 2e^- \rightarrow P$. Besides the consumption of Li^+ ions (and the correspondent reduction of the cell capacity), the inert byproduct P accumulates in the so-called SEI layer, increasing the overall resistance of the the cell (i.e. degrading the cell capability to provide high power values). This mechanism is common to most Li-ion cell chemistries and has been widely studied [7], [150]. Reference [151] proposes the formulation of a reduced order model for the SEI formation process. The current density of the side reaction j_{SEI} is provided by a non-linear function of the anode intercalation current j_n^{Li} and of the negative electrode equilibrium potential U_n. In the SPM the intercalation current j_n^{Li} is proportional to the cell current I_{app} and

139
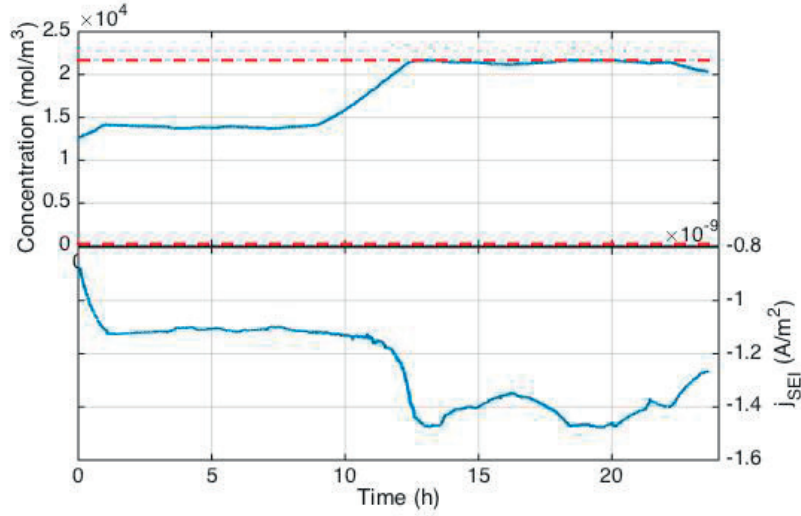
Figure 6.4 – **Top:** Profile of the ion concentration at the anode particle surface (blue line) and its boundaries (red dashed lines). **Bottom:** Profile of the current density of the parasitic reaction leading to SEI formation.

the negative equilibrium potential U_n is a function of anode surface concentration $c_n|_{r=R_n}$. Therefore, via the SPM and the proposed control framework, it is possible to formulate a constraint to j_{SEI} to remain below a desired treshold. Formally, j_{SEI} is formulated as the following non-linear function of $c_n|_{r=R_n}$ and I_{app}:

$$j_{SEI} = \frac{AB + A\sqrt{(B^2 + (1-2CA))}}{(1-2CA)} \tag{6.14}$$

with:

$$A = -i_{0,s}a_n \exp\left(\frac{F(U_s^{ref} - U_n(c_n|_{r=R_n}))}{2RT}\right) \tag{6.15}$$

$$B = -\frac{I_{app}}{2i_0 a_n V} \tag{6.16}$$

$$C = \frac{F}{2i_0 a_n}. \tag{6.17}$$

All but two parameters for this side reaction model are already defined for the cell SPM. As mentioned, U_n is an empirical non-linear function of $c_n|_{r=R_n}$. i_0 is the exchange current density, defined as in (4.5) and whose formulation is used in the SPM in the denominator of (5.6). Both U_n and i_0 are functions of $c_n|_{r=R_n}$, which is obtained by solving the anode radial diffusion PDE in (6.1). a_n and V are respectively the specific surface area of the anode and its volume. The two parameters specific to the degradation model are the equilibrium potential of the side reaction U_s^{ref} and the exchange current density for the side reaction $i_{0,s}$. In this Section, the first is set $U_s^{ref} = 0.4\ V$, as commonly done in the literature for this
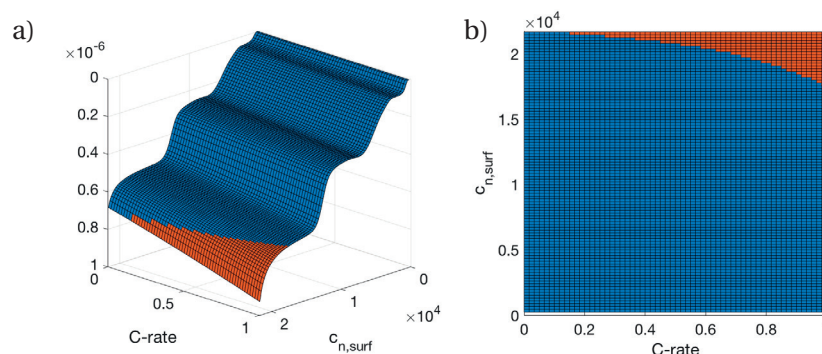
Figure 6.5 – SEI formation current density (mA/cm^3)

specific side reaction [16, 150]. The latter is set equal to $4 \cdot 10^{-11} \ A \cdot m^{-2}$. This value has been determined assuming SEI formation as the only degradation mechanism for a Li-ion cell capable to perform 3500 cycles at 1C before having the 20% of its capacity depleted. Figure 6.5 shows the magnitude of the side reaction current density j_{SEI} as a function of the C-rate (i.e. the cell input current I_{app}, divided by the cell nominal current) and $c_n|_{r=R_n}$. In order to be able to achieve a determined number of cycles before the BESS end of life, a threshold can be imposed to j_{SEI}. In the case represented in Figure 6.5 this is arbitrarily set to $7 \cdot 10^{-7} \ mA/cm^3$[5]. Values of j_{SEI} above this threshold are represented in blue, while values below are in red. Figure 6.5-a provides a 3-D plot, while Figure 6.5-b is a projection, orthogonal to the C-rate and $c_n|_{r=R_n}$ axes, of the same data. It has the purpose of showing more clearly the C-rate and $c_n|_{r=R_n}$ values that cause j_{SEI} to exceed the threshold. It is evident that the most detrimental operating condition for the cell is the simultaneous occurrence of high values of $c_n|_{r=R_n}$ and high C-rates.

The mapping shown in Figure 6.5 allows for an effective yet simple implementation of a set of linear constraints limiting SEI formation. By approximating the boundary between the "acceptable" domain (the blue one) and the "unacceptable" (red) one via a set of $l = 1, \ldots, L$ lines, it is possible to formulate a set of constraints as:

$$c_{n,j|k} + m_l i_{k|k} \leq Q_l \tag{6.18}$$

where m_l and Q_l are coefficients of the boundary L lines found from Fig. 6.5-b[6]. Relying on this same model, it is also possible to bound the overall loss of cyclable lithium over a given timespan, rather than the instantaneous value of the side reaction current density j_{SEI}. This quantity is proportional to the integral of j_{SEI} over the considered period [151]. In this case, a

---

[5]This value has been chosen for demonstrative purposes and different values may be determined based on the lifetime objective of the control.

[6]In Eqs. (6.18) and (6.19), it is implied that $c_{n,j|k}$ is the concentration at the surface of the particle, i.e. at $r = R_n$, although this is dropped in the subscript.

non-linear constraint such as

$$\sum_{j=k}^{k} j_{SEI} = \sum_{j=k}^{k} f(i_{j|k}, c_{n,j|k}) < Q_{\text{lost max}}, \tag{6.19}$$

where $Q_{\text{lost max}}$ is the maximum loss of cyclable lithium within the considered horizon[5], could be added to the framework exposed in equations 6.6-6.13.

6.4.5 Conclusive remarks

This Chapter has presented a proof of concept of the advantages of including advanced physics-based models in the control of BESSs, discussed in Sections 4.4. Notably, it shows: *i)* how it is possible, relying on a SPM, to estimate the principal internal states of Li-ion cells during the BESS operation, *ii)* how the operating domain of the BESS can be increased thanks to this increased insight in the cell dynamics and *iii)* how this insight is also at the basis of integrating policies to limit explicitly degradation phenomena of Li-ion cells. The proposed methods have been validated through simulations of the real-time control proposed in Chapter 1 of this thesis.

While the advantages of this approach are made clear, this still presents several challenges, as discussed in Chapter 4 (4.5, specifically). With respect to these, we observe that a linearized SPM poses no particular computational effort and that the parameters of an SPM can be determined as proposed in Chapter 5. However, in this Section we are relying on the assumption that all cells are equal and that the BESS behavior can therefore be modeled by scaling up that of one cell.

Conclusion

This thesis proposed a set of novel methodologies to effectively exploit battery energy storage systems. These methodologies focus on two main axes. First, a set of novel algorithms to provide via a BESS various grid services has been proposed and validated experimentally. These include the dispatch of the operation of an active distribution feeder, the levelling of its load, the provision and deployment of enhanced frequency response. Most notably, a framework to provide multiple among these services simultaneously has been proposed and validated. Second, the integration of advanced electrochemical models in BESS control has been discussed. In this respect, this thesis proposes and validates experimentally a method to identify the parameters of a single particle model of Li-ion cells and demonstrated the opportunity to integrate this model in the proposed control framework.

The feeder dispatch consists in computing the *dispatch plan*, that is the power profile that the feeder is expected to follow in the following 24 hours. This is done through the solution of a day-ahead robust optimization problem, considering the forecast and a set of scenarios of the feeder prosumption and the BESS state of energy. The resulting profile is such that, for all scenarios considered in the optimization, the state of energy of the battery will remain within proper bounds, so that the dispatch of the feeder can be achieved over the while 24 hours period. In real-time, the BESS is controlled so that the *dipatch plan* computed previously, is tracked, by means of a model predictive control algorithm. The proposed control strategy has been tested successfully, for a set of multiple days, on the 560 kWh/720 kVA BESS installed on the EPFL campus. The effectiveness of the day-ahead problem is demonstrated by the determination of dispatch plans that are successfully tracked during three different days. The real-time control achieves as well excellent performances, quantified by tracking errors of less than 0.5 kW.

The levelling of the feeder's load consists in extending the aforementioned control framework so to flatten the prosumption profile of the feeder. This is done by implementing a revised control objective in the day-ahead stage of the control, so that the resulting *dispatch plan* presents minimum variance. The real-time control is the same as before. The experimental validation demonstrates the effectiveness of the control and the ability of the battery to achieve the double objective of simultaneously dispatching the operation and levelling the load of the feeder. In fact, the tracking error remains quite low (about 2 kW) while the BESS shifts as much as 365 kWh from high- to low-demand period of the day.

The thesis proposes then an algorithm to provide enhanced frequency response. The quantification of the maximum deployable regulating power and the state-of-energy management mechanism are based on a statistical analysis of historical datasets of the frequency profile. In this respect, the thesis applies autoregressive models to predict the BESS energy need to respond to frequency deviations over a determined time interval. It demonstrates, that this method allows the provision of higher regulating power levels, compared to more traditional approaches. Moreover, an extensive experimental campaign (more than 250 hours of EFR provision and deployment) demonstrates how the proposed method is able to provide EFR with the desired reliability.

The last algorithm proposed in this thesis aims at providing multiple services simultaneously. This is with the objective of maximizing the utilization of valuable assets as BESSs. A formulation of the day-ahead problem that is agnostic to the considered services and rather based on energy and power budget is proposed. Its validity is then demonstrated using it to provide simultaneously dispatch and frequency response service. The framework is tested both in simulation and experimentally. This validation illustrates how the EPFL BESS, while dispatching the operation of the feeder, can provide up to 117 kW and 43 kW on average for EFR.

The methods and algorithms summarized above present some peculiar features, whose validation is of great importance. First, they exploit forecasting methods, such as those for the feeder loads and for the energy need required by frequency response. Second, the period-ahead problems provides operation planning that is robust toward the occurrence of worst case scenarios of the feeder prosumption and frequency deviations. By doing so, the proposed algorithm constitutes a promising basis to operate BESSs reliably as well as optimally. We want to stress that all the algorithms discussed above have been implemented in the control of a 560 kWh/720 kVA BESS installed at EPFL and validated experimentally. This validation proved their effectiveness and their deployability as well as the aptitude of this device to provide such services.

In Chapter 3, we take into account in the proposed framework also the ageing of BESSs. We demonstrate how to exploit an empirical degradation model - the weighted energy throughput - to assess and possibly reduce the ageing of these devices. We show how cycling ageing is of relatively little importance for a LTO-based BESS, as is the one installed at EPFL. Such device could provide load levelling and reach its end of life in as much as 40 years. A BESS based on a classical Li-ion chemistry, on the contrary may reach its end of life is as little as 7 years. In such case, we show how adding a constraint based on the weighted energy throughput in the day-ahead phase of the control framework described in Chapter 1 can ensure the achievement of a target lifetime.

The second part of the thesis focused on a different yet as important topic for the optimal operation of BESSs, i.e. the integration of advanced electrochemical models in their control. First, it has provided an in-depth analysis of the potential benefits and of the challenges of it.

144

The main benefits are the increased awareness of the control, the increased operating domain and the explicit and more precise description and limitation of battery ageing. The main challenges are the computational complexity of such models, the need of identifying all of their numerous parameters and the need to scale-up these models from cell to system level.

Second, it proposes a solution to the second of these challenges, i.e. the parameter identification of a single particle model of Li-ion cells. The proposed method is based on a reformulation to reduce the number of parameters necessary to represent the cell dynamics and on a set of tests that identify separately three subsets of the resulting parameters. These are a low-rate test, a pulse test and a GITT test. The method developed in this thesis successfully identifies the parameters of a reference model as well as those of a real LTO cell. The resulting model is able to simulate the Li-ion cell behavior with great accuracy, with RMS errors as low as 0.75% in the simulated profiles of the cell voltage and of the cell internal states.

Finally, the thesis "closes the loop" with the algorithms proposed in its first part by casting a single particle model in the MPC of the real-time phase of the framework to dispatch the operation of a distribution feeder via a BESS. It demonstrates, through simulations, that this increases the operating domain of the BESS and allows for the explicit integration of the main degradation phenomena of Li-ion cells.

Future works

Overall, the methods proposed in the two parts of this thesis allow to exploit BESSs more effectively and reliably. However, much can and should be still done in this direction. With respect to the algorithms presented in the first part of the thesis, for instance, several topics could be deepened. Examples are the sizing of BESSs providing such services, their siting (both geographically and "vertically", i.e. determining the voltage level that should host these devices) and their cooperation with wider sets of controllable resources, such as controllable demands and PVs.

It is also worth noting that the algorithms presented in this thesis focus on controlling the BESS active power injection. However, BESSs are typically equipped with four-quadrant converters and can therefore inject reactive power as well. BESSs could therefore be used to control the voltage levels of the local network, while also, for instance, dispatching its active power injection. In other words, the joint control of active and reactive power would increase the set of services that can be provided simultaneously. Nonetheless, this requires the careful development of planning and control strategies, since the operational constraints of the converter couple these two quantities. Developing such active and reactive power multiservice control framework is a subject surely worth of further investigation.

With respect to the integration in BESS control of physics-based models, we believe that we addressed and possibly untangled an important obstacle for this to happen: the parameter identification of such advanced models. However, as discussed in Chapter 4, a further issue

remains still unsolved. This is the proper coupling of cell-level models with system-level controls. There are, to date, few works on this issue and simplistic approaches (considering all cells perfectly homogeneous) are most commonly used. A more rigorous integration would be possibly based on a robust optimization approach, similar to the one used, in the first part of this thesis, to control a BESS considering different scenarios of the prosumption. In a similar way, a robust-MPC could be formulated, where the different cell states of a large set of inhomogeneous cells are used to formulate the problem constraints.Such an approach is still unexplored, although it may be a key to reach the complete and effective integration of physics-based models in the control of BESSs. We consider it therefore a very relevant topic for future investigations.

As the last two paragraphs have highlighted, much is still to be done to allow the effective and widespread deployment of BESSs in power systems and to achieve the important benefits that this integration would bring to these. With this thesis, however, we humbly believe that we have made few steps toward such an important goal.

A Appendices

A.1 Convex formulation of the Day-ahead problem for the dispatch

The formulation in (1.15)-(1.22) is nonconvex due to the relationship (1.10), which involves a nonlinear function of the decision variable. We apply an augmented formulation of what proposed in [89] to obtain a convex equivalent formulation of the original problem. We introduce:

$$K_i = F_i^o + L_i^{\downarrow} \tag{A.1}$$

$$G_i = F_i^o + L_i^{\uparrow} \tag{A.2}$$

which we decompose into their respective positive and strictly negative parts:

$$K_i = K_i^+ - K_i^-, \qquad\qquad K_i^+ \geq 0,\ K_i^- < 0 \tag{A.3}$$

$$G_i = G_i^+ - G_i^-, \qquad\qquad G_i^+ \geq 0,\ G_i^- < 0. \tag{A.4}$$

The quantities $K_i^+, K_i^-, G_i^+, G_i^-, i = 0,\dots,N-1$ become the decision variables of the problem. They are coupled by the relationships (A.1)-(A.2) because the offset plan F_i^o must be the same in the two cases. The coupling equality constraint is given by determining F_i^o in (A.1)-(A.2) and imposing F_i^o to be the same in (A.1) and (A.2), which gives:

$$K_i^+ - K_i^- - L_i^{\downarrow} = G_i^+ - G_i^- - L_i^{\uparrow}. \tag{A.5}$$

The quantity $K_i^{+o}, K_i^{-o}, G_i^{+o}, G_i^{-o},\ i = 0,\dots,N-1$ are finally given by the following linear (convex) program:

$$\underset{K^+,K^-,G^+,G^- \in \mathbb{R}^N}{\arg\min} \left\{ \sum_{i=1}^N \left(K_i^+ + K_i^- + G_i^+ + G_i^- \right) \right\} \tag{A.6}$$

subject to:

$$K_i^+ \geq 0 \tag{A.7}$$

$$K_i^- \geq 0 \tag{A.8}$$

$$G_i^+ \geq 0 \tag{A.9}$$

$$G_i^- \geq 0 \tag{A.10}$$

$$K_i^+ - K_i^- - L_i^\downarrow = G_i^+ - G_i^- - L_i^\uparrow \tag{A.11}$$

$$\mathrm{SOE}_{i+1}^\downarrow = \mathrm{SOE}_i^\downarrow + \beta^+ K_i^+ - \beta^- K_i^- \tag{A.12}$$

$$\mathrm{SOE}_{i+1}^\uparrow = \mathrm{SOE}_i^\uparrow + \beta^+ G_i^+ - \beta^- G_i^- . \tag{A.13}$$

$$\mathrm{SOE}_i^\uparrow \geq \mathrm{SOE}_{\min} \tag{A.14}$$

$$\mathrm{SOE}_i^\uparrow \leq \mathrm{SOE}_{\max} \tag{A.15}$$

$$K_i^+ - K_i^- \leq B_{\max} \tag{A.16}$$

$$K_i^+ - K_i^- \geq B_{\min} \tag{A.17}$$

$$G_i^+ - G_i^- \leq B_{\max} \tag{A.18}$$

$$G_i^+ - G_i^- \geq B_{\min} \tag{A.19}$$

for $i = 0, 1 \ldots, N - 1$. The dispatch plan is finally:

$$F_i^o = K_i^{+o} - K_i^{-o} - L_i^\downarrow, \qquad\qquad i = 0, \ldots, N - 1. \tag{A.20}$$

We also note that the relationship above is also linear, thus it can be used to formulate additional constraints for the offset plan (to implement for example peak shaving).

A.2   Derivation of the Transition Matrices for the MPC

We consider a linear dynamic model with the following discrete state-space representation (as those developed in Section 1.4.2 for the BESS SOC and voltage):

$$x_{k+1} = Ax_k + Bu_k \tag{A.21}$$

$$y_k = Cx_k + Du_k \tag{A.22}$$

where $x_k \in \mathbb{R}^n$ is the state vector at discrete time interval k, $u_k \in \mathbb{R}$ is the input, $y \in \mathbb{R}$ is the system output, A is the $n \times n$ system matrix, B is the $n \times 1$ input matrix, C is the $1 \times n$ output matrix, and the scalar D is the feed-forward gain. For the moment, we consider the case with only one input signal: the extension to multiple inputs is shown at the end of this section. The evolution of the state vector x from a known initial state x_0 as a function of a given input

sequence $u_0, u_1, \ldots, u_N$ using (A.21) is

$$x_1 = Ax_0 + Bu_0 \tag{A.23}$$

$$x_2 = Ax_1 + Bu_1 = A(Ax_0 + Bu_0) + Bu_1 =$$
$$= A^2 x_0 + ABu_0 + Bu_1 \tag{A.24}$$

$$x_3 = Ax_2 + Bu_2 =$$
$$= A^3 x_0 + A^2 Bu_0 + ABu_1 + Bu_2. \tag{A.25}$$

Iterating until the time interval N:

$$x_N = A^N x_0 + A^{N-1} Bu_0 + \cdots + A^0 Bu_{N-1}. \tag{A.26}$$

Applying (A.22) to (A.23)-(A.26) yields:

$$
\begin{bmatrix} y_0 \\ y_1 \\ y_2 \\ \vdots \\ y_N \end{bmatrix} =
\begin{bmatrix} C \\ CA \\ CA^2 \\ \vdots \\ CA^N \end{bmatrix} x_0 +
$$

$$
+ \begin{bmatrix}
D & 0 & \ldots & 0 & 0 \\
CA^0 B & D & \ldots & 0 & 0 \\
CA^1 B & CA^0 B & \ldots & 0 & 0 \\
\vdots & \vdots & \ddots & \vdots & \vdots \\
CA^{N-1} B & CA^{N-2} B & \ldots & CA^0 B & D
\end{bmatrix}
\begin{bmatrix} u_0 \\ u_1 \\ \vdots \\ u_{N-1} \\ u_N \end{bmatrix} \tag{A.27}
$$

which we write in compact form as:

$$\boldsymbol{y} = \phi x_0 + \psi_u \boldsymbol{u}. \tag{A.28}$$

where $\boldsymbol{y} = y_0, \ldots, y_N$, $x = x_0, \ldots, x_N$ and $\boldsymbol{u} = u_0, \ldots, u_N$. For the case of multiple inputs, we add an input $\boldsymbol{r} = r_0, \ldots, r_N$ to the state-space model (A.23)-(A.26):

$$x_{k+1} = Ax_k + B_u u_k + B_r r_k \tag{A.29}$$
$$y_k = Cx_k + D_u u_k + D_u r_k. \tag{A.30}$$

The system output is written by applying the transformation ψ_r to $\boldsymbol{r}$:

$$\boldsymbol{y} = \phi x_0 + \psi_u \boldsymbol{u} + \psi_r \boldsymbol{r}. \tag{A.31}$$

A.3 Alternative formulations for the multi-service scheduling.

The objective of the cost function (2.5) is maximising the battery energy capacity exploited during a period of operation T. We observe that the same framework can be exploited to optimise the BESS operation considering different objectives. For instance, one could seek the value of x that maximises the economical revenue of providing multiple concurrent services via an multi-objective optimization function such as:

$$x^o = \arg\max_x \sum r_j \tag{A.32}$$

subject to (2.6), (2.7) and:

$$r_j = f_j(\mathcal{E}_j, \mathcal{P}_j) \tag{A.33}$$

where r_j is the revenue that the application j can generate in period T, and is a function of the energy and power budgets reserved for that service. Similarly, if the objective is simply to find a value for x that ensures feasible operation, one could write:

$$x^o = \arg\max_x \quad 1 \tag{A.34}$$

subject to (2.6) (2.7).

With respect to the algorithms presented in Section 1.2, we highlight how, by exploiting a multi-objective optimization approach such as that in A.32, the framework presented in this section is suitable to integrate also a load-levelling goal. Notably, we can formulate the energy and power budgets of the three applications considered as:

$$\mathcal{P}_D = \{\left[L_k^\downarrow, L_k^\uparrow\right], k = 1,\ldots, N\}, \tag{A.35}$$

$$\mathcal{E}_D = \left[\frac{T}{N}\sum_{i=1}^{k}(L_i^\downarrow), \frac{T}{N}\sum_{i=1}^{k}(L_i^\uparrow)\right], \tag{A.36}$$

$$\mathcal{P}_{LL} = \{[F_k, F_k], k = 1,\ldots, N\}, \tag{A.37}$$

$$\mathcal{E}_{LL} = \left[\frac{T}{N}\sum_{i=1}^{k}(F_i), \frac{T}{N}\sum_{i=1}^{k}(F_i)\right], \tag{A.38}$$

$$\mathcal{P}_{FR} = [-0.2\alpha \cdot \mathbf{1}, 0.2\alpha \cdot \mathbf{1}], \tag{A.39}$$

$$\mathcal{E}_{FR} = \{\left[\alpha W_{f,k}^\downarrow, \alpha W_{f,k}^\uparrow\right], k = 1,\ldots, N\}, \tag{A.40}$$

with $k = 1,\ldots, N$. The revenues associated to the three services are:

$$r_D = w_1 \cdot 0, \tag{A.41}$$

$$r_{LL} = w_2 \cdot \left[-\left(\hat{L}_k - \hat{L}_{avg}\right) - F_k\right], \tag{A.42}$$

$$r_{FR} = w_3 \cdot \alpha, \tag{A.43}$$

Figure A.1 – Normal probability plot of $W_{f,N}$.

where the subscript LL indicates load-levelling and the remaining subscripts respect the notation introduced in Section 2.4. An optimization problem including these three services would have an objective function as A.32 subject to the constraints (2.6), (2.7) and where the weights w_2 and w_3 determine the priority given to the deployment of power and energy for each service.

A.4 Computation of the terms $\mathbf{W}_f^{\downarrow}$ and $\mathbf{W}_f^{\uparrow}$ used in Section 2.4

The terms $\mathbf{W}_f^{\downarrow}$ and $\mathbf{W}_f^{\uparrow}$, used to compute the energy budgets for PFR in Chapter 2, are computed on the basis of a statistical analysis of past data from the last two years of frequency deviations and assuming that the BESS under control does not influence the future frequency deviation. First, the daily profiles composed by $\mathbf{W}_f = W_{f,1}, \dots, W_{f,N}$ have been calculated from hystorical data, by integrating the frequency deviations measured in a set of 24 h periods. The mean $\mu_{W,k}$ and variance $\sigma_{W,k}^2$ of such values have then been computed for all $k = 1, \dots, N$. It can be observed that the set of $W_{f,k}$ values is close to normally distributed for any instant k. A Chi-square goodness-of-fit test on the dataset does in fact not reject the null hypothesis at the 5% significance level. In Fig. A.1, it is shown that the normal probability plot of the values assumed $W_{f,k}$ for $k = N$ (i.e. at the end of the 24 hours). We then define $W_{f,k}^{\uparrow}$ and $W_{f,k}^{\downarrow}$ for all k as a function of the mean value $\mu_{W,k}$ and the standard deviation $\sigma_{W,k}$ as

$$
\begin{aligned}
W_{f,k}^{\uparrow} &= \mu_{W,k} + 1.96\sigma_{W,k} \\
W_{f,k}^{\downarrow} &= \mu_{W,k} - 1.96\sigma_{W,k}, \text{ for } k = 1, \dots, N
\end{aligned}
\tag{A.44}
$$

to have a 95% confidence level that the realization of $W_{f,k}$ will lie between $W_{f,k}^{\uparrow}$ and $W_{f,k}^{\downarrow}$. Similarly, we can define $W_{f,k}^{\uparrow}$ and $W_{f,k}^{\downarrow}$ for any other confidence level.

A.5 Weighted energy throughput for various services

For the sake of completeness, we apply here the weighted energy throughput to assess the cycling ageing generated by several other BESS services considered throughout Chapter 3. Notably, we apply this metric to a BESS with the characteristics as above and to experimental data obtained for *i)* the dispatch application, shown in section 1.4 and *ii)* the experimental data for the EFR, considering a length of the interval for the state of energy management $T = 6\ h$. For each of these two services, data from one day of operation is used to assess the stress, in term of cycling ageing, that they cause. Given the short time frame of these data, these results are to be intended solely as a qualitative assessment. Table A.1 reports the main metrics. It is worth observing, that the dispatch generates a very limited BESS ageing, with

Table A.1 – Performances for BESS operation constrained to a lifetime of 30 years and employing cells with 5000 cycles

	E_{exch} [kWh]	N_c [$-$]	EOL [years]
dispatch	254	0.45	120.7
pfr, T=6h	1064	1.89	28.8

the BESS EOL being as far as 120 years (not considering calendar ageing). On the contrary, frequency response provokes a considerable cycling ageing, more than load levelling and considerably more than the dispatch. In fact, this is an expected result, since EFR is a "power intensive application" and the high power values that it requires are the cause of faster cycling ageing.

Bibliography

[1] M. A. Abdullah, K. M. Muttaqi, D. Sutanto, and A. P. Agalgaonkar. An effective power dispatch control strategy to improve generation schedulability and supply reliability of a wind farm using a battery energy storage system. *IEEE Transactions on Sustainable Energy*, 6(3):1093–1102, 2015.

[2] M. Abu Abdullah, K. Muttaqi, D. Sutanto, and A. Agalgaonkar. An effective power dispatch control strategy to improve generation schedulability and supply reliability of a wind farm using a battery energy storage system. *Sustainable Energy, IEEE Transactions on*, 6, 2015.

[3] H. Akhavan-Hejazi and H. Mohsenian-Rad. Optimal operation of independent storage systems in energy and reserve markets with high wind penetration. *IEEE Transactions on Smart Grid*, 5(2):1088–1097, 2014.

[4] P. Albertus, J. Christensen, and J. Newman. Experiments on and modeling of positive electrodes with multiple active materials for lithium-ion batteries. *Journal of the Electrochemical Society*, 156(7):A606–A618, 2009.

[5] D. Andre, C. Appel, T. Soczka-Guth, and D. U. Sauer. Advanced mathematical methods of soc and soh estimation for lithium-ion batteries. *Journal of Power Sources*, 224:20–27, 2013.

[6] D. Andre, M. Meiler, K. Steiner, C. Wimmer, T. Soczka-Guth, and D. Sauer. Characterization of high-power lithium-ion batteries by electrochemical impedance spectroscopy. i. experimental investigation. *Journal of Power Sources*, 196(12):5334–5341, 2011.

[7] D. Aurbach, B. Markovsky, M. Levi, E. Levi, A. Schechter, M. Moshkovich, and Y. Cohen. New insights into the interactions between electrode materials and electrolyte solutions for advanced nonaqueous batteries. *Journal of power sources*, 81:95–111, 1999.

[8] A. Azizivahed, E. Naderi, H. Narimani, M. Fathi, and M. R. Narimani. A new bi-objective approach to energy management in distribution networks with energy storage systems. *IEEE Transactions on Sustainable Energy*, 2017.

Bibliography

[9] M. Bahramipanah, D. Torregrossa, R. Cherkaoui, and M. Paolone. Enhanced electrical model of lithium-based batteries accounting the charge redistribution effect. In *Power Systems Computation Conference (PSCC)*, 2014.

[10] E. A. Bakirtzis, I. G. Marneris, D. I. Chatzigiannis, P. N. Biskas, and A. G. Bakirtzis. Storage management by rolling unit commitment for high renewable energy penetration. In *PowerTech, 2017 IEEE Manchester*, pages 1–6. IEEE, 2017.

[11] Balance group model (bgm) introduction. Technical report, SwissGrid, as seen on June 2016.

[12] A. Barai, W. D. Widanage, J. Marco, A. McGordon, and P. Jennings. A study of the open circuit voltage characterization technique and hysteresis assessment of lithium-ion cells. *Journal of Power Sources*, 295:99–107, 2015.

[13] A. K. Barnes, J. C. Balda, and A. Escobar-Mejía. A semi-markov model for control of energy storage in utility grids and microgrids with pv generation. *IEEE Transactions on Sustainable Energy*, 6(2):546–556, 2015.

[14] A. Barré, B. Deguilhem, S. Grolleau, M. Gérard, F. Suard, and D. Riu. A review on lithium-ion battery ageing mechanisms and estimations for automotive applications. *Journal of Power Sources*, 241:680–689, 2013.

[15] S. Barsali, R. Giglioli, G. Lutzemberger, D. Poli, and G. Valenti. Optimised operation of storage systems integrated with mv photovoltaic plants, considering the impact on the battery lifetime. *Journal of Energy Storage*, 12:178–185, 2017.

[16] S. Bashash, S. J. Moura, J. C. Forman, and H. K. Fathy. Plug-in hybrid electric vehicle charge pattern optimization for energy cost and battery longevity. *Journal of power sources*, 196(1):541–549, 2011.

[17] B. Belvedere, M. Bianchi, A. Borghetti, C. A. Nucci, M. Paolone, and A. Peretto. A microcontroller-based power management system for standalone microgrids with hybrid power supply. *Sustainable Energy, IEEE Transactions on*, 3(3):422–431, 2012.

[18] A. Bernstein, L. Reyes-Chamorro, J.-Y. Le Boudec, and M. Paolone. A composable method for real-time control of active distribution networks with explicit power set-points. part i: Framework. *Electric Power Systems Research*, 125:254–264, 2015.

[19] H. Bindner, T. Cronin, P. Lundsager, J. F. Manwell, U. Abdulwahid, and I. Baring-Gould. Lifetime modelling of lead acid batteries. *Risø National Laboratory*, 2005.

[20] C. R. Birkl, M. R. Roberts, E. McTurk, P. G. Bruce, and D. A. Howey. Degradation diagnostics for lithium ion cells. *Journal of Power Sources*, 341:373–386, 2017.

[21] A. Bizeray, S. Zhao, S. Duncan, and D. Howey. Lithium-ion battery thermal-electrochemical model-based state estimation using orthogonal collocation and a modified extended kalman filter. *Journal of Power Sources*, 296:400–412, 2015.

[22] A. M. Bizeray, J.-H. Kim, S. R. Duncan, and D. A. Howey. Identifiability and parameter estimation of the single particle lithium-ion battery model. *arXiv preprint arXiv:1702.02471*, 2017.

[23] S. Boyd and L. Vandenberghe. *Convex Optimization.* Cambridge University Press, 2004.

[24] M. Bozorg, A. Ahmadi-Khatir, and R. Cherkaoui. Developing offer curves for an electric railway company in reserve markets based on robust energy and reserve scheduling. *Power Systems, IEEE Transactions on*, 2015.

[25] F. Brahman, M. Honarmand, and S. Jadid. Optimal electrical and thermal energy management of a residential energy hub, integrating demand response and energy storage system. *Energy and Buildings*, 90:65–75, 2015.

[26] T. Brijs, F. Geth, S. Siddiqui, B. F. Hobbs, and R. Belmans. Price-based unit commitment electricity storage arbitrage with piecewise linear price-effects. *Journal of Energy Storage*, 7:52–62, 2016.

[27] L. Cai and R. E. White. Reduction of model order based on proper orthogonal decomposition for lithium-ion battery simulations. *Journal of The Electrochemical Society*, 156(3):A154–A161, 2009.

[28] A. Castillo and D. F. Gayme. Grid-scale energy storage applications in renewable energy integration: A survey. *Energy Conversion and Management*, 87:885–894, 2014.

[29] T. Chakraborty, D. Watson, and M. Rodgers. Automatic generation control using an energy storage system in a wind park. *IEEE Transactions on Power Systems*, 33(1):198–205, 2018.

[30] N. A. Chaturvedi, R. Klein, J. Christensen, J. Ahmed, and A. Kojic. Algorithms for advanced battery-management systems. *IEEE Control Systems*, 30(3):49–68, 2010.

[31] M. Chen and G. Rincon-Mora. Accurate electrical battery model capable of predicting runtime and i-v performance. *Energy Conversion, IEEE Transactions on*, 21, June 2006.

[32] M. Chen and G. A. Rincon-Mora. Accurate electrical battery model capable of predicting runtime and iv performance. *IEEE transactions on energy conversion*, 21(2):504–511, 2006.

[33] B. Cheng and W. Powell. Co-optimizing battery storage for the frequency regulation and energy arbitrage using multi-scale dynamic programming. *IEEE Transactions on Smart Grid*, 2016.

[34] J. Christensen. Modeling diffusion-induced stress in li-ion cells with porous electrodes. *Journal of the Electrochemical Society*, 157(3):A366–A380, 2010.

Bibliography

[35] J. Christensen and J. Newman. A mathematical model for the lithium-ion negative electrode solid electrolyte interphase. *Journal of The Electrochemical Society*, 151(11):A1977–A1988, 2004.

[36] J. Christensen and J. Newman. Cyclable lithium and capacity loss in li-ion cells. *Journal of the Electrochemical Society*, 152(4):A818–A829, 2005.

[37] J. Christensen and J. Newman. A mathematical model of stress generation and fracture in lithium manganese oxide. *Journal of The Electrochemical Society*, 153(6):A1019–A1030, 2006.

[38] J. Christensen and J. Newman. Stress generation and fracture in lithium insertion materials. *Journal of Solid State Electrochemistry*, 10(5):293–319, 2006.

[39] J. Christensen, V. Srinivasan, and J. Newman. Optimization of lithium titanate electrodes for high-power cells. *Journal of The Electrochemical Society*, 153(3):A560–A565, 2006.

[40] C. A. Correa, A. Gerossier, A. Michiorri, and G. Kariniotakis. Optimal scheduling of storage devices in smart buildings including battery cycling. In *PowerTech, 2017 IEEE Manchester*, pages 1–6. IEEE, 2017.

[41] Y. Dai. *Studying on capacity fade mechanisms of Li-ion batteries through modeling*. PhD thesis, University of South Carolina, 2013.

[42] R. Deshpande, M. Verbrugge, Y.-T. Cheng, J. Wang, and P. Liu. Battery cycle life prediction with coupled chemical degradation and fatigue mechanics. *Journal of the Electrochemical Society*, 159(10):A1730–A1738, 2012.

[43] D. Di Domenico, G. Fiengo, and A. Stefanopoulou. Lithium-ion battery state of charge estimation with a kalman filter based on a electrochemical model. In *2008 IEEE International Conference on Control Applications*, pages 702–707. Ieee, 2008.

[44] F. Díaz-González, G. Del-Rosario-Calaf, F. Girbau-Llistuella, and O. Gomis-Bellmunt. Short-term energy storage for power quality improvement in weak mv grids with distributed renewable generation. In *PES Innovative Smart Grid Technologies Conference Europe (ISGT-Europe), 2016 IEEE*, pages 1–6. IEEE, 2016.

[45] D. J. Docimo, M. Ghanaatpishe, M. J. Rothenberger, C. D. Rahn, and H. K. Fathy. The lithium-ion battery modeling challenge: a dynamic systems and control perspective. *Mechanical Engineering*, 136(6):S7, 2014.

[46] M. Doyle, T. F. Fuller, and J. Newman. Modeling of galvanostatic charge and discharge of the lithium/polymer/insertion cell. *Journal of the Electrochemical Society*, 140(6):1526–1533, 1993.

[47] E. Drury, P. Denholm, and R. Sioshansi. The value of compressed air energy storage in energy and reserve markets. *Energy*, 36(8):4959–4973, 2011.

[48] M. Dubarry and B. Y. Liaw. Development of a universal modeling tool for rechargeable lithium batteries. *Journal of Power Sources*, 174(2):856–860, 2007.

[49] I. Duggal and B. Venkatesh. Short-term scheduling of thermal generators and battery storage with depth of discharge-based cost model. *IEEE Transactions on Power Systems*, 30(4):2110–2118, 2015.

[50] B. Dunn, H. Kamath, and J.-M. Tarascon. Electrical energy storage for the grid: a battery of choices. *Science*, 334(6058):928–935, 2011.

[51] Enhanced frequency response (efr) - overview. https://www.nationalgrid.com/uk/electricity/balancing-services/frequency-response-services/enhanced-frequency-response-efr?overview. Accessed: 2018-04-17.

[52] J. F. Ellison, L. J. Rashkin, J. Serio, and R. H. Byrne. The benefits of grid-scale storage on oahu. *Journal of Energy Storage*, 15:336–344, 2018.

[53] S. Eshghi and R. M. Patil. Optimal battery pricing and energy management for micro-grids. In *American Control Conference (ACC), 2015*, pages 4994–5001. IEEE, 2015.

[54] J. Eyer and G. Corey. Energy storage for the electricity grid: Benefits and market potential assessment guide. *Sandia National Laboratories*, 20(10):5, 2010.

[55] L. Fabietti, T. T. Gorecki, E. Namor, F. Sossan, M. Paolone, and C. N. Jones. Dispatching active distribution networks through electrochemical storage systems and demand side management. In *Control Technology and Applications (CCTA), 2017 IEEE Conference on*, pages 1241–1247. IEEE, 2017.

[56] W. Fang, O. J. Kwon, and C.-Y. Wang. Electrochemical–thermal modeling of automotive li-ion batteries and experimental validation using a three-electrode cell. *International journal of energy research*, 34(2):107–115, 2010.

[57] J. C. Forman, S. Bashash, J. L. Stein, and H. K. Fathy. Reduction of an electrochemistry-based li-ion battery model via quasi-linearization and pade approximation. *Journal of the Electrochemical Society*, 158(2):A93–A101, 2011.

[58] J. C. Forman, S. J. Moura, J. L. Stein, and H. K. Fathy. Genetic identification and fisher identifiability analysis of the doyle–fuller–newman model from experimental cycling of a lifepo 4 cell. *Journal of Power Sources*, 210:263–275, 2012.

[59] P. Fortenbacher and G. Andersson. Battery degradation maps for power system optimization and as a benchmark reference. In *PowerTech, 2017 IEEE Manchester*, pages 1–6. IEEE, 2017.

[60] P. Fortenbacher, J. L. Mathieu, and G. Andersson. Modeling, identification, and optimal control of batteries for power system applications. In *Power Systems Computation Conference (PSCC), 2014*, pages 1–7. IEEE, 2014.

Bibliography

[61] P. Fortenbacher, J. L. Mathieu, and G. Andersson. Modeling and optimal operation of distributed battery storage in low voltage grids. *IEEE Transactions on Power Systems*, 32(6):4340–4350, 2017.

[62] P. Fortenbacher, A. Ulbig, and G. Andersson. Optimal placement and sizing of distributed battery storage in low voltage grids using receding horizon control strategies. *IEEE Transactions on Power Systems*, 2017.

[63] T. F. Fuller, M. Doyle, and J. Newman. Simulation and optimization of the dual lithium ion insertion cell. *Journal of the Electrochemical Society*, 141(1):1–10, 1994.

[64] A. Giannitrapani, S. Paoletti, A. Vicino, and D. Zarrilli. Optimal allocation of energy storage systems for voltage control in lv distribution networks. *IEEE Transactions on Smart Grid*, 8(6):2859–2870, 2017.

[65] D. Greenwood, K. Y. Lim, C. Patsios, P. Lyons, Y. S. Lim, and P. Taylor. Frequency response services designed for energy storage. *Applied Energy*, 203:115–127, 2017.

[66] S. Grillo, A. Pievatolo, and E. Tironi. Optimal storage scheduling using markov decision processes. *IEEE Transactions on Sustainable Energy*, 7(2):755–764, 2016.

[67] M. Guo, G. Sikha, and R. E. White. Single-particle model for a lithium-ion cell: Thermal behavior. *Journal of The Electrochemical Society*, 158(2):A122–A132, 2011.

[68] P. Haessig, H. Ben Ahmed, and B. Multon. Energy storage control with aging limitation. In *PowerTech, 2015 IEEE Eindhoven*, pages 1–6. IEEE, 2015.

[69] G. He, Q. Chen, C. Kang, P. Pinson, and Q. Xia. Optimal bidding strategy of battery storage in power markets considering performance-based regulation and battery cycle life. *IEEE Transactions on Smart Grid*, 7(5):2359–2367, 2016.

[70] G. He, Q. Chen, C. Kang, Q. Xia, and K. Poolla. Cooperation of wind power and battery storage to provide frequency regulation in power markets. *IEEE Transactions on Power Systems*, 32(5):3559–3568, 2017.

[71] B. Hredzak, V. G. Agelidis, and G. Demetriades. Application of explicit model predictive control to a hybrid battery-ultracapacitor power source. *Journal of Power Sources*, 277:84 – 94, 2015.

[72] B. Hredzak, V. G. Agelidis, and G. Demetriades. Application of explicit model predictive control to a hybrid battery-ultracapacitor power source. *Journal of Power Sources*, 277:84–94, 2015.

[73] X. Hu, S. Li, and H. Peng. A comparative study of equivalent circuit models for li-ion batteries. *Journal of Power Sources*, 198:359–367, 2012.

[74] X. Hu, S. Li, H. Peng, and F. Sun. Charging time and loss optimization for linmc and lifepo4 batteries based on equivalent circuit models. *Journal of Power Sources*, 239:449–457, 2013.

[75] R. A. Jabr, S. Karaki, and J. A. Korbane. Robust multi-period opf with storage and renewables. *IEEE Transactions on Power Systems*, 30(5):2790–2799, 2015.

[76] N. Jayasekara, M. A. Masoum, and P. J. Wolfs. Optimal operation of distributed energy storage systems to improve distribution network load and generation hosting capability. *IEEE Transactions on Sustainable Energy*, 7(1):250–261, 2016.

[77] R. Jobman, S. E. Trimboli, and G. L. Plett. Identification of lithium-ion physics-based model parameter values. *Journal of Energy Challenges and Mechanics*, 2(2):45–55, 2015.

[78] M. R. Jongerden and B. R. Haverkort. Which battery model to use? *IET software*, 3(6):445–457, 2009.

[79] S. Karagiannopoulos, A. Rigas, N. Hatziargyriou, G. Hug, and A. Oudalov. Battery energy storage capacity fading and control strategies for deterministic and stochastic power profiles. In *Power Systems Computation Conference (PSCC), 2016*, pages 1–7. IEEE, 2016.

[80] F. Kasten and G. Czeplak. Solar and terrestrial radiation dependent on the amount and type of cloud. *Solar Energy*, 24:177–189, 1980.

[81] M. Kazemi and H. Zareipour. Long-term scheduling of battery storage systems in energy and regulation markets considering battery's lifespan. *IEEE Transactions on Smart Grid*, 2017.

[82] M. Kazemi, H. Zareipour, N. Amjady, W. D. Rosehart, and M. Ehsan. Operation scheduling of battery storage systems in joint energy and ancillary services markets. *IEEE Transactions on Sustainable Energy*, 2017.

[83] F. Kazhamiaka, C. Rosenberg, and S. Keshav. Practical strategies for storage operation in energy systems: design and evaluation. *IEEE Transactions on Sustainable Energy*, 7(4):1602–1610, 2016.

[84] R. J. Kerestes, G. F. Reed, and A. R. Sparacino. Economic analysis of grid level energy storage for the application of load leveling. In *Power and Energy Society General Meeting, 2012 IEEE*, pages 1–9. IEEE, 2012.

[85] M. Khalid and A. V. Savkin. Model predictive control based efficient operation of battery energy storage system for primary frequency control. In *Control Automation Robotics & Vision (ICARCV), 2010 11th International Conference on*, pages 2248–2252. IEEE, 2010.

[86] H. Khani and M. R. D. Zadeh. Online adaptive real-time optimal dispatch of privately owned energy storage systems using public-domain electricity market prices. *IEEE Transactions on Power Systems*, 30(2):930–938, 2015.

[87] H. Khani, M. R. D. Zadeh, and A. H. Hajimiragha. Transmission congestion relief using privately owned large-scale energy storage systems in a competitive electricity market. *IEEE Transactions on Power Systems*, 31(2):1449–1458, 2016.

[88] M. Koller, T. Borsche, A. Ulbig, and G. Andersson. Review of grid applications with the zurich 1mw battery energy storage system. *Electric Power Systems Research*, 120:128–135, 2015.

[89] M. Kraning, Y. Wang, E. Akuiyibo, and S. Boyd. Operation and configuration of a storage portfolio via convex optimization. In *Proceedings of the 18th IFAC World Congress*, volume 18, pages 10487–10492. Citeseer, 2011.

[90] D. Krishnamurthy, C. Uckun, Z. Zhou, P. R. Thimmapuram, and A. Botterud. Energy storage arbitrage under day-ahead and real-time price uncertainty. *IEEE Transactions on Power Systems*, 33(1):84–93, 2018.

[91] N. Kristensen, H. Madsen, and S. Jørgensen. Parameter estimation in stochastic grey-box models. *Automatica*, 40(2), 2004.

[92] N. R. Kristensen and H. Madsen. Continuous time stochastic modelling, 2003.

[93] E. Krüger and Q. T. Tran. Minimal aging operating strategies for battery energy storage systems in photovoltaic applications. In *PES Innovative Smart Grid Technologies Conference Europe (ISGT-Europe), 2016 IEEE*, pages 1–6. IEEE, 2016.

[94] C. Kupper, S. Wussler, H. Buqa, and W. Bessler. Combined modelling and experimental charactrization of titanate-based lithium-ion batteries. In *Kraftwerk Batterie*, 2015.

[95] J. L. Lee, A. Chemistruck, and G. L. Plett. One-dimensional physics-based reduced-order model of lithium-ion dynamics. *Journal of Power Sources*, 220:430–448, 2012.

[96] J. Li, B. Greye, M. Buchholz, and M. A. Danzer. Interval method for an efficient state of charge and capacity estimation of multicell batteries. *Journal of Energy Storage*, 13:1–9, 2017.

[97] B. Lian, A. Sims, D. Yu, C. Wang, and R. W. Dunn. Optimizing lifepo4 battery energy storage systems for frequency response in the uk system. *IEEE Transactions on Sustainable Energy*, 8(1):385–394, 2017.

[98] B. Y. Liaw, G. Nagasubramanian, R. G. Jungst, and D. H. Doughty. Modeling of lithium ion cells—a simple equivalent-circuit model approach. *Solid State Ionics*, 175, 2004.

[99] J.-M. Ling and P.-L. Chen. Planning framework of the residential-scale microgrid with battery storage. In *PowerTech, 2017 IEEE Manchester*, pages 1–5. IEEE, 2017.

[100] M. Liu, W. Li, C. Wang, M. P. Polis, L. Y. Wang, and J. Li. Reliability evaluation of large scale battery energy storage systems. *IEEE Transactions on Smart Grid*, 8(6):2733–2743, 2017.

[101] C. H. Lo and M. D. Anderson. Economic dispatch and optimal sizing of battery energy storage systems in utility load-leveling operations. *Energy Conversion, IEEE Transactions on*, 14(3):824–829, 1999.

[102] C. V. Loan. Computing integrals involving the matrix exponential. *IEEE Transactions on Automatic Control*, 23(3):395–404, Jun 1978.

[103] A. Lorca and X. A. Sun. Multistage robust unit commitment with dynamic uncertainty sets and energy storage. *IEEE Transactions on Power Systems*, 32(3):1678–1688, 2017.

[104] J. M. Lujano-Rojas, R. Dufo-López, J. L. Bernal-Agustín, and J. P. Catalão. Optimizing daily operation of battery energy storage systems under real-time pricing schemes. *IEEE Transactions on Smart Grid*, 8(1):316–330, 2017.

[105] F. Luo, K. Meng, Z. Y. Dong, Y. Zheng, Y. Chen, and K. P. Wong. Coordinated operational planning for wind farm with battery energy storage system. *IEEE Transactions on Sustainable Energy*, 6(1):253–262, 2015.

[106] H. Madsen. *Time Series Analysis*. Chapman & Hall/CRC Texts in Statistical Science. Taylor & Francis, 2007.

[107] K. Mamadou, E. Lemaire, A. Delaille, D. Riu, S. Hing, and Y. Bultel. Definition of a state-of-energy indicator (soe) for electrochemical storage devices: application for energetic availability forecasting. *Journal of The Electrochemical Society*, 159(8):A1298–A1307, 2012.

[108] M. Marinelli, F. Sossan, G. Costanzo, and H. Bindner. Testing of a predictive control strategy for balancing renewable sources in a microgrid. *IEEE Transactions on Sustainable Energy*, 2014.

[109] M. Marinelli, F. Sossan, G. T. Costanzo, and H. W. Bindner. Testing of a predictive control strategy for balancing renewable sources in a microgrid. *IEEE Transactions on Sustainable Energy*, 5(4):1426–1433, Oct 2014.

[110] O. Mégel, J. L. Mathieu, and G. Andersson. Maximizing the potential of energy storage to provide fast frequency control. In *Innovative Smart Grid Technologies Europe (ISGT EUROPE), 2013 4th IEEE/PES*, pages 1–5. IEEE, 2013.

[111] O. Mégel, J. L. Mathieu, and G. Andersson. Scheduling distributed energy storage units to provide multiple services under forecast error. *International Journal of Electrical Power & Energy Systems*, 72:48–57, 2015.

[112] O. Mégel, J. L. Mathieu, and G. Andersson. Stochastic dual dynamic programming to schedule energy storage units providing multiple services. In *PowerTech, 2015 IEEE Eindhoven*, pages 1–6. IEEE, 2015.

Bibliography

[113] P. Mercier, R. Cherkaoui, and A. Oudalov. Optimizing a battery energy storage system for frequency control application in an isolated power system. *Power Systems, IEEE Transactions on*, 24(3):1469–1477, 2009.

[114] A. Millner. Modeling lithium ion battery degradation in electric vehicles. In *Innovative Technologies for an Efficient and Reliable Electricity Supply (CITRES), 2010 IEEE Conference on*, pages 349–356. IEEE, 2010.

[115] H. Mohsenian-Rad. Coordinated price-maker operation of large energy storage units in nodal energy markets. *IEEE Transactions on Power Systems*, 31(1):786–797, 2016.

[116] R. Moreno, R. Moreira, and G. Strbac. A milp model for optimising multi-service portfolios of distributed energy storage. *Applied Energy*, 137:554–566, 2015.

[117] T. Morstyn, B. Hredzak, and V. G. Agelidis. Distributed cooperative control of microgrid storage. *IEEE transactions on power systems*, 30(5):2780–2789, 2015.

[118] S. J. Moura. Estimation and control of battery electrochemistry models: A tutorial. In *2015 54th IEEE Conference on Decision and Control (CDC)*, pages 3906–3912. IEEE, 2015.

[119] S. J. Moura, J. L. Stein, and H. K. Fathy. Battery-health conscious power management in plug-in hybrid electric vehicles via electrochemical modeling and stochastic control. *IEEE Transactions on Control Systems Technology*, 21(3):679–694, 2013.

[120] E. Namor, F. Sossan, R. Cherkaoui, and M. Paolone. Load Leveling and Dispatchability of a Medium Voltage Active Feeder through Battery Energy Storage Systems: Formulation of the Control Problem and Experimental Validation. *Submitted for IEEE ISGT 2016. Available online.*, 2016.

[121] A. Narayanan, T. Kaipia, and J. Partanen. Interruption reduction in secondary substations using battery energy storage systems. In *2017 IEEE PES Innovative Smart Grid Technologies Conference Europe (ISGT-Europe)*, 2017.

[122] J. Newman and W. Tiedemann. Porous-electrode theory with battery applications. *AIChE Journal*, 21(1):25–41, 1975.

[123] T. A. Nguyen and M. Crow. Stochastic optimization of renewable-based microgrid operation incorporating battery operating cost. *IEEE Transactions on Power Systems*, 31(3):2289–2296, 2016.

[124] M. Nick, R. Cherkaoui, and M. Paolone. Optimal allocation of dispersed energy storage systems in active distribution networks for energy balance and grid support. *IEEE Transactions on Power Systems*, 29(5):2300–2310, 2014.

[125] G. Ning, R. E. White, and B. N. Popov. A generalized cycle life model of rechargeable li-ion batteries. *Electrochimica acta*, 51(10):2012–2022, 2006.

[126] A. Nottrott, J. Kleissl, and B. Washom. Energy dispatch schedule optimization and cost benefit analysis for grid-connected, photovoltaic-battery storage systems. *Renewable Energy*, 55:230–240, 2013.

[127] A. Nourai, V. Kogan, and C. M. Schafer. Load leveling reduces t&d line losses. *Power Delivery, IEEE Transactions on*, 23(4):2168–2173, 2008.

[128] A. Nuhic, T. Terzimehic, T. Soczka-Guth, M. Buchholz, and K. Dietmayer. Health diagnosis and remaining useful life prognostics of lithium-ion batteries using data-driven methods. *Journal of power sources*, 239:680–688, 2013.

[129] S. Nykamp, A. Molderink, J. L. Hurink, and G. J. Smit. Storage operation for peak shaving of distributed pv and wind generation. In *Innovative Smart Grid Technologies (ISGT), 2013 IEEE PES*, pages 1–6. IEEE, 2013.

[130] C. O'Dwyer and D. Flynn. Using energy storage to manage high net load variability at sub-hourly time-scales. *IEEE Transactions on Power Systems*, 30(4):2139–2148, 2015.

[131] F. Oldewurtel, A. Parisio, C. Jones, M. Morari, D. Gyalistras, M. Gwerder, V. Stauch, B. Lehmann, and K. Wirth. Energy efficient building climate control using stochastic model predictive control and weather predictions. In *American Control Conference (ACC), 2010*, pages 5100–5105, 2010.

[132] A. Oudalov, R. Cherkaoui, and A. Beguin. Sizing and optimal operation of battery energy storage system for peak shaving application. In *Power Tech, 2007 IEEE Lausanne*, pages 621–625. IEEE, 2007.

[133] I. Papič. Simulation model for discharging a lead-acid battery energy storage system for load leveling. *Energy Conversion, IEEE Transactions on*, 21(2):608–615, 2006.

[134] C. Patsios, B. Wu, E. Chatzinikolaou, D. J. Rogers, N. Wade, N. P. Brandon, and P. Taylor. An integrated approach for the analysis and control of grid connected energy storage systems. *Journal of Energy Storage*, 5:48–61, 2016.

[135] A. Perez, R. Moreno, R. Moreira, M. Orchard, and G. Strbac. Effect of battery degradation on multi-service portfolios of energy storage. *IEEE Transactions on Sustainable Energy*, 7(4):1718–1729, 2016.

[136] H. Perez, N. Shahmohammadhamedani, and S. Moura. Enhanced performance of li-ion batteries via modified reference governors and electrochemical models. *IEEE/ASME Transactions on Mechatronics*, 20(4):1511–1520, 2015.

[137] R. D. Perkins, A. V. Randall, X. Zhang, and G. L. Plett. Controls oriented reduced order modeling of lithium deposition on overcharge. *Journal of Power Sources*, 209:318–325, 2012.

[138] M. Pignati, M. Popovic, S. Barreto, R. Cherkaoui, G. Dario Flores, J.-Y. Le Boudec, M. Mohiuddin, M. Paolone, P. Romano, S. Sarri, et al. Real-time state estimation of the epfl-campus medium-voltage grid by using pmus. In *Innovative Smart Grid Technologies Conference (ISGT), 2015 IEEE Power & Energy Society*, pages 1–5. IEEE, 2015.

[139] Pjm learning center - regulation market. http://learn.pjm.com/three-priorities/buying-and-selling-energy/ancillary-services-market/regulation-market.aspx. Accessed: 2018-04-17.

[140] G. L. Plett. Extended kalman filtering for battery management systems of lipb-based hev battery packs-part 1. background. *Journal of Power Sources*, 134(2):252–261, 2004.

[141] G. L. Plett. Extended kalman filtering for battery management systems of lipb-based hev battery packs: Part 2. modeling and identification. *Journal of power sources*, 134(2):262–276, 2004.

[142] G. L. Plett. Extended kalman filtering for battery management systems of lipb-based hev battery packs: Part 3. state and parameter estimation. *Journal of Power sources*, 134(2):277–292, 2004.

[143] G. L. Plett. Sigma-point kalman filtering for battery management systems of lipb-based hev battery packs: Part 1: Introduction and state estimation. *Journal of Power Sources*, 161(2):1356–1368, 2006.

[144] G. L. Plett. Sigma-point kalman filtering for battery management systems of lipb-based hev battery packs: Part 2: Simultaneous state and parameter estimation. *Journal of power sources*, 161(2):1369–1384, 2006.

[145] G. L. Plett. Efficient battery pack state estimation using bar-delta filtering. In *EVS24 international battery, hybrid and fuel cell electric vehicle symposium*, pages 1–8, 2009.

[146] G. L. Plett. *Battery management systems, Volume I: Battery modeling*, volume 1. Artech House, 2015.

[147] E. Prada, D. Di Domenico, Y. Creff, J. Bernard, V. Sauvant-Moynot, and F. Huet. A simplified electrochemical and thermal aging model of lifepo4-graphite li-ion batteries: Power and capacity fade simulations. *Journal of The Electrochemical Society*, 160(4):A616–A628, 2013.

[148] H. Qian, J. Zhang, J.-S. Lai, and W. Yu. A high-efficiency grid-tie battery energy storage system. *IEEE transactions on power electronics*, 26(3):886–896, 2011.

[149] D. Rakhmatov, S. Vrudhula, and D. A. Wallach. Battery lifetime prediction for energy-aware computing. In *Proceedings of the 2002 international symposium on Low power electronics and design*, pages 154–159. ACM, 2002.

[150] P. Ramadass, B. Haran, P. M. Gomadam, R. White, and B. N. Popov. Development of first principles capacity fade model for li-ion cells. *Journal of the Electrochemical Society*, 151(2):A196–A203, 2004.

[151] A. V. Randall, R. D. Perkins, X. Zhang, and G. L. Plett. Controls oriented reduced order modeling of solid-electrolyte interphase layer growth. *Journal of Power Sources*, 209:282–288, 2012.

[152] K. Rumpf, M. Naumann, and A. Jossen. Experimental investigation of parametric cell-to-cell variation and correlation based on 1100 commercial lithium-ion cells. *Journal of Energy Storage*, 14:224–243, 2017.

[153] A. Saez-de Ibarra, A. Milo, H. Gaztañaga, V. Debusschere, and S. Bacha. Co-optimization of storage system sizing and control strategy for intelligent photovoltaic power plants market integration. *IEEE Transactions on Sustainable Energy*, 7(4):1749–1761, 2016.

[154] M. Safari, M. Morcrette, A. Teyssot, and C. Delacourt. Multimodal physics-based aging model for life prediction of li-ion batteries. *Journal of The Electrochemical Society*, 156(3):A145–A153, 2009.

[155] S. Santhanagopalan, Q. Guo, P. Ramadass, and R. E. White. Review of models for predicting the cycling performance of lithium ion batteries. *Journal of Power Sources*, 156(2):620–628, 2006.

[156] D. U. Sauer and H. Wenzl. Comparison of different approaches for lifetime prediction of electrochemical systems-using lead-acid batteries as example. *Journal of Power Sources*, 176(2):534–546, 2008.

[157] A. P. Schmidt, M. Bitzer, Á. W. Imre, and L. Guzzella. Experiment-driven electrochemical modeling and systematic parameterization for a lithium-ion battery cell. *Journal of Power Sources*, 195(15):5071–5080, 2010.

[158] A. Seaman, T.-S. Dao, and J. McPhee. A survey of mathematics-based equivalent-circuit and electrochemical battery models for hybrid and electric vehicle simulation. *Journal of Power Sources*, 256:410–423, 2014.

[159] S. Shafiee, M. Fotuhi-Firuzabad, and M. Rastegar. Impacts of controlled and uncontrolled phev charging on distribution systems. In *9th IET International Conference on Advances in Power System Control, Operation and Management (APSCOM)*, page 154. IET, 2012.

[160] Z. Shen, L. Cao, C. D. Rahn, and C.-Y. Wang. Least squares galvanostatic intermittent titration technique (ls-gitt) for accurate solid phase diffusivity measurement. *Journal of The Electrochemical Society*, 160(10):A1842–A1846, 2013.

[161] Y. Shi, B. Xu, Y. Tan, and B. Zhang. A convex cycle-based degradation model for battery energy storage planning and operation. *arXiv preprint arXiv:1703.07968*, 2017.

[162] Y. Shi, B. Xu, D. Wang, and B. Zhang. Using battery storage for peak shaving and frequency regulation: Joint optimization for superlinear gains. *arXiv preprint arXiv:1702.08065*, 2017.

[163] Y. Shi, B. Xu, and B. Zhang. Optimal battery control under cycle aging mechanisms. *arXiv preprint arXiv:1709.05715*, 2017.

[164] K. A. Smith, C. D. Rahn, and C.-Y. Wang. Model-based electrochemical estimation and constraint management for pulse operation of lithium ion batteries. *IEEE Transactions on Control Systems Technology*, 18(3):654–663, 2010.

[165] E. Sortomme and M. El-Sharkawi. Optimal power flow for a system of microgrids with controllable loads and battery storage. In *Power Systems Conference and Exposition, 2009. PSCE'09. IEEE/PES*, pages 1–5. IEEE, 2009.

[166] F. Sossan, V. Lakshmanan, G. T. Costanzo, M. Marinelli, P. J. Douglass, and H. Bindner. Grey-box modelling of a household refrigeration unit using time series data in application to demand side management. *Sustainable Energy, Grids and Networks*, 5, 2016.

[167] F. Sossan, E. Namor, R. Cherkaoui, and M. Paolone. Achieving the dispatchability of distribution feeders through prosumers data driven forecasting and model predictive control of electrochemical storage. *IEEE Transactions on Sustainable Energy*, 7(4):1762–1777, Oct 2016.

[168] E. Stai, L. Reyes-Chamorro, F. Sossan, J.-Y. Le Boudec, and M. Paolone. Dispatching stochastic heterogeneous resources accounting for grid and battery losses. *IEEE Transactions on Smart Grid*, 2017.

[169] R. Stengel. *Optimal Control and Estimation*. Dover Publications, 1994.

[170] P. Stenzel, A. Schreiber, J. Marx, C. Wulf, M. Schreieder, and L. Stephan. Environmental impacts of electricity generation for graciosa island, azores. *Journal of Energy Storage*, 15:292–303, 2018.

[171] D. Stimoniaris, D. Tsiamitros, and E. Dialynas. Improved energy storage management and pv-active power control infrastructure and strategies for microgrids. *IEEE Transactions on Power Systems*, 31(1):813–820, 2016.

[172] V. R. Subramanian, V. D. Diwakar, and D. Tapriyal. Efficient macro-micro scale coupled modeling of batteries. *Journal of The Electrochemical Society*, 152(10):A2002–A2008, 2005.

[173] F. Sun, X. Hu, Y. Zou, and S. Li. Adaptive unscented kalman filtering for state of charge estimation of a lithium-ion battery for electric vehicles. *Energy*, 36(5):3531–3540, 2011.

[174] M. Swierczynski, D.-I. Stroe, A.-I. Stan, R. Teodorescu, R. Laerke, and P. C. Kjaer. Field tests experience from 1.6 mw/400kwh li-ion battery energy storage system providing primary frequency regulation service. In *Innovative Smart Grid Technologies Europe (ISGT EUROPE), 2013 4th IEEE/PES*, pages 1–5. IEEE, 2013.

[175] X. Tan, Y. Wu, and D. H. Tsang. A stochastic shortest path framework for quantifying the value and lifetime of battery energy storage under dynamic pricing. *IEEE Transactions on Smart Grid*, 8(2):769–778, 2017.

[176] S. Teleke, M. Baran, S. Bhattacharya, and A. Huang. Rule-based control of battery energy storage for dispatching intermittent renewable sources. *Sustainable Energy, IEEE Transactions on*, 1, 2010.

[177] S. Teleke, M. E. Baran, S. Bhattacharya, and A. Q. Huang. Optimal control of battery energy storage for wind farm dispatching. *IEEE Transactions on Energy Conversion*, 25(3):787–794, 2010.

[178] S. Teleke, M. E. Baran, A. Q. Huang, S. Bhattacharya, and L. Anderson. Control strategies for battery energy storage for wind farm dispatching. *Energy Conversion, IEEE Transactions on*, 24, 2009.

[179] J.-H. Teng, S.-W. Luan, D.-J. Lee, and Y.-Q. Huang. Optimal charging/discharging scheduling of battery storage systems for distribution systems interconnected with sizeable pv generation systems. *Power Systems, IEEE Transactions on*, 2013.

[180] Y. Tsividis and J. Milios. A detailed look at electrical equivalents of uniform electrochemical diffusion using nonuniform resistance–capacitance ladders. *Journal of Electroanalytical Chemistry*, 707:156–165, 2013.

[181] W. van Schalkwijk and B. Scrosati. *Advances in lithium-ion batteries*. Springer Science & Business Media, 2007.

[182] J. Vetter, P. Novák, M. Wagner, C. Veit, K.-C. Möller, J. Besenhard, M. Winter, M. Wohlfahrt-Mehrens, C. Vogler, and A. Hammouche. Ageing mechanisms in lithium-ion batteries. *Journal of power sources*, 147(1):269–281, 2005.

[183] E. Vrettos and G. Andersson. Combined load frequency control and active distribution network management with thermostatically controlled loads. In *Smart Grid Communications (SmartGridComm), 2013 IEEE International Conference on*, pages 247–252. IEEE, 2013.

[184] B. Wasowicz, S. Koopmann, T. Dederichs, A. Schnettler, and U. Spaetling. Evaluating regulatory and market frameworks for energy storage deployment in electricity grids with high renewable energy penetration. In *European Energy Market (EEM), 2012 9th International Conference on the*, pages 1–8. IEEE, 2012.

Bibliography

[185] D. Watson, C. Hastie, B. Gaudette, and M. Rodgers. Demonstrating stacked services of a battery in a wind r&d park. *IEEE Transactions on Power Systems*, 2017.

[186] B. Weißhar and W. G. Bessler. Model-based lifetime prediction of an lfp/graphite lithium-ion battery in a stationary photovoltaic battery system. *Journal of Energy Storage*, 14:179–191, 2017.

[187] C. J. Wen, B. Boukamp, R. Huggins, and W. Weppner. Thermodynamic and mass transport properties of lial. *Journal of The Electrochemical Society*, 126(12):2258–2266, 1979.

[188] Y. Wen, C. Guo, D. S. Kirschen, and S. Dong. Enhanced security-constrained opf with distributed battery energy storage. *IEEE Transactions on Power Systems*, 30(1):98–108, 2015.

[189] Y. Wen, W. Li, G. Huang, and X. Liu. Frequency dynamics constrained unit commitment with battery energy storage. *IEEE Transactions on Power Systems*, 31(6):5115–5125, 2016.

[190] D. Wu, D. Aliprantis, and L. Ying. Load scheduling and dispatch for aggregators of plug-in electric vehicles. *Smart Grid, IEEE Transactions on*, 3, 2012.

[191] D. Wu, C. Jin, P. Balducci, and M. Kintner-Meyer. An energy storage assessment: Using optimal control strategies to capture multiple services. In *Power & Energy Society General Meeting, 2015 IEEE*, pages 1–5. IEEE, 2015.

[192] M. A. Xavier and M. S. Trimboli. Lithium-ion battery cell-level control using constrained model predictive control and equivalent circuit models. *Journal of Power Sources*, 285:374–384, 2015.

[193] X. Xi, R. Sioshansi, and V. Marano. A stochastic dynamic programming model for co-optimization of distributed energy storage. *Energy Systems*, 5(3):475–505, 2014.

[194] R. Xiong, J. Cao, Q. Yu, H. He, and F. Sun. Critical review on the battery state of charge estimation methods for electric vehicles. *IEEE Access*, 6:1832–1843, 2018.

[195] B. Xu, A. Oudalov, J. Poland, A. Ulbig, and G. Andersson. Bess control strategies for participating in grid frequency regulation. *IFAC Proceedings Volumes*, 47(3):4024–4029, 2014.

[196] B. Xu, Y. Shi, D. S. Kirschen, and B. Zhang. Optimal regulation response of batteries under cycle aging mechanisms. *arXiv preprint arXiv:1703.07824*, 2017.

[197] L. Yang, J. Zhang, and H. Poor. Risk-aware day-ahead scheduling and real-time dispatch for electric vehicle charging. *Smart Grid, IEEE Transactions on*, 5, 2014.

[198] Z. Yang, K. Long, P. You, and M.-Y. Chow. Joint scheduling of large-scale appliances and batteries via distributed mixed optimization. *IEEE transactions on power systems*, 30(4):2031–2040, 2015.

[199] J. Yi, P. F. Lyons, P. J. Davison, P. Wang, and P. C. Taylor. Robust scheduling scheme for energy storage to facilitate high penetration of renewables. *IEEE Transactions on Sustainable Energy*, 7(2):797–807, 2016.

[200] C. Zhang, Y. Xu, Z. Y. Dong, and J. Ma. Robust operation of microgrids via two-stage coordinated energy storage and direct load control. *IEEE Transactions on Power Systems*, 32(4):2858–2868, 2017.

[201] S. Zhang, Y. Mishra, and M. Shahidehpour. Fuzzy-logic based frequency controller for wind farms augmented with energy storage systems. *IEEE Transactions on Power Systems*, 31(2):1595–1603, 2016.

[202] H. Zhao, Q. Wu, S. Hu, H. Xu, and C. N. Rasmussen. Review of energy storage system for wind power integration support. *Applied Energy*, 137:545–553, 2015.

EMIL NAMOR

Rue de la Blancherie 17 ⋄ 1022 Chavannes-près-Renens, Switzerland
+41 (0) 78 682 98 79 ⋄ emil.namor@epfl.ch

RESEARCH INTERESTS

· Battery energy storage systems
· Provision of services via BESSs
· Battery modelling, parameter identification

EDUCATION

École Polytechnique Fédérale de Lausanne   January 2015 - present
PhD in Energy, Power Systems Group   *Lausanne, Switzerland*
· Thesis title: "Advanced models and algorithms to provide multiple grid services with battery
storage systems" (supervisor: Dr. Rachid Cherkaoui)

Università degli studi di Padova   October 2012 - October 2014
Msc in Electrical engineering   *Padova, Italy*
· Thesis title: Insulation coordination of a 220 kV hybrid electrical substation - comparison be-
tween analytical analysis according to IEC standard and numerical simulations (supervisor: Prof.
Roberto Caldon).
· Final mark: 110/110.

École Centrale de Lille   September 2010 - June 2012
Msc in Industrial Engineering   *Lille, France*
· Degree obtained within the double degree program "Top Industrial Managers for Europe" (TIME).
· Final report title: "Experimental validation of a supercapacitor equivalent circuit model" (super-
visor: Prof. Xavier Guillaud).

Università degli studi di Padova   October 2008 - November 2012
Bsc in Energy engineering   *Padova, Italy*
· Thesis title: "Experimental validation of a supercapacitor equivalent circuit model" (supervisor:
Prof. Roberto Benato).
· Final mark: 104/110.

PROFESSIONAL EXPERIENCE

S.T.E. Energy   August 2013 - September 2013
Intern   *Padova, Italy*
· Insulation coordination analysis for the HV substation of a hydro-power plant and assessment of
its compliance to IEC 60071 standard.
· Time domain simulations of electrical transients through DigSilent PowerFactory.

IZEN Energy Systems   January 2011 - February 2011
Intern   *Lille, Belgium*
· Support in the project management for the realization of a 1 MW photovoltaic power plant.

SCIENTIFIC PUBLICATIONS

Journals

1. Torregrossa D.; Bahramipanah M.; Namor E.; Cherkaoui R.; Paolone M. "Improvement of dynamic modeling of supercapacitor by residual charge effect estimation." IEEE Transactions on Industrial Electronics 61.3 (2014): 1345-1354.

2. Sossan F.; Namor E.; Cherkaoui R.; Paolone M. "Achieving the dispatchability of distribution feeders through prosumers data driven forecasting and model predictive control of electrochemical storage." IEEE Transactions on Sustainable Energy 7.4 (2016): 1762-1777.

3. Namor E.; Torregrossa D.; Cherkaoui R.; Paolone M. "Parameter identification of a lithium-ion cell single-particle model through non-invasive testing." Journal of Energy Storage 12 (2017): 138-148.

4. Namor E.; Sossan F.; Cherkaoui R.; Paolone M. "Control of Battery Storage Systems for the Simultaneous Provision of Multiple Services." IEEE Transactions on Smart Grid (2018).

5. Fabietti L.; Gorecki T.; Namor E.; Sossan F.; Paolone M.; Jones C. "Enhancing the dispatchability of distribution networks through utility-scale batteries and flexible demand." Energy and Buildings (2018)

Conferences

6. Sossan F.; Torregrossa D.; Namor E.; Cherkaoui R.; Paolone M. "Control of a battery energy storage system accounting for the charge redistribution effect to dispatch the operation of a medium voltage feeder." PowerTech, 2015 IEEE Eindhoven. IEEE, 2015.

7. Namor E.; Torregrossa D.; Sossan F.; Cherkaoui R.; Paolone M. "Assessment of battery ageing and implementation of an ageing aware control strategy for a load leveling application of a lithium titanate battery energy storage system." Control and Modeling for Power Electronics (COMPEL), 2016 IEEE 17th Workshop on. Ieee, 2016.

8. Namor E.; Sossan F.; Cherkaoui R.; Paolone M. "Load leveling and dispatchability of a medium voltage active feeder through battery energy storage systems: Formulation of the control problem and experimental validation." PES Innovative Smart Grid Technologies Conference Europe (ISGT-Europe), 2016 IEEE. IEEE, 2016.

9. Namor E.; Sossan F.; Torregrossa D.; Cherkaoui R.; Paolone M. "Battery storage system optimal exploitation through physics-based model predictive control." PowerTech, 2017 IEEE Manchester. IEEE, 2017.

10. Fabietti L.; Gorecki T.; Namor E.; Sossan F.; Paolone M.; Jones C. "Dispatching active distribution networks through electrochemical storage systems and demand side management." Control Technology and Applications (CCTA), 2017 IEEE Conference on. IEEE, 2017.

11. Gupta R.; Sossan F.; Scolari E.; Namor E.; Fabietti L.; Jones C.; M Paolone "An ADMM-based Coordination and Control Strategy for PV and Storage to Dispatch Stochastic Prosumers: Theory and Experimental Validation." Power Systems Computation Conference (PSCC), 2018. IEEE, 2018.

12. Schiapparelli G.; Namor E.; Sossan F.; Cherkaoui R.; Massucco S.; Paolone M. "Quantification of primary frequency control provision from battery energy storage systems connected to active distribution networks." Power Systems Computation Conference (PSCC), 2018. IEEE, 2018.

13. Namor E.; Sossan F.; Scolari E.; Cherkaoui R.; Paolone M. "Experimental Assessment of the Prediction Performance of Dynamic Equivalent Circuit Models of Grid-connected Battery Energy Storage Systems" PES Innovative Smart Grid Technologies Conference Europe (ISGT-Europe), 2018 IEEE. IEEE, 2018. (accepted)

14. Sossan F.; Scolari E.; Namor E.; Paolone M. "Myopic and Predictive Control Policies for Photovoltaic and Storage-based Energy Ecosystems: a Technical and Economical Assessment." 35th European PV Solar Energy Conference and Exibition (EU PVSEC 2018), 2018 (accepted).

PATENTS

Sossan F.; Namor E.; Paolone M. "System and Method for Dispatching an Operation of a Distribution Feeder with Heterogeneous Prosumers." U.S. Patent Application No. 15/633,788.

RESEARCH PROJECTS

Osmose   January 2018 - present
- Demonstration of system integration with smart transmission grid and storage technologies with increasing share of renewables
- Project financed by the European Union's Horizon 2020 research and innovation program under agreement no. 773406

EPFL Battery Energy Storage System   January 2015 - June 2018
- 500 kWh energy storage pilot system for the control of distribution grids integrating distributed generation
- Project financed by Swiss Vaud Canton within the initiative "100 millions pour les energies renouvelables et lefficacité energétique

INDUSTRIAL COLLABORATIONS

Leclanché   October 2017 - present
- Definition of the specifications for the Battery Energy Storage System to be installed in Onnens in the context of the REel-DEMO project

Natron Energy   August 2017
- Independent testing of sodium-ion cell prototypes

SUPERVISED STUDENTS

- Abdoul Haime A. (1) "Evaluation of SOC estimation algorithms for a grid scale battery system" B.Sc. semester project, Spring semester 2015-2016.
- Numa Gueissaz N., "Primary frequency regulation through distributed storage", M.Sc. semster project, Autumn semester, 2016-2017.
- Doppler S.; "Li-ion battery characterization through electrochemical impedance spectroscopy" B.Sc. semester project, Spring semester 2016-2017.
- Schiapparelli G., "Primary frequency control provision from battery energy storage systems" M.Sc. thesis project, Spring semester 2016-2017.
- El Bachir Wade M.; "Efficient State Estimation of Li-ion cells within a battery pack" B.Sc. semester project, Autumn semester 2017-2018
- Abdoul Haime A. (2) "Provision of multiple services with battery storage systems" M.Sc. semester project, Autumn semester 2017-2018.
- Dussaux P.; "Design of a battery pack for a Fomula Student car" M.Sc. semester project, Spring semester 2017-2018.

TEACHING EXPERIENCE

· Assistant lecturer for the "Energy Conversion", "Laboratory in Energy Conversion" and "Electrical Networks" courses, B.Sc. in Electrical Engineering, EPFL, 2016-present

PEER REVIEWS

· Elseview Sustainable Energy, Grids and Networks Journal, since 2016
· IEEE PES Innovative Smart Grid Technologies Coneference Europe (ISGT Europe), 2017
· 20th Power Systems Computation Conference (PSCC), 2018

LANGUAGE SKILLS

Italian	Mother tongue
English	Full professional proficiency
French	Full professional proficiency
German	B1 Level (Zertificat Deutsch, 2013)
Slovenian	B1 Level